SOME ASPECTS OF THE AERODYNAMICS OF BLUFF BODIES IN PROXIMITY TO THE GROUND

by

David W. Hurst, B.Sc.(Hons.)

Thesis submitted for the degree of Doctor of Philosophy
in the Faculty of Engineering and Applied Sciences,
University of Southampton.

August, 1981

UNIVERSITY OF SOUTHAMPTON

ABSTRACT

FACULTY OF ENGINEERING AND APPLIED SCIENCE

DEPARTMENT OF AERONAUTICS AND ASTRONAUTICS

Doctor of Philosophy

SOME ASPECTS OF THE AERODYNAMICS OF BLUFF BODIES IN PROXIMITY TO THE GROUND

by David William Hurst

A series of tests has been undertaken to investigate the aerodynamics of a simple rounded edge bluff body mounted in proximity to a ground plane. The tests were carried out with the model mounted at zero degrees yaw in a wind tunnel using both moving and stationary ground simulation. Several configurations were available to produce different model taper and cambers.

The overall forces and surface pressure distribution, including the base area, were recorded throughout large incidence ranges with the model mounted at two ground clearances. Extensive flow visualization was undertaken in the wind tunnel with additional base flow visualization carried out in a water tunnel.

It was observed that two different base flowfields and associated base surface pressure distributions existed. The nature of the flowfield was primarily dependant on the magnitude of the trailing edge separation angles.

Large variations in the overall model forces were recorded when the ground belt was stopped due to the thick ground plane boundary layer. Vertical total pressure traverses under the model showed that no ground plane boundary layer was produced when the belt was moving synchronously with the freestream airflow. The changes in underbody flow characteristics produced by the attachment of an airdam and distributed roughness were also examined.

Surface pressure distributions obtained in the wind tunnel using vehicle models were compared with distributions recorded during full-scale tests. Good agreement was observed between the two sets of results.

A survey of the theoretical techniques employed to calculate the surface pressure distribution of a bluff body was carried out. A source/vortex panel method was used to calculate the pressure distribution around the bluff body used in these tests.

ACKNOWLEDGEMENTS

The author wishes to thank his supervisor, Mr. K. Burgin, for the assistance and encouragement given during this research programme and in addition to Professor G. M. Lilley for his comments.

The wind tunnel technical staff, Mr. J. Graham, Mr. M. Grinter and Mr. D. A. Odgers are thanked for all their help given during the experimental wind tunnel test programmes.

The assistance given by Mr. G. A. Allcock and the staff of the Electronics Laboratory must be acknowledged.

To the typist, Mrs. P. V. Ayre, thanks are due for her patience in coping with the manuscript.

Mr. R. Herd of March Engineering Ltd., is gratefully acknowledged for providing the racing car model.

The author was in receipt of the Spitfire Mitchell Research Studentship during the period of this research and also acknowledges the Science Research Council for additional financial support.

LIST OF CONTENTS

LIST OF SYMBOLS

α	angle of incidence
C_D	drag coefficient
C_{DW}	drag coefficient of wheel
C_L	lift coefficient
C_{LW}	lift coefficient of wheel
$\frac{dC_L}{d\alpha}$	lift curve slope
C_M	pitching moment coefficient
$\frac{C_M}{C_L}$	rate of change of pitching moment with lift
C_p	pressure coefficient
C_{pb}	base pressure coefficient
δ^*	boundary layer displacement thickness
H	ground clearance
h	model base height
L	body length
L/D	lift/drag ratio
P_{TL}	local total pressure
P_{S_∞}	freestream static pressure
S_p	source panel area
σ	source strength
V	freestream velocity
V_I	total induced velocity
V_{QS}	source induced velocity
V_{QV}	vortex induced velocity
Γ	vortex strength
X/L	fraction of body length
Forebody	this is used to designate all the body upstream of the base

LIST OF FIGURES

LIST OF TABLES

LIST OF PLATES

INTRODUCTION

The characteristics of the flow around streamlined bodies have been thoroughly investigated and are now well understood, whereas the aerodynamics of three dimensional bluff bodies, of which road vehicles are an important example, have not received the same attention. A major difference with the flow around a bluff body is the high suction present in the complex wake flow downstream of the body, which results in the generation of a large drag force.

The aerodynamic drag of a road vehicle can be typically 50% of the total drag force when it is travelling at a speed of 90 kph. The recent rise in the price of petroleum fuel has greatly increased operating costs, therefore the lowering of aerodynamic drag would result in a significant reduction in these costs. For this reason, further investigation of the parameters which determine the magnitude of the aerodynamic drag of vehicles is necessary.

Although the reduction of the drag of the vehicle is of great importance there is also a need, as their maximum speed and acceleration increase, to improve the stability not only in cross wind situations but also during acceleration and braking when relatively large ground clearance and incidence changes can be encountered with possible large adverse effects on the vehicle handling characteristics. The solution of these problems, reduction of drag and improvement of stability, requires a deeper understanding of the aerodynamics of bluff bodies in ground effect. Although the vehicle manufacturers have undertaken many experimental programmes they have followed the optimization approach and concentrated on the effects produced by detail changes in body geometry because of the limitations imposed by the conventionally accepted vehicle shapes. Therefore in order to obtain a deeper understanding it is necessary to undertake fundamental ground effect bluff body research programmes to determine the effect of basic parameter changes. The flow field around a bluff body in ground effect is complex, especially near the base area, and is therefore difficult to model mathematically with the result that the majority of investigations on this subject, to date, have been of an experimental nature.

The experimental investigations of three dimensional bluff bodies in ground effect commenced with studies of thick, low aspect ratio wing bodies in tests undertaken by Stollery[35] on a NACA 0010 wing section and Waters[39] on 40% thick ellipse and 20% thick half ellipse sections of aspect ratios varying from 0.58 to 1.00. Three symmetrical and cambered

streamlined bodies of aspect ratio 0.25 and thickness to chord ratio of 9%, 18% and 27% were tested by Carr[9]. Although these were not true three dimensional bluff bodies with blunt bases, they allowed the importance of the various test parameters, e.g. incidence, thickness, ground clearance and camber to be determined. Stollery[35] also tested a whale like body of aspect ratio 0.36 and thickness to chord ratio of 0.21. The base area was progressively increased by the blunting of the trailing edge. The blunting produced a large increase in drag with little variation of the lift force.

Most road vehicles are of a moderately bluff shape with little or no camber and can be approximated by rectangular blocks, either singly to represent truck shapes or as a composite to form a saloon car geometry. For this reason simple rectangular blocks have been the subject of many investigations, e.g. Carr[8], to determine the effect of ground clearance, edge radius and yaw angle. Howell[20] concentrated on the measurement of the wake flow properties and Nakaguchi[24] varied the length to width ratio of the bodies. There has been a large amount of work undertaken, of an applied nature, to examine possible methods of reducing the drag of vehicles, especially trucks, but the methods employed were constrained by practical considerations. However, these investigations have been augmented by fundamental tests on simple rectangular blocks where the changes produced by the addition of splitter plates, guide vanes and base cavities have been investigated.

The majority of these tests were carried out with the model mounted above a fixed ground board and the incorrect flow simulation could introduce significant errors in the results. The errors introduced by a ground plane boundary layer have been examined by many investigators, e.g. Berry[5], East[13], Fackrell[15] and Hucho[21] and it was found that in general the removal of the boundary layer produced an increase in $\partial C_L/\partial_\alpha$, a decrease in lift but little change in the drag force.

In all the investigations undertaken of bluff bodies in ground effect it has been shown that the changes produced by the variation of ground clearance, body geometry and incidence are complicated and inter-related. A requirement was therefore seen to exist for an experimental programme to determine the effects produced on the overall forces of a three dimensional bluff body in ground effect by the variation of all three of the primary parameters in the unyawed state, i.e. ground clearance,

body geometry and incidence. To obtain a deeper understanding of the changes produced by alterations in the test variables than can be obtained from analysis of the overall force measurements, the pressure distribution over the entire model surface, including the base area, was examined.

The tests were carried out using a rectangular three dimensional bluff body with rounded leading edges mounted above the moving ground belt facility in the University of Southampton 2.1m x 1.7m wind tunnel at airspeeds of 26 m/sec with the ground belt moving synchronously with the airflow and stationary. The model geometry could be altered to provide different upper and lower surface side elevations, base areas, underbody channel sections and camber. The combination of ground clearances and incidences tested covered the range likely to be encountered by a road vehicle during steady state, acceleration and braking conditions. The higher incidences at which the model was tested are limited in their application to road vehicles but they can be used in conjunction with the flow field produced by large rear loading cargo aircraft when they are in close proximity to the ground during take off and landing.

All the bluff body experimental programmes mentioned have been carried out in the artificial environment produced by the wind tunnel which does not usually provide correct simulation of the earth's boundary layer and atmospheric turbulence levels. It has been shown in several wind tunnel test programmes that the presence and size of any free stream turbulence, introduced in these cases by grids mounted upstream of the working section, can have a significant effect on the forces generated by a bluff body. In addition to this there are problems introduced by the model and full scale Reynolds number discrepancy and the interference produced by the blockage of the model on the constrained wind tunnel airflow. The testing of full scale vehicles in their natural environment must be undertaken to allow comparison with the results obtained during the model scale tests carried out in the wind tunnel to determine the magnitude of the errors introduced by inaccurate flow field simulation. Several investigators have undertaken comparison studies of this nature. Carr[10] achieved good correlation between the centre line pressure distributions obtained from the road tests of a full scale vehicle and wind tunnel tests using a scale model of the vehicle. The most difficult area to achieve accurate flow representation is the under body channel and this region has received detailed examination by Buckley .

It was decided to investigate the accuracy of the results obtained in the University of Southampton 2.1m x 1.7m wind tunnel during the testing of an $\frac{1}{8}^{th}$ scale model of a container lorry, by comparison with the results recorded during the road testing of the full scale vehicle. Good correlation between the two sets of results was obtained, as shown in Ref. 2.

It has already been mentioned that the flow field around a three dimensional bluff body in ground effect is very complicated, especially near the base region. This has led to great difficulty in the development of mathematical models which would enable adequate prediction of the surface pressure distribution. There have been two approaches towards the solution of the three dimensional problem. The first is to solve the potential flow problem for the flow over the body by the representation of the wake and body surfaces with singularities. Using this approach several investigators have employed source and doublet distributions, e.g. Ahmed[1], over the body and wake wetted surfaces respectively while Stafford[33] used a vortex lattice representation of the surfaces with a source to represent the wake flow. The ground plane streamline is produced by the presence of an image of the model. Although the potential flow assumed seems far removed from a real viscous fluid, it still produces adequate prediction of the surface pressure distribution for all except extreme body geometries, where large areas of separated flow are present. The assumption of inviscid flow introduces a major drawback in this approach because of the need to apply empirical data to specify the flow conditions in the areas which are dominated by the viscous separated shear layers, near the separation points and over the wake surface.

The second approach for the theoretical solution of the flow field around bluff bodies in ground effect was used by Hirt and Ramshaw[18], who employed the full Navier Stokes equations to develop a finite difference method by which the turbulent flow past bluff bodies with or without sharp edges can be calculated. Further development of this method is limited by two factors, firstly the lack of knowledge about turbulent shear stresses, and secondly by the inability of the size and speed of the present generation of computers to allow an adequate grid of control points for accurate flow definition.

It is accepted that theoretical methods will not replace experimental testing for many years. However they can be employed very

successfully as a guide during experimental work to provide additional understanding of the flow field. For this reason a potential flow solution is developed and theoretical results are compared with the empirically derived results obtained during the wind tunnel tests.

SECTION 1

EXPERIMENTAL PROGRAMME

1.1 DESCRIPTION OF MODEL

The principal model used for the investigations described in this thesis is shown in Figs. 1 and 2 and Plates 1 and 2. The main dimensions are as follows:-

length 1.07m (42")
span 0.46m (18")
height 0.31m (12")

The wooden model was of basic rectangular shape, in both side and plan elevations, with the nose of 15.2cm (6") radius in the vertical and horizontal planes. The longitudinal edges of the upper and lower surfaces were radiied 5cm (2") and the knee of the ramp upsweeps were also radiied 2.5cm (1"). The radii were incorporated to prevent excessive sharp edge flow separation and the formation of vortices over the model surface. A problem encountered during previous testing of bluff bodies without a blunt base, has been the movement of the position of the base flow separation over large distances of the body length when changes of model incidence or ground clearance were made. It is advantageous for a fundamental study, as described in this thesis, to remove the complications introduced into the analysis of the flow field by movement of the position of the base flow separation. This was achieved by the inclusion of a blunt base area into the design of the model. The problems encountered when attempting a theoretical solution of the flow field are also greatly reduced when the separation points are fixed.

The geometry of the rear 0.46m (18") of the model could be varied by the alteration of the three upper and three lower sections of upsweep angles 0°, 10° and 20° i.e. nine combinations. This enabled many different underbody channel flow conditions to be investigated when incidence and height variations were added as further variables.

Similarly, many upper surface configurations could be researched. The changes in the rear geometry of the model also altered the initial conditions of the model wake flow. This was achieved by changing, firstly, the flow characteristics over the model surfaces upstream of the base, secondly the base flow separation angles and finally the base area of the model. Five different base areas could be produced which were associated with the base heights, 15.2cms (6"), 22.9cms (9"), 30.5cms (12"), 38.1cms (15") and 45.7cms (18").

The model was attached to the three component mechanical balance mounting arms by a horizontal cylindrical bar of 2cm diameter which passed through the model at the position shown in Fig. 1. The bar was extended 0.15m either side of the model, to reduce the interference of the balance support arms on the airflow around the model. The pitching moment wire, which by adjustment of its length provided the incidence changes, was attached to the nose mounting point for the force and overall pressure measurements. For the later nose and base pressure investigations the wire was attached to a bar mounted inside the model and passed through a slit in the upper surface. Both arrangements are shown in Fig. 2.

The rear and centre sections of the model were hollow to allow easy installation of the surface pressure tappings, 0.045" internal diameter, in these areas. Their positioning over the model surface is displayed in Fig. 3. The number of tappings on the model was limited by the 124 measuring ports of the pressure scanning system. The distribution of the tappings covered only the port half of the model because of the symetrical nature of the airflow in the working section. The majority of the tappings were placed on the upper and lower flat surfaces of the model with reduced coverage given to the nose section because of the difficulty of inserting and laying the tubes along the surface of the solid wooden nose. The side surface of the model was also given reduced coverage, especially at the rear, due to the influence of the cylindrical model mounting bar and its wake on the local flow field. The number of tappings in the base was limited to six, during the first series of pressure investigations, and these were spaced to determine if any large pressure changes occurred over the base area. No tappings were placed directly on either of the ramp knees because of the local high/low velocities at these points and their large effect on the surface isobar contours to be obtained later.

After the first series of pressure distributions had been analysed it was discovered that the definition achieved by the nose tappings was not precise enough to allow accurate positioning of the stagnation point. Large variations in the levels of suction over the base area of the model had been recorded. A large number of tappings were therefore inserted in these areas, as displayed in Figs. 3 and 4, to enable further examination. A hollow glass fibre nose section was manufactured to facilitate the easier insertion of the pressure tappings, with the original wooden nose used as the mould. The ordinates of the surface pressure tappings are listed in Table 2. For a later series of tests supervised by the author and undertaken by Frost[16], the coverage of the pressure tappings was increased to include the starboard half of body. This was to allow the examination of the surface pressure distribution when the angle of yaw of the body was varied. The symmetrical pressure distributions obtained during these later tests when the body was mounted at zero degrees yaw angle, clearly demonstrated that the assumption of flow symmetry was correct.

During both the overall force and pressure investigations several configurations of the model were tested with an airdam and/or an area of distributed roughness fitted to the undersurface of the model. The airdam was attached to the undersurface of the nose at the position indicated in Fig. 2. It was aligned in the spanwise direction and lay in the vertical plane when the model was at an incidence of zero degrees. Its dimensions were 30.5cm (12") long x 2cm (0.75") high. The area of distributed roughness that was attached to the undersurface of the model centre section covered an area of 30.5cms (12") x 35.3cms (14") as displayed in Fig. 2. It consisted of a sheet of thin plastic with short cylindrical protrusions on its outer surface which were equally spaced in both the streamwise and spanwise directions, their size and spacing are shown in Fig. 5. The pressure tappings were extended through to the outer surface of the plastic sheet for the measurement of the surface pressure distribution when the roughness was in position.

Geometry of Model

There are nine geometries of the bluff body model that have been tested in the present investigation. To simplify their description in the test it has been necessary to introduce a shorthand notation, in the form of two hyphernated numbers as follows:

1-2

where 1 denotes the upper surface ramp angle.

2 denotes the lower surface ramp angle.

e.g. O-2O, denotes the zero degree upper surface geometry fitted in conjunction with the 20 degree lower surface geometry.

1.2 TEST PROGRAMME

The bluff body model, shown in Fig. 1, was used in an extensive test programme undertaken in the University of Southampton 2.1m x 1.7m low speed wind tunnel with ground simulation provided by a moving belt facility. The tunnel and its ancilliary equipment, e.g. balance, are described in detail by Davies[12].

The model was mounted throughout the test programme in the working section of the tunnel on the support arms of the three component mechanical balance positioned above the wind tunnel, as shown in Fig. 7. The balance measured the lift and drag forces and pitching moment generated by the model. The pitching moment was measured by a wire which was attached to the nose of the model in all cases except during the measurement of the detailed nose pressure distributions when its attachment point was moved to a downstream position, as shown in Fig. 2, to remove any interference with the flow over the nose.

Changes in the incidence of the model were made by adjustment of the length of the pitching moment wire with rotation occurring about the axis of the mounting bar. The length of the balance support arms was adjustable to enable the alteration of the model ground clearance.

The majority of the tests were carried out at an airspeed of 26 m/sec. which produced a Reynolds number of 1.8×10^6 based on body length.

The sequence of the test programme was:-

(1) flow visualization of forebody and wake flows
(2) overall force measurements
(3) surface pressure distributions
(4) time dependence of the pressure results
(5) total pressure traverses across the channel between body undersurface and ground

1.2.1 Bluff body flow visualization: Prior to the commencement of any of the force or pressure tests, an investigation into the position of natural boundary layer transition was undertaken

using the china clay technique developed by Richards[29]. The nose section of the model was sprayed with a china clay mixture, as listed in Table 3, which after drying produced a smooth white surface. Immediately prior to the commencement of the tests this surface was sprayed again with Methyl Salicylate, which returned the surface to its original matt black appearance. The heat transfer coefficient of a boundary layer increases as transition occurs from the laminar to turbulent state. During the test the different evaporation rates of the two boundary layer states over the nose surface allowed the determination of the transition line downstream of which the turbulent boundary layer had evaporated the Methyl Salicylate and returned the surface to the white, china clay, colour. The natural position of transition occurred at approximately ten per cent of the model length with only small variations produced by changes in incidence or ground clearance. It was decided to artificially trip the boundary layer at ten per cent of the model length using a 0.6cm wide band of carborundum grit (grade 80) to ensure uniformity during the tests.

In addition to the visualization of the transition point of the boundary layer, extensive flow visualization was undertaken using wool tufts. The surface flow was examined using white wool tufts of approximately 4cm length distributed over the surface. The wake flow and the under body channel flow were visualized using long wool streamers with small, light paper cones attached to their downstream ends. Typical results obtained using these techniques are displayed in Plates 3-8. Examination of the photographs taken during this phase of the testing produced a large amount of information which complemented that obtained from the pressure distributions and traverses to enable a deep understanding of the flow to be gained.

Flow visualization of the wake flow was also undertaken using a smaller model mounted in a water tunnel and results obtained during this investigation are

displayed in Plates 9-18.

1.2.2 Overall force measurements: It was necessary to undertake the force investigations independent of the pressure tests because of the unknown forces exerted by the surface pressure connecting tubes. The determination of the overall forces generated by the model was undertaken before the measurement of the surface pressure distributions because the ease of obtaining the overall coefficients. This allowed the investigation of all possible test configurations and observation of any trends which enabled efficient choice of the configurations to be tested in the more complex and time consuming surface pressure investigations.

The model was tested in each of its nine ramp geometries at two ground clearances, 4cms and 14.5cms. These distances were the gaps between the horizontal undersurface of the model and belt surface when the model was mounted at 0° incidence. The lift, drag and pitching moment generated by the model were recorded at incidences throughout the possible range, limited by the nose or trailing edge fouling the belt, at increments of three degrees, as shown in Table 1. At the lower ground clearance the tests were repeated with the belt stationary to check the sensitivity of the forces on the body to the ground plane boundary layer. Incorrect interaction between the boundary layers on the body and fixed ground plane could have resulted in misleading effects produced by the ground plane. It also allowed comparison with results obtained when ground simulation was produced using a fixed ground board, although the rough surface texture of the belt resulted in a thicker boundary layer than that developed over a conventional smooth ground board.

It was decided to undertake a series of tests to obtain both force and pressure data to allow examination of the effects produced by the alteration of the flow conditions in the channel underneath the body which were produced by the attachment of an airdam to the undersurface of the nose, and also an area of distributed roughness to the lower surface of the model, as shown in Fig. 2. Only one body geometry, zero degree top surface and the ten degree lower ramp, was tested with the

devices attached, for reasons described in Section 3.

The force coefficients obtained were based on the frontal area of the basic model with no upswept ramps fitted, 0.137 sq.m and the reference length for the moment coefficients was taken as the length of the body, i.e. 1.07m (42").

1.2.3 Bluff body surface pressure distributions: This section of the investigation was undertaken in two stages. During the first the emphasis was placed on recording the distributions over the upper and lower surfaces and side of the model. Insufficient definition was obtained over the nose and base of the model during this phase of the testing and it was necessary to repeat the first series of tests to obtain adequate definition in the distributions over these areas. The surface pressure distributions were obtained for the selected configurations, listed in Table 1, which had been previously tested during the series of force investigations. The 0-10 geometry was selected as being representative of typical conditions produced and was used for further tests with the ground belt stationary and the airdam and/or distributed roughness attached.

1.2.4 Time dependence of surface pressures: All the surface pressures that were measured by the scanning system were time averaged values due to the length of the transmission tubing between the model and pressure transducer and also the integrating voltmeter used in the data acquisition system. It was thought that these values, especially in the base area, may fluctuate by appreciable amounts and therefore the mean pressures obtained using the scanning system could be misleading. To investigate this possible problem, the time history of the pressures at several points were recorded using a transducer mounted flush to the model surface, the output of which was connected directly to a pen recorder. The areas chosen for the investigation were in the base region and near the longitudinal edges of the rear ramp sections as it was thought that the fluctuations would be greatest in these areas.

1.2.5 Underbody channel total pressure traverses: The flow under the model was of great importance and in order to investigate the flow conditions in the underbody channel, vertical total pressure traverses were measured on the centre line at two longitudinal stations for the model geometries listed in Table 22, mounted at the lower ground clearance, i.e. H = 4cms. The main objectives of these traverses were to determine the effect of test configuration, body geometry and incidence on the channel flow properties, i.e. model boundary layer thickness, depth of any separated flow regions, relative maximum velocities in the channel and also the thickness of the ground belt boundary layer when the belt was stationary.

1.2.6 Racing car aerodynamics: Tests were carried out on a one third scale model of a racing car which was mounted in the wind tunnel over a moving ground belt facility. The basic parameters of the model, e.g. ground clearance, incidence and geometry, were altered during the test programme with the aim of increasing the downforce generated. The overall forces generated by the model were measured using the three component mechanical balance. Pressure distributions over the undersurface of the car were obtained from sixty-four tappings distributed over this area and emphasis was placed on these, during the analysis of the results, to obtain an understanding of the flow field in the channel between the car undersurface and ground. The distribution of the undersurface tappings and principal model dimensions are shown in Fig. 88.

1.2.7 Full-model scale pressure correlation: The surface pressure data obtained from tests on an eighth scale articulated container vehicle model in the wind tunnel and the full scale vehicle on the test track were compared to determine the accuracy obtained by the wind tunnel simulation of the conditions in the natural environment. A system incorporating a Scanivalve module and small cassette tape recorder was developed to improve the techniques that have been previously employed for the recording and analysis of the pressure data

during the full scale tests. This work was undertaken as part of an investigation into the generation of water spray by road vehicles[2].

1.3 MOVING GROUND FACILITY

In view of the greater interest shown in ground effect and vehicle aerodynamics, much research has been undertaken in the development of an accurate representation of the ground plane in the wind tunnel. Most investigators agree that the moving ground belt produces the most accurate simulation of the real flow conditions.

To obtain accurate representation of the ground plane in the Dept. of Aeronautics 2.1m x 1.7m low speed wind tunnel, a moving belt facility has been developed. The apparatus is shown in Plate 19 and Fig. 7. When this facility is required for use in the wind tunnel a three metre length of the working section floor is removed and the ground belt, mounted in its steel framework, is raised from below the tunnel into position with the belt surface at a height of 7.5cms above the level of the original tunnel floor. The rubber impregnated canvas belt is 1.07m (42") wide and the distance between the crests of the two 33cms (13") diameter crowned rollers is 2.03m (80"). The upper half of the belt rests on a base board which is positioned at the same height as the crests of the rollers. The upper surface of the base board is coated with P.T.F.E. to reduce the frictional force between the belt and board surfaces. The lower half of the belt loop is supported by a small guide roller which assists the tracking of the belt.

The facility is powered by a 30 kW (40 H.P) hydraulic motor which drives the downstream roller through a toothed transmission belt. The speed of the belt is monitored using an electronic tachometer fitted to the free running upstream roller. The speed of the belt is infinitely variable between 0m /sec to its maximum operational speed of approximately 30m/sec. The rollers were accurately balanced to ensure that no mechanical vibration was experienced throughout the operational speed range of the belt.

A 30cm(1') chord rounded leading edge board spans the tunnel immediately upstream of the belt at the same height as the belt, i.e. 7.5cms above the original tunnel floor. The lead in board is 0.95cms (⅜") thick, and the tunnel floor boundary layer which at this station in the tunnel is 4cms (1.5") thick, is removed under the board. No

suction is applied to the surface of the board to remove the thin boundary layer produced along its length. It is removed by the boundary layer control created by air passing through the small gap between the trailing edge of the board and the belt. Typical velocity traverses close to the belt surface measured at its mid point, both moving and stopped, are shown in Fig. 8. The boundary layer thickness when the belt is stopped is greater than that produced on a conventional ground board due to the rough texture of the belt surface. The five per cent velocity deficit recorded just above the belt when it was moving synchronously with the free stream airflow can be removed, if required, by slight overspeeding of the belt surface.

There are two major factors which limit the maximum operating speed of the facility. The first of these is the lateral tracking of the belt which prevents its central running. This problem was reduced by crowning the two rollers but can be totally removed by making a small realignment of the upstream free running roller. This adjustment can be adequately carried out manually and there is no intention of introducing an automatic tracking system using, for example, photo electric sensors.

The second limit on the maximum running speed of the belt is the lifting of the belt away from the ground board. This is caused by the suctions present above the belt when the tunnel is running and also the large centrifugal force generated by the belt at high speeds. The problem can be reduced by applying suction through the base board to the undersurface of the belt. The volume underneath the base board is divided into three independent spanwise plenum chambers through which differential pressure can be applied to the upstream, central or downstream areas of the belt. Although the suction removes the problem at low speeds, the lifting of the belt remains the limit to the maximum speed attainable and restricts the present belt speed to approximately 30m/sec., which restricts the airflow to this speed for synchronous belt and tunnel airflow operation.

1.4 MEASUREMENT AND ANALYSIS OF PRESSURES

During the test programme emphasis was placed on the analysis of the results obtained from the extensive pressure plotting of both the basic bluff body model and the racing car model. In order to enable both rapid monitoring of the pressures in the wind tunnel and fast

reduction of the data, it was necessary to develop an efficient recording and analysis system which incorporated several Scanivalve modules, data logging system and computer to fill the requirement. Multi bank manometers were not used because of both the slow recording time and the laborious analysis of the results.

The pressure tubes 0.16cm ($\frac{1}{16}$") I.D., were led from the model and connected, using a junction board situated below the working section of the tunnel, to larger bore pipes 0.48cm ($\frac{3}{16}$") I.D., which were permanently connected to a two ladder Scanivalve system. The length of the pressure tubes from the model to the scanning transducer was of the order of five metres producing a settling time of 45 secs. for the system. This duration of time was allowed to elapse after the airflow and moving ground had attained their correct speeds before a survey of the pressures was commenced. The averaging effect of the long length of tubing which connected the model tappings to the Scanivalve modules precluded the use of the system for the measurement of time dependant pressures and can therefore only be used in situations where time-averaged values are meaningful. Each time the stepping motor rotated the Scanivalve module to monitor a new port the change in volume below the diaphragm of the transducer was 0.005cu.ins. i.e. negligible compared to the volume of the long length of connecting tubing. Hence the inter port settling time before the new pressure could be recorded was minimal.

Four Scanivalve modules were incorporated into the system, each capable of sequentially monitoring sixty four pressures. In order to improve the accuracy of the system every alternate Scanivalve port was employed to measure the dynamic head of the freestream flow. This allowed the monitoring of any slight velocity variation within the tunnel working section during a scan of the ports. Another port in each module was used as a reference zero value, resulting in each transducer being capable of measuring thirty one model pressures. The transducers installed in the system were of the capacitance type manufactured by Setra Systems with ranges as follows:

1 x ± 1.0 p.s.i. (.0703 kg/sq.cm.) 1 x ± 0.5 p.s.i. (.035 kg/sq.cm.)

1 x ± 0.25 p.s.i. (.0176 kg/sq.cm.)

1 x ± 4.0 p.s.i. (.2812 kg/sq.cm.)

The transducers were connected to tappings from areas of the model where pressures compatible to their different sensitivities would be recorded.

The transducer output voltages were input via a digital volt meter, with a sensitivity of 1 micro volt, to a Solartron Data Transfer Unit (D.T.U.). The D.T.U. acted as an interface between the D.V.M. and the output device, either a KODE M33 terminal unit (teletype) or a Facit 3245 high speed paper tape punch. The D.T.U. had a capacity of up to twenty channels, of which four were used, the rest being shorted out. The D.T.U. was of modular construction and the modules fitted were varied according to the application. The basic modules fitted included Power Unit, Controller, Clock, Output Driver, Head Units (channels) and Interface. The Controller terminated each scan after the required number of channels had been scanned and also controlled the print out line length. The Output Driver enabled the data to be recorded. The data was output during these tests using the Facit 3245 paper tape punch. The system is displayed in block diagram form in Fig. 9.

The pressure data was processed using a P.D.P. 11-45 computer system which had been designed with efficient data analysis as the objective. The paper tapes of the results were input into the computer and the calculated pressure coefficients could be output numerically or graphically in any of the forms shown in this thesis. It is hoped to improve the pressure scanning system by including on-line facilities to the P.D.P. 11-45 or the University's I.C.L. 2970 computer to remove the necessity for the transfer of data by paper tape.

1.5 DISCUSSION OF ERRORS

Flow Conditions

Before the errors introduced during the measurement of the aerodynamic coefficients are considered, the conditions of the airflow within the working section of the wind tunnel must be determined. The working section was calibrated by Davies[12] and the following were the error bands placed on the relevant flow parameters:-

flow direction $\pm 0.5^{\circ}$ yaw, $\pm 0.2^{\circ}$ pitch

turbulence level rms level less than 0.001V.

These values were acceptable for the tests undertaken on the models described in this thesis.

Pressure Measurements

In addition to errors introduced by the pressure recording system, the magnitude of any error produced by the finite hole size of the pressure

tappings in the model surface must be determined. This problem has been investigated by Shaw[31] who stated that the error, for a hole of $\frac{1}{16}$" diameter, was 0.2% in velocity or 0.4% in $\frac{1}{2}\rho V^2$.

The use of the Scanivalve and data analysis system has enabled a large number of pressure investigations to be undertaken. The accuracy of the system had to be determined before the results could be used with confidence. The specification of the transducers, relating to their accuracy, was as follows:

non linearity	<	±1.0% of full range output
thermal zero shift	<	2.0% of full range/100°F, 0°F to 150°F
thermal coefficient of sensitivity	<	2.0% of full range/100°F, 0°F to +150°F
output noise	<	2mV R.M.S.

The major contribution to the probable error in the measuring system was output noise from the transducer. The transducers were calibrated for linearity and were found to be within the specification. The thermal errors were removed because all the pressures, both surface and dynamic head, were measured over a very short time period during which the possible temperature variation was negligible. Therefore, an output noise of the maximum specification level would have led to a percentage error of 0.79% for a typical static pressure coefficient. Any possible errors introduced by the remainder of the data analysis system were negligible.

The errors present in the system were less than 1% according to the specification. When results from repeated tests of the same configuration were compared, the error band was found in practice to be less than 0.5%; an acceptable level.

The data analysis system continually recorded the air velocity in the working section of the tunnel. This allowed the use of the correct instantaneous tunnel velocity in the calculation of each pressure coefficient and removed any error in the results due to variation in the velocity of the air during a test run. A small error would have been introduced if a single mean value of velocity had been used for the calculation of all the pressure coefficients.

Force Measurements

The sensitivities of the force balance used for the determination of the overall coefficients were as follows:-

lift	± 0.02lbs	± 0.089N
drag	± 0.005lbs	± 0.022N
pitching moment	± 0.01 ft.lbs.	± 0.014Nm

To enable confident use of the coefficients obtained from the force testing it was necessary to determine the possible error in each parameter. The following error bands were determined by the checking of the repeatibility of the results throughout the tests.

α ± 0.1°

C_L ± 0.003

C_D ± 0.002

C_M ± 0.03

SECTION 2

OVERALL FORCE INVESTIGATION

2.1 INTRODUCTION

A fundamental study of the aerodynamics of bluff bodies in ground effect must investigate the effects of Reynolds number, ground clearance and incidence. The basic model should be representative of vehicles that operate in an "in ground" environment.

The overall aerodynamic lift, drag and pitching moment generated by a suitable bluff body model, as shown in Fig. 1, were measured during tests undertaken in the University of Southampton 2.1m x 1.7m low speed wind tunnel. Variation of the principal test parameters, e.g. incidence and ground clearance, through appropriate ranges, resulted in the investigation of a large number of test conditions. The geometry of the model had been selected after a careful survey of the results of a wide range of previous studies. The following is an outline of the studies that have been undertaken using bodies of basic geometry which are applicable to the present investigation.

Carr[8] undertook a series of tests to investigate the aerodynamics of rectangular blocks mounted over a fixed ground board and the principal parameters varied were edge radius, yaw angle and ground clearance. The results clearly demonstrated the dependance of the drag force on the size of the edge radius and it was shown that when the radius was reduced below 6.7% of the body height, the formation of separation bubbles could not be suppressed.

Howell[20] tested similar shaped bodies over a fixed ground board, however in this series of tests the interest was centered on incidence and body length changes. The results obtained showed that the forces generated were insensitive to model length and demonstrated the need for correct ground simulation to prevent the separation of the ground plane boundary layer when large adverse pressure gradients were produced with the model mounted at incidence. The results demonstrated negligible Reynolds number variations.

The changes in the force coefficients of rectangular bodies produced by alteration of the length to width ratio and incidence were investigated by Nakaguchi[24]. Considerable variation in the drag coefficient was recorded as the length to width (L/W) ratio was varied from 0 to 5. The character of the variation of the drag and lift coefficients with angle of incidence changed drastically when L/W reached 1.6. Flow visualization showed this was accompanied by a change in flow pattern.

The importance of correct ground simulation has been demonstrated by the results obtained from tests undertaken by Stollery and Burns[35] and Fackrell[15] with the models mounted over a moving ground belt facility. Comparison between the results obtained when the ground belt was moving synchronously with the airflow, and stationary, showed large differences in the aerodynamic coefficients which were caused by the presence of the ground plane boundary layer. The large adverse pressure gradients produced downstream of the small nose radius on the idealised vehicle model tested by Fackrell showed clearly the inaccuracies introduced by incorrect ground simulation. The tests carried out by Stollery and Burns showed large variations in the drag generated by the model when the base area was varied. The lift force showed little dependance on the size of the base area.

In this section of the presentation of the results obtained from the tests carried out on the basic bluff body model shown in Fig. 1, only the overall effects produced by the variation of test parameters will be discussed. The detailed causes will be discussed in the analysis of the surface pressure distributions in Section 3.

Lift, drag and pitching moment were recorded for all the test configurations listed in Table 1. The results are presented graphically, in Figs. 11-40, and numerically in Tables 4-13. The coefficients were based on the frontal area of the basic model without any ramps fitted, 0.137 sq.m., and the reference length for the moment coefficients was taken to be the length of the body, i.e. 1.07m (42").

Prior to the main force investigations some tests were undertaken to determine if the forces generated by the body were dependant on Reynolds number. Several model geometries were examined at varying incidences and both ground clearances through a Reynolds number range

of 1.09×10^6 to 1.8×10^6 and no Reynolds number dependance was displayed. This was in agreement with the results obtained by other investigators. The tests were carried out at a Reynolds number of 1.8×10^6.

2.2 DOWNFORCE

A symmetrical flow field was obtained when the model, in its O-O configuration, was mounted at zero degrees incidence in the centre of the wind tunnel. This resulted in no downforce being generated. Reduction in the ground clearance of the model produced a small downward movement of the stagnation point, as discussed in Section 3, which increased the flow velocity over the upper surface of the nose and with the associated rise in pressure over the lower nose surface generated a small uplift as shown in Fig. 11 and Table 4. It can be clearly observed that the ground effect for this model geometry was negligible when mounted at an incidence of zero degrees, implying that only small movements in the position of the stagnation point were experienced. At zero degrees incidence no significant vertical force was generated by the model when mounted at either of the ground clearances. When the incidence was increased in the positive, nose up, sense an upforce was generated. This was a result of two changes in the flow conditions, firstly the downward movement of the stagnation point produced an increase in the flow velocities over the upper surface of the nose. Secondly, an upforce was also produced by the rise in pressure under the model caused by the convergent nature of the channel between the model undersurface and ground plane. The upforce increased as the ground clearance was reduced because of the increasing convergence of the underbody channel and the resultant rise in underbody pressure.

At negative incidences the model produced a downforce because of the upward movement of the stagnation point and the suctions generated in the venturi channel under the nose of the model. The downforce increased as the ground was approached due to the increasing strength of the venturi channel under the nose.

The addition of a 10° undersurface ramp to the rear 43% (45.7cms, 18") of the model, as shown in Fig. 1, produced a downforce due to the acceleration of the airflow over the ramp knee. The increase in downforce, $+C_L$ in the sign convention used in this thesis, when compared

to the O-O geometry, with the model mounted at zero degrees at the two ground clearances of 4cms and 14.5cms, was 0.718 and 0.382 respectively. A large increase in downforce was recorded as the ground was approached when the model was mounted at an incidence of zero degrees. This was a result of the increased suctions generated by the lower ramp knee. However, as the incidence of the model was increased, the rise in downforce due to ground effect reduced. This was a combined result of the rise in pressure in the convergent channel under the model, higher suctions generated over the upper surface of the nose due to the movement of the stagnation point and the change in effectiveness of the lower ramp knee. The reduction in ground effect as the incidence was increased resulted in a negligible increase in downforce as the ground was approached when the model was mounted at an incidence of 10^{o}

When the model was mounted at negative angles of attack a rise in downforce was recorded as the ground was approached for all cases tested. The increase became larger as the negative incidence was increased in the nose down sense. This was primarily due to the increasing effect of the venturi channel under the nose of the model as the incidence was reduced.

The downforce generated by the model when it was mounted at both ground clearances reduced as its incidence was increased. This was a result of the higher velocities produced over the upper surface of the nose caused by the downward movement of the stagnation point. The increase in upforce produced by these suctions was greater than the rise in downforce produced by the increasing effectiveness, due to reduced flow separation, of the lower ramp knee.

When the model was mounted at the greater ground clearance and zero degrees incidence, an increase in the lower surface ramp angle to twenty degrees caused a rise in the downforce generated by the model, as shown in Fig. 14 and Table 7. However, the increase when compared to the O-10 geometry was substantially less than the increment produced by the first ten degrees upsweep. The smaller increase was due to flow separation over the lower ramp surface, as discussed later in Section 3. A large increase in downforce was generated by this lower surface geometry at all incidences as the ground clearance was reduced due to the rise in level of suction generated by the lower ramp knee. The downforce reduced as the incidence of the model was increased, at both

ground clearances, as previously discussed when considering the 10° lower ramp.

A rise in the magnitude of the downforce generated by the model occurred when the upper surface ramp angle was increased. The increment produced by the twenty degree upsweep was nominally twice that generated by the ten degree angle, as shown in Tables 4, 8 and 11. The increase in downforce, due to the rise in upsweep of the upper surface, reduced with increasing angle of attack because of the reduction in the effective angle of upsweep. The reduction displayed a smaller dependance on the angle of incidence of the model than that of the complicated lower surface ramp venturi flow. An increase in the lower ramp angle always produced a greater rise in downforce than an equal increase on the upper surface for any test condition.

The generation of downforce was dominated by the high velocities produced in the channel flow under the model, due to the venturi created under the nose at negative angles of attack and the ramp knee, when fitted, at positive incidences. The suctions produced in these two areas were not limited to local influence but raised the suction, and hence downforce, over the entire undersurface, as discussed in Section 3.

The increase in pressure recorded near the centre line of the upper surface as a result of an increase in ramp upsweep had only a small effect on the production of downforce because it was opposed by the suctions created by the spanwise outflow of air, as discussed in Section 3. An increase in the upper surface ramp angle was therefore of secondary importance in the generation of downforce.

The increase in downforce as the ground was approached, when body geometries incorporating the zero degree lower ramp were mounted at negative incidences, was due to the strengthing of the venturi channel under the nose. The reduction, when these model geometries were mounted at positive incidences, was caused by the high underbody pressures created by the increasing convergence of the channel between the model undersurface and ground, as the ground was approached. When an undersurface ramp was fitted, an increase in the downforce generated by the model was recorded throughout the incidence range covered by these tests, as the ground was approached. This was due to the increase in the levels of suction produced in the venturi channel under the ramp knee at positive incidences and under the nose at negative incidences.

The only variation in the magnitude of the vertical force generated by the upper surface as the ground was approached, was due to the change in flow velocity over the nose surface. The flow over the ramp surface was not significantly changed by variation in ground clearances, as discussed in Section 3.

The reduction in ground clearance produced changes in downforce equivalent to those generated by an incidence change of approximately seven degrees and three degrees for all the twenty and ten degree lower ramp geometries respectively. The nature of the variations produced by a reduction of ground clearance for the zero degree lower geometries did not allow the determination of a similar induced incidence change for these cases.

The dependance of the level of downforce generated by the model on the lower surface geometry and ground clearance is illustrated by the values of lift curve slope shown in Table 14. The signs of the slopes were the same for all configurations, i.e. downforce reduced with increasing incidence. The variation of ground clearance had the major effect on the gradients and at a given height the dependance on lower ramp angle was dominant with the upper angle having negligible effect on the lift slopes. The gradient could therefore be classified using the lower ramp angle and ground clearance.

The magnitude of the lift curve slopes reduced with increasing lower surface ramp angle because of the increased separation effects at negative incidences and the reduction in pressure rise under the model at positive incidences.

The C_L-α plots were linear throughout the incidence range for all configurations except the twenty degree lower ramp configurations mounted at the reduced ground clearance. In these cases the slopes increased in magnitude at the higher positive angles of attack due to the reduction in the severe separation experienced over the lower ramp surface when the model was mounted at negative incidences.

The downforce generated by the different sections of the body is discussed in Section 3.

2.3 DRAG

The overall drag force generated by a bluff body originates from the following sources; forebody pressure, skin friction and base pressure drag.

The variation of the pressure drag of the centre and ramp sections with test configuration is analysed in Section 3 of this thesis and it is shown that this component does not vary significantly.

The skin friction drag component, although it cannot be quantified, will produce only small changes in the total drag when compared to the large changes generated by the pressure contributions.

When the body was mounted at large negative incidences, i.e. high downforce cases, the drag component due to lift would be at a maximum. The magnitude of this contribution to the total drag force would reduce as the incidence of the model was increased, reducing the downforce, until a zero value was generated at the zero downforce incidence. When the incidence of the body was increased further, the drag force rose as the positive lift that was noe being generated increased. This resulted in a "U" shaped variation of the drag contribution with incidence.

The magnitude of the base pressure was dependant on the size of the trailing edge flow separation angles. In Section 4 of this thesis it is shown that the base pressure reduced significantly when a large positive trailing edge separation angle was produced. This occurred when an upper surface ramp angle was fitted or with the zero degree upper surface fitted when the model was mounted at a negative incidence. Therefore, in general, as the incidence of the body was raised, and hence the trailing edge separation angle reduced, the base suction and its contribution to the total drag force would decrease. This would continue until the incidence had risen high enough to produce a positive separation angle at the lower surface trailing edge whereupon the suction and drag would rise again, resulting in a "U" shaped variation of the base drag with incidence, as listed in Table 21.

The variation of these two major drag components explains the typically "U" shaped variation of the total drag with incidence as shown in Figs. 21-30. The incidence at which the minimum drag occurred was clearly dependant on the separation angle of the base flow and magnitude of downforce generated.

The drag coefficient that was generated by the O-O body geometry, when the model was mounted at an incidence of zero degrees, was approximately 0.5 and nominally independant of ground clearance because of the negligible variations in base pressure and downforce produced by varia-

tions of ground clearance for this configuration.

The magnitude of the drag force was reduced when the model geometry was changed to 0-10, as displayed in Fig. 22. This was principally due to the reduction in base area produced by the geometry change. A further reduction was observed, for the same reason, when the geometry was altered to 0-20.

The importance of the size of base area and the magnitude of the suction acting over it resulted in the upper ramp angle being dominant in the determination of the level of drag produced. Both the base area and base suction, as discussed in Section 4, increased as the upper ramp angle was raised. This produced larger changes in the total drag force than any other drag contributions which resulted from changes in the lower surface geometry. The overall drag of the body increased as the upper ramp angle was raised due to the higher base suction and larger base area that were produced.

When the lower surface ramp angle was increased, a rise in the downforce generated by the model occurred together with the associated increase in drag. However, the increase in ramp upsweep reduced the base area of the model and hence reduced the base drag generated. These two effects were opposing and this resulted in the lower ramp angle having less influence on the overall drag force of the body than the upper surface.

The 0-0 geometry produced negligible change in drag throughout the incidence range as the ground was approached. Results obtained with the 10-0 and 20-0 geometries displayed an increase in the drag force as the ground clearance was reduced, when the model was mounted at a positive angle of attack, while at negative incidences the drag reduced as the ground was approached, as shown in Figs. 25 and 28. Throughout the incidence range covered by the tests, no large areas of flow separation were experienced by these three geometries upstream of the base. Therefore the drag variations produced by alteration of the model ground clearance were due to changes in the base and incidence contributions. The drag increased for all three geometries, i.e. 0-0, 10-0 and 20-0, as the ground was approached when the model was mounted at positive incidence because of the rise in base suction generated by the high speed underbody flow as discussed in Section 4. The fall in the drag force generated by the 10-0 and 20-0 geometries as the ground

was approached, when the model was mounted at negative incidences, was caused by the rise in base pressure, as listed in Table 21 and discussed in Section 4. The reduction in the base contribution predominated the change in drag force.

The small positive separation angle produced at the upper surface of the O-O geometry, in the negative incidence range tested, had negligible effect on the base pressure. Therefore, the rise in drag as the ground was approached for this model geometry when mounted at negative incidences was a result of the rise in the contribution caused by the greater downforce generated at the lower ground clearance.

The drag force generated by all the geometries incorporating the ten and twenty degree lower ramp angles increased as the ground clearance was reduced. The increase was produced by two principal causes. The first contribution towards the increase was the more severe separation over the lower ramp surface, at low incidences, which was produced by the large adverse pressure gradients downstream of the ramp knee. The second contribution was the generation of drag created by the higher downforces generated at the lower ground clearance.

The variation in the drag force generated by the upper surface as the ground was approached was principally due to the change in flow velocities produced over the upper surface of the nose. Consequently the downforce generated and associated drag contribution were therefore changed. The flow over the remainder of the upper surface was mostly unaffected. The small induced incidence change in the upper surface base flow separation angle, produced by the alteration of ground clearance, had negligible effect on the magnitude of the base drag.

The sum of the forebody, i.e. skin friction, pressure and drags can be obtained by subtraction of the base component from the total drag. This source of drag was dependant on the lower ramp angle, with little change recorded when the upper angle was altered. At zero degrees and all positive angles of attack the forebody pressure drag component increased as the ground clearance was reduced. When the angle of incidence was negative the drag force increased because of the greater separation over the lower ramp surface and the greater downforce generated.

The pressure distributions were integrated over the surface of the body and the drag contributions from this source for the various sections of the body are discussed in Section 3 of this thesis.

LIFT DRAG RATIO

The lift to drag ratio increased for each configuration as the angle of incidence of the model was reduced. This was a result of the relatively large lift variations throughout the incidence range when compared to the small corresponding drag variations and the trend of the ratio between downforce and drag was dominated by the downforce contribution. The ratio also increased as the camber was increased and the ground clearance reduced as shown in Table 4-13.

2.4 PITCHING MOMENT

Care must be taken when using the pitching moment obtained for a bluff body to determine for example, the centre of pressure of the body. When streamlined bodies are considered, the moment about the pivot point of the model introduced by the drag force is correctly, in the majority of situations, assumed to be zero. However, with bluff bodies the drag force can be equal, if not greater, in magnitude than the lift and the resultant force is at a large angle to the vertical. In this case it is more meaningful to discuss overall pitching moment coefficients and detailed surface pressure distributions rather than calculate the centre of pressure position in the traditional manner.

The pitching moment coefficients were calculated for all body configurations that were tested and are displayed graphically in Figs. 31-40 and numerically in Table 4-13.

For all body geometries the pitching moment increased in the positive, nose up, direction as the incidence of the model was increased.

When the model was mounted at the greater ground clearance a nose down pitching moment was recorded for all model configurations, except the 20-20 geometry, at negative angles of attack due to the high

velocities produced in the venturi channel between the model under-surface and ground. The 20-20 geometry generated a nose up pitching moment at an incidence of -3^{o} as a result of the downforce produced over the rear area of the model by both ramp surfaces.

At positive angles of attack the pitching moment altered to a positive nose up value due to the downward movement of the stagnation point which together with the weakening of the nose venturi reduced the suctions under the nose and generated high suction levels over the upper half of the nose producing an upforce in this area. This was reinforced by the downforce produced by the ramps. When no lower ramp was fitted the pressure rise under the model did not produce a large enough moment to overcome the positive moment generated over the forward areas of the model when mounted at the greater ground clearance. The venturi created under the knee of any lower ramp reinforced the nose up pitching moment at positive incidences.

A reduction in the ground clearance of the model always produced a more negative (nose down) pitching moment when the model was mounted at negative angles of attack. This was caused by the greater velocities produced under the nose by the strengthening of the venturi channel as its height was reduced.

The increase in the nose down pitching moment, as the ground was approached, was maintained throughout the positive incidence range for the geometries incorporating the zero degree lower ramp. This was caused by the greater pressure rise generated under the model at the reduced ground clearance. When either the ten or twenty degree lower ramps were fitted, the increase in downforce produced by the ramp knee, as the ground was approached, resulted in a more nose up pitching moment at positive or small negative incidences. The increase in downforce produced by the lower ramp knee at the rear of the model was reinforced by the high flow velocities over the upper surface of the nose at the front of the model.

The incidence for zero moment occurred at a higher negative angle of attack when the twenty degree ramp was fitted due to the greater rear downforce produced by this ramp. It also became slightly more negative as the upper ramp angle was reduced because of the movement of the stagnation point and the effect on velocities over the upper surface of the body.

The magnitude of C_{MO} increased as the camber of the body was increased. It also increased as the ground was approached, indicating an increase in effective camber induced by the closer proximity of the ground.

The gradients of $\partial C_M / \partial C_L$ for all configurations became more positive as the angle of incidence of the model was reduced. At both ground clearances a forward movement of the centre of pressure of the model was recorded as the angle of attack of the model was reduced. The movement occurred over a longer distance as the ground clearance was reduced because of the larger changes in suction levels at the lower height, as the incidence of the model was varied.

The pitching moment generated by the different flat surfaces of the model is discussed in Section 3.

2.5 VARIATIONS IN FORCES AND MOMENTS PRODUCED BY THE ADDITION OF THE UNDERSURFACE ROUGHNESS

The examination of the underbody flow, especially downstream of the ramp knee, was an area of great interest in the work which has been undertaken. To allow a deeper investigation of the flow in this area, a more stable and thicker boundary layer was created over the undersurface of the body by forming an area of distributed roughness as shown in Fig. 2. The dimensions of the size of the roughness are shown in Fig. 5. The model, with the roughness attached, was tested in the O-10 geometry, and mounted at the lower ground clearance. The measurement of the total lift, drag and pitching moment allowed the overall effects produced by the presence of the roughness to be observed and these results are presented graphically in Figs. 13, 23 and 33 and numerically in Table 6. The detailed effects, as displayed by the surface pressure distribution, produced by the roughness are discussed in Section 3.

The addition of the roughness had two main effects; firstly it reduced the level of suction recorded over the ramp knee and secondly it reduced the severity of the separation downstream of the knee. This resulted in higher suctions over the ramp surface.

These were opposing results in the generation of downforce. Therefore at incidences where the flow separation over the ramp was small, at positive angles of attack, the roughness caused a reduction in the magnitude of the downforce generated. At negative incidences

the two effects cancelled out and there was negligible change in the downforce that was generated.

The addition of the roughness produced a small increase in drag. There was no equivalent rise in downforce, base suction or integrated suctions over the undersurface and therefore the source of the increase in the force was the turbulence and rise in skin friction over the rough undersurface.

2.6 GROUND BELT STATIONARY

When the model was mounted at the reduced ground clearance, the overall forces were measured twice. Firstly with the ground belt moving synchronously with the airflow and again with the belt stationary. This allowed the effects produced by a ground plane boundary layer to be investigated.

The presence of the boundary layer on the surface of the belt produced two changes in the test configuration:-

(a) a reduction in the effective ground clearance of the body

(b) an induced positive incidence on the airflow around the body.

These caused a small downward change in the position of the stagnation point on the model and an upward movement of the flow streamlines. The loss of momentum in the flow under the body also affected the forces generated.

The thickness of the boundary layer on the belt surface was measured, for several configurations, at the two longitudinal centre line stations of the model shown in Fig. 2. These traverses are displayed in Figs. 81-84 and discussed in Section 5 of this thesis. There were large spanwise velocity gradients recorded under the model, demonstrating the highly three dimensional nature of the underbody flow. Therefore, to allow a quantitative examination of the changes produced by the presence of the ground plane boundary layer it would have required a knowledge of its three dimensional growth in the region of the model. It was not feasible to measure the boundary layer thickness at an adequate number of points to allow this to be achieved and therefore the following discussion is of a qualitative nature.

The changes in the magnitude of the overall downforce generated by the model when the ground belt was stopped can be observed in Figs. 11-20 and Tables 4-13. An increase in downforce was recorded for all the

zero degree lower ramp geometries when the ground belt was stationary. In these cases the reduced ground clearance of the model generated greater increases in downforce than the reductions produced by the induced incidence changes.

However, in general, less downforce was generated by the geometries incorporating a lower ramp upsweep when the ground belt was stationary. This was because of two factors. Firstly, the presence of the ground plane boundary layer reduced the amount of airflow under the model which lowered the level of suction over the lower ramp knee. Secondly, the positive incidence change of the airflow over the model induced by the growth of the displacement thickness of the ground plane boundary layer resulted in a reduction in the magnitude of the downforce generated. The changes produced by these causes were greater than the increase in downforce produced by the reduction in the effective ground clearance due to the ground belt boundary layer displacement thickness.

A departure from this trend was exhibited by the 20-10 geometry which generated more downforce when the ground belt was stationary. In this case the large upper surface ramp dominated any variations in the flowfield, and the changes in downforce observed when the ground belt was stationary, followed the same trends as observed with the zero degree lower surface geometries. When the upper ramp upsweep was lowered to produce the 10-10 geometry, the influence of the upper ramp was reduced and the change in downforce produced by the presence of the ground plane boundary layer became similar to that measured with the twenty degree lower ramp geometries.

The changes in overall drag which were produced by stopping the ground belt can be observed in Figs. 21-30 and Tables 4-13. In the majority of cases the changes in drag followed the same trends as the variations in downforce. A reason for this was the dependance of the induced drag on the downforce generated by the body. The small positive induced incidence change produced by the growth of the ground plane boundary layer tended to increase the base pressure and hence reduce the base drag, as discussed in Section 4 of this thesis.

A departure from this trend occured when the 0^{o} lower surface geometries were mounted at positive incidences, where less downforce and more drag were generated when the ground plane boundary layer was removed. In these cases a small gap was produced between the model trailing edge and ground belt surface. The flow passed through this

gap at a greater velocity when the belt was moving and was directed away from the base of the model, as discussed in Section 4, resulting in large reductions in the base pressure. These changes were greater than the variations in the induced drag component and therefore produced the observed increase in drag.

The changes in the pitching moment coefficients caused by the presence of the ground belt boundary layer can be observed in Figs. 31-40 and Tables 4-13. Two opposing effects, as discussed earlier, were produced by the stationary belt. Firstly, it caused a downward movement of the flow stagnation point on the nose of the body which resulted in higher flow velocities over the upper surface of the nose. Secondly, the reduced airflow under the body would weaken the venturi under the lower ramp knee, when fitted. The first of these effects would produce a greater nose up pitching moment, whilst the second would result in a lower value of pitching moment as the knee was downstream of the balance arms.

When no undersurface ramp was incorporated in the model geometry, i.e. 0° lower surface, a more positive pitching moment was recorded throughout the incidence range when the belt was stationary. The reduction in the strength of the venturi under the twenty degree lower surface knee when the belt was stopped was displayed by the more negative pitching moment recorded throughout the incidence range. An increase in pitching moment was recorded for the majority of the ten degree lower surface geometries. This was principally due to the reduced suctions generated over the forward undersurface of the body.

The results obtained when the ground belt was stationary followed the same trends which were recorded when the distributed roughness was attached to the undersurface of the body, as observed by comparison of Tables 5 and 6.

SECTION 3

SURFACE PRESSURE DISTRIBUTIONS

3.1 INTRODUCTION

The measurement of the total downforce, drag and pitching moment generated by the model has permitted the analysis of the overall effects produced by variations of incidence, ground clearance and body geometry. In order to ascertain the local effects caused by changes in the test parameters, it was necessary to obtain the pressure distribution over the surface of the model. This investigation was carried out in two separate programmes, as described in Section 1.2, for all the configurations listed in Table 1.

The pressure distributions over two dimensional bluff bodies have been extensively documented. However, there is a lack of published results obtained from the testing of three dimensional bluff bodies in ground effect. During the three dimensional tests the emphasis has usually been placed on the attainment of a comprehensive set of overall force and moment coefficients.

Carr[8] undertook a series of tests using a set of rectangular bodies mounted over a fixed ground board. The results obtained in the channel between the model and ground board were inaccurate due to the underbody method of mounting the model, in addition to the incorrect ground simulation. The results show the effects produced by the alteration of the edge radius, ground clearance and yaw angle of the model.

Two separate series of experiments have been undertaken by Morel[23], and Janssen and Hucho to investigate the effect of a slanted base on the flowfield around a body. The preliminary examinations were carried out using generalised axisymmetric and rectangular section bodies. It was observed that the base flow field could take two forms and was dependant on model geometry. At low slant angles a closed recirculating region was observed over the base area. At slant angles above 50° a highly three dimensional flow field existed with

two streamwise vortices, approximately parallel to the slanted surface, one on each side of the body. The vortices tended to produce reattachment in the central region of the base area.

The 3-D flow field around any body of small aspect ratio is very complex. However, at zero yaw the longitudinal centre line pressure distributions adequately display the majority of the effects produced by changes in ground clearance, incidence and body geometry, as discussed in Section 3.2 and displayed in Figs. 41-55. The three-dimensional surface pressure distributions are given as isobar contours in Figs. 56-67 and are integrated over the upper and lower flat surfaces to obtain the local forces listed in Tables 17-20. For all the isobar contours displayed in this section only selected contours are given values to avoid confusion. The intermediate contours represent equal valued steps.

3.2 LONGITUDINAL CENTRE LINE PRESSURE DISTRIBUTIONS

3.2.1 General observations

The effects produced by variations in body geometry are best demonstrated by examination of the centre line pressure distributions obtained with the model mounted at its greater ground clearance and an incidence of zero degrees.

The lower surface distribution, of the O-O geometry, displayed a high suction peak over the nose downstream of the stagnation point. It rapidly reduced in level over the downstream nose surface and this was followed by a more gradual reduction in suction level along the flat undersurface. At approximately 70% of the model length the suctions began to rise due to the influence of the high downstream base suction, as shown in Fig. 41.

When an undersurface ramp was fitted, the lower surface distribution was similar over the nose and forward area of the centre section, but as the knee was approached a rise in suction was produced by the upstream effect of the suctions created over the ramp knee. A characteristic "U" shaped distribution was produced over this section. A rapid rise and fall in suction was experienced over the knee which limited the effects produced by the different base suctions,

to nearer the trailing edge than recorded with the O-O geometry, as shown in Fig. 41.

On examination of the zero degree upper surface centre line pressure distributions, shown in Fig. 41, it can be seen that an alteration of the lower surface geometry had little effect on the upper surface distributions. The only variation among the three curves, corresponding to different lower ramp angles, was present over the rear thirty per cent of the body length. This was caused by the change in base suction produced by the alteration in lower ramp angle.

The upper surface centre line distribution with the model at 0^{o} incidence and the zero degree upper ramp fitted, exhibited a high level of suction over the nose which rapidly reduced over the flat upper surface to a nominally constant level. The suction increased over the rear thirty per cent of the body length due to the influence of the base suction, as shown in Fig. 42.

The addition of a ramp to the upper surface geometry slightly reduced the level of suction over the upper half of the nose and the pressure increased as the flat centre section was traversed, reaching a peak at the ramp knee, as shown in Fig. 42. Downstream of the knee the pressures reduced towards the trailing edge, assisted by the upstream effect of the high base suctions.

The three under surface pressure distributions corresponding to the different upper surface geometries, demonstrated that a change in upper surface geometry had negligible effect on the pressure distribution around the lower half of the nose, as shown in Fig. 42. The three curves diverged over the flat surface of the model because of the influence of the different base suctions.

The effects of change in ground clearance for the O-O geometry at zero degrees incidence are displayed in Fig. 43. The reduction in ground clearance produced an induced camber on the model and a slight downward displacement of the stagnation point. Negligible change in the upper surface centre line distribution was recorded. The effect on the lower surface

was much greater because of the increased venturi effect under the model when it was mounted at the reduced ground clearance. This resulted in the generation of a greater suction peak on the nose with the higher suction levels maintained over the mid section, 20-60%, of the body length.

There are two important points to be noted from the results, obtained with the model mounted at zero degrees incidence, that have been discussed above. The two pressure distributions, upper and lower surfaces, interact slightly due to the movement of the stagnation point and changes in base pressure, but it can be clearly observed that there were no significant changes in the pressure distribution over the lower surface resulting from changes in upper surface geometry and vice versa. The close proximity of the ground to the undersurface produced larger changes to this surface than the upper surface. The model has been mounted at 0^{o} incidence for all the cases discussed above; however similar effects were observed with the model mounted at different incidences.

3.2.2 O-O Geometry

When the model was mounted at the greater ground clearance the flow field was affected by the presence of the ground. This was demonstrated by the slight downward movement of the stagnation point over the nose of the O-O model geometry when mounted at zero degrees incidence. Thus the effect of the ground was to produce an induced incidence. The movement of the stagnation point generated higher suctions over the upper surface of the nose than the lower with minimum pressure coefficients of -1.11 and -0.93 respectively. As the flow passed under the model downstream of the stagnation point, a weak venturi was produced which resulted in slightly greater suctions over the flat undersurface than the upper surface, as shown in Fig. 41. In both cases the suctions remained nominally constant up to a distance of approximately 70% body length downstream of this point they increased because of the influence of the larger base suctions. Negligible spanwise gradients were recorded over both surfaces for this test configuration, as shown in Fig. 57.

As the angle of incidence of the model was increased above zero degrees, the stagnation point moved further down around the nose resulting in the development of larger suctions over the upper nose surface, as displayed in Fig. 44. The increase in suction over the upper nose surface rapidly decreased along the downstream flat surface and the differences between the suctions generated over the downstream section at different model incidences were negligible, up to 70% of body length. Downstream of this point the suctions were affected by the changes in base pressure. The downward movement of the stagnation point reduced the level of suction over the lower surface of the nose and the centre line suctions recorded over the flat undersurface reduced with increasing incidence due to the convergence of the channel between the model and ground.

When the model was mounted at a negative angle of attack the stagnation point moved onto the upper half of the nose surface. This resulted in lower suction levels over the upper nose and forward flat surfaces although, as when the model was mounted at positive incidences, the suctions recorded over the downstream flat surfaces were very near to the free stream value, with little dependance on incidence. Any variations were limited to the region near the trailing edge and were due to the upstream effect of the different base pressures. The venturi created under the nose at these incidences resulted in the generation of higher suctions over the lower nose surface. The suction levels quickly reduced in the diverging channel produced between the model undersurface and ground.

A reduction in ground clearance of the model, when mounted at an incidence of zero degrees, produced a small induced incidence change which lowered the stagnation point a small distance around the nose, as shown in Fig. 43. The variation of ground clearance produced little alteration to the upper surface centre line pressure distribution over the incidence range tested, i.e. -3° to $+2^{\circ}$. The variations were limited to a slight increase in suction over the upper half of the nose and along the rear 30% of the model length where the suction level was influenced by the different base pressure produced

at each incidence.

Due to the close proximity of the ground, the incidence effects on the under surface pressure distribution of the model, although similar to those recorded at the higher clearance, were of greater magnitude. At positive angles of attack the greater convergence of the flow channel under the model produced a reduction in centre line suctions and an increase in spanwise gradients when compared to the results obtained at the greater clearance. At negative angles of incidence the height of the venturi channel produced under the nose of the model was reduced generating higher suctions under the nose but these reduced in the diverging underbody channel. Over the incidence range tested there was no separation of the flow upstream of the base, due to the large radius of the nose and the radiied longitudinal edges.

3.2.3 O-10 Geometry

The fitting of the ten degree lower surface ramp when the model was mounted at 0° incidence, and the higher ground clearance, produced little change in the upper surface pressure distribution. The only significant variation was recorded over the rear section of the model and this was a result of the slight alteration in the level of base suction, as displayed in Fig. 41.

No significant movement of the stagnation point was produced by the change in geometry. Therefore, the increase in the suctions along the lower centre line downstream of the nose was principally due to the influence of the suctions generated by the ramp knee. At this ground clearance the channel flow area ratios under the model, together with the relatively small acceleration over the ramp knee radius, produced negligible separation of the flow over the lower ramp surface.

When the incidence of the model was increased, the suctions generated over the lower half of the nose decreased due to the downward movement of the stagnation point. The peak suction coefficients generated by the knee throughout the incidence range were very similar, varying from -0.55 at 0° to -0.58 at $+9^{\circ}$. The uniformity in the peak suctions generated over the ten degree ramp knee demonstrated the insensitivity of the

venturi effect at this height to any change in model incidence and that the major contribution was produced by acceleration over the knee radius. The centre line distributions diverged towards the trailing edge due to the upstream effect of the different base pressures.

As the incidence of the O-10 model geometry was increased, the suctions generated over the upper surface of the nose increased, as shown in Fig. 44. This increase was caused by the downward movement of the stagnation point. Downstream of the nose the suctions reduced to nominally constant similar levels over the flat surface throughout the incidence range.

When the ground clearance of the O-10 geometry was reduced, the upper surface pressure distribution showed little change with the suction levels similar to the values recorded at the higher ground clearance.

At an angle of attack of -3^{o} a strong venturi effect was created between the undersurface of the nose and ground belt. This generated a larger nose suction peak further downstream than that produced at the other ground clearance, $C_p = -2.05$ at a ground clearance of 4cm and $C_p = -1.16$ at a ground clearance of 14.5cms. Flow separation downstream of the suction peaks was prevented by the large radius of the nose. The influence of the larger suction under the nose, together with the stronger venturi under the knee of the ramp at this ground clearance, retained the increased suctions until immediately downstream of the knee. The peak knee suctions were $C_p = -0.618$ and $C_p = -0.55$ at the ground clearances of 4cm and 14.5cms respectively. When the model was mounted at the reduced ground clearance the more severe flow separation downstream of the knee resulted in the higher suctions generated at the knee being reduced downstream of the knee to levels similar to those recorded at the greater ground clearance.

When the angle of incidence was increased, the suctions developed under the nose were reduced by the weakening in the strength of the venturi and downward movement of the stagnation point. The centre line suctions over the lower flat surface reduced as the incidence was increased in a similar manner to

those recorded at the higher ground clearance. However the shallower underbody channel at this ground clearance increased the area ratios under the model producing a greater effect, and at $+9^{\circ}$ positive pressures were recorded on the centre line upstream of the knee. The venturi under the knee increased in strength as the incidence was raised producing a maximum suction of -1.045 at $+9^{\circ}$ incidence. The reduced underbody channel divergence angle downstream of the knee at the higher model incidences progressively removed the separation over the ramp surface as the incidence was increased with the associated increase in suction.

3.2.4 10-0 Geometry

When the model was mounted at the greater ground clearance and an incidence of zero degrees, the addition of the ten degree upper ramp to the model in its zero degree lower geometry resulted in a slight decrease in the level of suction over the upper half of the nose surface when compared to that recorded on the zero degree upper surface. This was due to the upstream effect of the increase in pressure produced by the ramp upsweep. As the ramp was approached over the flat centre section the ramp induced pressure rise caused the two upper surface centre line distributions to diverge, as shown in Fig. 42. Downstream of the pressure peak, situated at the ramp knee, the pressure reduced and became increasingly influenced by the base pressure as the trailing edge was approached.

The addition of the 20 degree upper ramp produced equal further reductions in suction to those created by the ten degree ramp. However, in this case larger spanwise gradients were introduced and therefore the isobar contours are employed for the analysis of this geometry.

The downward movement of the stagnation point produced by a positive increase in model incidence created higher suctions over the upper nose surface. The magnitude of the differences between the distributions recorded at the three incidences, $+2^{\circ}$, 0° and -3°, were nominally constant over the flat surface upstream of the ramp. The pressure produced by the ramp at -3° incidence remained greatest because of its more bluff nature.

The differences in suction levels were maintained aft of the knee, due to the effect of the different downstream base suctions.

When the ground clearance of the model was reduced, the upper surface centre line pressure distributions displayed little variation. The only area where any measureable change occurred was over the surface of the nose. This was caused by the downward movement of the stagnation point as the ground clearance was reduced. The flow remained attached to the surface of the model throughout the incidence range.

The effects produced on the lower surface by a change in the upper surface geometry were largely associated with the change in base suction. A small local decrease in suction was recorded over the forward nose of the 0^{o} lower surface configuration due to the slight movement of the stagnation point. The increase in base suction produced by the larger upper surface ramp angles was evident in the divergence of the three plots as the lower surface was traversed. This effect was largest when the zero degree lower ramp was fitted. When the lower surface was upswept the large suction produced by the knee reduced the influence of the varying base pressure.

3.3 DISCUSSION OF THREE DIMENSIONAL PRESSURE DISTRIBUTIONS AND FLOWFIELDS

3.3.1 Intoduction

All the previous discussion on the results of the surface pressure investigation has only considered the longitudinal centre line distributions. Although this has neglected the three dimensionality of the flowfield around the model, it was felt in a large number of cases, that they provided a simple and adequate method of determining the trends produced by changes in body geometry, incidence or ground clearance. However, when a surface of the model was at a high angle of attack to the free stream, large spanwise pressure gradients were produced. To enable a thorough understanding of the flow over the model to be obtained, the surface isobar contours should be examined. Results obtained during the investigation are displayed in Figs. 56-67.

The large spanwise pressure gradients were produced, when no upswept ramps were fitted, by mounting the model at high incidences. The gradients were increased for a given model incidence by increasing the upsweep of either the upper or lower surfaces.

3.3.2 Lower surface

At the greater ground clearance, a large inflow into the underbody channel occurred and this together with a lower effective diffusion angle resulted in (a) no significant areas of flow separation experienced by the 20° ramp and (b) its total absence when the 10° ramp was fitted. However, at the reduced ground clearance and small angles of incidence, increased adverse pressure gradients were generated downstream of the knee as a result of the large diffuser angle of the underbody channel and the high suctions over the knee. In some cases this resulted in the inability of the model boundary layer to remain attached and a large separated region was produced over the ramp undersurface. The severity of the separation over the 20° ramp at an incidence of 0° is displayed by the diminished suction peak over the ramp knee, as shown in Fig. 59. The depth of the separated region can be clearly observed from the centre line vertical total pressure traverse shown in Fig. 84.

The suctions created in the diverging channel caused strong inflow under the ramp which produced two vortices from the spanwise ends of the ramp knee. They converged slightly in the downstream direction and their effects can be observed in the flow visualization photographs. These vortices controlled the inflow under the ramp and tended to induce reattachment of the flow in the separated region. The size of the separated area was therefore reduced by the presence of the inflow and associated vortices.

To determine the dependance of the size of the separated region on the amount of inflow, it was decided to prevent the inflow by the attachment of sidewalls, extending to the ground, over the entire length of the model. No measurements, force or pressure, were taken with the sidewalls in position. Flow

visualization photographs of the underbody flow are shown in Plates 7 and 8.

The flow separated over the 10° lower ramp surface when the sidewalls were fitted, although the separation was not as severe as that recorded with the 20° ramp geometry. In the case of the 20° ramp, the separated region covered the entire area of the ramp and sidewalls. The large inflow and smaller separated flow region under the 20° ramp could be observed when the sidewalls were removed. The photographs obtained of the 10° ramp underbody flow, without the sidewalls, displayed attached flow.

The addition of the sidewalls had produced a channel under the model which could be compared to a two dimensional diffuser section with the ground plane representing the horizontal centre line of the device. The performance of two dimensional diffusers has been investigated by Johnson[7,28] and his results confirmed that large transitory stall occurred for diffusers with the aspect ratios produced by both ramp geometries when the sidewalls were in place. The inflow permitted by the removal of the sidewalls reduced the effective aspect ratio of the diffuser and removed the stall conditions for the 10° ramp and reduced the severity of the stall for the 20° example.

The phenomenon just described is very similar to that observed by Morel[23] who tested an axisymmetric model with a slant base in free air conditions. In the tests undertaken by Morel, the vortices were not created until a slant angle of approximately 40° was presented to the flow. In the current programme the flow field is complicated by the presence of the ground plane and the vortices appear at an angle between 10° and 20°.

An increase in the upper ramp angle in all tests with the ten degree lower surface geometry, mounted at both ground clearances, produced higher suctions over the lower knee. This was due to the upstream effect of the higher base suctions. In these cases negligible flow separation was observed over the lower ramp surface.

The same results were recorded when the twenty degree lower

surface geometry was mounted at the greater ground clearance. In this case the underbody flow separation was again minimal. When the ground clearance of this geometry was reduced, the underbody flow separation experienced at small incidences removed the upstream effect of the base suctions and lower knee suctions were recorded. At higher angles of attack, where no significant flow separation occurred, the beneficial upstream effect of the base suction was again observed.

3.3.3 Upper surface

Spanwise velocities towards the longitudinal edges of the model were produced by mounting the model at negative incidences or by upsweeping the rear ramp section. The direction of the airflow was towards the centre line when the model was mounted at positive incidences.

An adverse pressure gradient was experienced over the rear section of the upper nose surface, however the large radius of the nose prevented any flow separation at this point. In some cases large spanwise velocities were generated over the upper surface but the radiied longitudinal edges prevented separation due to this cause. The only flow separation on the upper surface occurred at the knee of the twenty degree ramp where a small spanwise separation bubble was produced. Typical results obtained during the investigation can be observed in Figs. 58 and 59.

3.4 INTEGRATED DOWNFORCE

The magnitude of the downforce was calculated by integrating the surface pressure distributions over the flat upper and lower surfaces of the model. The nose of the model was not investigated because of the poor definition given by the relatively small number of tappings in this area. All the coefficients quoted are based on the area of the respective surface. Values of downforce coefficients for both upper and lower surfaces are listed in Tables 17-19.

3.4.1 Lower surface downforce, O-O geometry

The magnitude of the downforce generated by both underbody areas of the zero degree geometry, ramp and centre, reduced with increasing angle of attack, as shown in Table 17. The reductions in downforce were recorded at both ground clearances

although they were larger when the model was mounted at the lower height because of the closer proximity of the ground. At the greater ground clearance the rear section generated more downforce than the centre area. However, when the model ground clearance was reduced to 4cms, the centre area produced more downforce than the rear section when the model was mounted at negative angles of attack as a result of the influence of the large upstream lower surface nose suctions. At positive incidences the greater pressure build up under the rear section also resulted in the centre section generating more downforce.

3.4.2 Lower surface downforce, 10° and 20°, lower ramp geometries

The downforce generated by both under surface areas, centre and ramp, increased as the ground clearance was reduced. The ramp generated downforce increased with increasing incidence while the centre section downforce reduced. This opposing trend produced the results shown in Table 17.

At the greater ground clearance there was negligible difference, as the incidence was varied, in the level of downforce generated by either the ten degree or twenty degree lower ramp surfaces. Typically it varied from 0.3 at -3° incidence to 0.35 at $+18^{\circ}$. This was because the channel area ratios produced under the model throughout the incidence range when it was mounted at this ground clearance did not create widely varying suction levels over the ramp knee. This resulted in a similar flowfield downstream of the ramp knee. The presence of separation over the ramp surface was very limited but reduced with increasing model incidence. The reduced flow separation and influence of the high knee suctions resulted in the greatest downforce being produced at $+18^{\circ}$ incidence.

The downforce generated by the lower surface ramp section increased as the ground clearance of the model was reduced, as shown in Table 17. This was due to the larger suctions generated in the venturi channel under the model at this height. A larger increase in downforce was recorded through the incidence range than that produced when the model was

mounted at the greater ground clearance. This was because of the greater changes in suction levels and severity of flow separation experienced at this ground clearance.

In the cases where extensive flow separation was experienced over the lower ramp surface little variation in the downforce generated occurred when changing the upsweep angle of the lower ramp. For example, when the model was mounted at -3° incidence, the downforce produced by the 10° and 20° lower ramps was 0.33 and 0.36 respectively. When the flow was attached, large changes were recorded, as demonstrated by the results obtained when the model was mounted at an incidence of $+9^{\circ}$. In these cases the downforces produced were 0.41 and 0.66 for the 10° and 20° ramp respectively. The changes produced in the later cases were principally due to the influence of the different knee suctions.

The downforce generated by the bottom centre section reduced as the incidence of the model was increased, at both ground clearances, with higher values obtained when it was mounted at the lower height. The reduction through the incidence range was caused by the pressure build up under the model due to the increasing convergence of the channel created between the model undersurface and ground. The higher downforces recorded at the lower ground clearance were principally due to the upstream influence of the higher knee suctions produced at the lower ground clearance. This is demonstrated by the increase in downforce generated by the centre section as the ramp angle was increased.

3.4.3 Upper surface downforce, 0-0 geometry

The zero degree upper surface geometry generated an uplift throughout the incidence range, as shown in Table 17. In the majority of cases the magnitude of the lift produced by both areas, centre and ramp, increased as the angle of attack of the model rose, principally as a result of the increase in the suctions over the upper half of the nose. A reversal of this trend was observed at extreme negative incidences resulting from the reduction in base pressure as the incidence was increased. This raised the level of suction over the rear section, creating an increase in the magnitude of the uplift generated over this area, as the incidence was reduced. The

smaller reduction in the uplift produced at negative incidences over the central section was caused primarily by the reduction in nose suctions rather than the upstream influence of the base pressure variation. The increase in uplift over the rear section did not reverse the trend of the reduction of total upper surface uplift with reducing angle of attack although it did produce a smaller reduction.

3.4.4 Upper surface downforce, 10° and 20° upper ramp geometries

The two sections of the upper surface had opposing trends in the generation of downforce as the incidence of the model was increased. The ramp produced more downforce while less was generated by the centre section. The increase in downforce created by the ramp was due to the reduction in the bluffness of this section. This reduced the spanwise airflow over the model surface and reduced the suctions near the longitudinal edges of the body. A small opposing effect, present near the trailing edge, was generated by the reduction in base pressure and associated lowering of the suctions over the rear of this area.

The reduction in downforce produced by the centre section with rising angle of attack was due to two complementary factors. Firstly the reduced pressure build up in front of the ramp knee and secondly was the higher nose suctions produced by the downward movement of the stagnation point over the nose surface which increased the suctions over the forward part of the central section.

The model geometries chosen to illustrate these effects on the upper surface were the 10-10 and 20-10 examples. The 10° lower ramp was chosen to allow an acceptable incidence range at the lower ground clearance. The downforce calculated for the two areas, ramp and centre section, are listed in Table 17. It should be noted that the variations in the downforce generated by the individual areas through the incidence range were small and because they were opposing, the change in downforce produced by an alteration in the angle of attack was negligible. The change in geometry of the model from 10-10 to 20-10 altered the direction of the force from an uplift of 0.03

to a downforce of 0.05. Both of these forces were small when compared to the magnitude of the forces produced by the lower surface. It was observed that the upper surface performed a secondary role in the generation of the total downforce of the model. This is supported by the results obtained during the overall force investigations.

All results show little change in the level of upper surface downforce was produced by a change in ground clearance.

3.5 INTEGRATED DRAG

The component pressure drag of the bluff body model was obtained by the integration of the horizontal component of the surface pressure distributions over both the centre and rear, upper and lower flat surfaces. The results obtained demonstrate their small contribution to the overall drag. The dominance of the base drag is illustrated by comparing the results with the overall drag measurements displayed in Figs. 21-30 and the mean base pressure coefficients shown in Table 21.

A mean suction was recorded over the undersurface of the body throughout the incidence range when no lower ramp was fitted. This resulted in the surface producing a thrust at positive incidence while at negative angles of attack, a drag force was generated.

The addition of a lower ramp to the undersurface geometry increased the suction over the centre section resulting in a higher drag or thrust, the direction of the force again dependant on the incidence of the model. The integrated suction which was generated over the ramp surface produced a drag force throughout the incidence range.

The mean suction recorded over the upper surface, 0^{o} ramp geometry, at all angles of attack resulted again in the direction of the horizontal force being dependant on the angle of incidence of the model. At positive incidences it generated a drag while at negative incidences it produced a thrust.

When either of the ramps were fitted to the upper surface the mean positive pressure which was generated over the central section at all incidences produced a drag at negative angles of attack and a thrust at positive angles. The mean suction recorded over the ten degree ramp generated a thrust at angles of attack less than ten degrees.

Above this value the direction of the force was altered to a drag because of the change in the change of the relative incidence of the surface from a negative to positive value. The relative angle of attack of the twenty degree ramp did not change sign throughout the incidence range with the result that the mean positive pressure measured over this area produced a drag force for all test cases.

3.6 GROUND BELT STATIONARY - 0-10 GEOMETRY

The surface pressure distributions of the 0-10 body geometry were obtained at three incidences at the lower ground clearance with the ground belt stationary to allow an investigation of the effects produced by the boundary layer on the belt surface. Only the 0-10 body geometry was used in this section of the tests. The 0° top section was fitted for two reasons; firstly it had the least effect of any of the upper ramp sections on the magnitude of the base pressure and hence the suction levels towards the rear of the lower surface. Secondly, the pressure distribution over the 0° top section was uniform and any variations produced in it by changes in flow conditions would be more easily observed when superimposed on this uniform distribution than on the more complex distributions obtained when an upswept ramp was fitted. The 10° lower ramp was tested because of the moderate results it produced when compared to the 20° example, especially in regard to the reduced flow separation. It would, therefore, enable any detail flow changes which were produced to be clearly examined with minimal influence from other sources.

This part of the investigation was undertaken with the model mounted at three incidences, -3°, 0° and $+9^{\circ}$. The centre line pressure distributions are shown in Figs. 50-52.

Stopping the belt produced a slight downward movement of the stagnation point but this caused negligible change in the upper surface pressure distribution and the downforce that it generated.

The reduction in the suction levels generated over the undersurface of the nose, central section and ramp knee when the belt was stationary, can be clearly observed. The reduction in the suction levels generated over the lower surface ramp knee reduced the adverse pressure gradient and flow separation downstream of the knee. The greater flow separation

experienced at lower incidences when the belt was moving resulted in the reduction of the suctions downstream of the knee, to the levels recorded when the belt was stationary.

The removal of the flow separation over the ramp surface when the model was at an incidence of $+9^{\circ}$, caused by the reduced divergence of the underbody channel, allowed the higher suctions obtained when the belt was in motion to be maintained to the trailing edge.

The pressure distributions over both areas of the undersurface, centre section and ramp, obtained with the belt stopped, followed the same trends as when the belt was moving.

A small decrease in the overall downforce generated by the undersurface of the body was recorded when the ground belt was stationary, as displayed in Table 18.

3.7 AIRDAM AND DISTRIBUTED ROUGHNESS ADDED - O-10 GEOMETRY

Two devices, an airdam and distributed roughness, were fitted to the undersurface of the model to investigate their effect on the flowfield around the body. Their positions on the model are shown in Fig. 2. The surface pressure distributions were recorded at three incidences, -3°, 0° and $+9^{\circ}$, with the model mounted at the reduced ground clearance. The -3° incidence case could not be tested when the airdam was fitted because at this incidence the airdam fouled the ground belt. The tests were undertaken twice, ground belt moving and stationary, to investigate the effect of the ground belt boundary layer. Only the O-10 body geometry was tested in this greater depth, for the same reasons as described in Section 3.6.

The changes produced by the devices, in most cases had little effect on the upper surface pressure distributions. The upper surface will, therefore, only be mentioned in tests where variations were recorded.

3.7.1 Airdam

The changes produced in the centre line pressure distributions by the attachment of the airdam can be observed in Figs. 54 and 55.

The blockage to the underbody channel flow produced by the airdam caused the removal of the suction peak over the ramp knee at 0° incidence. When the incidence was increased to $+9^{\circ}$, the

smaller percentage of underbody blockage produced by the airdam resulted in a peak being produced although much smaller than the one recorded on the basic model.

At $+9^{o}$ incidence the only change to the upper surface centre line pressure distribution, resulting from the addition of the airdam, was a small reduction in peak suction over the nose surface. The influence of the airdam on the upper surface distribution was also limited to the nose at 0^{o} incidence, but as shown in Fig. 54, the increased underbody blockage at this incidence extended the variation in the upper surface distribution slightly further downstream.

To determine the overall effects produced on the flowfield by the addition of the airdam, the isobar contours and integrated downforce results should be consulted, as shown in Figs. 62-63 and Table 18.

The lower suctions generated over the knee of the model, at an incidence of 0^{o} with the airdam fitted, resulted in negligible separation over the ramp surface. This created higher suctions over the majority of the ramp surface but the effect was opposed by the higher suctions recorded downstream of the knee of the basic model. The result was that no change in the downforce generated by the lower ramp was experienced. An increase in downforce over the centre section at 0^{o} incidence was recorded, as expected, when the airdam was attached. The increase, from 0.473 to 0.515, was produced by the central high suction area immediately downstream of the airdam but this was reinforced by the large suctions along the edges of the model resulting from the spanwise inflow. Immediately upstream of the knee, the suctions produced under the basic model were greater due to the higher suctions generated over the knee.

At an incidence of $+9^{o}$, the addition of the airdam had an adverse effect on the production of downforce by the ramp surface. This was due to the generation of higher suctions over the ramp knee of the basic model produced by the greater underbody flow. The small divergence angle of the channel between the ground and ramp undersurface removed any flow separation over the undersurface of the body. This produced

higher suction levels over all the under surface of the ramp of the basic model.

The airdam did not allow the pressure build up under the model when mounted at higher incidences, which removed the large suctions generated at the edges by the spanwise outflow from the high pressure region near the centre line of the basic model. The blockage produced by the airdam reduced the level of suction attained under the knee which reduced the upstream suctions over the adjacent centre section.

The overall downforce generated by both areas of the model with the airdam fitted, centre section and ramp, reduced as the incidence was increased resulting in downforces of 0.87 and 0.40 at 0° and 9° respectively, compared to values of 0.83 and 0.61 for the basic model. At zero degrees incidence the airdam had negligible effect on the downforce generated by the ramp surface with the result that the relatively small increase in downforce was produced by the centre section. At $+9^{\circ}$ the airdam had an adverse effect on the downforce produced by both sections. The reduction over the centre section was 0.08 and the ramp, 0.13.

At both incidences negligible change was recorded in the downforce generated over the upper surface by the addition of the airdam.

3.7.2 Distributed roughness

The changes in the centre line pressure distributions of the O-10 geometry produced by the addition of the area of distributed roughness to the undersurface of the model, when it was mounted at incidences of -3°, 0° and $+9^{\circ}$, are displayed in Figs. 53-55. The variations in the overall isobar contours and integrated downforces are shown in Figs. 62 and 63 and Table 18.

It can be clearly observed from the figures that the upper surface pressure distribution was negligibly affected by the addition of the roughness and will therefore not be discussed in this section.

Examination of the centre line pressure distributions shows

that the thicker boundary layer has resulted in a restriction to the under body flow and this has caused a slight downward movement of the stagnation point resulting in smaller forward peak suctions. The reduced adverse pressure gradient experienced in the majority of cases downstream of the knee resulted in less flow separation than in the basic case.

At angles of attack of 0° and 9°, the turbulence introduced by the distributed roughness caused a reduction in the peak suction over the knee. The lack of flow separation over the ramp surface when the model was mounted at $+9^{\circ}$ resulted in the reduction being recorded to the trailing edge. When the incidence was reduced to -3°, greater flow separation occurred over the lower surface ramp of the basic model when compared to the modified case. This occurred because of two reasons. Firestly, greater adverse pressure gradients existed under the basic model and secondly, the separation would also be reduced because the turbulence introduced by the roughness tended to keep the boundary layer attached. The greater flow separation present under the basic model reduced the suctions downstream of the knee to levels below those recorded when the roughness was attached.

A major effect produced by the addition of the area of distributed roughness was a reduction in the spanwise pressure gradients over the under surface of the body and therefore for a detailed discussion of the flow field, the overall isobar contours and integrated downforces must be examined.

There were two opposing trends in the production of downforce by the ramp which were introduced by the presence of the roughness induced turbulence. Firstly, there was a reduction in the suction levels over the knee and along the longitudinal edges of the ramp, i.e. reduced inflow under the model. Secondly, the smaller suction peaks over the ramp knee produced a reduction in the flow separation over the ramp and hence tended to raise the levels of the downstream suctions.

At -3° incidence no significant change in downforce was recorded when the distributed roughness was attached. The severity of the flow separation reduced as the angle of incidence

was increased and the difference in the levels of suction generated over the knee increased. This resulted in the ramp of the basic model producing more downforce. The values at an incidence of $+9^{\circ}$ were 0.37 and 0.41 for the modified and basic model ramps respectively.

When the results of the centre section of the undersurface were observed it was noted that at -3° and 0° angles of attack, the downforce was increased by the turbulence due to the upstream influence of the reduced flow separation over the ramp surface, as discussed above. At $+9^{\circ}$ a reduction was recorded when the roughness was added because of the reduced level of suction generated over the knee.

The effects produced over the ramp and centre section surfaces were in opposition and the total undersurface downforce must be observed to determine if the addition of the roughness was beneficial. It was found that the roughness had very little overall effect at 0° and -3° angles of attack and a detrimental effect at $+9^{\circ}$ incidence principally due to the reduced suctions over the ramp knee, as shown in Table 18. These findings were supported by the overall force coefficients.

SECTION 4

BASE PRESSURE SURVEY

4.1 INTRODUCTION

An important contribution to the drag force generated by a bluff body is the base drag produced by the large suctions present in the wake downstream of the body. The base pressure of the body is therefore of great significance and a thorough understanding of the parameters which determine its magnitude is important.

The shape of the forebody and the angle of the separating shear layers, with respect to the free stream direction, are prime factors in the determination of the parameters, e.g. Strouhal number and vortex formation length which define the size of the wake and level of base pressure. These parameters have been widely investigated by many experimenters using two dimensional models.

Nash, Quincey and Callinan[25] undertook an extensive two dimensional investigation using a model with a wedge forebody and parallel sided afterbody. Good correlation was obtained between probe readings taken at a distance of 0.025cm from the base surface of the model and the base pressures measured at tappings on the model surface.

To determine the dependance of base pressure and the wake parameters on the angle of separation of the shear layers at the base of a body, Simmons[32] used two dimensional wedge models of different included angles ranging between 0^{o} and 90^{o}. It was found that both the base pressure and Strouhal number reduced as the angle of the wedge was increased. The distance from the base to the position of minimum pressure increased as the wedge angle was increased. Similar results were obtained by Tanner, Roshko and Lau.

Bearman[3] has carried out work to investigate the effect of splitter plates in the wake on the base flow of two dimensional cylinders of various cross sections. The addition of the splitter plates increased the vortex formation length and raised the base pressure thus reducing the drag. They also increased the Strouhal number of the base flow

but an increase in their length over 1.5 times the base height resulted in a rapid drop in the Strouhal number.

Base pressure distributions have been obtained for a small number of three dimensional bodies, e.g. cube and rectangular blocks. However, in no cases has a systematic investigation been undertaken to determine the effect of, for example, body geometry on the base surface pressure distributions.

Throughout all the test programmes, both two dimensional and three dimensional, the forebody pressure distribution and wake characteristics have been extensively documented but little emphasis has been placed on the determination of the pressure distribution over the base area of the model. The base pressure was usually assumed to be constant, resulting in a minimal number of tappings being inserted into the base area. It was felt that this neglected topic should be investigated and the model used in the present series of tests would prove the ideal subject because of the wide range of forebody geometries, incidences and base areas that could be tested.

4.2 SURVEY OF INSTANTANEOUS SURFACE PRESSURES

A major problem with the measurement of the base pressure distributions was that if they were obtained in the usual way by using surface tappings, connected by tubes to liquid manometers or Scanivalve modules, time averaged results would be recorded. This could provide misleading results due to the fluctuating pressure produced in the base area by the unsteady wake flow.

Howell[20] has extensively investigated the conditions in the wakes of three dimensional bluff bodies in ground effect and found little periodic phenomenae but it was still thought necessary to measure the instantaneous pressures over the base area of the body and determine that any fluctuations in their levels were small enough to ensure that the time averaged results were meaningful.

The measurement of the instantaneous pressures required the removal of all the time dependance from the recording apparatus. This was achieved by mounting a sensitive capacitance type pressure transducer flush to the surface of the model. The output voltage from the transducer was connected directly to a pen recorder. The frequency response of the system was checked during experiments in another wind tunnel prior to this series of tests in order to ensure that it would

allow accurate measurement in the range of frequencies that were recorded by Howell[20] in experiments using bodies of similar geometry to the model used in the present investigation. A trial was undertaken in the wind tunnel at the correct airspeed with the transducer insulated from any pressure variations to ensure that none of the recordings would be influenced by mechanical vibration of the diaphragm. The results of this trial displayed negligible model vibration induced fluctuations on the output trace.

The position of the transducer was varied over the base for each of the configurations tested to investigate the existence of any localised effects. The transducer was also mounted on the undersurface of the model, at a position 1cm. aft of the ramp knee and 2.5cms. inboard of the edge, for each configuration to investigate the steadiness of the flow in this region.

There were no localised effects recorded over the base area and typical recordings obtained for both the undersurface and base area are displayed in Fig. 68. It was observed in both cases that the fluctuations recorded were small, a maximum of 5% of the mean value on the base and 4% on the ramp. This meant that the time averaged pressure distributions could be analysed with confidence. It was not possible to obtain an accurate value for the frequency of the fluctuations using the traces but it can be seen that although the percentage level of the variations in the pressure over the knee were smaller, the oscillations were at a much higher frequency. This was associated with the greater velocity of the flow over the model surface at this point.

4.3 POSITIONING OF BASE AREA PRESSURE TAPPINGS.

In the first series of experiments, undertaken to determine the forebody surface pressure distribution of the body, it was decided to insert six pressure tappings into the base of the model to investigate any variations in the surface pressure over this area. On analysis of the results obtained from these tests it was found that not only the mean base pressure of the different test configurations varied but also that the distribution of the base pressure varied for many geometries as the incidence was altered. The results were systematic with test configuration changes and it was therefore decided to undertake a thorough examination of the base area pressure distribution.

A grid of tappings was inserted in the port half of the base of each of the six rear sections of the body. The spanwise spacing of the tappings was constant at 5cm (2"), but the vertical spacing was varied because of the different heights of the base sections, as shown in Fig. 4. The nearest tappings to the edge were placed at a distance of 2.5cms. The number of tappings in the base varied from 33 for the 45.7cm (18") base height to 13 for the 15.25cm (6") base height.

It should be noted that the isobar contours displayed in Figs. 69-80 only cover the area enclosed by the surface tappings and not the entire surface of the base. The lack of coverage of the area near the edge of the base was because of the expected large pressure gradients in that region, as observed by Eldred[14]. It would have required an unacceptably large number of tappings in this domain to provide adequate definition. The greater time dependance of the base pressures in this region would not allow adequate analysis of the mean values recorded using the Scanivalve system.

4.4 FLOW VISUALIZATION OF THE BASE FLOW IN THE WATER TUNNEL

On examination of the base pressure distributions obtained, after analysis of the recorded data, it was observed that two basic patterns existed. The first consisted of vertically orientated isobars over the entire base area as shown in Fig. 69c, and second, a pattern was obtained where the vertically orientated isobars were replaced over a section of the base by isobars in the horizontal direction, as displayed in Fig. 70a. This suggested that two basic base flow-fields existed and in order to assist in the understanding of the flow mechanisms which produced them, flow visualization of the wake flow was undertaken.

When the model was mounted in the wind tunnel, three methods of visualizing the base flow were employed. Firstly, wool tufts of varying length were attached to the base and trailing edge, secondly a mineral oil and flourescene dye mixture was painted over the base area, thirdly a smoke probe was used to inject smoke into the airflow immediately upstream of the base and also directly into the base region. All these techniques resulted in very limited success and a different approach was required to provide acceptable visualization.

The Department of Aeronautics and Astronautics 0.3m x 0.3m water tunnel provided a suitable alternative method for the visualization of the base flow using any of the accepted water tunnel techniques, e.g. neutrally buoyant polystyrene spheres, air bubbles and dye.

A one-sixth scale model, as shown in Fig. 6, was constructed of the 0-0, 0-20 and 20-0 geometries of the wind tunnel models. These three geometries were chosen because they produced the largest change in both the mean value and distribution of the base pressure coefficient and would therefore provide the best examples to exhibit any change in the base flow mechanisms.

The scale of the model resulted in a similar blockage ratio as produced by the larger model in the wind tunnel.

A difference in test conditions between the wind tunnel and water tunnel tests was a discrepancy in Reynolds number. The tests in the water tunnel were carried out at a Reynolds number, based on model length of 3.1×10^5, whereas the wind tunnel tests were conducted at a Reynolds number of 1.8×10^6. The negligible dependance on Reynolds number of the forces generated by the model during the wind tunnel tests implied that the flowfield was unaffected by the change in Reynolds number.

A second difference in test conditions was introduced by the change of ground plane simulation from a moving belt in the wind tunnel to a fixed ground board representation in the water tunnel. The small induced change in incidence and ground clearance introduced by the ground board boundary layer in the water tunnel would have little effect on the base flow of the configurations tested, as can be observed from the wind tunnel results obtained with the ground belt stationary.

The model was located in the water tunnel by four horizontal mounting bars extending from the side of the model with their ends fitted over threaded vertical posts fastened to the ground board, as shown in Fig. 6. The location of the mounting bars on the vertical posts was fixed by locking nuts. The mounting bars were fitted at the same relative height on the model side as on the wind tunnel model. The ground clearance and incidence of the model could be altered by the movement of the mounting bars along the vertical posts.

The tests were carried out in the water tunnel with the model mounted at zero degrees incidence and a ground clearance of 2.42cm (0.95"),

equivalent to the greater ground clearance at which the model was tested in the wind tunnel. The maximum speed of the water in the empty working section was 3.5m/sec. However, after a series of photographs had been taken at different water velocities and camera settings it was decided that a velocity of approximately 2m/sec. provided the best photographic results. The change in velocity produced negligible change in the base flowfield.

The three usual water tunnel visualization techniques were attempted, i.e. small neutrally buoyant polystyrene spheres, air bubbles injected into the water using a small probe and dye injected into the base region of the model again using a small probe. The air bubbles produced superior results and therefore this technique was employed throughout the investigation.

4.5 DESCRIPTION OF THE BASE FLOW CHARACTERISTICS

The isobar contours obtained in the wind tunnel and the flow visualization carried out in the water tunnel showed that two basic flow fields could exist in the base region downstream of the model. The symmetrical base flow shown in Plates 9 and 12, and Fig. 69c, existed when the angle between the horizontal separating shear layers and the free stream was below approximately ten degrees. When the shear layer separation angle increased above this value, by alteration of model incidence or geometry, and also when the zero degree lower geometries were mounted at small positive incidences at the reduced ground clearance, the flow field changed to that displayed in Plates 13 and 14, and Fig. 70b.

An example of the symmetrical flow field was obtained when the O-O geometry was mounted at zero degrees incidence. The base surface isobars are displayed in Fig. 69c and the flow visualization of this configuration, carried out in the water tunnel, is shown in Plates 9-12. Plates 9-11 inclusive, show the flow in the vertical plane. The air bubbles were injected into the water on the upstream centre line of both the upper and lower surfaces in Plate 9 and in Plates 10 and 11 along the upstream lower and upper surfaces respectively. Plate 12 illustrates the flow in the horizontal plane when the bubbles were injected at the mid height of the upstream model sides.

Plate 12 clearly shows two recirculation bubbles in the horizontal plane immediately downstream of the base which were formed by the

entrainment of the free stream flow into the turbulent wake. The velocity of the entrained flow reduced and curved inwards with some bubbles drawn towards the base. The continuity of mass was maintained in the low pressure region by the entrainment and return of the fluid between the wake and free stream flows.

Plate 9 shows the presence of two recirculation bubbles in the vertical plane of the wake flow. They were formed by the same mechanisms as those observed in the horizontal plane. Their definition and effect were not as great as the horizontal pair due to their closer spacing and resultant interaction.

The greater influence and strength of the horizontal bubble pair determined the vertical alignment of the base pressure isobars displayed in Fig. 69c. The suctions varied across the base in the range between -0.3 and -0.22 with the highest suctions recorded on the vertical centre line because of the combined scavenging of the two recirculation bubbles. The entrainment and scavenging in the vertical plane, although of secondary effect, influenced the height of the base suction peak. It was positioned above the mid height of the base due to the presence of the ground.

A base cavity of approximate length 0.9h, where h is base height, was formed by the base flow although the curvature of the enclosing shear layers was not large as can be clearly observed from the Plates 9-12.

A fundamental change in the base flow field occurred when the trailing edge flow separation angle obtained a positive value of approximately ten degrees. This occurred when either of the 10° or 20° upper surface ramps was fitted and also when a zero degree ramp surface was placed at a high angle of attack. The change occurred for the zero degree lower surface geometries at a greatly reduced positive angle of attack, e.g. 2°, when the model was mounted at the lower ground clearance. This was because in these cases the proximity of the ground produced a small gap between the lower trailing edge and the ground which generated a high speed jet flow near the ground and this directed the flow away from the base in the same way as the large positive trailing edge angles.

The causes of the change in base flow characteristics were investigated by using the $\frac{1}{6}$th scale model of the 20-0 geometry mounted at an incidence of zero degrees. Photographs obtained during these tests are shown in Plates 13-15. Plates 13 and 14 were taken in the vertical

plane with the air bubbles entering the flow on the upstream lower and upper surfaces respectively. Plate 15 displays the base flow in the horizontal plane when the bubbles were injected into the flow at the mid height position of the model's sides.

It can be observed that the flow pattern changed dramatically from the O-O geometry flowfield. The flow which separated from the upper edge of the base was directed away from the base by the vertical component induced on the free stream by the upswept ramp surface. This resulted in little flow being entrained into the base area and of this, only a small fraction reached below the horizontal centre line of the base, as shown in Plate 14. The flow that separated from the lower edge was able to turn through the angle necessary for entrainment to occur. Some of the flow entrained from below the model crossed the entire height of the base and was then entrained by the upper shear layer, the remainder producing a recirculation bubble over the lower half of the base.

A flowfield dominated by two horizontal recirculation bubbles, similar to that observed in tests carried out on the O-O geometry model existed over the lower section of the base. However, over the upper section of the base no recirculation bubbles were present and the flow field was dominated by the entrainment of the base flow by the upper shear layer which produced a vertical flow velocity over this area. The suction levels reduced from the high values near the bottom of the base, produced by the scavenging, to levels nearer free stream values at the top.

This flow field is displayed by the base isobar distribution of the 20-O geometry in Fig. 70b, where the lower section, dominated by the pair of recirculating bubbles had isobars with a vertical orientation. Over the upper area, where the flow was dominated by the vertical velocity, the isobars had a horizontal alignment.

The recirculation bubble in the vertical plane near the base was better defined than in the O-O geometry case due to the removal of the interference from the upper surface separated shear layer.

When the zero degree lower surface geometries were mounted at positive angles of incidence the base flow field was inverted. The horizontal alignment of the isobars was now present over the lower half of the base, as shown in Fig. 69d. The base flow field of the O-20 body geometry was also examined in the water tunnel and the photographs obtained are displayed in Plates 16-18. Plates 16 and 17 were taken

in the vertical plane with the bubbles injected into the water along the upstream lower and upper surface centre lines respectively. Plate 18 displays the flow field in the horizontal plane with the bubbles passing along the sides at mid height.

The small base height did not allow the independant development of the upper and lower surface separated shear layers. This also occurred in the horizontal plane where the small base height, together with the vertical velocity component of the flow, resulting from the presence of the ramp upsweep, did not allow the formation of well-defined recirculating bubbles. The lack of any distinct base flow pattern is displayed in the isobar contour of this geometry in Figs. 72a-d. Little variation in pressure was recorded over the base.

The base flow downstream of this geometry was basically similar to that generated by the O-O geometry but the reduced base height and vertical velocity component generated greater interference between the separated shear layers and prevented the growth of the distinct re-circulation bubbles observed with the O-O geometry.

It can be observed in the photographs that the flow along the sides of the model was entrained into the wake region to produce a pair of distinct recirculation bubbles in the horizontal plane. These dominated the base flow in all cases apart from when large positive separation angles were present, or for small base height geometries.

4.6 CHANGES IN BASE FLOW CHARACTERISTICS AND INTEGRATED BASE PRESSURE COEFFICIENT PRODUCED BY VARIATION OF TEST CONFIGURATION

The characteristics of the base flow field and magnitude of the integrated base pressure were dependant on several parameters, e.g. incidence and ground clearance. The most important was the value of the trailing edge separation angle. Changes in the base flow field and magnitude of base pressure by variation of the major test conditions will now be discussed.

4.6.1 Body geometry

An increase in the upper surface ramp angle when the model was mounted at a constant incidence and either ground clearance always produced a reduction in the magnitude of the integrated base pressure, as shown in Table 21. This was caused by the

increase in upsweep angle producing an equal rise in the upper surface trailing edge separation angle. The base flow field characteristics changed when the addition of a larger ramp upsweep raised the trailing edge separation angle to a value above approximately 10°, relative to the free stream direction. The vertical alignment of the isobar distributions were then replaced over the upper half of the base with contours of horizontal orientation. The isobar distributions of the 0-0 and 20-0 geometries mounted at 0° incidence are displayed in Figs. 69 and 70. The respective integrated base pressure coefficients were -0.252, and -0.395. An increase in the upsweep of the lower surface generally caused a reduction in the magnitude of the integrated base pressure although the changes were not as large as those produced by similar upper surface geometry changes. The only lower surface geometry which produced a change in the pattern of the base flow field from that shown in Plates 9-12, was the 0° lower surface geometry when the model was mounted at positive incidences, i.e. when a positive trailing edge separation angle of approximately 10° was created. The resultant flowfield is shown in Plates 13-15. The change in the base flow pattern occurred at a much reduced angle of incidence, approximately 2°, when the model was mounted at the lower ground clearance. This was due to the high speed underbody flow produced by the closer ground proximity.

It can be observed that the size of base area was of secondary importance in the determination of the integrated base pressure.

The underbody flow, apart from the 0° cases mentioned above, had relatively little effect on the pattern of the base surface isobars and the integrated base pressure. This was because when the surface was upswept, the channel flow under the ramp for small divergence angle configurations, was dominated by a high velocity attached airstream. When the angle of divergence was increased to a high value, i.e. incidence reduced, or increased ramp upsweep, this flow was replaced by a largely separated flow field over the ramp surface. Both the separated and high velocity attached

airflow tended to reduce the base pressure. Therefore, as the effect of the high velocity airstream reduced as the ramp upsweep was increased, the increase in severity of the flow separation tended to maintain a similar effect on the base flow. This reduced any effects due to changes in lower surface model geometry. The variations produced in the magnitude of the integrated base pressure were a complex interaction between the effects produced by the flow separation and high velocity airstream under the model. In most cases the two effects combined to produce a higher base suction as the upsweep angle of the undersurface was increased.

After analysis of the results it is clear that in order to design a low drag vehicle it is necessary to remove any large positive base separation angles. This is especially true at the undersurface trailing edge where the close proximity of the ground plane accentuates the problem. It is therefore advisable to upsweep the undersurface to prevent the production of a positive trailing edge angle. In addition to increasing the mean base pressure, the upsweeping of the undersurface also reduces the base area, which in turn reduces the drag force.

4.6.2 Model incidence

The dependance of the magnitude of the base pressure on the flow separation angles at the trailing edges of the upper and lower surfaces was clearly shown when the variations in base pressure produced by changes in the angle of attack of the model are examined. They are listed in Table 21.

In all cases, except those incorporating the zero degree lower ramp, the magnitude of the base pressure increased as the angle of incidence of the model was increased throughout the incidence range. This was caused by the reduction in the positive value of the upper surface flow separation angle. For all these geometries the production of a positive separation angle at the lower trailing edge did not occur in the incidence range tested.

When the zero degree lower ramp surface was fitted it allowed the generation of a positive flow separation angle at

the lower surface trailing edge when the model was mounted at positive model angles of attack. This produced a reversal in the trend experienced with the other geometries and caused a reduction in base pressure through the positive incidence range. This effect was greater at the reduced ground clearance because of the small gap between the lower surface trailing edge and the belt which produced a high velocity jet flow near the ground which directed flow away from the base.

The variation of integrated base pressure coefficient can be demonstrated by examination of the results obtained when the incidence of the O-O geometry, mounted at the greater ground clearance was varied from $+9^{\circ}$ to -9°. The isobars obtained for these test configurations are displayed in Fig. 69.

When the model was at an incidence of $+9^{\circ}$ the integrated base pressure coefficient was -0.460 with the horizontal alignment of the isobars adjacent to the lower surface, where the positive trailing edge separation angle had been produced. The pressure coefficient rose to -0.292 and the horizontal isobars were removed as the incidence and lower trailing edge angle were reduced to $+2^{\circ}$. The maximum base pressure occurred at an incidence slightly less than zero degrees. The small negative value was a result of the induced incidence change produced by the presence of the ground. As the incidence was lowered a positive trailing edge angle was produced at the opposite surface, and when the incidence was lowered to -9°, the pressure coefficient had reduced to -0.311 with the horizontal isobars produced over the upper half of the base, again adjacent to the positive trailing edge separation angle. A larger varition in the integrated base pressure coefficient was recorded through the positive incidence range because of the close proximity of the lower surface trailing edge to the ground plane.

The reduction in integrated base pressure through the positive incidence range was not observed when a lower upswept ramp, 10° or 20° was fitted, because it did not allow the production of a positive trailing edge separation angle.

4.6.3 Ground clearance

It can be observed from the base pressure isobar contours shown in Figs. 69-80 that an alteration in the ground clearance of the model produced, in the majority of cases, no change in the overall shape of the distributions although the magnitude of the coefficients showed small variations. The only test configurations for which a change in the shape of the distribution was recorded were the zero degree bottom ramp geometries when mounted at positive angles of attack.

As discussed in Section 3, the principal changes in the flowfield around the model generated by a reduction in ground clearance, were the increased velocities under the model. In addition, small positive incidence and camber changes were induced on the flowfield over the model by the closer proximity of the ground.

The magnitude of the variation in base pressure produced by a reduction in ground clearance was determined by two opposing effects. Firstly, the increase in velocity under the model would tend to decrease the base pressure while the small induced reduction in trailing edge separation angle would tend to raise it.

The greater effect of the increased velocities under the model at the reduced ground clearance produced the expected result, in the majority of cases, of reducing the integrated pressure measured over the base areas, as listed in Table 21. A reduction in the mean base pressure was produced as the model was lowered when a large upper surface flow separation angle was presented to the flow.

An increase in base pressure as the ground was approached only occurred in cases where the dominance of the upper separation angle had reached a level where the small induced incidence change produced a greater effect than that generated by the increased velocities under the model. It should be noted that for these test cases at zero or negative angles of attack the change in the underbody velocities produced by a variation in ground clearance was minimal.

The changes in the integrated value of base pressure as the ground clearance of the model was varied has been shown to be a complex interaction between two opposing effects; increased velocities under the model and the induced incidence change. To determine the relative magnitude of these effects an examination of Table 21 must be undertaken. However, to serve as an example, the 10-10 geometry produced a negligible change in base pressure as the ground clearance was reduced when mounted at 0^{o} and -3^{o} incidence where the two effects cancelled each other out. However at an incidence of $+9^{o}$ the increased suctions under the model generated a lower base pressure at the reduced ground clearance of -0.278 compared to -0.265 recorded when the model was mounted further away from the ground. The effects are shown by local changes near the top and bottom of the distributions.

4.6.4 Stationary belt

The base pressure distribution was measured with the ground belt stationary for only one model geometry, 0-10, mounted at the lower ground clearance. The isobar contours, both belt moving and stationary, are displayed in Figs. 76 and 77 and the integrated pressure coefficients are shown in Table 21. It can be clearly observed that stopping the ground belt produced no significant variation in the shape of the pressure distribution over the base. However, it produced a general reduction in the level of suction which is demonstrated by the increased mean base pressure which, at each incidence tested, had a magnitude between those recorded at the two ground clearances when the belt was in motion.

The changes in the overall flow field must be examined to explain the changes in base pressure produced by the presence of the ground belt boundary layer and reduced momentum under the model when the belt was stationary. The displacement thickness of the boundary layer produced an effective reduction in the model ground clearance and its growth in the streamwise direction induced a positive

incidence on the flow over the model. These effects, although of reduced magnitude, were similar to those induced by a reduction on the ground clearance when the belt was in motion. This was displayed by the values of the mean base pressure coefficients obtained which had values between the two results obtained at the two different ground clearances when the belt was in motion. The increase in base pressure, produced when the ground belt was stationary, was generated by the reduction in the upper surface trailing edge produced by the positive incidence change induced by the growth of the belt boundary layer displacement thickness and also the reduced velocities in the underbody channel.

The negligible change in the base pressure isobar distributions produced by stopping the ground belt demonstrated the justification of undertaking the flow visualization of the model base flow using the water tunnel and fixed ground board simulation.

SECTION 5

VERTICAL UNDERBODY CHANNEL FLOW TRAVERSES

5.1 INTRODUCTION

The series of investigations undertaken using the bluff body shown in Fig. 1 produced many channel flow sections between the body and ground. This resulted in the generation of large adverse streamwise pressure gradients under the model, with their associated effect on the boundary layers of the stationary ground belt and model. It was therefore desirable to obtain vertical total pressure traverses at centre line longitudinal stations under the model with the belt moving, and stationary, to determine the thickness of the boundary layers and the depth of any separated flow regions.

5.2 ACQUISITION OF DATA

The total pressure traverses between the model undersurface and belt surface were measured at two model centre line positions, as shown in Fig. 2, for the configurations listed in Table 22. The forward traversing position was chosen because it was immediately downstream of the ramp knee, and in the region of the most severe adverse pressure gradients where flow separation was most likely to occur. The second position was selected because it was the most rearward station of the model and would therefore allow measurement of the maximum boundary layer thicknesses under the model.

A problem associated with the upswept angles of the undersurface was the large variation in the incident angle of the flow on the total head probe during a traverse of the channel. It was therefore decided to employ a Kiel[22] probe, (1mm diameter and outer tube of 0.4cms diameter) which removed any errors from this cause. However its construction prevented the measurement of the pressure at distances of less than 0.2cms to the model or belt surfaces. This distance was acceptable because any significant separated region would have a greater depth than this relatively small dimension and would therefore be detected.

The stem of the Kiel probe passed completely through the model and was clamped to a vernier screw gauge mounted to the upper surface of

the model. The 0^{o} top section of the model was employed to allow easy installation of the device and also because this upper section had least influence on the underbody flow as the incidence of the model was varied. The Kiel probe was connected by tubing, 0.158cms ($\frac{1}{16}$") internal diameter, to a Betz manometer. The working section free stream static pressure was used as the manometer reference pressure. This apparatus was used to measure the vertical total pressure traverse across the channel for the first configuration but the small diameter of the Kiel probe, length of connecting tubing and the relatively slow response of the manometer resulted in a long settling time at each measuring point.

The total pressure was measured, typically, every 0.25cms vertically through the channel. It was therefore decided to utilise a different, more rapid measuring system. A small Scanivalve module, fitted with a Setra System capacitance pressure transducer of range ±0.25 p.s.i., was mounted in the rear hollow section of the model. The output voltage from the transducer was displayed using a digital volt meter. The length of connecting tubing was reduced from approximately 4 metres to 0.7 metre. The free stream static pressure was again used as the reference pressure and the pressure from the Kiel tube was connected to the port of the Scanivalve which the transducer was constantly monitoring. The calibration of the transducer was checked and found to be satisfactory before any readings were recorded. This new system provided accurate measurements and quicker run times.

5.3 DISCUSSION OF RESULTS

The maximum pressures obtained during each traverse are listed in Table 22, and four of the pressure profiles are displayed in Figs. 81-84. Several general results were observed, the first was that the maximum pressure obtained from a traverse at the rear of the model was always less than the value obtained when the probe was mounted near the ramp knee. This was expected because of the energy loss due to the separation over the knee and the resultant downstream mixing. The maximum pressure recorded for the two traverses obtained with the belt stationary were greater than the values obtained with the belt moving. This was associated with the reduced area of separation over the knee of the ramp because of the lower adverse pressure gradient.

Figures 81 and 82, traverses obtained at the rear of the model, show clearly the effect of the moving belt. The boundary layer on the

model surface, approximately 4cms thick, was thinner when the ground belt was stationary because of the reduced adverse pressure gradients. When the ground belt was stationary the maximum pressure was attained only over a very short vertical distance before the pressure dropped as a result of the ground belt boundary layer, which at this station was 6.25cms thick. At the forward traversing point the thickness of the ground belt boundary layer was only 2cms therefore the adverse pressure gradient present between these two positions produced the expected thickening.

All the pressure traverses recorded under the O-10 geometry body, when the belt was moving, exhibited similar characteristics as the ground plane was approached. At the rear measuring station the maximum pressure was recorded at a height of 6cms above the belt surface and the magnitude of the pressure displayed no large variations as the ground clearance of the Kiel probe was reduced until the probe was at a height of approximately 0.5cms above the belt where the pressure ratio had lowered to 95% of its maximum value. Below this height the pressure rapidly increased due to the local effect of the belt surface. The dimensions of the Kiel probe did not permit any pressures to be recorded closer than 0.2cms to the belt surface. The pressure would rise to the free stream value at the belt surface due to the motion of the belt. Below a height of 6cms the pressure profiles that were measured, with the model in position, were the same shape as the calibration traverse which was recorded when the working section of the tunnel was empty. The belt speed had been adjusted to be equal to the free stream airflow velocity.

The presence of the model above the ground belt produced a flow field which resulted in a discrepancy in the velocities of the local airflow immediately above the ground belt and the surface of the ground belt. The velocity discrepancy could produce a boundary layer on the belt surface which could be investigated using the vertical underbody pressure traverses. The geometry of the undersurface of the model created large streamwise adverse pressure gradients which would, at least, create thickening of any belt surface boundary layer or, possibly, its separation from the belt surface. No variation in the pressure profile immediately above the belt surface was recorded when the model was in position which suggested that the velocity discrepancy between the local airflow and belt, produced by the presence of the model did not

create a boundary layer of any significant depth.

A further traverse, as shown in Fig. 83, displays the effect of incidence on the boundary layer on the model surface. The reduction of incidence had increased the depth of the reduced pressure immediately below the model surface from 4.0cms to 6.8cms, as shown by comparison of Figs. 81 and 83. It also demonstrated that this had no effect on the gradient of the traverse near to the ground which was similar to that observed with the model at 0° incidence.

A traverse was obtained for the 0-20 configuration at 0° incidence, as shown in Fig. 84. The traverse, measured at the rear station, showed a region of low pressure below the model surface. The maximum pressure in the channel was recorded for only a short distance before it reduced to the usual 5% deficit at a height of 0.5cms above the surface of the ground belt.

SECTION 6

THEORY

6.1 INTRODUCTION

Early theoretical techniques concentrated on determining the potential flow around two dimensional bluff bodies. The techniques became more sophisticated with the advancement of computer technology and have been extended to solve the three dimensional problem. Methods using the three dimensional finite difference solutions of the Navier Stokes equations have been developed which are capable of including real flow effects. The following is a summary of the principal theoretical techniques.

The free streamline method of Roshko[30] was one of the first techniques to calculate the time averaged potential flow around simple, two dimensional bluff shapes. Empirical data was employed to fix the position of the separated free streamlines in the complex velocity and potential planes. The real flow was determined by conformally transforming these planes to the physical plane. This method was improved by Parkinson and Jandali[26] who defined the position of the free streamlines by placing two sources on the surface of the body. In both these cases, the flow inside the separated streamlines was ignored.

Although the free streamline method produced good correlation with empirical results, it was limited to cases where suitable transformations existed. This resulted in the development of a more general two dimensional method by Bearman and Fackrell[4] where the surface of the body was represented by a sheet of vorticity with two sources to provide the wake flow. The vortex distribution was determined by splitting the surface into discrete segments of constant vorticity. The boundary condition of zero total velocity, freestream and induced, normal to the surface was employed to allow calculation of the singularity strengths and hence, the flowfield. A similar method was used by Smith and Hess[17] who represented the body surface by a series of discrete segments of constant source strength.

In the majority of cases when the body is mounted in ground effect, the ground plane streamline is produced by employing an image body. This

procedure is used in the calculation of both two and three dimensional flowfields.

Tuck[37] developed a different approach to calculate the potential flow around a simple two dimensional vehicle shape moving close to the ground plane. The analysis was in the form of a small gap asymptotic expansion and results agreed well with those obtained in a direct numerical computation.

All the methods described above provide time averaged solutions of the potential flow field around a two dimensional bluff body. Clements[11] has developed an inviscid model of two dimensional vortex shedding behind a square based section. The free shear layers were represented using discrete vortices and good agreement has been obtained with empirical results.

In cases where little spanwise flow was experienced, the two dimensional potential flow methods could be employed to predict the pressure distributions around the longitudinal centre line of three dimensional bodies. However, the range of these applications was limited, resulting in the development of three dimensional methods.

The methods of Smith and Hess and Tuck were extended to allow solution of three dimensional flowfields. Several other potential flow techniques were developed which used different singularity distributions to represent the body and wake surfaces. Stafford[33] employed a vortex lattice representation of both surfaces together with a source positioned within the body to provide the wake flow. Source and doublet distributions were employed by Ahmed[1] to represent the body and wake surfaces respectively.

Although several different potential flow methods have been developed to calculate the flow around a bluff body, a common major problem has been encountered. This was a result of attempting to use potential flow techniques to represent the highly viscous and turbulent wake flow. There was therefore a need to input empirical data to specify the flow conditions near the wake region and any areas of significant flow separation.

In an attempt to remove the requirement for empirical data, several investigators, e.g. Hirt and Ramshaw[18], have developed techniques which included real flow effects by using the three dimensional finite difference solutions of the Navier Stokes equations. However, their performance and

further development were limited because of two major problems. Firstly, the present generation of computers cannot provide the storage and speed of operation necessary for the calculation of the flow properties at the large number of grid points required for adequate flow field definition. Secondly, the approximations in the modelling of the turbulent shear stresses in the flow introduced errors in the results.

The techniques which produce the finite difference solutions of the Navier Stokes equations have greater long term potential. However, their present limitations have resulted in the majority of investigators continuing to use the potential flow methods.

The development of suitable theoretical techniques to calculate the pressure distribution around bluff bodies in ground effect contributes to the understanding of the flow around bodies of this type. In addition, once they have been shown to provide satisfactory results, they can be employed to produce significant reductions in the cost and duration of experimental investigations by predicting the effects of changes in basic test parameters, e.g. body shape and incidence, prior to the experimental work.

It is important that suitable experimental data is available which can be used to assess the performance of a method, prior to its wider use, and define the test configurations that can be successfully modelled theoretically. The experimental results described in this thesis which were obtained using the body shown in Fig. 1, provided the required data and therefore allowed a satisfactory theoretical investigation to be undertaken.

After a survey of theoretical methods it was decided to develop a potential flow technique to predict the pressure distribution over the surface of the body. It was felt that the small number of test cases where significant flow separation was experienced upstream of the base did not justify the use of more complex theoretical techniques which include the viscous effects of the flow, e.g. finite difference solutions of the Navier Stokes equations or the inclusion of boundary layer routines. Errors would be introduced by the inaccurate representation of the wake flow. However these would be limited to areas close to the trailing edge and again did not justify the use of more complex techniques.

6.2 DESCRIPTION OF THEORETICAL TECHNIQUE

A three dimensional potential flow technique has been developed in which the body and wake surfaces are represented by a distribution of singularities. The surfaces of the body and wake were divided into many small quadrilateral areas, called panels. The distribution of panels used in this investigation is shown in Fig. 86. A source distribution of constant strength was carried by each panel on the body surface. Each wake panel had a line vortex around its perimeter to produce a vortex lattice representation of the wake. The vorticity associated with each panel was constant around its perimeter.

Source panels were employed to represent the body surface because a panel of this type, when placed in a freestream flow, produces a flow similar to that over a body of finite thickness. The vortex panels were used to present the wake surface because they produce the necessary velocity jump across the wake surface.

The ground plane streamline was produced by the introduction of an image of the body.

Using the notation of Fig. 85, the induced velocity at a point Q due to a source panel of strength σ and area Sp is:

$$V_{Qs} = \text{grad} \left[-\tfrac{1}{4\pi} \iint_{Sp} \frac{\sigma\,(Sp)}{r}\, dSp \right]$$

A full derivation of the mathematical representation of a source panel can be found in Reference 17.

The representation of the panel could be simplified as the distance between the field point Q and the panel increased. This distance, when divided by the length of the source panel diagonal was denoted by d. If the value of d was less than 2.45 it was necessary to employ the exact representation of the source panel. When d increased to be within the range 2.45 to 4.0 it was possible to simplify the panel to a quadropole representation. In cases where d was greater than 4.0 the source panel could be represented by a point source positioned at the geometric centre of the panel. The two simpler representations produced savings in computational time with no significant loss in accuracy.

The induced velocity at a field point Q due to a line vortex, as shown in Fig. 85, is:

$$V_{Q_{AB}} = \frac{\Gamma}{4\pi} \frac{\underline{a} \wedge \underline{b}}{\underline{a} \wedge \underline{b} . \underline{a} \wedge \underline{b}} \{a + b\} \left\{1 - \frac{\underline{a} . \underline{b}}{ab}\right\}$$

This equation was used for each side of the panel and the total panel induced velocity was obtained by summing the induced velocities due to each side, i.e.,

$$V_{QV} = \sum_{i=1}^{4} V_{Q_{AB}}$$

The vectors $\underline{a}$ and $\underline{b}$ moved sequentially around the panel in a clockwise direction as each side was considered. The total velocity at any point in the flowfield was the addition of the induced velocities due to each of the singularities, representing both the real and image bodies, and the free stream velocity. To produce the surface of the body and wake as a streamline in the flowfield, it was required that there was zero total velocity normal to these surfaces. This condition was satisfied at the geometric centre of each panel which was called the panel control point. Using this condition, the following equation was formed.

$$\underline{V}_\infty \cdot \underline{n}_Q + \underline{V}_I \cdot \underline{n}_Q = 0$$

where V_∞ = free stream velocity

$\underline{n}_Q$ = unit vector normal to the surface at point Q

$\underline{V}_I$ = total induced velocity at Q due to the singularities

In its full form this became:

$$\sum_{j=1}^{m} \frac{\sigma_j}{4\pi} \left[\left(- \text{grad} \iint_{S_j} \frac{1}{r} \, d S_j \right) . \underline{n}_Q \right]$$

$$+ \sum_{j=1}^{n} \sum_{i=1}^{4} \left[\frac{\Gamma_j}{4\pi} \frac{\underline{a} \wedge \underline{b}}{\underline{a} \wedge \underline{b} . \underline{a} \wedge \underline{b}} \{a + b\} \left\{1 - \frac{\underline{a} . \underline{b}}{ab}\right\} \right] . \underline{n}_Q$$

$$= -\underline{V}_\infty \cdot \underline{n}_Q$$

where m = number of source panels

n = number of vortex panels

This equation was produced for each control point resulting in the following linear matrix being formed with the above equation representing one row. The matrix comprised of m + n equations with m unknown source strengths and n unknown vortex strengths.

$$\begin{bmatrix} A_{11}, A_{12}, \cdots\cdots A_{1m}, B_{11}, B_{12}, \cdots\cdots B_{1n} \\ A_{21}, A_{22}, \cdots\cdots A_{2m}, B_{21}, B_{22}, \cdots\cdots B_{2n} \\ A_{m1}, A_{m2} \qquad\qquad A_{mm}, B_{m1}, B_{m2} \cdots B_{mn} \\ A_{(m+1)1}, A_{(m+1)2} \cdots \qquad B_{(m+1)1}, B_{(m+1)2} \cdots B_{(m+1)n} \\ A_{(m+n)1} \cdots\cdots \qquad A_{(m+n)m}, B_{(m+n)1} \cdots\cdots B_{(m+n)_n} \end{bmatrix} \begin{bmatrix} C_1 \\ C_2 \\ C_m \\ D_1 \\ D_n \end{bmatrix} = \begin{bmatrix} E_1 \\ E_2 \\ E_m \\ E_{(m+1)} \\ E(_{m+n}) \end{bmatrix}$$

where

$$A_{Qj} = \left\{ - \text{grad} \iint_{S_j} \frac{1}{r} \, d S_j \right\} \cdot \underline{n}_Q ,$$

$$= \underline{F}_{Qj} \cdot \underline{n}_Q$$

$$B_{Qj} = \left[\sum_{i=1}^{4} \frac{\underline{a} \wedge \underline{b}}{\underline{a} \wedge \underline{b} . \underline{a} \wedge \underline{b}} \{a + b\} \left\{ 1 - \frac{\underline{a} . \underline{b}}{ab} \right\} \right]$$

$$= \underline{G}_{Qj} \cdot \underline{n}_Q$$

$$C_j = \frac{\sigma_j}{4\pi} , \quad D_j = \frac{\Gamma_j}{4\pi} , \quad E_j = -\underline{V}_\infty \cdot \underline{n}_Q$$

The terms A_{Qj} and B_{Qj} depended on the geometry of the body, the components C_j and D_j were the source and vortex strengths respectively and E_j was the normal component of the freestream velocity. $\underline{F}_{Qj}$ and $\underline{G}_{Qj}$, which are usually called the influence coefficients were stored in the computer for use when calculating the tangential surface velocity at each control point later in the program. This removed the necessity to recalculate them and hence reduced the solution time.

Purcells orthoganalisation method was employed for the solution of the matrix which provided the source or vortex strength of each panel.

Knowledge of the singularity strengths allowed the calculation of the total surface tangential velocity, i.e. freestream and induced, and hence pressure coefficient, at each control point.

6.3 PROGRAMMING TECHNIQUES

A major factor which restricted the scope of this technique was the limit imposed on the number of panels by both computer storage size and solution time. It was therefore important that all techniques were employed to reduce the computer storage and solution time required for the number of panels that were necessary for adequate surface representation.

Two techniques have already been mentioned, in Section 6.2, which reduced the solution time of the method. They were, firstly, storage of the influence coefficient of each panel so they could be reused in the calculation of the surface tangential velocity near the end of the program and, secondly, the simplification of the mathematical representation of the source panel as the distance between the source panel and control point increased.

A major problem was associated with the size and time required for the solution of the matrix to obtain the singularity strengths.

Other techniques have been employed in the program to reduce this problem. Firstly, in order to reduce the effective number of panels yet still maintain adequate surface representation, the two planes of symmetry present in the test configuration were employed. They were the ground plane between the real body and its image and the longitudinal centre line of both bodies. The body was positioned at zero degrees yaw to the flow in all cases. The use of the two planes of symmetry reduced the number of unknown singularity strengths and panels for which, for example, geometric parameters and pressure coefficients had to be calculated to one quarter of the original number. This resulted in the need to represent only one half of the real body and wake surfaces with panels.

The total induced velocity produced by a panel and its three images, across the planes of symmetry, could be inserted into the

influence matrix as a single summation because they were all associated with the same singularity strength. The summation of the real and image induced velocities reduced the number of columns in the influence matrix which combined with the smaller number of control points, i.e. rows, produced a matrix one quarter of its original size. This resulted in significant savings in the time taken to solve the matrix.

In order to further reduce the computational time a technique was employed which used only the real panel in the calculation of the induced velocities due to itself and its images. This removed the necessity to calculate any geometric parameters of the image panels. The technique was to calculate the induced velocities due to the real panel at each of the three images of the real control point. To transfer these to the induced velocities at the real control point due to the image panels, it was necessary to consider each image induced velocity individually and change the sign of the velocity components normal to each plane of symmetry across which it was necessary to pass in order to reach the relevant image panel from the real control point. If the image was across the ground plane and/or longitudinal centre line planes of symmetry, a change in the size of the calculated W and/or V velocity components was required.

A further decrease in the time required for the solution of the influence matrix was achieved by employing the successive orthogonalisation technique developed by Purcell[27]. This method is both rapid and requires only a relatively small one dimensional array for the calculation of the solution. The maximum size of this array for an N x N array of influence coefficients is

$$\frac{N}{2}\left\{1 + \frac{N}{2}\right\}.$$

6.4 PANEL DISTRIBUTION

The theoretical method described in Section 6.2 was employed to calculate the pressure distribution around the bluff body which was used in the experimental investigation described in this thesis. The geometry of the body is shown in Fig. 1. Comparison of the experimental and theoretical results allowed an assessment of the performance of the theoretical technique in predicting the pressure distribution around the O-O body geometry and the changes produced by variations in body geometry, incidence and ground clearance.

Two hundred and twenty two source panels were distributed over the surface of the body in an array of eighteen rows and twelve columns. A nineteenth row of six panels was produced at the nose. The distribution of the panels is shown in Fig. 86. As previously stated in Section 6.3, only one half of the body and wake was represented by the panels.

This number of panels was used to represent the body after an investigation into the dependance of the predicted pressure distribution on the number and distribution of the singularity panels had been undertaken. It was observed that little change in the magnitude of the predicted pressure coefficients occurred if more than two hundred and twenty two panels were used to represent the body. When the number of panels was reduced, small changes in the values of the predicted pressure coefficients were again observed but poor definition in the longitudinal position of suction/pressure peaks was obtained. The two hundred and twenty two panels used during the major part of this investigation produced satisfactory resolution in the pressure distribution and the number was not increased due to the associated large increase in computational time.

The primary objective of the theoretical investigation was to produce longitudinal centre line pressure distributions. For this reason, emphasis was placed on producing better geometrical definition in the longitudinal direction than the spanwise direction. This resulted in the greater number of rows than columns. The density of the rows was increased over the nose in order to improve the geometrical definition required by the surface curvature. The flat downstream surfaces could be adequately represented using larger panels.

The vortex panels which represented the wake, commenced at the trailing edge and continued downstream in six rows to a distance of one body length downstream of the trailing edge, as shown in Fig. 86. Increases in the length of the vortex wake above this value produced negligible variations in the pressure distribution over the body. The same number of columns of vortex panels was used as with the source panels which represented the body. This resulted in the use of seventy two vortex panels to represent the wake surface. The wake was of constant cross-sectional area, equal to the base area of the body, and continued downstream in the freestream direction.

This approximation to the wake shape was made in order to remove the requirement for empirical input. The errors introduced by this simplification are discussed in Section 6.5.

6.5 DISCUSSION OF RESULTS

The theoretical predictions of the longitudinal centre line pressure distributions around the bluff body will now be compared with the relevant experimental results.

6.5.1 Variation of upper surface body geometry

Figure 87a shows the predicted pressure distributions for the 0-0, 10-0 and 20-0 geometries when the body was positioned at an incidence of 0° and ground clearance of 14.5cms. Comparison of these with the experimental data, displayed in Fig. 42, show satisfactory overall agreement.

The magnitude of the suction peak on the upper surface of the nose was accurately predicted but the position was slightly further downstream in the experimental case. This was due to the inability of the prediction method, using discrete panels, to accurately represent the nose geometry and position of the stagnation point. The absence in the theoretical method of the representation of boundary layer growth and circulation in the flow around the body would also introduce errors in the prediction of the pressure distribution around the nose. The reduction in the magnitude of the suction peak on the upper surface of the nose, observed in the experimental results as the upper surface ramp angle was increased, was successfully predicted. The experimental and theoretical results agreed downstream of the nose with satisfactory prediction of the increases in pressure which were produced by the 10° and 20° ramps. The only significant errors in the theoretical pressure distributions were experienced close to the trailing edge and were due to the omission in the theoretical method of the viscous effects of the real wake flow.

The reasons for the differences between the experimental and predicted centre line pressure distributions close to the trailing edge can be discussed by considering the effect of body geometry, and hence trailing edge flow separation angle.

It can be seen that the predicted pressure coefficients near the trailing edge varied from -0.22 for the 0-0 geometry to -0.28 for the 20-0 geometry. The corresponding experimental values, which varied over a much smaller range, were -0.17 and -0.12 respectively. The predicted coefficient for the 0-0 geometry was therefore less than the experimental value. The opposite occurred with the 20-0 geometry where the predicted value was greater. The theoretical and experimental values for the 10-0 geometry agreed well.

The reason for the low predicted value for the 0-0 geometry was that the base suction, and hence flow acceleration towards the trailing edge, present in the experimental case, was not represented in the theoretical potential flow technique. The increase in velocity was not produced in the theoretical case due to the streamwise, constant cross section shape of the wake which was employed.

The same representation of the wake was used for the 20-0 geometry. However, in this case a twenty degree angle was created at the upper surface trailing edge between the sloping upper ramp surface of the body and the streamwise wake. This produced a flow acceleration towards the trailing edge. The predicted increase in flow velocity due to the trailing edge separation angle was greater than that produced by the wake entrainment in the experimental situation.

The accurate prediction of the variation in pressure coefficient towards the trailing edge which was achieved for the 10-0 geometry was because the ten degree angle at the upper surface trailing edge produced a flow acceleration similar to that generated in the experimental case by the wake entrainment.

An accurate prediction of the surface pressure near the trailing edge could have been achieved in all cases by varying the shape of the wake, i.e. trailing edge separation angle, to produce an acceleration similar to that generated by the real viscous wake. However, this approach was not followed because it required the input of empirical data and it was decided to judge the performance of the technique without empirical input.

The experimental and theoretical lower surface pressure distributions of these geometries also showed good agreement. The negligible effect of upper surface geometry on the lower surface pressure distributions was reproduced in the theoretical results. The nose suction peak was satisfactorily predicted, together with the downstream variation in the pressure distributions. The slightly higher predicted values were due to the lack of viscosity in the representation of the underbody flow. Errors in the predicted pressure coefficients were observed over the rear twenty percent of the body length and were due to inaccurate modelling of the wake flow.

6.5.2 Variation of lower surface body geometry

The predicted pressure distributions of the O-O and O-10 geometries mounted at 0^{o} and a ground clearance of 14.5cms are shown in Fig. 87b and can be compared with the experimental results shown in Fig. 41.

Good agreement with the experimental results was observed in the upper surface distributions with negligible change produced by the variation of lower surface geometry. The only errors were towards the rear of the model where the effects of the inaccurate wake modelling were experienced.

The overall prediction of the lower surface pressure distributions was satisfactory for both the O-O and O-10 geometries. The nose suction peaks were of the correct magnitude, with the O-10 geometry having the greater value due to the downstream suctions generated by the ramp. The presence of the underbody ramp, in the O-10 geometry, increased the discrepancy between the magnitude of the experimental and theoretical pressure coefficients caused by the absence of viscosity in the theoretical representation of the flowfield. The effect of increasing the amount of flow resistance in the underbody channel was observed in the experimental results when the ground belt was stopped. The increased flow resistance resulted in a reduction in the magnitude of the suctions generated. The increase in pressure towards the trailing edge in the predicted results for the O-10 geometry was again due to the inaccurate wake modelling.

The pressure distribution around the O-2O body geometry was not predicted due to the difficulty in representing the vortices and large viscous effects produced in the flow under the highly upswept ramp of the lower surface.

6.5.3 Variation of body incidence

The changes in the predicted pressure distributions around the longitudinal centre line of the O-lO geometry body which were produced by variation of body incidence, -3° and $+9^{\circ}$ are shown in Fig. 87c. They can be compared with the corresponding experimental data which is displayed in Fig. 44. The O-lO geometry was chosen because this body geometry allowed a further assessment of the ability of the method to predict the changes which were produced by variation of the model incidence in one of the most complex flow areas around the body, i.e. lower surface ramp and knee. The O-2O geometry was not investigated due to the significant viscous effects present in the underbody flow.

The wake was aligned in the freestream flow direction during this section of the investigation in order to maintain continuity with the other cases.

The movements of the flow stagnation point caused by the changes in incidence were satisfactorily predicted. The remainder of the upper surface pressure distribution, e.g. magnitude of nose suction peaks and the increase in pressure to a near constant value over the flat downstream surface was also adequately predicted.

A good agreement between the theoretical and experimental lower surface nose and knee suction peaks was observed. The absence of viscosity in the theoretical model was demonstrated by the larger predicted pressure coefficients upstream of the knee.

6.5.4 Variation of ground clearance

The variations in the predicted longitudinal pressure distributions around the O-O and lO-O geometries which were produced by a change in ground clearance, from 14.5cms to 4cms, are displayed in Fig. 87d. The corresponding experimental results are shown in Figs. 44 and 45.

Good overall prediction of the upper surface pressure distribution was achieved with negligible change produced by the reduction in ground clearance.

When the lower surface results are compared, the only significant discrepancy between the experimental and theoretical distributions was the magnitude of the nose section peaks. Variation of the size of the panels representing the nose surface showed that the magnitude of the nose suctions had no significant dependance on panel size. The principal reason for the error was the lack of circulation around the body in the theoretical model. This prevented accurate positioning of the flow stagnation point which resulted in the calculation of greater flow velocities under the body. The errors in the prediction of flow velocities over the lower nose surface due to the inaccurate positioning of the stagnation point were amplified when the model was at its lower ground clearance due to the smaller gap under the model.

6.6 CONCLUSIONS

It has been shown that the theoretical technique described in this thesis has satisfactorily predicted, without empirical input, the changes in the longitudinal centre line surface pressure distributions which were produced by variation of body geometry and incidence. The errors observed in the prediction of the changes produced by alteration of the ground clearance of the body could be significantly decreased by the introduction of circulation around the body in the theoretical model.

Errors were observed in the pressure distributions near the trailing edge. These were due to the simple wake geometry that was used. The errors could be greatly reduced by variation in the shape of the wake in order to produce similar flow velocities at the trailing edge to those generated by the flow entrainment of the real viscous wake. This was not done in order to remove the necessity of empirical input.

In this investigation, emphasis has been placed on the calculation of the theoretical longitudinal centre line pressure distributions. However, examination of the theoretical spanwise pressure distributions

showed satisfactory agreement with the relevant experimental data. The cases where any errors were observed were produced by spanwise flow near the radiied longitudinal edges when the surface was at a large incidence relative to the free stream direction. This was caused by the poor surface definition in this area because of the limited number of panels that were available for body representation because of the reasons previously stated in Section 6.3.

SECTION 7

RACING CAR AERODYNAMICS

7.1 INTRODUCTION

When completing a lap of an average racing circuit only one fifth of the time is spent near maximum speed and the remainder in cornering, braking and acceleration, when adhesion (increased by aerodynamic downforce) is more important than drag. To produce an increase in performance by improvement of the aerodynamics, or to complement any other performance increase, it is important that the downforce generated by the car should be increased. The first approach followed to achieve this aim was the mounting of high downforce aerofoils on long support struts at the rear of the car. When mounted in this position they were very effective because they were situated in the clean airflow, away from the turbulence produced by the car's bodywork. In 1969 there were several spectacular accidents caused by the failure of the long aerofoil mounting struts and it was then decided to introduce rules to limit the size, location, methods of installation and operation of aerodynamic devices. The aerofoils are now limited in size to a span of 110 cms and must have no part extending higher than 90 cms above the ground or further than 80cms behind the centre line of the rear axle. The rules, although greatly improving the safety of the cars, have significantly reduced the potential of the aerodynamic devices previously developed. Therefore, emphasis has now been placed on the development of the car bodywork to produce the necessary large downforce to supplement that produced by the aerofoil The high suctions that can be generated by the venturi channel between the vehicle undersurface and the ground suggested that this could be a profitable area to investigate.

7.2 DESCRIPTION OF MODEL AND TEST PROGRAMME

The first investigations into this method of increasing the downforce were carried out using a one-third scale model of a Formula One March 761 monocoque and nose, as shown in Plate 19. The model, although accurately dimensioned did not include components that would appear to be necessary for correct flow simulation to be achieved, e.g. rear wing, wheels and engine. It will be shown later that the flow

between the monocoque and ground was not significantly affected by the omission of these items. Due to the basic nature of the model and also the desire to investigate detail effects of the flow under the vehicle, it was decided to omit the measurement of the overall forces and measure only the pressure distribution over the monocoque undersurface. The change in downforce produced by an alteration of the model configuration could be determined by the integration of the pressure distribution over the undersurface of the model. There were fifty nine pressure tappings, 0.11cms internal diameter, inserted in the monocoque undersurface, as shown in Fig. 88. Three tappings were placed in the base of the monocoque and the same number under the nose to enable the measurement of any alteration in the level of suction in these areas produced by a change in underbody configuration. The model was mounted, as in Plate 19, by a sting attached to its base. The pressure tubes were led from the tappings through the cockpit and along the sting to the Scanivalve connection board positioned under the working section.

The testing was carried out in the University of Southampton 2.1m x 1.7m low speed wind tunnel with the ground plane represented by the moving belt facility, as described in Section 1.3, at an airspeed of 26 m/sec which produced a Reynolds number of 1.24×10^6 based on monocoque length. The ground belt was operated to run synchronously with the airflow. However, for several configurations the pressures were also recorded with the ground belt stationary to determine the effect of the ground belt boundary layer. The pressures were recorded using the Scanivalve and data logging system described in Section 1.4. The results were analysed and presented in various forms using a PDP 11-45 computer system.

All the changes in the configuration of the model were produced by fitting skirts of different planforms to the undersurface of the monocoque. The skirts were thin sheets of durable nylon which extended vertically from the undersurface of the monocoque to the ground in an attempt to alter the under body channel flow conditions in a favourable manner by increasing the suction levels. Table 23 lists the important configurations which were tested and the arrangements of the skirts are shown in Figs. 91-93.

No artificial boundary layer trip was attached to the undersurface of the monocoque because of the small radius of the lower leading edge

which would naturally trip the boundary layer. The testing was carried out with the model at its correct scaled ride heights of:-

front of nose	2.45cms
front of monocoque	2.06cms
rear of monocoque	2.41cms

i.e. with the monocoque at a negative incidence of 0.34 degrees.

7.3 DISCUSSION OF SURFACE PRESSURE RESULTS

The flow under the model separated at the leading edge of the nose and produced a large vortex under the nose, generating suctions of the order of Cp $\approx$ -0.5. The reduction in channel area under the front of the monocoque produced a venturi effect, Cp $\approx$ -0.25. The level of suction reduced rapidly downstream, due to spanwise outflow, and the pressure increased until a distance of approximately 40% of the monocoque length was covered, after which the flow became influenced by the base suction and the undersurface suctions began to rise. The centre line and overall pressure distributions of the model undersurface in its basic, clean configuration are shown in Figs. 89 and 91.

One of the dominant features of the level of undersurface suction obtained was the strength of the venturi effect under the front of the monocoque. When the height of the model above the ground was increased the venturi reduced in strength with a resultant drop in the level of suction. When the incidence of the model was increased, nose down, a larger venturi effect was produced and this was fed downstream producing a higher overall downforce. This increase was limited at high angles of attack by the onset of separation produced by the large adverse longitudinal pressure gradients. The presence of the higher suctions under the front of the monocoque was observed in the forward movement of the centre of pressure of the undersurface.

The addition of the V skirts to the undersurface of the monocoque, as shown in Fig. 92, reduced the magnitude of the suctions generated under the nose because of the stagnation pressure present upstream of the skirts. The suctions immediately downstream of the V were very high, Cp $\approx$ -0.6, as displayed on the isobar contour of Fig. 92. Although these suctions reduced towards the rear of the monocoque, because of the inflow, the levels remained higher than those recorded on the clean undersurface, producing a greater downforce under the monocoque.

A significant increase in downforce was also generated when skirts were attached along the total length of the monocoque sides, as shown in Fig. 90. They produced a high suction, Cp = -0.5, under the front of the monocoque because of the venturis in both the vertical, and horizontal planes. These large suctions had a greater effect on the remainder of the under surface than the V because the skirts along the sides prevented an increase in the pressure produced by spanwise outflow of air. These two configurations were combined, as shown in Fig. 92, in an attempt to maintain the high suctions generated by the V further downstream by preventing the inflow with the monocoque side skirts. Again, this produced a noteable increase in downforce over the monocoque undersurface.

The centre line pressure distributions shown in Fig. 89 illustrate the effect of the moving ground belt. The mean suction generated under the monocoque was always reduced by stopping the ground belt. The large suctions at the front of the monocoque were smaller with the belt stopped, although after a short distance downstream, the stopped and moving centre line distributions collapsed onto the same curve, as shown in Fig. 89. When the belt was stopped the rapid growth of the boundary layers produced by the large adverse pressure gradient caused the underbody flow to stall/choke generating an increase in pressure. The growth of the ground belt boundary layer was increased by the rough surface texture of the belt. The position where the stall occurred moved rearwards as the ground clearance of the model was increased.

The suction recorded under the nose was always slightly higher when the belt was moving. This was due to the presence of the boundary layer on the stationary belt reducing the strength of the vortex under the nose, which in turn impeded the passage of the smooth flow under the front of the monocoque resulting in an increase in pressure. The reduction in airflow under the model when the belt was stationary also produced an increase in pressure.

Examination of the undersurface isobar contours suggested that the "V" configuration, alone or in conjunction with the side skirts, was a more effective downforce generating device than the side skirts along the total length of the monocoque. However the "V" produced an increase in the pressure under nose, whereas the monocoque side skirts produced no adverse effect under the nose, and when this was included into the calculation of overall downforce it resulted in the side skirts

generating the largest overall increase in downforce.

An extra advantage of the monocoque sides skirts was the small variation in downforce produced by changes in the angle of incidence of the monocoque, when compared to other devices. The removal of pitch sensitivity is an important parameter of the design of a neutrally handling racing car.

The dependance of the level of downforce generated on the depth of the skirts was investigated and, as expected, the downforce increased as the gap between the bottom of the skirt and ground was reduced with a maximum obtained when the gap was sealed, as displayed in Table 23.

These tests produced significant increases in downforce and it was decided to continue the investigation with a more complex model incorporating four wheels and a representation of the engine, gearbox and rear wing, as shown in Fig. 88. No overall forces were measured during this series of tests and accurate flow simulation could therefore be achieved by resting the wheels on the ground belt to produce the correct rotational speed when the belt was in motion. The results obtained with the new model were very similar to those recorded during the previous series of tests. The major difference in the pressure distribution of the basic model was a slight reduction in the level of suctions under the nose and front of the monocoque, which was due to the production of stagnation pressure in front of the bluff front wheels. This adverse effect was reduced when the monocoque side skirts were fitted because of the isolation of the wheels from the channel flow under the monocoque.

A significant rise in the level of suction was being generated under the monocoque by the addition of the skirts and in an attempt to increase the downforce further it was decided to extend the monocoque under-surface and skirts to the rear of the engine block. This increased the area over which the downforce produced by the undersurface of the car could act but there was an opposing suction produced on the upper surface of the undertray by the base pressure at the rear of the monocoque. With the undertray mounted at a relative incidence of 0° to the under-surface of the monocoque the level of suction generated was not high enough to overcome the opposing uplift produced on the upper surface of the plate by the base pressure. The insulation of the under surface from the base pressure resulted in a reduction of the level of suction over the area of the monocoque which was previously affected by the base pressure.

This caused a further reduction in the downforce generated by the attachment of the undertray. To increase the pressure differential across the undertray it was decided to incline it at -8^{o} in an attempt to obtain the high suctions over the knee that were experienced with the bluff body model, as described in Section 3.3. These high values were not observed and the flow separated over the knee due to the lack of inflow and vortices associated with the previously tested three dimensional bluff body underbody flow. The addition of the side skirts had produced a 2-D underbody flow channel which could be compared to a 2-D diffuser with the ground plane representing the horizontal centre line of the device. After examination of two dimensional diffuser design data[7] it was observed that the angle of the undertray would have to be reduced to a value of -4^{o} to remove the geometry from the regime of large transitory stall, but at this angle the undersurface would not produce large enough suctions to overcome the base suctions acting over the upper surface of the undertray. This problem resulted in no further development of the device because of the lack of time to test the same configuration in the 3-D state, i.e. without side skirts.

7.4 FORCE INVESTIGATIONS

In both the previously described series of tests, pressures acting over a horizontal plane had been measured and although no large variations in monocoque base pressure had been recorded, it was necessary to carry out an investigation to determine the overall forces acting on the model to ensure that the large increases in downforce had been obtained with no significant drag penalty. The model was attached to a three component mechanical balance, as described in Ref. 12, to measure the lift, drag, and pitching moment of the model. In addition to measuring the drag, the pitching moment and lift results allowed the determination of the centre of pressure of the model which is an important parameter in racing car design. The model was attached to the mechanical balance mounting arms at the end of an 8" extension of the front axle on both sides of the model. This method produced the least interference to the airflow over the model.

When the model was attached to the balance, no contact between the model and belt could occur because of the transmission of forces. This created a problem with the attainment of the correct flow simulation around the wheels. If a gap of 0.5cm was left between the wheel and belt it would produce a strong venturi, and the suctions produced would create a large downforce. The problem is greater than that encountered

with saloon cars because of the greater width of the tyres. Several investigators have examined this problem. Stapleford[34] has tested a model with exposed wheels and several wheel-ground conditions. His results showed that the values of lift (C_{LW}) and drag (C_{DW}) generated by rotating wheels with zero ground clearance are obtainable with stationary wheels at a ground clearance in the order of 4% of the wheel diameter. The flow field over the top of the wheel would differ between the stationary and rotating cases but the effect of this on the airflow over other components would be negligible. For the same reason the skirts could not rub against the ground belt and a gap of 0.16cms had to be left. This gap would also be present on the race car due to the abrasion of the skirts against the ground caused by suspension movement. Therefore full scale and model skirt depths were equivalent. A gap of 0.3cm was left between the wheels and belt to remove the possibility of the wheels fouling the belt. The flow channel height under the model remained representative of the clearance under the car during a race where the gap is constantly changing due to the suspension travel associated with acceleration, braking and the lightening of the fuel load.

The results obtained from this series of overall force investigations are shown in Table 23, and it can be observed that the large gains in downforce produced by the skirts did not increase the drag of the car by a significant amount. The monocoque side skirts remained the best device. The high suctions produced under the front of the monocoque by the addition of the skirts is demonstrated by the forward movement of the centre of pressure.

SECTION 8

FULL SCALE - MODEL SCALE SURFACE PRESSURE CORRELATION

8.1 INTRODUCTION

During recent years there has been a large increase in the amount of small scale automobile/ground effect vehicle aerodynamic testing carried out in wind tunnels. Small scale testing of models introduces several possible sources of error between the results obtained in ideal wind tunnel conditions and those obtained from full scale vehicle testing in the natural environment, they are:-

(1) Ground simulation
(2) Reynolds number effect
(3) Blockage constraints on the wind tunnel airflow
(4) Simulation of the earths boundary layer and atmospheric turbulence conditions.

The problem of correct ground simulation can be easily removed by using one of the accepted methods, as discussed in Section 9 of this thesis. The moving ground belt technique is generally considered to be the most accurate and a typical facility of this type is described in Section 1.3 of this thesis.

The errors introduced by a discrepancy between full scale and model scale Reynolds numbers can be greatly reduced by the artificial tripping of the model boundary layer with carborundum strips or transition wires placed in the appropriate positions. This problem is greatly reduced when attempting to attain correct flow simulation under a typical vehicle because of the turbulence introduced by the usual undersurface roughness which reduces the Reynolds number dependence. The importance of Reynolds number similarity is also reduced with the introduction of flow separation by the presence of any sharp edges on the body.

The interference on the airflow in the wind tunnel produced by the model blockage can be easily removed by sensible scaling of the models to produce blockage ratios of up to 10% based on model and working section frontal areas.

Turbulence grids can produce small scale turbulence in the wind tunnel but to reproduce the correct large scale vortices and shear layers present in the earths boundary layer is very difficult. This is the area where most of the discrepancies between model and full scale results would occur.

It is because of these problems that it was felt necessary to undertake an investigation into the degree of correlation between the pressure measurements obtained using small scale models in wind tunnels and full scale vehicles undergoing road tests. The measurement of surface pressures, instead of overall forces, was carried out because they were easier to record and would also allow any local flow discrepancies to be observed.

Carr[10] has undertaken a study of this kind and used several vehicles for his tests ranging from a small car through to a three ton flat bed lorry. Pressures were measured around the longitudinal centre line contour of the vehicle and rakes were placed in the channel flow between the vehicle undersurface and ground. The pressure measurements both in the wind tunnel, which had a fixed board simulation of the ground plane, and on the road were taken using the same manometer banks. The conditions of the vehicle in the wind tunnel were made as representative of the road test conditions as possible, e.g. ride attitude and the engine running at the correct speed. When the steady state was obtained during each test the manometers were clamped and photographed. Reasonable correlation was achieved between the two sets of results except for the pressure rakes and tappings underneath the vehicle. The discrepancy in this area was due to the presence of the wind tunnel ground plane boundary layer altering the channel conditions between the vehicle undersurface and ground.

Buckley[6] employed a pressure recording system on the moving vehicle very similar to the one used by Carr, i.e. photography of U-tube manometers, but unlike Carr he analysed the dynamics of the manometer system in some detail. The main aspect that he investigated was the oscillatory motion of the manometer fluid induced by vehicle vibrations and in order to minimize the manometer response time it was necessary to have a high natural frequency of the fluid column, i.e. a small height of liquid in the manometer tube. Restrictions in the transmission tubes can also be used to reduce the oscillations of the fluid, but they must

be used carefully as their response to disturbances is non-linear. By suitable choice of pressure connecting tube diameter the response time of the system was reduced to a reasonable duration, i.e. approximately 0.2 seconds.

Although Buckley has investigated the manometer tube method of recording pressures in some depth and developed the design of a much improved system, it was felt that many problems were inherent in the system. Most of the drawbacks were encountered during the analysis of the results, i.e. the reading of the data from the photographs and its subsequent analysis and presentation. When surveying the various methods of measuring pressures on moving vehicles, great importance was attached to the ease and speed of data analysis. The use of a small forty eight port Scanivalve module, pressure transducer and portable stereo cassette recorder, with the associated electronic circuitry, was finally chosen as the most efficient recording system.

8.2 DESCRIPTION OF PORTABLE PRESSURE SCANNING SYSTEM

The largest component of the recording system was the water proof plastic control box (35cm x 25 cm x 14 cm) which contained the electronic circuits and voltage convertors. The connecting sockets for the Scanivalve module, transducer, tape recorder and battery were positioned on the front face of the box. This size of box was necessary to house the voltage convertors that were required to enable all components of the system to operate off a single twelve volt battery power supply. The modulating and demodulating circuits together with the electronics necessary for the control of the Scanivalve module rotational speed, occupied minimal space. The system is displayed in block diagram form in Fig. 94.

The Scanivalve module could be positioned up to a maximum distance of two metres from the control box. This was advantageous because it allowed the shortening of the pressure transmission tubes between the module and the tappings on the surface of the vehicle. However the length of the connecting wires between the Scanivalve module and control box was limited by the unacceptable level of interference superimposed on the transducer output voltage by the induced magnetic field produced by the large pulses of current, required by the stepping motor, which passed along the wires. This distance was extended to two metres by twisting the stepping motor power wires around each other

and thereby producing two nominally equal and opposite magnetic fields.

The time required for one scan of the forty eight pressures was variable with three possible pre-set values, 12 secs, 6 secs, or 3 secs resulting in 4, 8 and 16 ports scanned per second respectively. As with all Scanivalve modules the interport pressure settling time was negligible. A manual stepping speed was also available to enable the scanning speed to be varied beyond the pre-set values. A scan could be initiated from a switch on the front of the control box, or if this was not easily accessible, it could be triggered remotely from a convenient position. When a scan of the pressures was required, the system was triggered manually and the ports were scanned at the selected speed. The system automatically stopped when the forty eigth port had been reached and a further manual trigger was required for a second scanning sequence to be undertaken. A homing switch was incorporated to provide a rapid return to the starting point for the case when the manual scanning speed was being used and a scan was halted midway through the scan length.

During the scanning sequence the output voltage from the transducer was passed through a frequency modulating circuit to allow the recording of the signal on the cassette player. The modulating circuitry consisted of a modulator and carrier generator incorporating a voltage controlled multi vibrator. The modulating carrier frequency was 5.5 kHz. and the frequency deviation was set to a level of 30%. These values were chosen in order to obtain an acceptable signal to noise ratio. The voltage output level of the electronics was 0.7v peak to peak, to be compatible with the input requirements of the cassette recorder.

To analyse the recordings, the output from the tape recorder was fed into a demodulating circuit to convert it into a voltage signal. The frequency demodulator consisted of a limiter using an operational amplifier which was followed by an integrated circuit phase lock loop discriminator. After this section, it was passed through a low pass filter. Finally there was a buffer output stage with a gain of seven to match the output signal to the input requirements of the display device, e.g. pen recorder, oscilloscope or computer. The linearity and rise time of the system was checked and found to be satisfactory.

The specification of the cassette player was thoroughly analysed before it was included into the system as the data recording device.

It was found that although its specification was inferior in most areas, e.g. frequency response and wow and flutter, to the possible reel to reel alternatives, the specification was acceptable. The compact nature of the cassette recorder together with the ease of operation associated with the cassette tapes resulted in the inclusion of the cassette player into the system.

During the initial tests using this equipment, only the output voltage of the pressure transducer was recorded using a mono cassette recorder. However, in some cases during the analysis of the results, difficulty was experienced in identifying the port switching points of the Scanivalve module. It was therefore decided, in order to aid the data analysis, to record the port switching points on a second channel in the form of pulses generated by the electronics controlling the Scanivalve module stepping motor. After examination of the specifications of suitable recorders, the mono cassette recorder was replaced by an ITT studio recorder 720 stereo cassette recorder.

8.3 DESCRIPTION OF FULL SCALE AND MODEL SCALE TESTS

The system has been used to investigate the correlation between the model and full scale results obtained from tests on a large articulated container vehicle, as described in Ref. 2. The full scale testing was carried out in August 1976, on the T.R.R.L. test track at Crowthorne, Berkshire, using two six metre containers mounted on a trailer behind a Foden tractor unit. It was thought unnecessary to lock the suspension of the vehicle because the track was smooth and vertical vehicle movement would be negligible. The model scale tests were undertaken using a $\frac{1}{8}$th scale model of the same Foden tractor unit with a trailer and single ten metre container and were carried out in the University of Southampton 2.1m x 1.7m wind tunnel with the moving ground belt facility used to provide ground simulation.

During the full scale tests the forty two surface pressure tappings on the front container were connected by 5mm inside diameter tubing to the Scanivalve module and recording equipment which were mounted on the front of the trailer headboard. The tappings on the model, 0.11cms (0.043") internal diameter, were inserted in the same relative positions as the full scale vehicle. The major problem encountered during the full scale tests was the positioning of the pressure tappings on the ribbed container. As there would be local flow separation ahead of and down-

stream of the ribs it was decided that the best position for the tappings would be two thirds back from the forward edge of a rib. The container for the model tests had plane surfaces.

The reference free stream static pressure was measured during the full scale testing by a pitot static tube mounted on a boom three metres above the top of the container. The total pressure was fed to four of the Scanivalve ports to monitor any variation in the steady state conditions caused by, for example, wind gusts or variation in vehicle velocity. The vehicle on the test track travelled at a constant 50 m.p.h. The scanning was initiated remotely from the vehicle cab and a scanning speed of six seconds was used which allowed three sets of data to be recorded per test run. To remove any error due to headwind etc., test runs were repeated with the vehicle travelling in the opposite direction and the results averaged over two runs in each direction. Free-stream static pressure was used as the reference in both series of tests.

The model was positioned in the wind tunnel with the wheels in contact with the moving belt and was mounted by a single sting support attached to the base of the model. Lateral stability of the model was improved by tensioned wires which passed between the front of the model and the tunnel side walls. The pressure tubes were led from the model along the sting and connected under the working section to the scanning system, which is described in Section 1.4.

The Reynolds numbers, based on container length, were 9.07×10^6 and 1.80×10^6 for the full scale and model scale tests respectively.

Both model and full scale results were analysed using a PDP 11-45 computer system.

8.4 DISCUSSION OF RESULTS

Surface pressure isobars obtained for two vehicle configurations, basic and with cab mounted plate, during the model and full scale tests are displayed in Figs. 95 and 96.

A reduction in the severity of the flow separation over the leading edges of the container, produced by the addition of the cab mounted plate, can be clearly observed in both the model and full scale distributions by the difference in the magnitude of the suctions near the forward edges of the container, which in all cases are followed by a reduction in the level of suction in the downstream direction. This rise in

pressure continues with the values of the pressure coefficients rising to near free stream values until a distance of approximately seventy per cent of the body length is covered, downstream of which the pressure coefficient values reduce because of the influence of the high base suctions.

A good correlation was obtained between the model and full scale results and it demonstrated that the flowfield around the full scale vehicle was accurately reproduced during the wind tunnel tests. Any discrepancy between the distributions was caused by the lack of detail surface geometry on the model or by the different lengths of containers and the associated greater influence of the base pressure on the levels of suction generated over the upstream surfaces of the shorter model container.

The good correlation obtained over the upper and side surfaces of the container demonstrated the accurate representation of the flow in the gap between the cab and container. The flow through this gap is dependant on the underbody flow conditions. Therefore, although no pressures were measured on the undersurface of the vehicle, the results obtained demonstrated that accurate underbody flow simulation had been achieved by using the moving ground belt facility in the wind tunnel tests.

SECTION 9

GROUND PLANE REPRESENTATION

In the natural environment, assuming still air conditions, no ground plane boundary layer is produced. In the majority of cases of ground effect testing in wind tunnels, the ground plane is represented by a fixed board. The movement of the freestream airflow over the board creates an unrepresentative ground plane boundary layer. This produces incorrect flow conditions between the undersurface of the body and the ground plane which can result in significant changes in the forces generated by the body. There has been a large amount of research carried out to produce the correct simulation of the ground in the wind tunnel by removing the effects of the ground plane boundary layer.

The presence of a ground plane boundary layer introduces a momentum deficit into the airflow near the ground. In addition, the displacement thickness of the boundary layer reduces the effective ground clearance of the body and its downstream growth induces a positive incidence on the airflow around the model. It is, therefore, very important to determine the magnitude of the errors introduced by the inaccurate simulation of the airflow. The problem has been examined by several investigators who have undertaken correlation exercises to determine the relative merits of the different ground plane simulation techniques by comparison of results obtained in the wind tunnel. Full scale road tests have also been employed to provide data.

Using scale models of automobiles it has been shown that the drag increased and the lift was reduced when the ratio of displacement thickness to model height was reduced. Turner[38] showed that the existence of the ground plane boundary layer produced an increase in the magnitude of the lift generated by a ⅜ scale automobile model with negligible change to the other force and moment coefficients. As expected, a flush undersurface produced a greater reduction than a detailed representation due to the introduction of turbulence into the under body flow in the latter case. An idealised vehicle model was tested by Fackrell[15] and it was shown that the ground boundary layer increased the lift and reduced

$\partial C_L/\partial_\alpha$ but produced negligible change to the drag force. It was determined by Hucho[21] that the presence of a vehicle greatly reduced the ground board boundary layer displacement thickness when compared to that measured when the vehicle was absent.

The principal techniques that have been developed to simulate the ground plane are:-

(1) moving ground belt

(2) fixed ground board

(3) image technique

(4) blowing/suction - single slot, multi-slot or porous.

(1) The moving ground belt method is generally accepted as the most accurate, especially where rapid thickening or separation of the ground plane boundary layer could occur because of large adverse pressure gradients. This technique, however, is not always used because of the assumed increase in complexity when compared to the majority of the other methods. A typical installation is shown in Fig. 7. The tunnel floor boundary layer is removed by suction upstream of the belt or by the raising of the lead in board above the level of the floor boundary layer. The small blockage that is introduced into the working section when this type of facility is installed is a major advantage when compared to other methods of ground simulation. The main problems associated with the running of the rig are the central tracking and lifting of the ground belt at high speeds. The tracking problem can be removed by adjusting the alignment of the free running crowned roller. Suction applied through the base board to the undersurface of the belt prevents any lifting. With the belt running at its design speed, synchronously with the tunnel airflow, there is negligible velocity defect near the belt surface as shown by the velocity traverses obtained in Fig. 8, which were obtained from a typical installation. The moving belt facility installed in the Department of Aeronautics and Astronautics, 2.1m x 1.7m wind tunnel is described in more detail in Section 1.3 of this thesis.

Several investigators have attempted to reduce the size of the belt, and hence the tracking and lifting problems, by

reducing the belt width to the same width as the undersurface of the model. Although this reduced the magnitude of the difficulties, e.g. tracking, it introduced inaccuracies in the flow simulation at the moving belt-stationary ground interface. For this reason the modified ground belt approach has had little success and is no longer used.

(2) The most widely used method of ground plane simulation is the fixed ground board which spans the width of the tunnel above the floor boundary layer. The boundary layer on this board is much thinner than the tunnel floor boundary layer and the model is mounted as near to the rounded leading edge of the board as possible without producing errors in the pressure field upstream of the model. The circulation generated around the ground board by the presence of the model can be removed by equalising the blockage ratio on the opposite side of the board with the addition of a flap at the trailing edge. The incidence of the flap is adjusted until the upper and lower surface pressures at the same longitudinal station of the ground board are equal. A major disadvantage of this technique is caused by the raising of the ground board above the tunnel floor. This reduces the effective area of the tunnel and limits, because of the increased blockage ratio, the maximum size of model that can be tested. The usual method of correcting for the presence of the ground board boundary layer is by raising the model to a height equal to the boundary layer displacement thickness. However, this distance is difficult to accurately determine because δ^* is usually measured with the model absent and it has been shown that the presence of the model could induce pressure gradients along the ground producing changes in the displacement thickness.

An alternative method, to allow for the ground plane boundary layer, is to position the model in its correct 'full scale' position and correct for the boundary layer effect using the method developed by East[13] who has shown that the experimental values of C_L, C_D and C_M are dependent on δ^*/H, where δ^* is the displacement thickness of the ground plane boundary layer and H is the model ground clearance. The relations are reasonably linear and their slopes

increase with model angle of attack. The correlation for the presence of the boundary layer can be calculated by using the following expression:

$$C_{corr.} = C_{meas.} + \frac{\delta^*}{H} \frac{\partial C}{\partial(\delta^*/H)} + \frac{\partial \delta^*}{\partial x} \left(\frac{\partial C}{\partial(\partial \delta^*/\partial x)} \right)$$

where the gradients of C, the force coefficient, are determined by carrying out an additional test with a different ground board configuration yielding another value of δ^*. The fixed ground board with either of these correction methods produces adequate results provided there are no large adverse pressure gradients present along the ground board which would cause separation of the ground boundary layer.

(3) The image technique, as the name suggests, utilises two identical models with the ground plane represented by the plane of symmetry between them. The major problem associated with this method is the interaction between the vortices shed in the wakes of the models but this can be prevented by the positioning of a thin splitter plate along the plane of symmetry in the wake. The use of two models doubles the model blockage and therefore reduces the size of model that can be tested. For this reason, and also the increased cost involved in the building of two models, this technique is rarely used.

(4) A fourth possible method of producing correct ground simulation is the removal of the ground plane boundary layer, by boundary layer control in the form of suction or blowing through single slot, multi-slot or porous surfaces. The major difficulty, apart from the design complexity of the system, is the prevention of any vertical velocity component induced on the free stream by the flow passing through the ground plane The correct adjustment of the blowing/suction for each individual model plus the complexity and cost of the rig results in this method rarely being used.

Although the four techniques described above are the main methods that have been employed to simulate the presence of the ground plane, there have been several other attempts which have all resulted in limited success. One such example is when the vehicle, due to blockage or weight limitations, must be mounted

directly on the tunnel floor and it has been necessary to try to reduce the tunnel floor boundary layer thickness. One method that was attempted used swept fillets attached to the floor upstream of the model position. These reduced the boundary layer thickness by fifty per cent when the vehicle was absent. However, when this configuration was tested with vehicles in position it was shown that they had no influence on the aerodynamic forces of a passenger car and only minor influence was observed on a sports car model. A major disadvantage introduced by this method was the outflow, in the horizontal plane, produced by the swept fillets.

SECTION 10

CONCLUSIONS

Many aspects of the aerodynamics of bluff bodies in ground effect have been covered in this thesis. Overall forces and surface pressure distributions were measured in wind tunnel tests over a moving belt simulation of ground effect and flow visualization was supplemented by tests in a water tunnel. Model results were compared with full-scale results. Theoretical techniques were investigated.

(1) For the majority of configurations tested, the model generated a downforce and the overall drag force was dominated by the base contribution.

(2) The overall downforce of the model reduced with increasing incidence and increased when the upsweep of either the upper or lower surfaces was raised. Smaller increases in downforce were produced by changes in upper surface geometry than produced by equal changes in the lower surface upsweep. A reduction in ground clearance increased the downforce generated by the model in all cases except the zero degree lower surface geometry when mounted at positive incidences.

(3) The overall drag of the model had a "U" shaped dependance on incidence. This was a result of both the base and forebody pressure drag contributions following this trend. Larger increases in the drag of the model were produced by raising the upsweep of the upper surface geometry than with similar changes to the lower surface, due to the increase in base drag resulting from the increase in base area and reduction in base pressure.

(4) The pitching moment of the model increased with increasing incidence. A reduction in ground clearance generally produced a more negative moment when the model was mounted at negative incidences and a more positive moment when mounted at positive incidences. An increase in the upsweep of either the upper or lower surface produced a more positive nose up pitching moment.

(5) An area of distributed roughness was attached to the undersurface of the model. This resulted in a small reduction in the overall downforce and a small increase in the drag force generated by the model.

(6) The surface pressure distributions were measured to determine the local changes produced by variation of test configuration. Observation of the surface pressure distributions showed that the reduction in downforce as the incidence increased, was primarily due to a rise in the magnitude of the suction levels over the upper surface of the nose, resulting from the downward movement of the stagnation point. The pressure distribution over the majority of the upper surface of the model was independant of the geometry of the lower surface and vice versa. The areas where any dependance was observed were near the stagnation point and base of the model.

Negligible change in the upper surface pressure distribution was recorded as the ground clearance of the model was reduced. Generally higher suctions were recorded over the majority of the lower surface due to the reduced height of the underbody flow channel.

The pressure distributions were integrated over four sections of the model surface, the central and ramp areas of the upper and lower surfaces, to allow observation of the local downforce and drag variations. An increase in the upsweep of either the upper or lower surfaces produced a rise in the downforce caused by both sections, central and ramp, of that surface. The downforce of the lower ramp reduced as the incidence was raised, whereas the downforce increased for the other three areas investigated.

The integrated local forebody pressure drag forces were very small and the principal observation was the dominance of the base drag contribution to the overall drag force.

(7) The pressure distributions over the base area were also recorded. Examination of the base surface isobars showed that two different patterns could exist:

(a) vertically orientated isobars over the total base area.

(b) the vertical isobars were replaced by isobars with a horizontal orientation in areas adjacent to the upper or lower trailing edge where large trailing edge separation angles were present.

Flow visualization, using a scale model in a water tunnel, was undertaken to investigate the causes of the change in the pattern of the isobars. It was observed that when either trailing edge separation angle was greater than approximately ten degrees, a change in base flow occurred which was associated with the change in isobar pattern from (a) to (b).

The value of the mean base pressure coefficient was principally dependant on the magnitude of the trailing edge separation angle and reduced as this angle was increased, e.g. greater upper surface upsweep or reduction in model incidence. The magnitudes of the mean base pressure coefficients demonstrated the dependance of the overall drag force on the base drag contribution.

(8) Extensive flow visualization of the airflow around the model was undertaken in the wind tunnel. A vortex was observed to exist in an approximately streamwise direction from each end of the lower surface ramp knee, when the lower surface was upswept. The two vortices increased spanwise inflow under the model and greatly reduced the severity of the flow separation over the lower ramp surface.

(9) Tests were undertaken with the ground belt stationary in order to determine the effects produced by the ground plane boundary layer. Vertical underbody total pressure traverses were measured at two points on the longitudinal centre line of the model to determine the growth of the model boundary layer and ground plane boundary layer, when present. No ground plane boundary layer was observed when the belt was moving synchronously with the free stream airflow. The presence of the ground plane boundary layer, when the belt was stationary, produced in many cases, large changes in the overall forces and pressure distributions. This demonstrated that correct ground simulation was necessary.

(10) A potential flow theoretical prediction method was developed to allow calculation of the surface pressure distribution around the body. Source and vortex panels were employed to represent the body and wake surfaces respectively. The number of test configurations for which the technique could be satisfactorily used was limited due

to the empirical data required to allow for real flow effects.

(11) The measurement of the surface pressure distributions of full-scale road vehicles during tests in the natural environment was followed by similar tests using scale models in the wind tunnel. This allowed the opportunity to compare the two sets of data. A portable electronic pressure scanning system was developed for the full-scale experiments. Good correlation was achieved between the two sets of results. This demonstrated that data obtained during full-scale tests of typical bluff bodies in the natural environment can be obtained at model scale in a wind tunnel.

REFERENCES

1. Ahmed, S. R. and Hucho, W. H. — The calculation of the flow field past a van with the aid of a panel method. S.A.E. Paper 770390 (1977).

2. Allan, J. W., Burgin, K. and Lilley, G. M. — On water spray generation by road vehicles and methods for its control. Contract report for Department of Environment, Transport and Road Research Laboratory, July, 1977.

3. Bearman, P. W. — Investigation of the flow behind a two dimensional model with a blunt trailing edge and fitted with splitter plates. J. Fluid Mech. 21, pp. 241-255 (1965).

4. Bearman, P. W. and Fackrell, J. E. — Calculation of two dimensional and axisymmetric bluff body potential flow. Imperial College Aero. Report No. 74.07 (1974).

5. Berry, A. J. — An experimental investigation of ground effect using a moving surface simulation. University of London, M.Phil. Thesis (1968).

6. Buckley, B. S. — Road test aerodynamic instrumentation. S.A.E. Paper 741030 (1974).

7. Carlson, J. J., Johnston, J. P. and Sagi, C. J. — Effects of wall shape on flow regimes and performance in straight 2-D diffusers. J. of Basic Engineering, March, 1967.

8. Carr, G. W. — The aerodynamics of basic shapes for road vehicles. Part 1 - Simple rectangular bodies. M.I.R.A. Report No. 1968-2 (1968)

9. Carr, G. W. — The aerodynamics of basic shapes for road vehicles. Part 3 - Streamlined bodies. M.I.R.A. Report No. 1970-4 (1970).

10. Carr, G. W. — Correlation of pressure measurements in model and full scale wind tunnels and on the road. S.A.E. Paper 750065 (1975).

11. Clements, R. R. — An inviscid model of two dimensional vortex shedding. J. Fluid Mech. 57, pp. 321-336 (1973).

12. Davies, P. O. A. L. — The new 7' x 5½' and 12' x 15' low speed wind tunnel at the University of Southampton. A.A.S.U. Report No. 202 (1961).

13. East, L. F. — The measurement of ground effect using a fixed ground board in a wind tunnel. R.A.E. Tech. Report No. 70123. Aero. Res. Com. R. & M. 3689 (1972).

14. Eldred, K. — Base pressure fluctuations. The Jrnl. of the Acoustical Soc. of America 33, No. 1 (1961).

15. Fackrell, J. E. — The simulation and prediction of ground effect in car aerodynamics. Imperial College Report No. 75-11 (1975).

16. Frost, R. — Aerodynamics of bluff bodies in ground effect. Dept. of Aero. and Astro., University of Southampton, third year B.Sc. Hons. project report (1979).

17. Hess, J. L. and Smith, A. M. O. — Calculation of potential flow about arbitrary bodies. Prog. Aero. Sci. 8, pp. 1-138 (1967).

18. Hirt, C. W. and Ramshaw, J. D. — Prospects for numerical simulation of bluff body aerodynamics. Los Alamos Scientific Lab. Report LA-UR-76-2112 (1976).

19. Hoerner, S. F. — Fluid Dynamic Drag. published by author, Brick Town, N.J. (1965).

20. Howell, J. P. — Force and wake characteristics of road vehicles and simple bluff bodies near to the ground with an examination of the loads on road vehicles in proximity to others. City University, Ph.D. Thesis (1977).

21. Hucho, W. H., Janssen, L. J. and Schwartz, G. — The wind tunnel's ground plane boundary layer - its interference with the flow underneath cars. S.A.E. 750066 (1975).

22. Kiel, G. — A total head meter with a small sensitivity to yaw. N.A.C.A. TM 775 (1935).

23. Morel, T. — The effect of base slant on the flow pattern and drag of three dimensional bodies. G.M. Symposium - Aerodynamic drag mechanisms of bluff bodies and road vehicles (1976).

24. Nakaguchi, H. — Recent Japanese research on three dimensional bluff body flows relevant to road vehicle aerodynamics. G.M. Symposium - Aerodynamic drag mechanisms of bluff bodies and road vehicles (1976).

25. Nash, J. F., Quincey, V. C. and Callinan, J. — Experiments on 2-D base flow at subsonic and transonic speeds. Aero. Res. Coun. R. & M. 3427 (1966).

26. Parkinson, G. V. and Jandali, T. — A wake source model for bluff body potential flow. J. Fluid Mech. 40, (1970).

27. Purcell, E. W. — The vector method of solving simultaneous linear equations. Jrnl. of Math. Physics 23, p. 180 (1953).

28. Reneu, L. R., Johnson, J. P. and Kline, S. J. — Performance and design of straight 2-D diffusers. Jrnl. of Basic Engineering, ASME, 89 (1967).

29. Richards, E. J. and Burstall, F. H. — The china clay method of indicating transition. R.A.E. Tech. Note Aero. 1466 (1945).

30. Roshko, A. — A new hodograph for free streamline theory. N.A.C.A. TN 3168 (1954).

31. Shaw, R. — The measurement of static pressure. J. Fluid Mech. 7, pp.550-564 (1960).

32. Simmons, J. E. L. — Two dimensional vortex wakes. University of Cambridge, Engineering Dept. Ph.D. Thesis (1973).

33. Stafford, L. G. — Calculation of the pressure distribution over the surface of a ground vehicle. City University, Ph.D. Thesis (1972).

34. Stapleford, W. R. and Carr, G. W. — Aerodynamic characteristics of exposed rotating wheels. M.I.R.A. Report No. 1970-2.

35. Stollery, J. L. and Burns, W. K. — Forces on bodies in the presence of the ground. Road Vehicle Aerodynamics Symposium, City University (1969).

36. Tanner, M. — Theoretical prediction of base pressure for steady base flow. Prog. in Aerospace Sciences 14, pp.177-225 (1973)

37 Tuck, E. O. — Irrotational flow past bodies close to a place surface. J. Fluid Mech. 50, pp. 481-491 (1971).

38. Turner, T. R. — Wind tunnel investigation of a 3/8 scale automobile model over a moving belt ground plane.
N.A.S.A. TN D-4229 (1967).

39. Waters, D. M. — Thickness and camber effects on bodies in ground proximity.
Advances in Road Vehicle Aerodynamics,
B.H.R.A. Fluid Engineering.
Cranfield, Paper 12 (1973).

BIBLIOGRAPHY

Acherbach, E. — Vortex shedding from spheres. J. Fluid Mech. 62, pp.202-221 (1974).

Apelt, C. J. and West, G. S. — The effects of wake splitter plates on bluff body flow in the range $10^4 < R < 5 \times 10^4$. Part 1. J. Fluid Mech. 61, p.187 (1973). Part 2. J. Fluid Mech. 71, pp.145-160 (1975).

Bearman, P. W. — A study of unsteady base flows. Cambridge University Engineering Department Ph.D. Thesis (1965).

Bearman, P. W. — An investigation of the flow around rectangular cylinders. Aero. Quarterly, August, 1972.

Bearman, P. W. and Wadcock, A. J. — The interaction between a pair of circular cylinders normal to a stream. J. Fluid Mech. 61, pp.499-511 (1973).

Bearman, P. W. — Some measurements of the distortion of turbulence approaching a 2-D bluff body. J. Fluid Mech. 53, pp.451-467 (1972).

Beauvais, F. N., Tignor, S. C. and Turner, T. R. — Problems of ground simulation in automotive aerodynamics. S.A.E. Paper 680121 (1968).

Bettes, W. H. and Kelly, K. B. — The influence of wind tunnel solid boundaries on automotive test data. Advances in Road Vehicle Aerodynamics, B.H.R.A. Fluid Engineering, Cranfield, Paper 16 (1973).

Boldman, D. R., Brinich, P. F. and Goldstein, M. E. — Vortex shedding from a blunt trailing edge with equal and unequal external mean velocities. J. Fluid Mech. 75, pp.721-735 (1976).

Bryer, D. W. — Pressure probe methods for determining wind speed and flow direction. H.M.S.O. (1971).

Buckley, S. B. — Vehicle - surface interaction. University of California, Berkeley, Ph.D. Thesis (1972).

Buckley, S. B. and Laitone, E. V. — Airflow beneath a vehicle. S.A.E. Paper 741088 (1974).

Butler, S. F., Moy, B. A. and Pound, T. N.
A moving belt rig for ground simulation in low speed wind tunnels.
R.A.E. Tech. Note Aero. 2937 (1963).

Carr, G. W.
The aerodynamics of basic shapes for road vehicles.
Part 2. Saloon car bodies.
M.I.R.A. Report No. 1968-9 (1968).

Carr, G. W. and Stapleford, W. R.
A further study of the simulation problem in wind tunnel tests of road vehicles.
M.I.R.A. Report No. 1971-6 (1971).

Carr, G. W. and Rose, M. J.
Wind tunnel tests of vehicle models using a moving ground surface.
M.I.R.A. Report No. 1966-13 (1966).

Carr, G. W. and Rose, M. J.
Correlation of full scale wind tunnel and road measurements of aerodynamic drag.
M.I.R.A. Report No. 1964-5 (1964).

Carr, G. W. and Hassell, T. P.
A simple device for reducing wind tunnel boundary layer thickness.
M.I.R.A. Bulletin No. 5 (1968).

Doberenz, M. E. and Selberg, B. P.
A parametric investigation of the validity of $^{1}/_{25}$th scale automobile aerodynamic testing.
S.A.E. Paper 760189 (1976).

Ehlers, F. E., Johnson, F. T. and Rubbert, P. E.
Advanced panel type influence coefficient methods applied to subsonic and supersonic flows.
N.A.S.A. SP 347, pp.939-984 (1975).

Fage, A. and Johanson, F. C.
The structure of vortex sheets.
Aero. Res. Coun. R. & M. 1143 (1928).

Fackrell, J. E. and Harvey, J. K.
The aerodynamics of an isolated road wheel.
A.I.A.A. Second Symposium on Aerodynamics of Sports and Competition Automobiles, pp. 119-125 (1974).

Fisher, A. B. and Langley, M. J.
An investigation of the forces on a finite aspect ratio wing where the trailing edge is blunt.
Unpublished University of Cambridge report (1966).

Gerrard, J. H.
The mechanics of the formation region of vortices behind bluff bodies.
J. Fluid Mech. 25, pp.401-413 (1966).

Grabowski, W. J. and Berger, S.A.
Solution of the Navier-Stokes equations for vortex breakdown.
J. Fluid Mech. 75, pp.525-544 (1976).

Griffin, O. M. and Ramberg, S. E.
On vortex strength and drag in bluff body wakes.
J. Fluid Mech. 69, pp.721-728 (1975).

Gross, D. S. and Sekscienski, W. S.
Some problems concerning wind tunnel testing of automotive vehicles.
S.A.E. Paper 660385 (1966).

Heald, R. H.
Comparison of the ground plane and image methods for representing ground effect in tests on vehicle models.
U.S. Nat. Bureau of Standards Jrnl. of Research 13 (1934).

Hucho, W. H.
The aerodynamic drag of cars - current understanding, unresolved problems and future prospects.
G.M. Symposium, Aerodynamic drag mechanisms of bluff bodies and road vehicles (1976).

Hunt, J. C. R.
A theory of turbulent flow around 2-D bluff bodies.
J. Fluid Mech. 61, pp.625-706 (1973).

Knauss, D. T.
The influence of flow orientation on the vortex frequencies of bluff bodies at low Reynolds numbers.
Maryland University.
Ph.D. Thesis (1974).

Kramer, C., Gerhardt, H. J., Jaeger, E. and Stein, H.
Wind tunnel tests on underbody aerodynamics.
Symposium on Road Vehicle Aerodynamics, Aachen (1974).

Landahl, M. T.
Numerical modelling of blunt body flows - Problems and prospects.
G.M. Symposium, Aerodynamic drag mechanisms of bluff bodies and road vehicles (1976).

Larrabee, E. E.
Small scale research in automobile aerodynamics.
S.A.E. Paper 660384 (1966).

Mabey, D. G.
Some measurements of base pressure fluctuations at subsonic and supersonic speeds.
Aero. Res. Coun. C.P. 1204 (1970).

Mair, W. A.
Reduction of base drag by boat tailed afterbodies in low speed flow.
Aero. Quart. 20, pp.307-320 (1969).

Mair, W. A.
Blockage corrections for blunt based bodies of revolution.
J. Roy. Aero. Soc. 72, p.1058 (1968).

Maskell, E. C.
A theory of the blockage effects on bluff bodies and stalled wings in a closed wind tunnel.
Aero. Res. Coun. R. & M. 3400 (1963).

Mason, W. T. and Sovran, G.
Ground plane effects on the aerodynamic characteristics of automobile models - an examination of wind tunnel test technique.
Advances in Road Vehicle Aerodynamics, B.H.R.A. Fluid Engineering, Cranfield, Paper 17 (1973).

Maull, D. J. and Young, R. A.
The wake of a three dimensional bluff body in uniform and non-uniform streams.
Symposium on External Flows, Bristol (1972).

Metz, L. D. and Sensenbrenner, K.
The influence of roughness elements on laminar to turbulent boundary layer transition as applied to scale model testing of automobiles.
S.A.E. Paper 730233 (1973).

Morelli, A.
Theoretical method for determining the lift distribution on a vheicle.
F.I.S.I.T.A. Congress, 1964.

Nash, J. F.
A review of research on two dimensional base flow.
Aero. Res. Coun. R. & M. 3323 (1963).

Ono, M.
On the representation of a ground in a wind tunnel.
J. Aero. Sci. 3 (1935).

Pope, A. and Harper, J. J.
Low speed wind tunnel testing. (1966)

Rainbird, W. J.
Errors in measurement of mean static pressure of a moving fluid due to pressure holes.
Nat. Res. Coun. Canada Report DME/NAE 1967(3).

Roshko, A.
On the drag and shedding frequency of two dimensional bluff bodies.
N.A.C.A. TN 3169 (1954).

Rubbert, P. E. and Saaris, G. R.
A general 3-D potential flow method applied to VSTOL aerodynamics.
S.A.E. Transportation meeting, New York (1968).

Schlicting, H.
Aerodynamic problems of motor cars.
Agard Report 307 (1960).

Sievers, J.
Study of ground effect in a wind tunnel.
ONERA TN 87 (1965).

Simmons, J. E. L.
Effect of separation angle on vortex streets.
J. Of the Eng. Mech. Div., Oct. 1975.

Simmons, J. E. L.
Similarities between two dimensional and axisymmetric vortex wakes.
Aero. Quart., Feb. 1977.

Simmons, J. E. L.
Phase angle measurements between hot wire signals in the turbulent wake of a two dimensional bluff body.
J. Fluid Mech. 64 (1974).

Snowden, D. D.
The steady separated flow past bluff objects.
Stanford University,
Ph.D. Thesis

Stafford, L. G.
A numerical method for the calculation of the flow field around a motor vehicle.
Advances in Road Vehicle Aerodynamics,
B.H.R.A. Fluid Engineering, Cranfield,
Paper 11 (1973).

Stalker, E. A.
A reflection plate representing the ground.
Jrnl. Aeronautical Sciences 1, pp. 151-152 (1934).

Sykes, D. M.
Blockage corrections for large bluff bodies in wind tunnels.
Advances in Road Vehicle Aerodynamics,
B.H.R.A. Fluid Engineering, Cranfield (1973).

Thommen, H. V. and Magnus, R. J.
Numerical calculation of separated flow fields.
AGARD Separated Flows, Fluid Dynamics Panel,
10-13th May, 1966.

White, R. G. A. and Paish, M. G.
A study of vehicle aerodynamic lift.
M.I.R.A. Report No. 1966-16 (1966).

Wright, P. G.
Aerodynamics for formula one.
Aero. Jrnl., May, 1974.

Wu, T. Y.
A wake model for free streamline theory.
J. Fluid Mech. 73, pp.161-181 (1976).

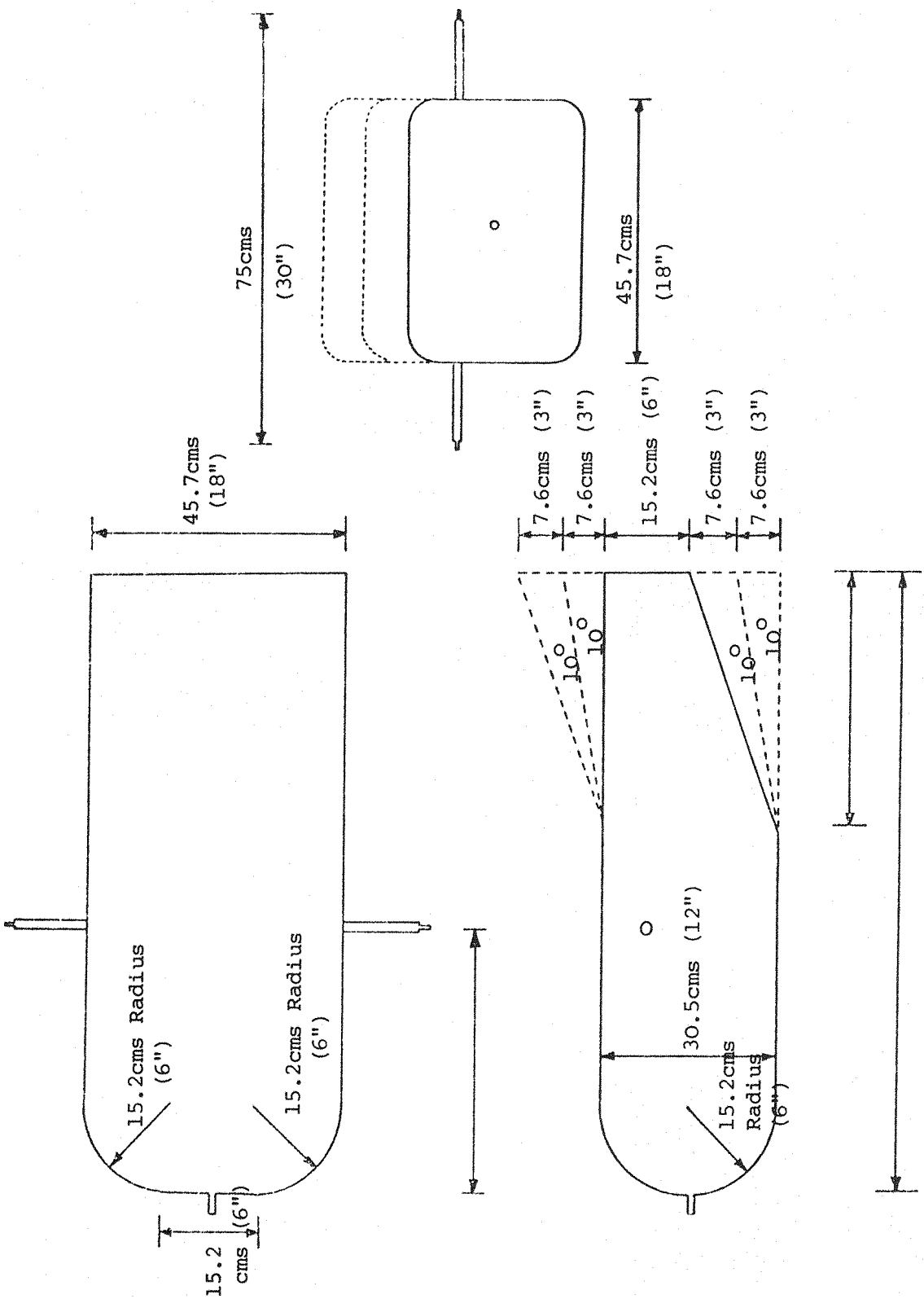

FIGURE 1 GEOMETRY OF BLUFF BODY MODEL

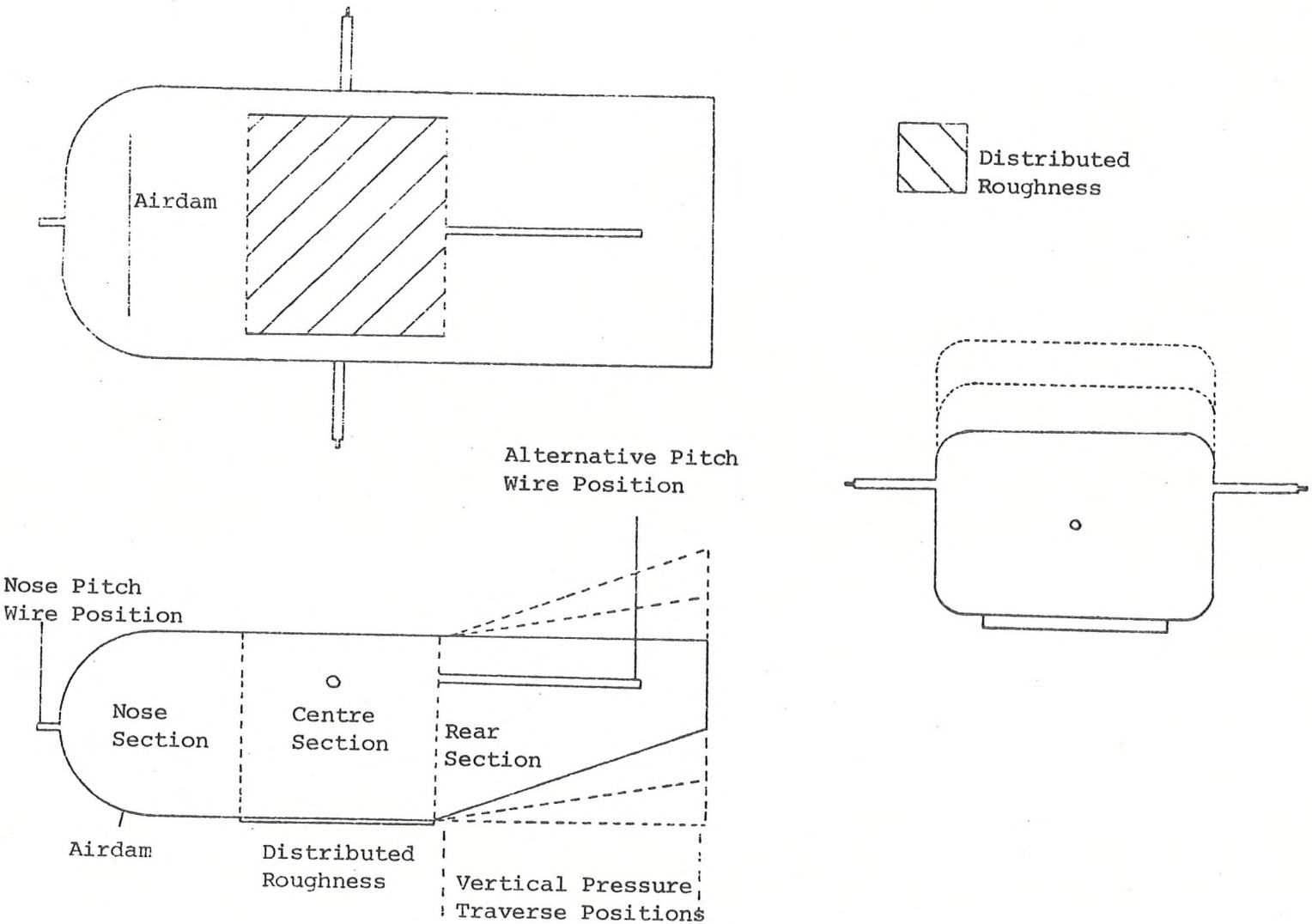

FIGURE 2 BLUFF BODY MODEL TEST CONFIGURATIONS

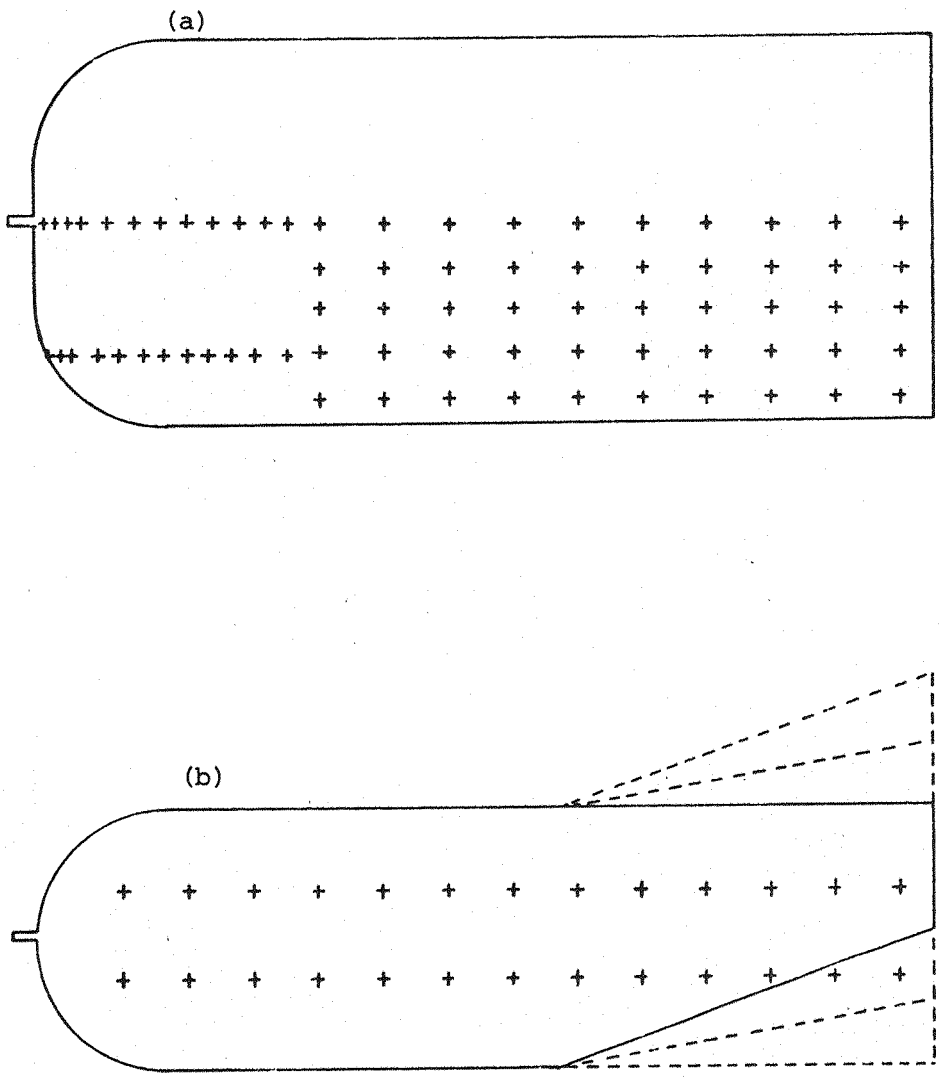

FIGURE 3 DISTRIBUTION OF BLUFF BODY FOREBODY PRESSURE TAPPINGS

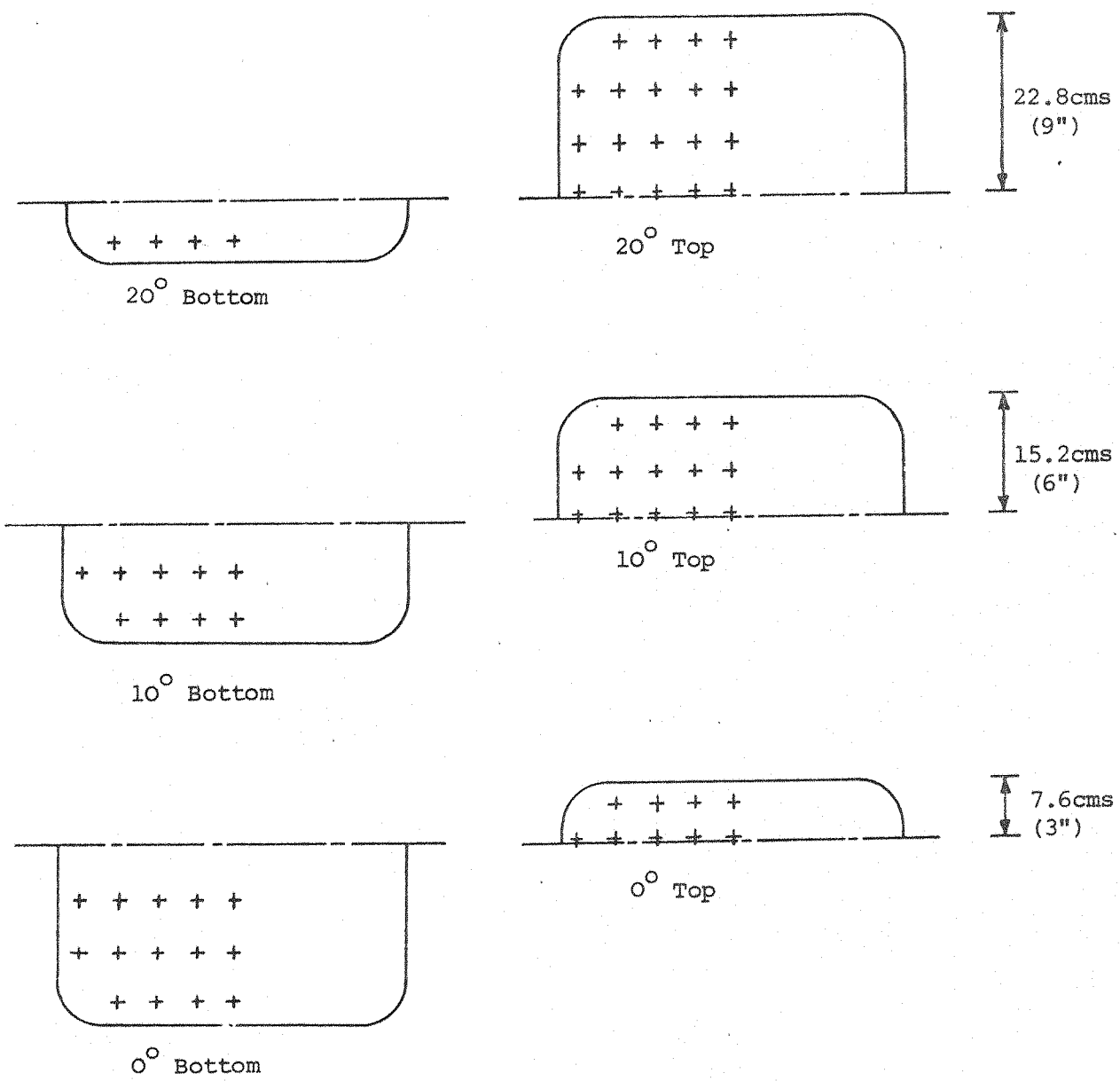

FIGURE 4 DISTRIBUTION OF BLUFF BODY BASE PRESSURE TAPPINGS

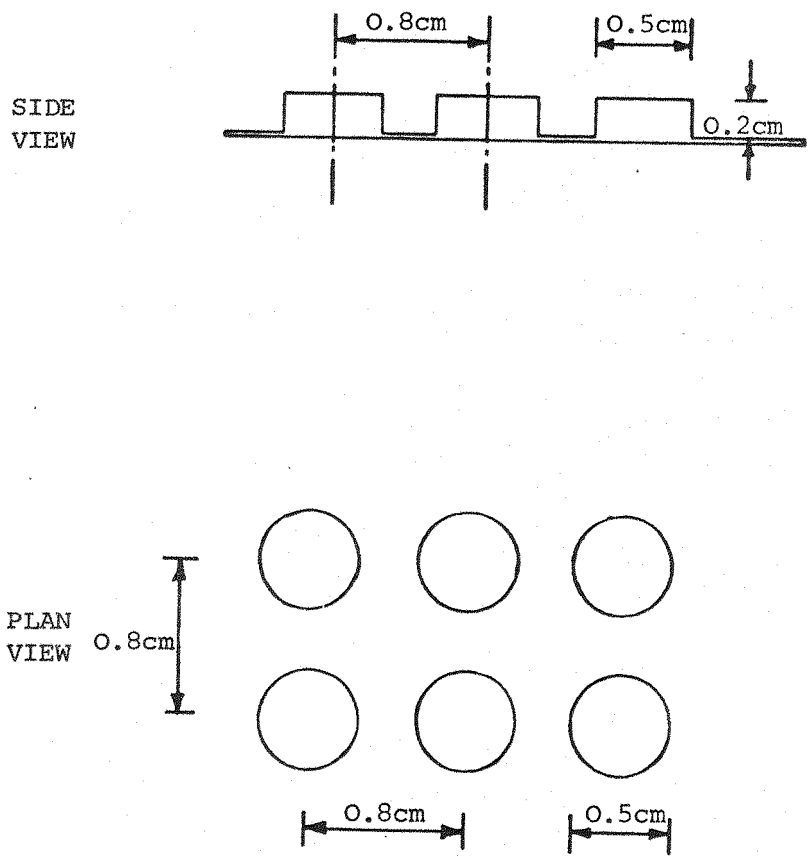

FIGURE 5 DIMENSIONS OF DISTRIBUTED ROUGHNESS

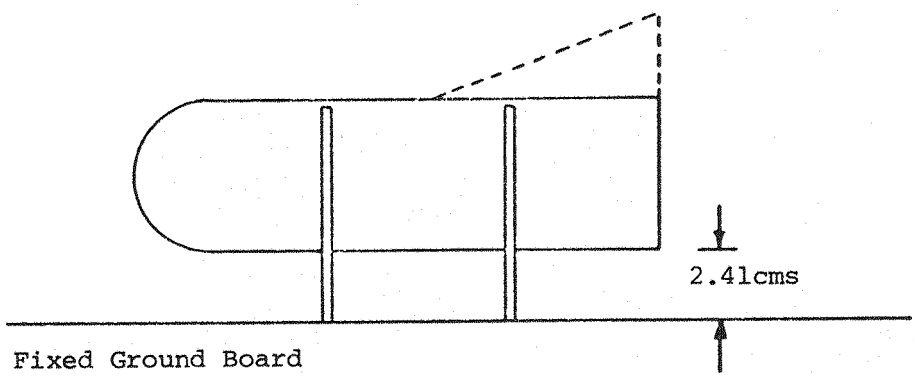

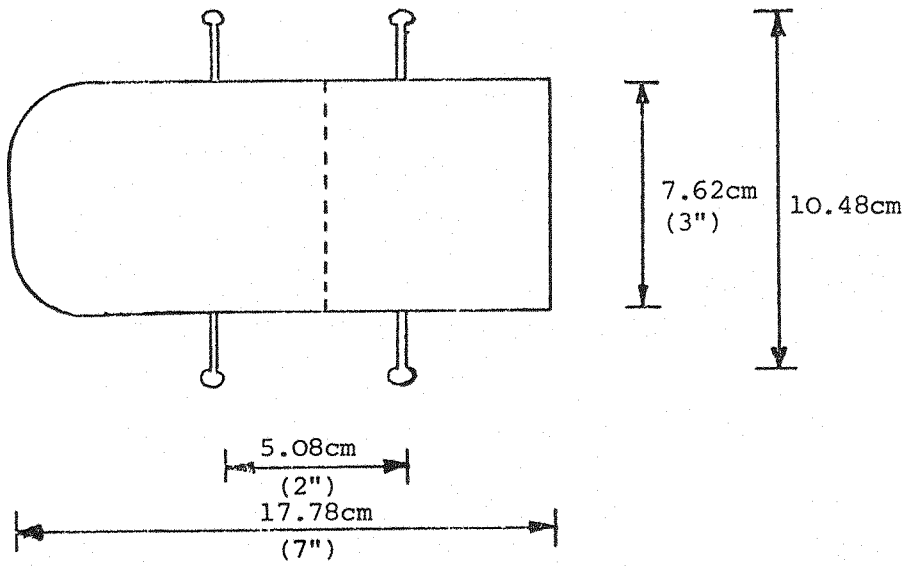

FIGURE 6 WATER TUNNEL MODEL

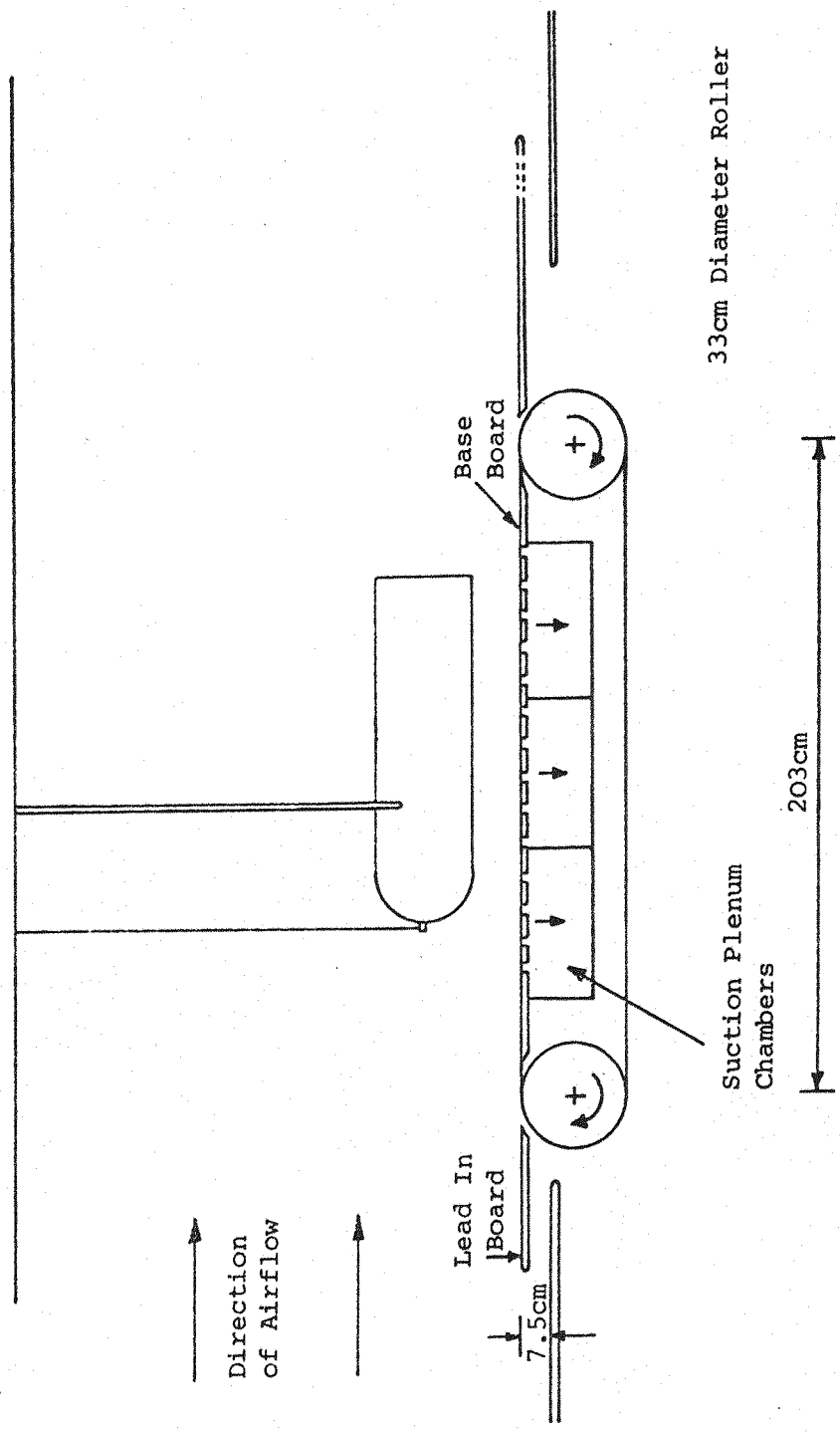

FIGURE 7 MOVING GROUND BELT FACILITY

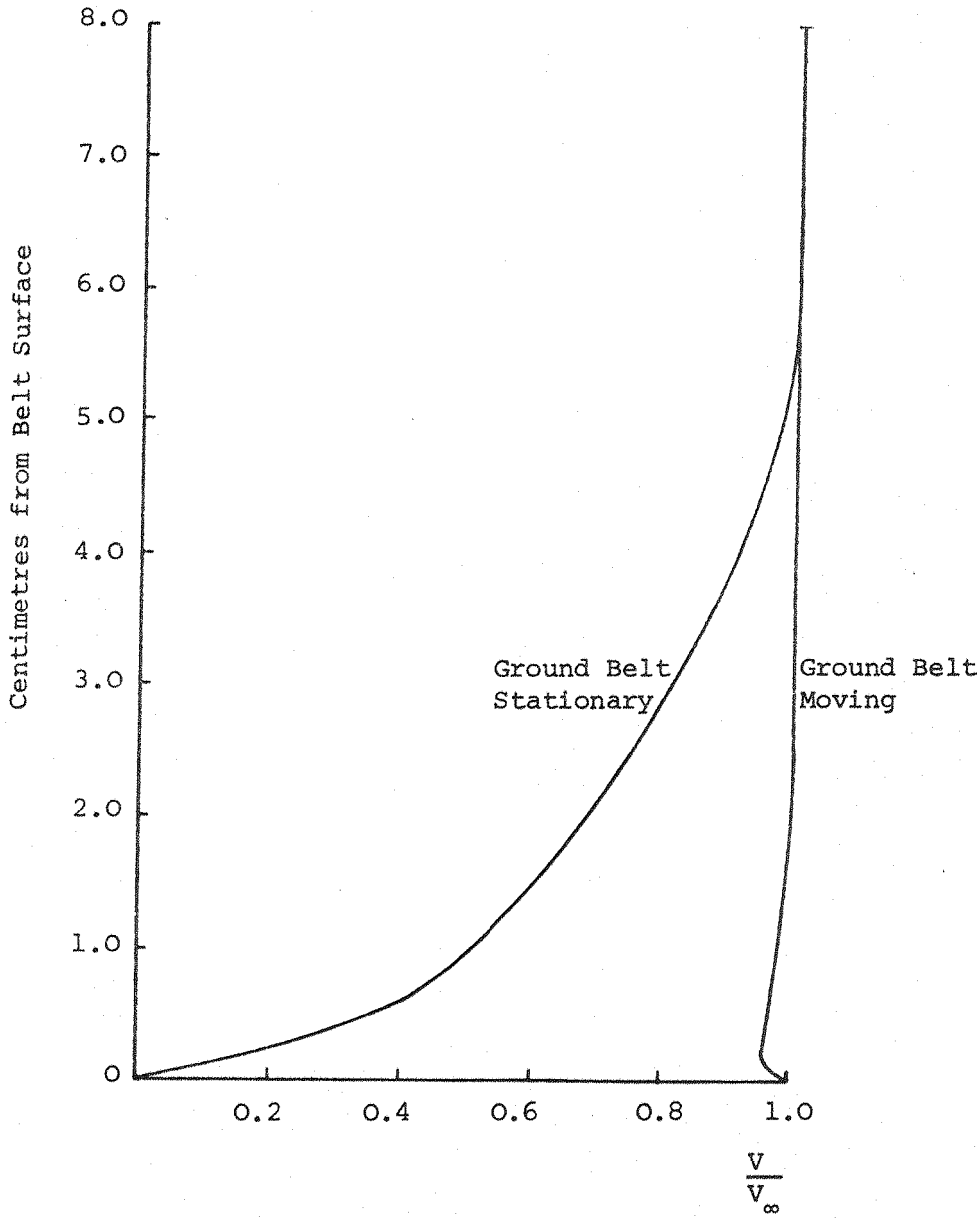

FIGURE 8 VERTICAL VELOCITY PROFILES ABOVE GROUND BELT SURFACE BELT MOVING AND STATIONARY

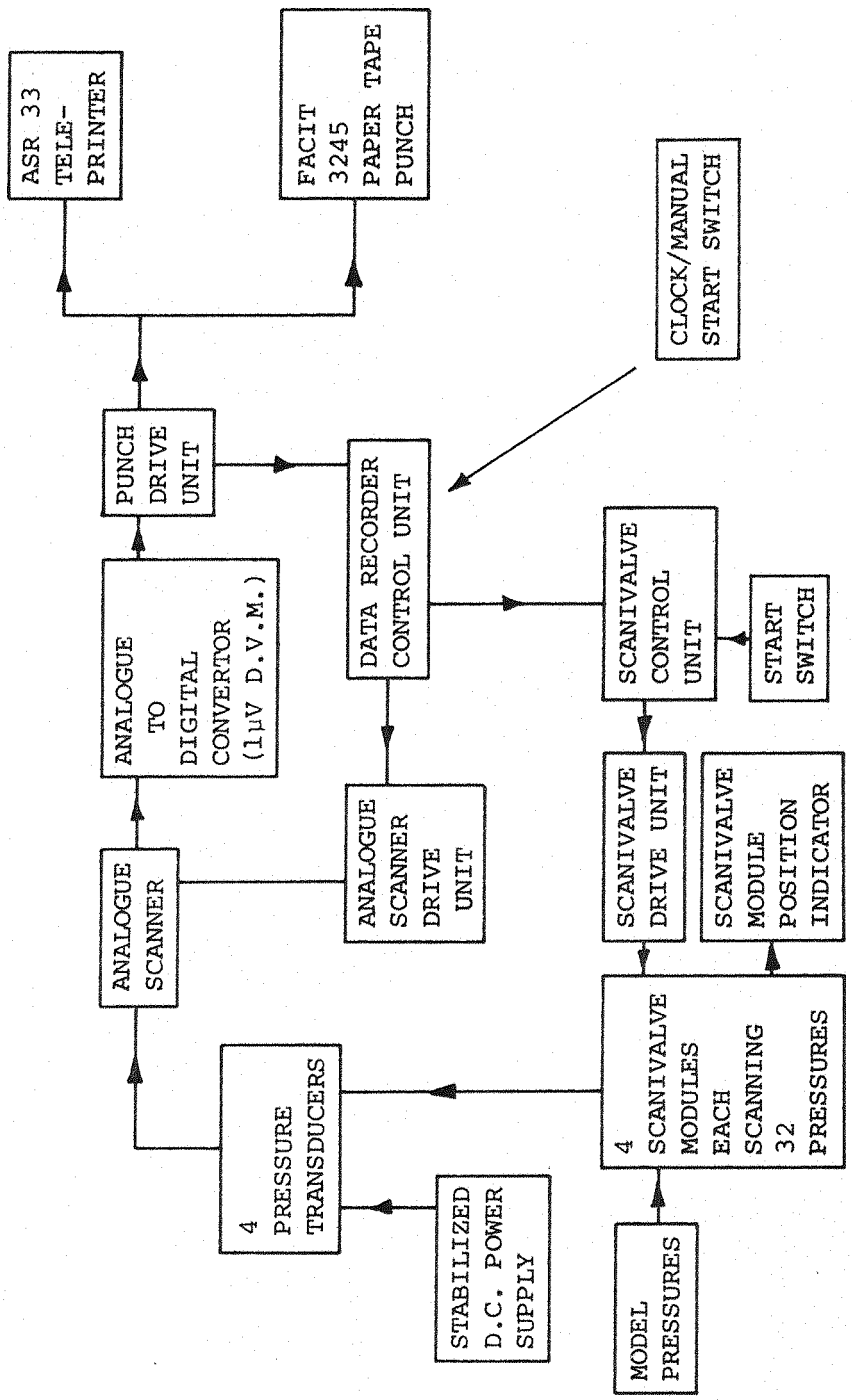

FIGURE 9 BLOCK DIAGRAM OF SCANIVALVE PRESSURE RECORDING SYSTEM

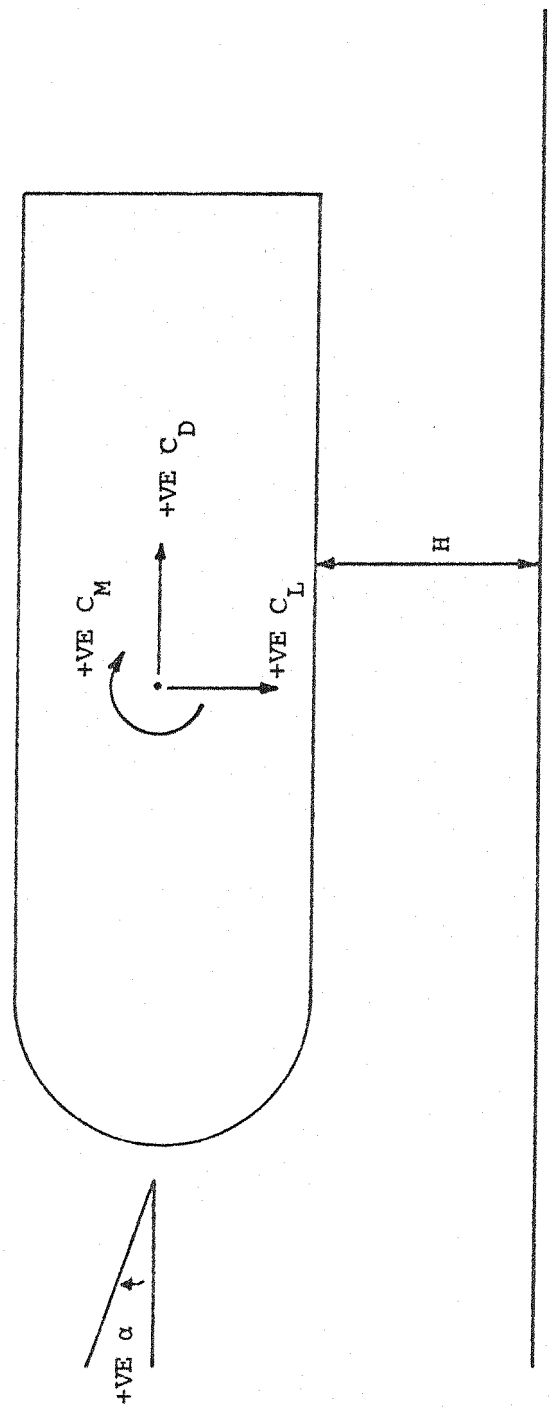

FIGURE 10 SIGN CONVENTION

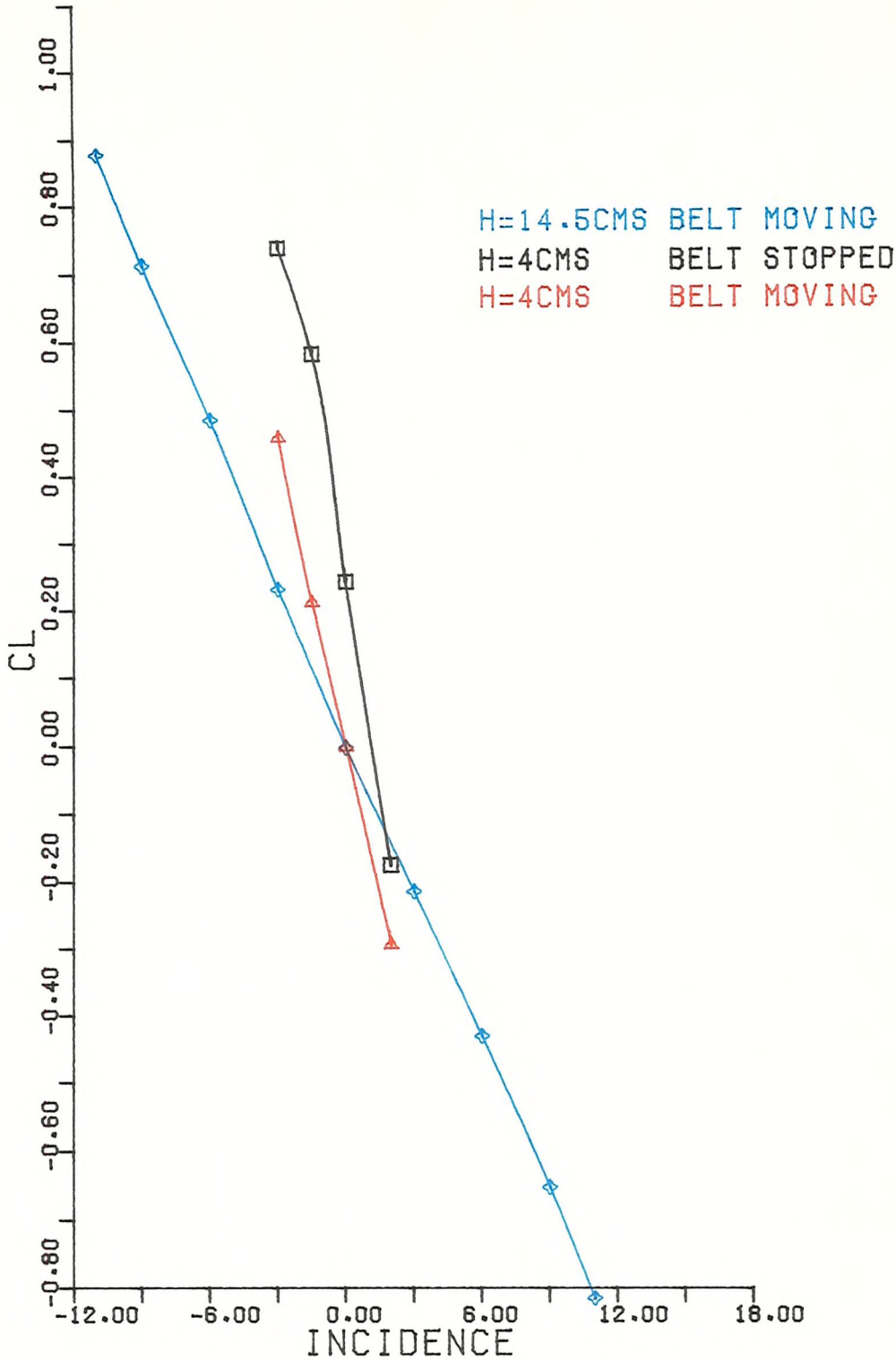

DOWNFORCE

0 TOP 0 BOTTOM

FIGURE 11

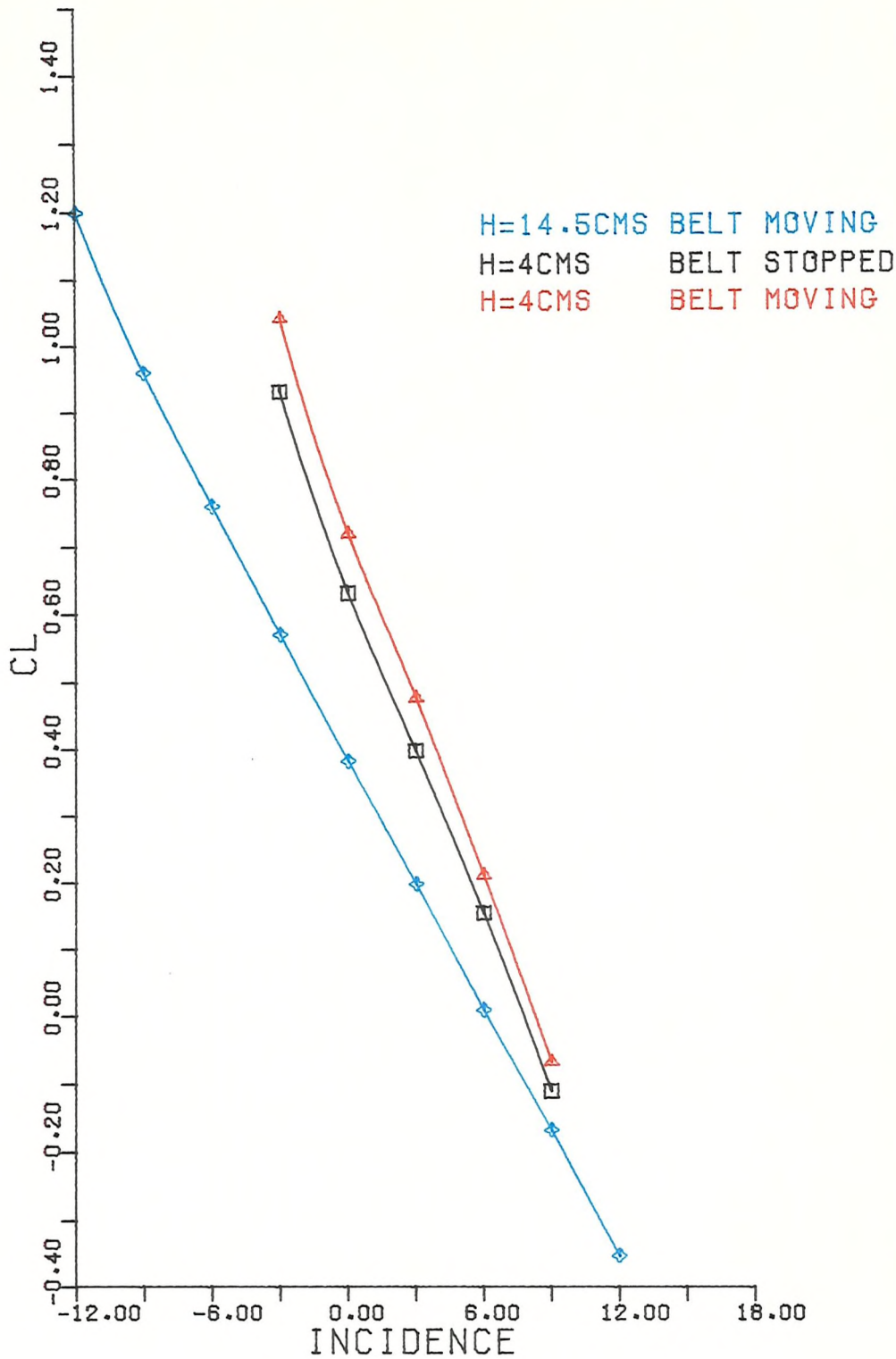

DOWNFORCE

0 TOP 10 BOTTOM

FIGURE 12

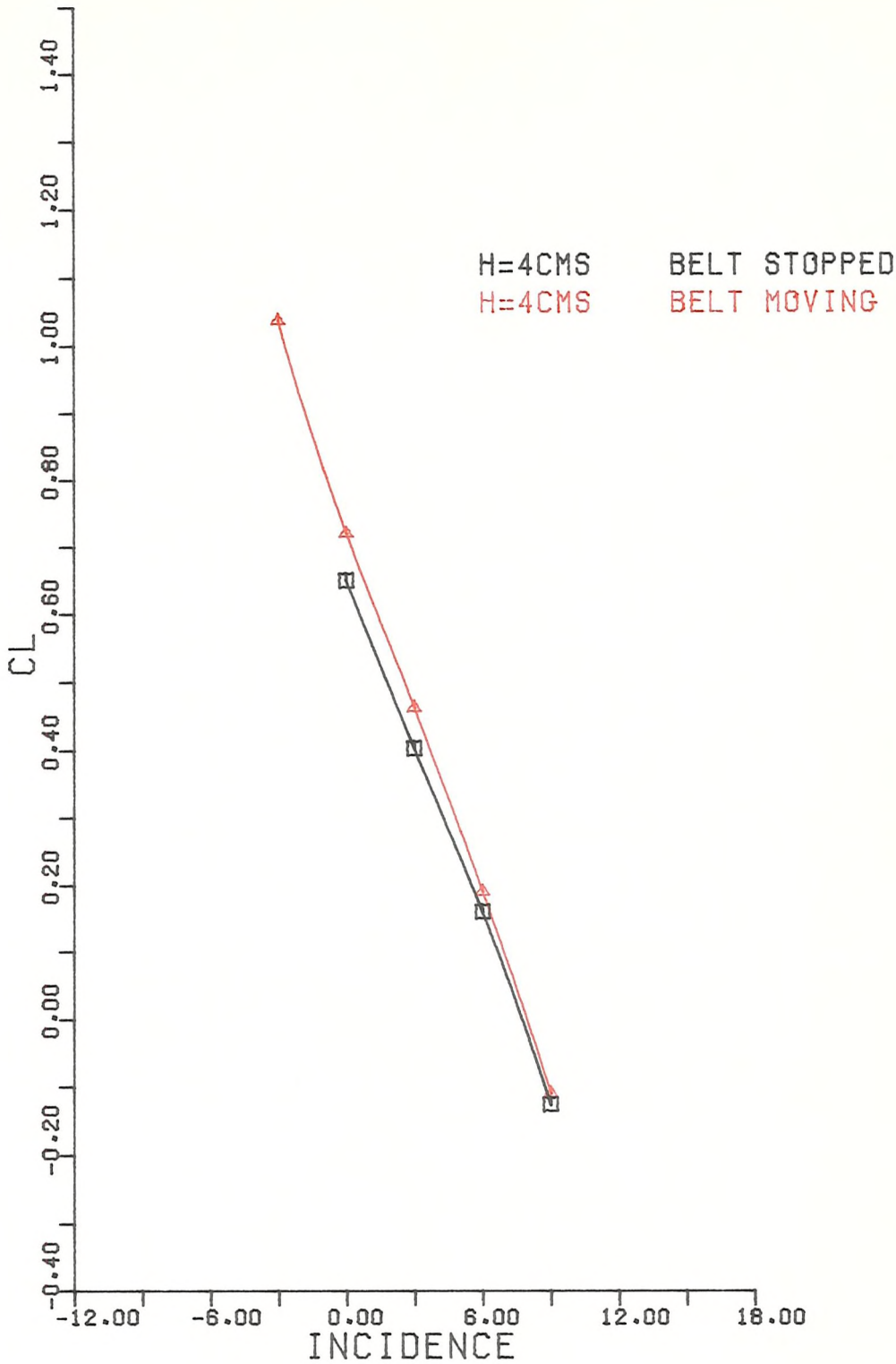

DOWNFORCE

0 TOP 10 BOTTOM

WITH DISTRIBUTED ROUGHNESS

FIGURE 13

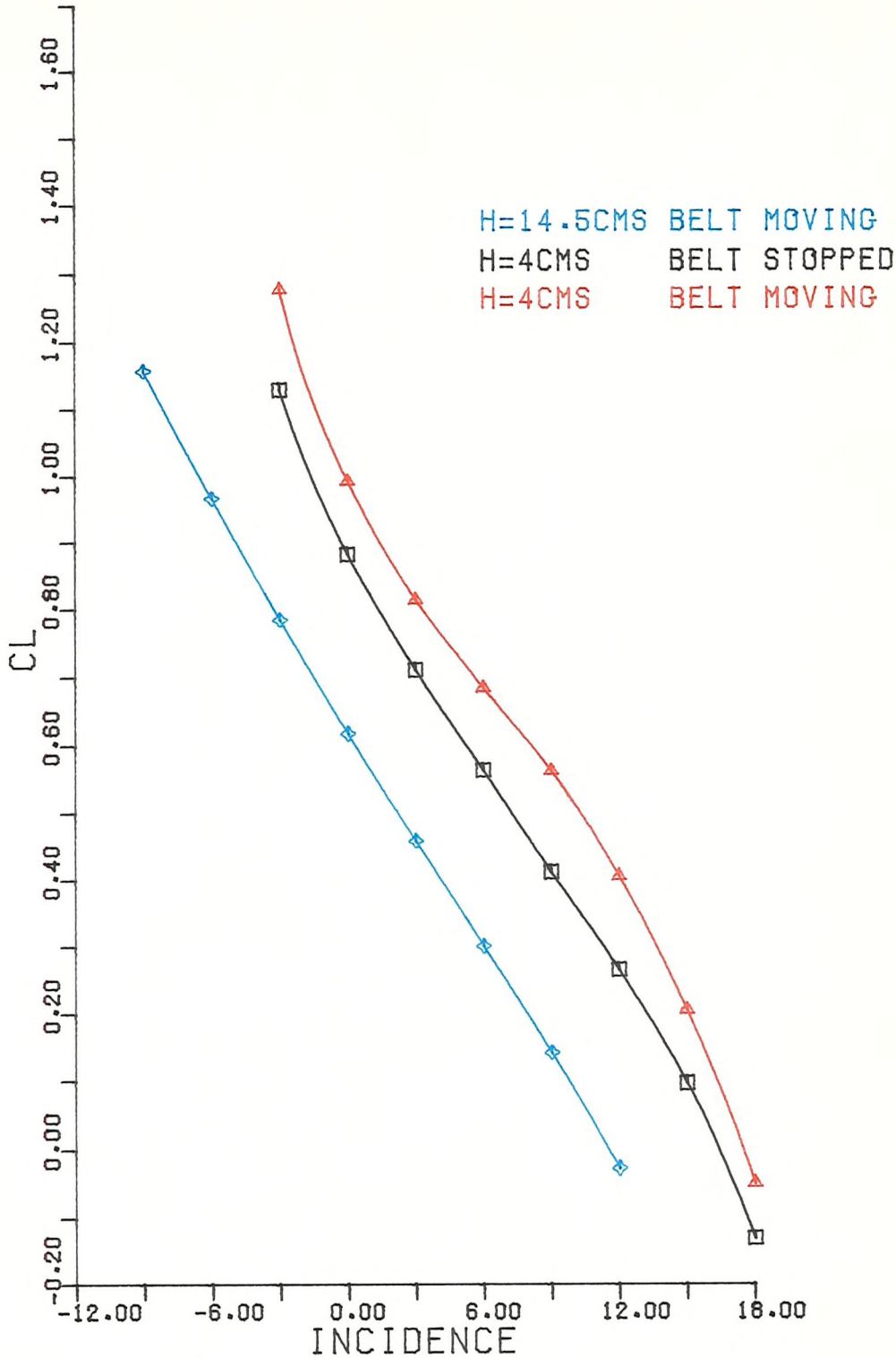

DOWNFORCE

0 TOP 20 BOTTOM

FIGURE 14

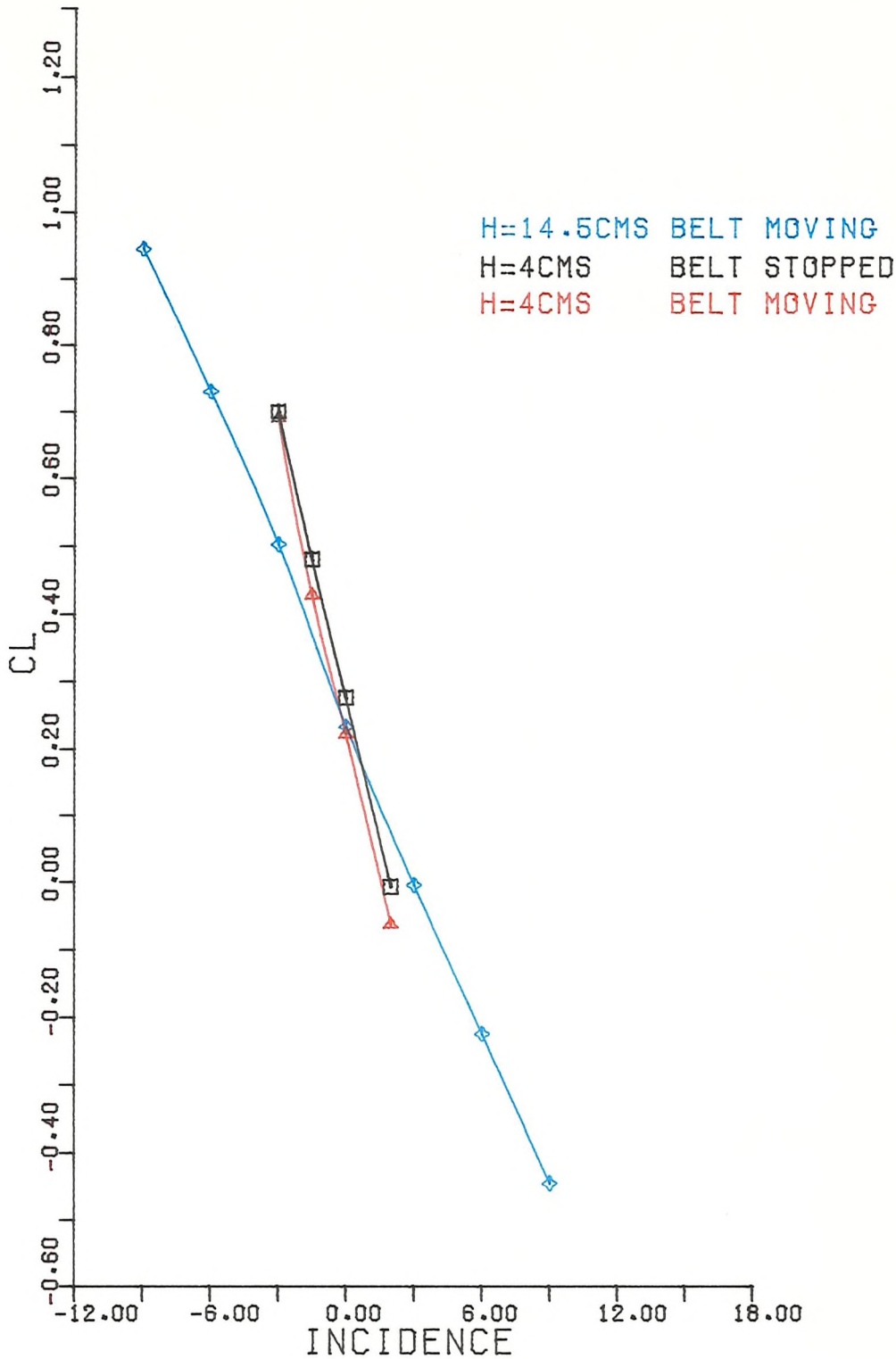

DOWNFORCE

10 TOP 0 BOTTOM

FIGURE 15

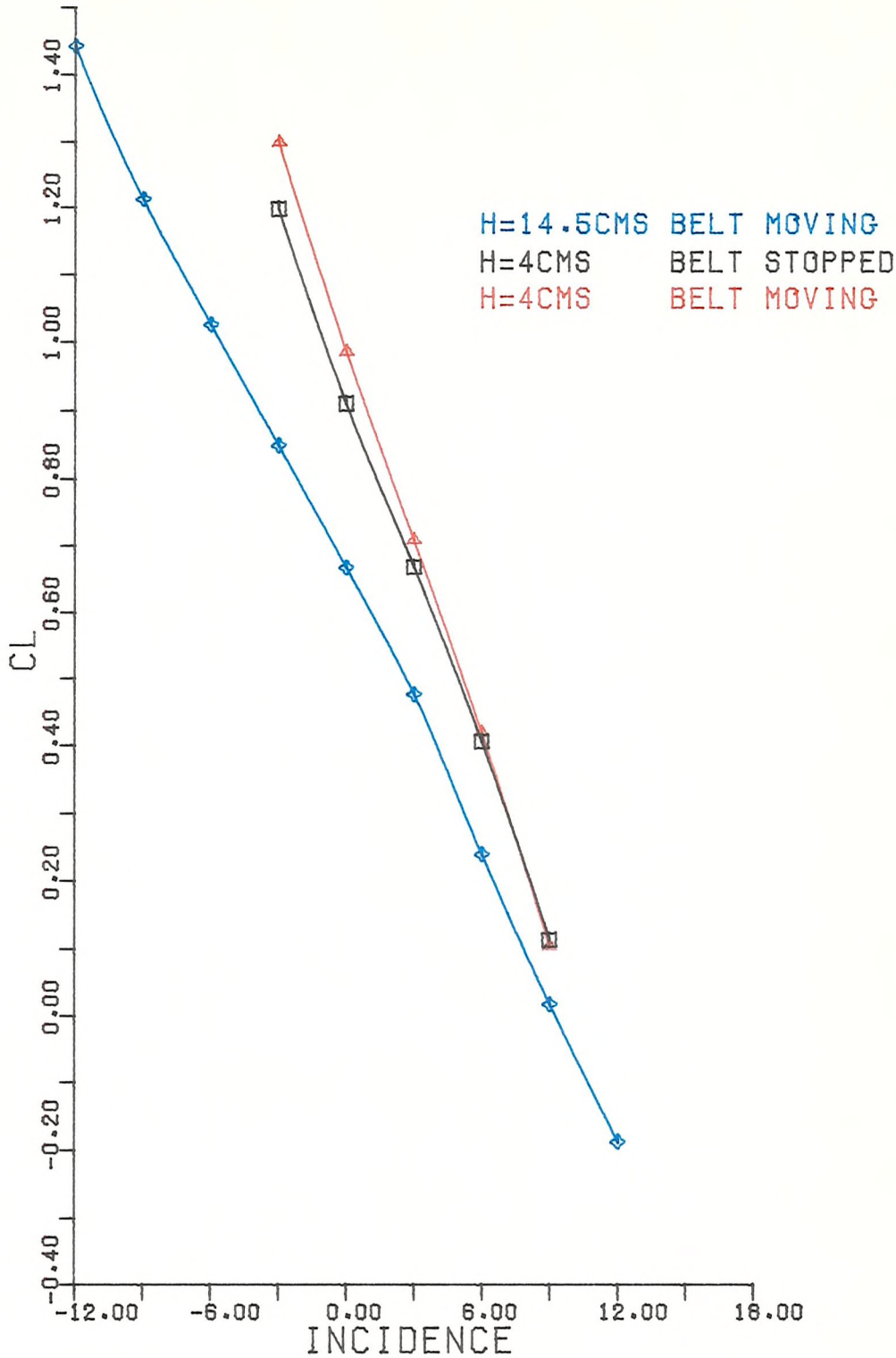

DOWNFORCE

10 TOP 10 BOTTOM

FIGURE 16

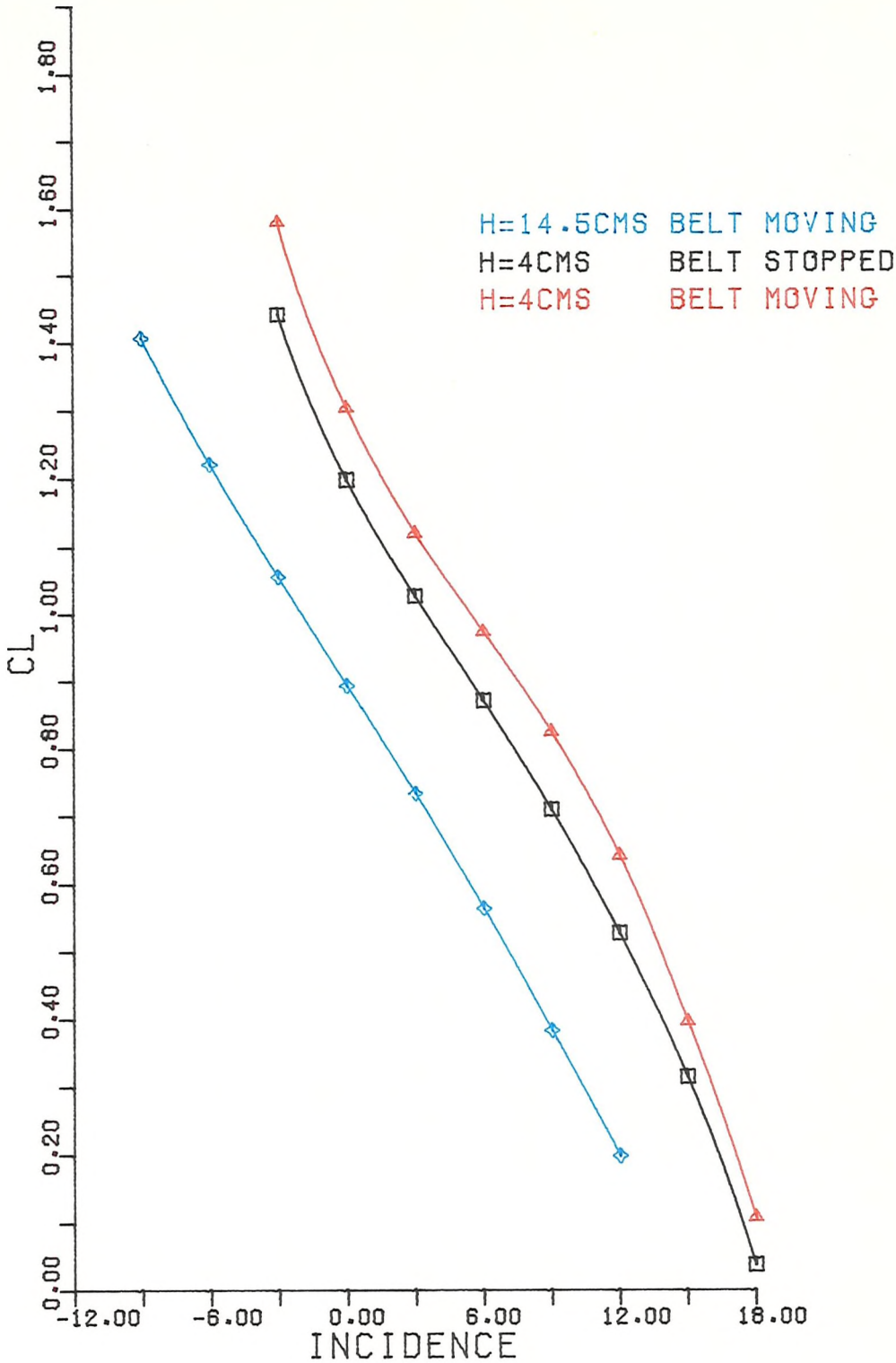

DOWNFORCE

10 TOP 20 BOTTOM

FIGURE 17

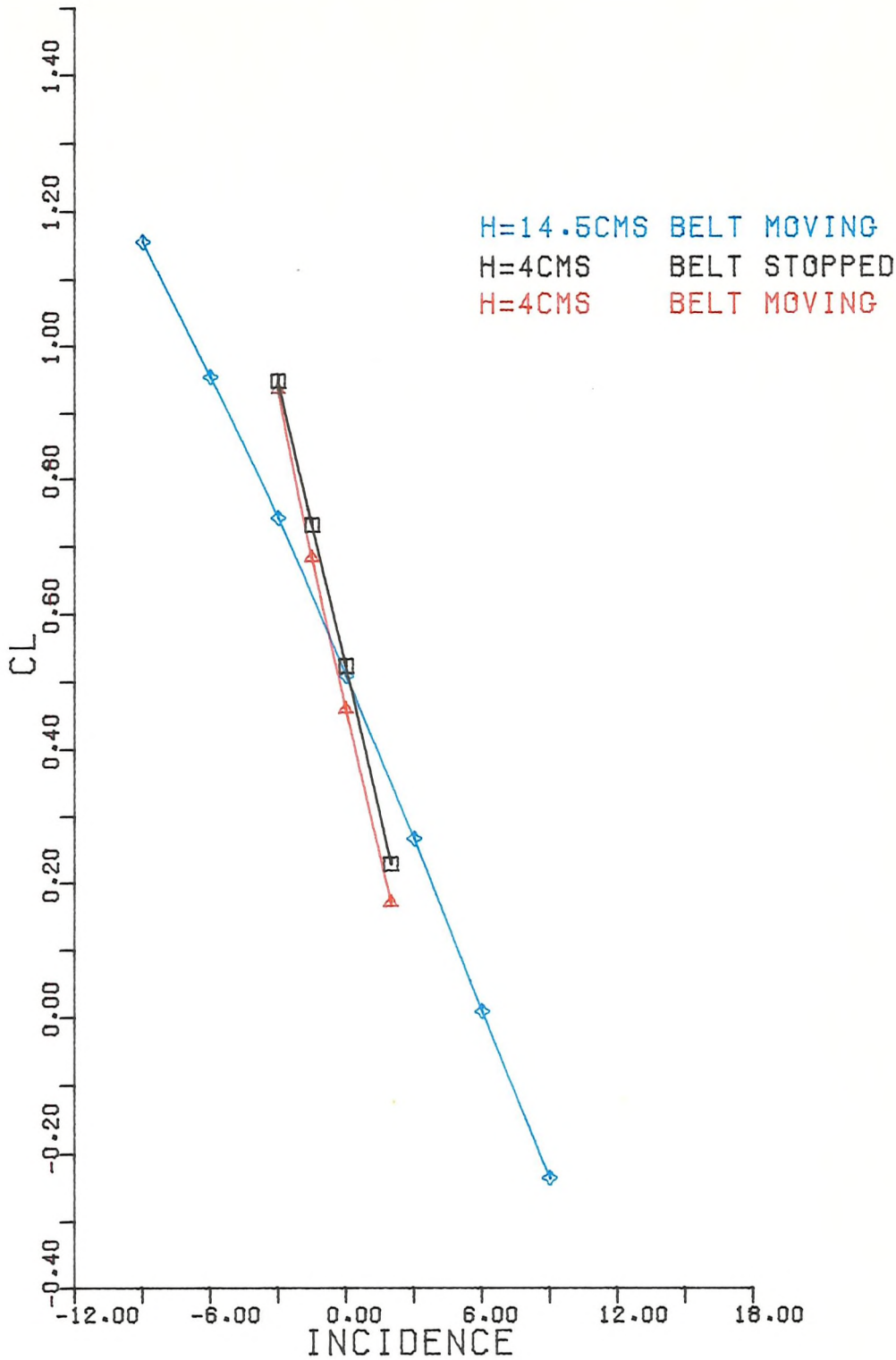

DOWNFORCE

20 TOP 0 BOTTOM

FIGURE 18

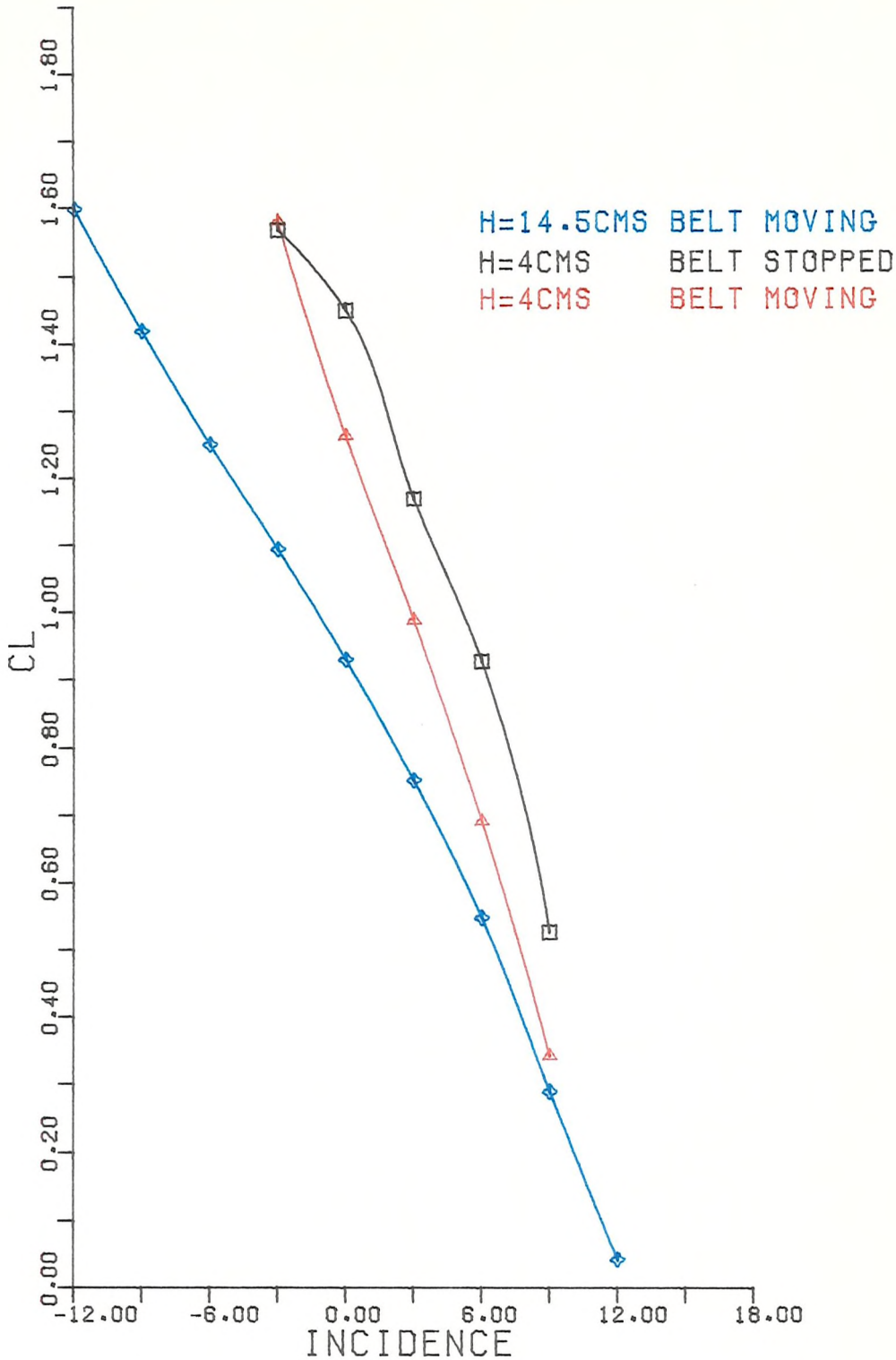

DOWNFORCE

20 TOP 10 BOTTOM

FIGURE 19

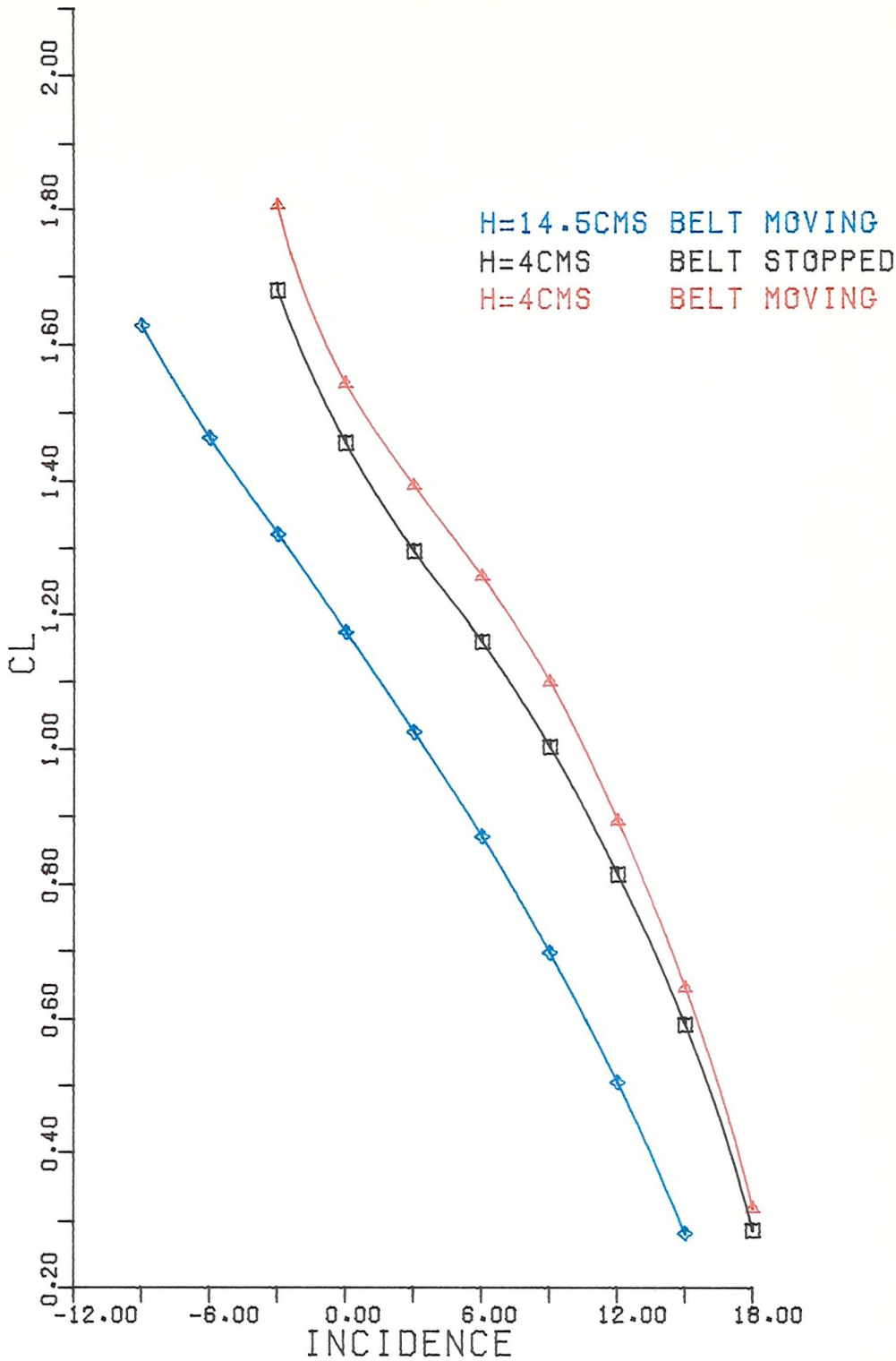

DOWNFORCE

20 TOP 20 BOTTOM

FIGURE 20

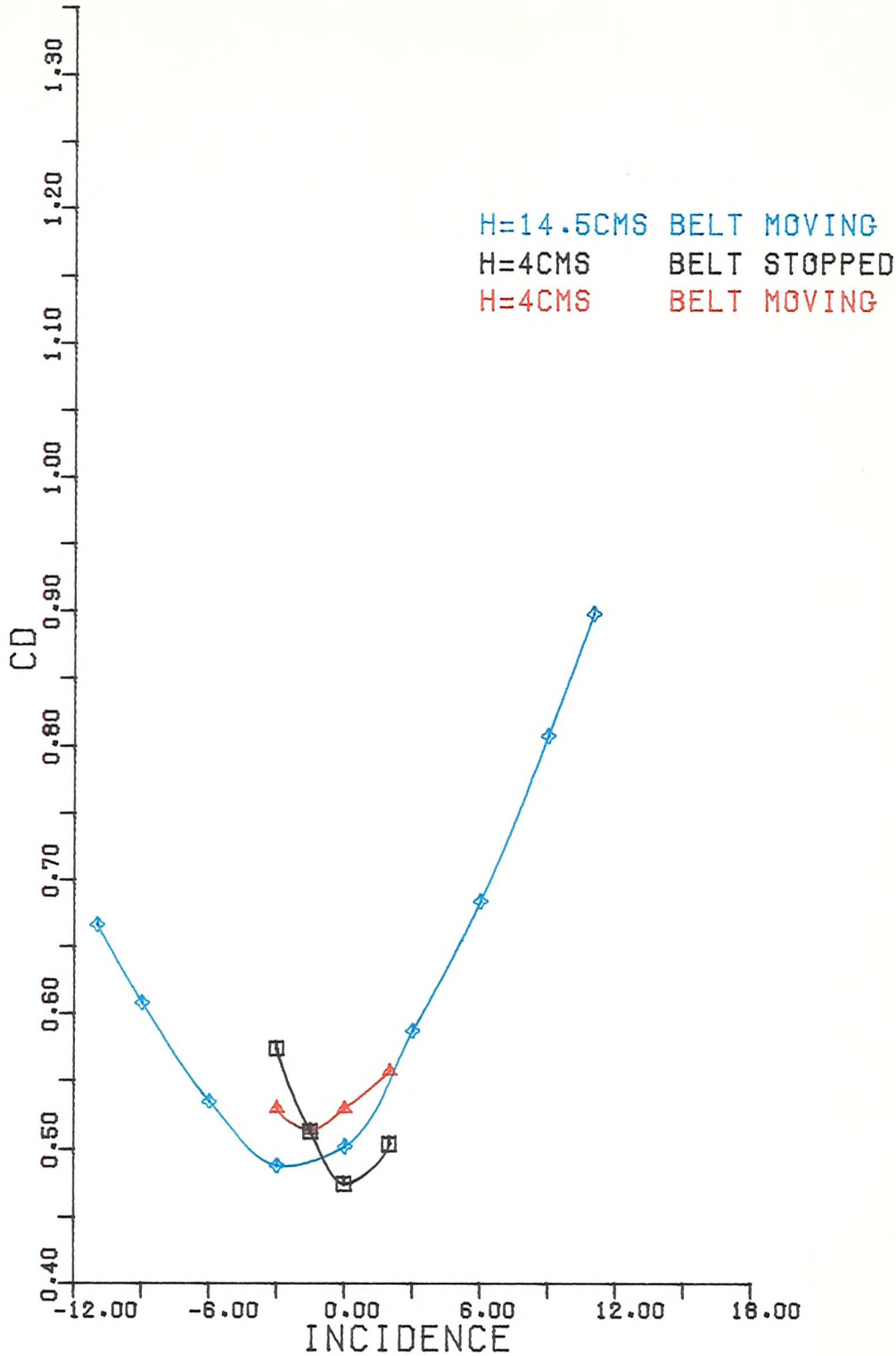

DRAG

0 TOP 0 BOTTOM

FIGURE 21

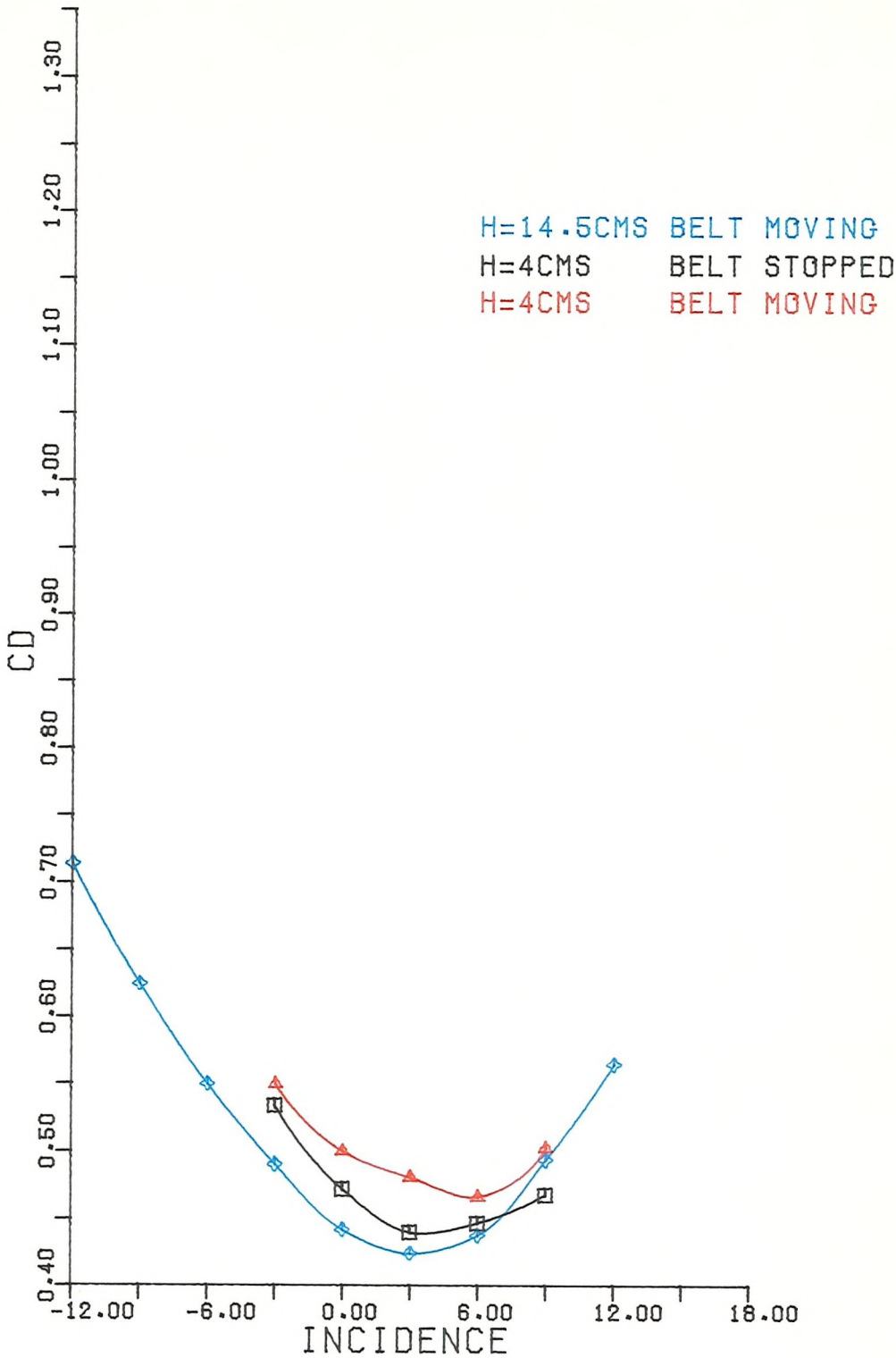

DRAG

0 TOP 10 BOTTOM

FIGURE 22

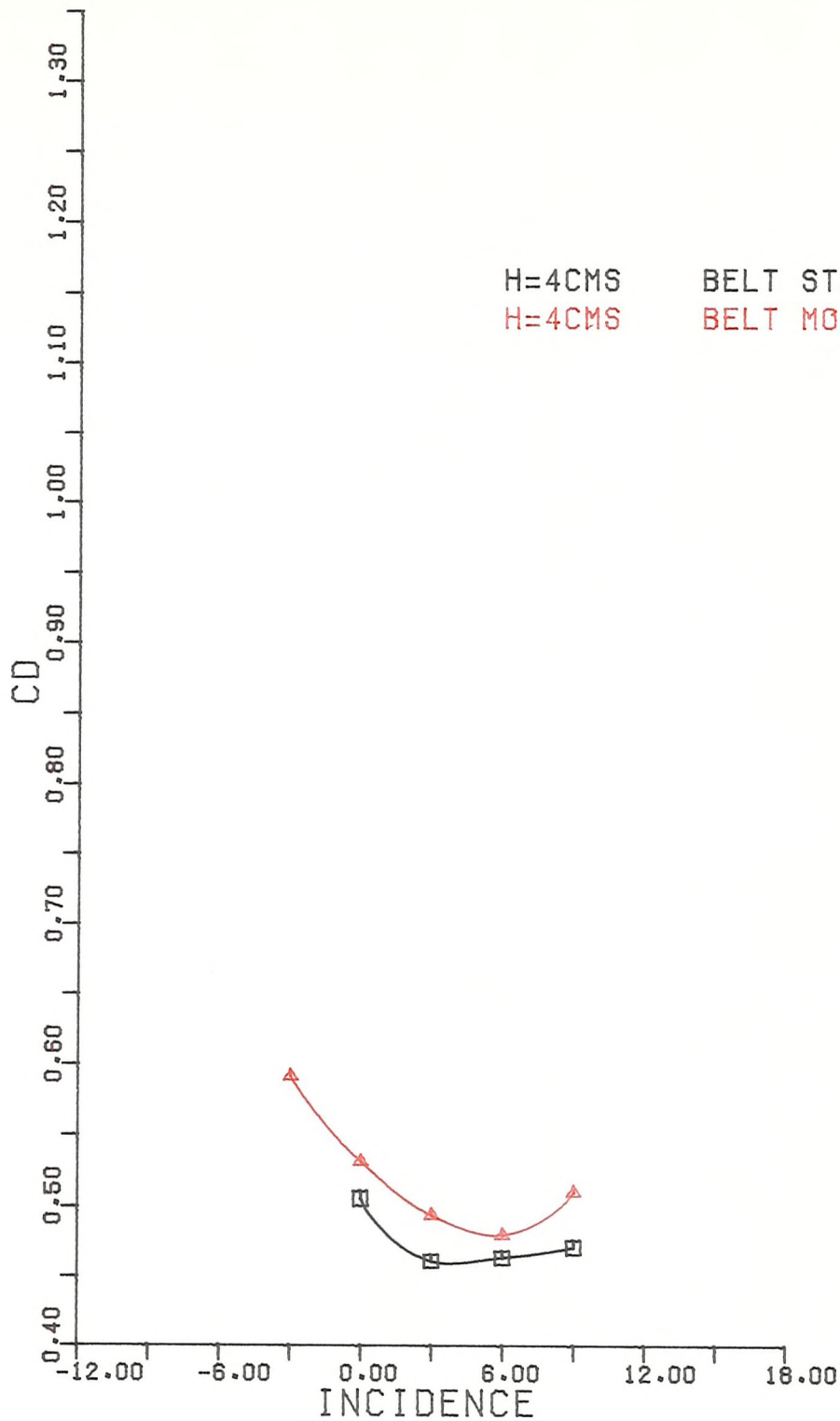

DRAG

0 TOP 10 BOTTOM

WITH DISTRIBUTED ROUGHNESS

FIGURE 23

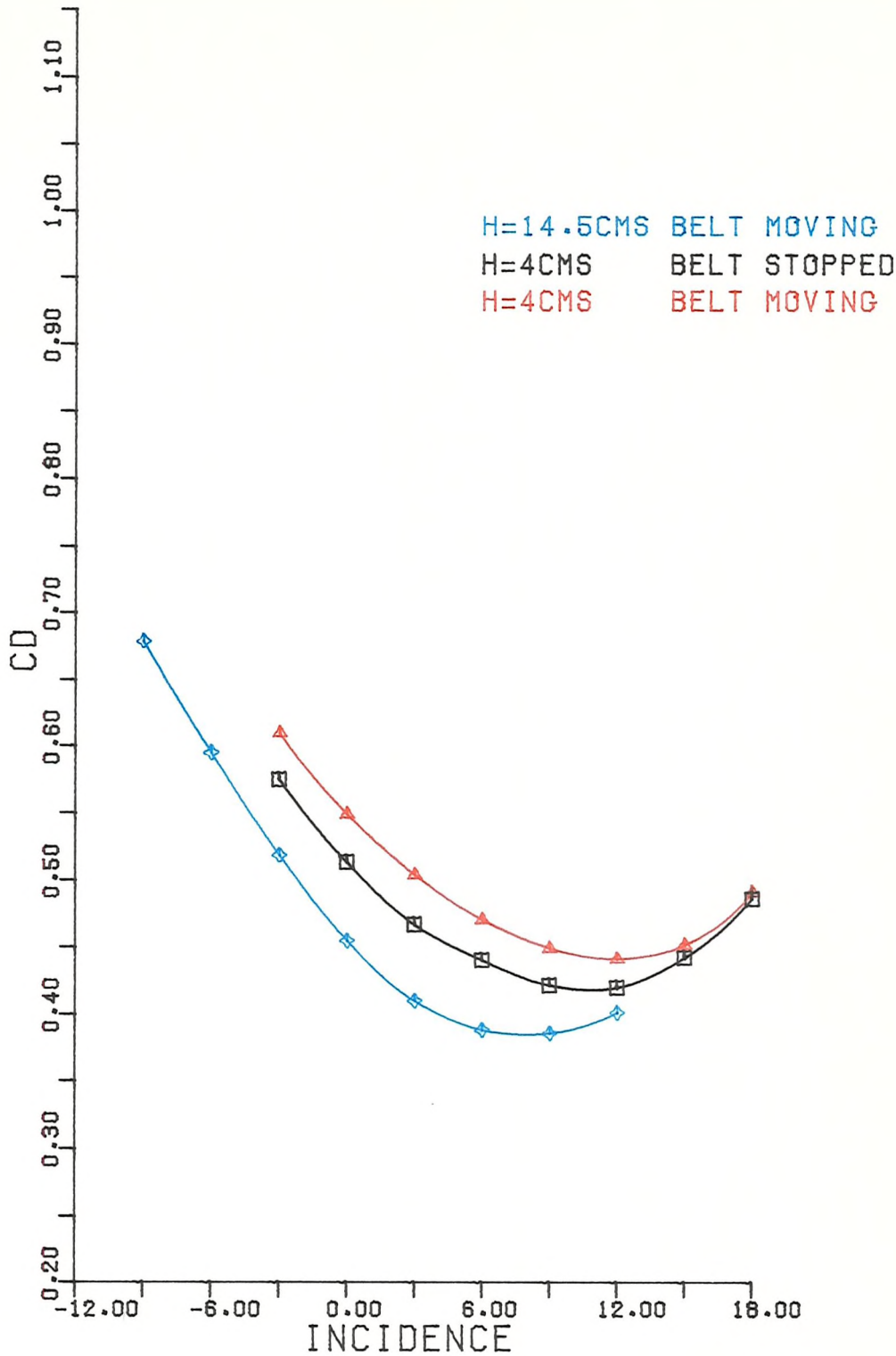

DRAG

0 TOP 20 BOTTOM

FIGURE 24

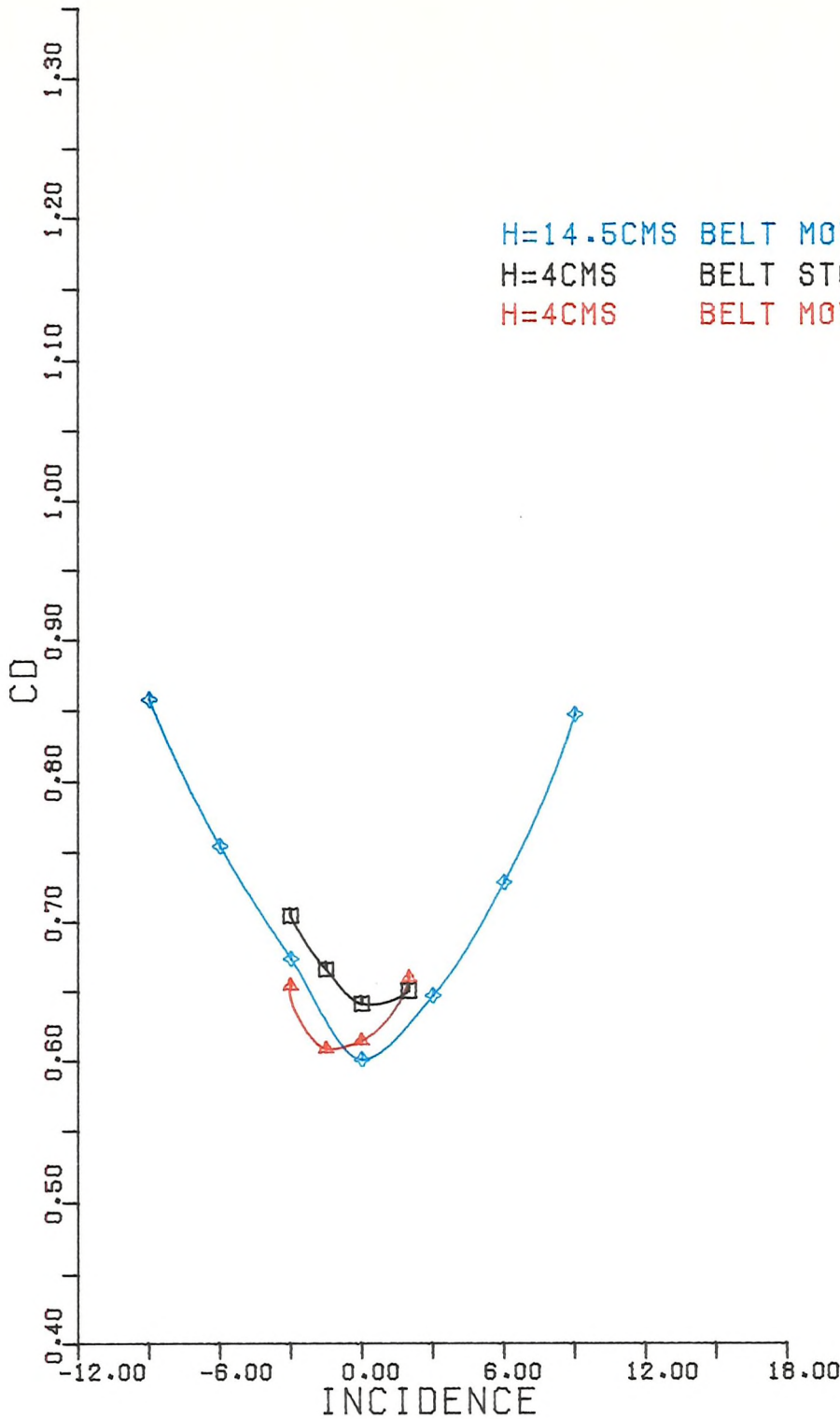

DRAG

10 TOP 0 BOTTOM

FIGURE 25

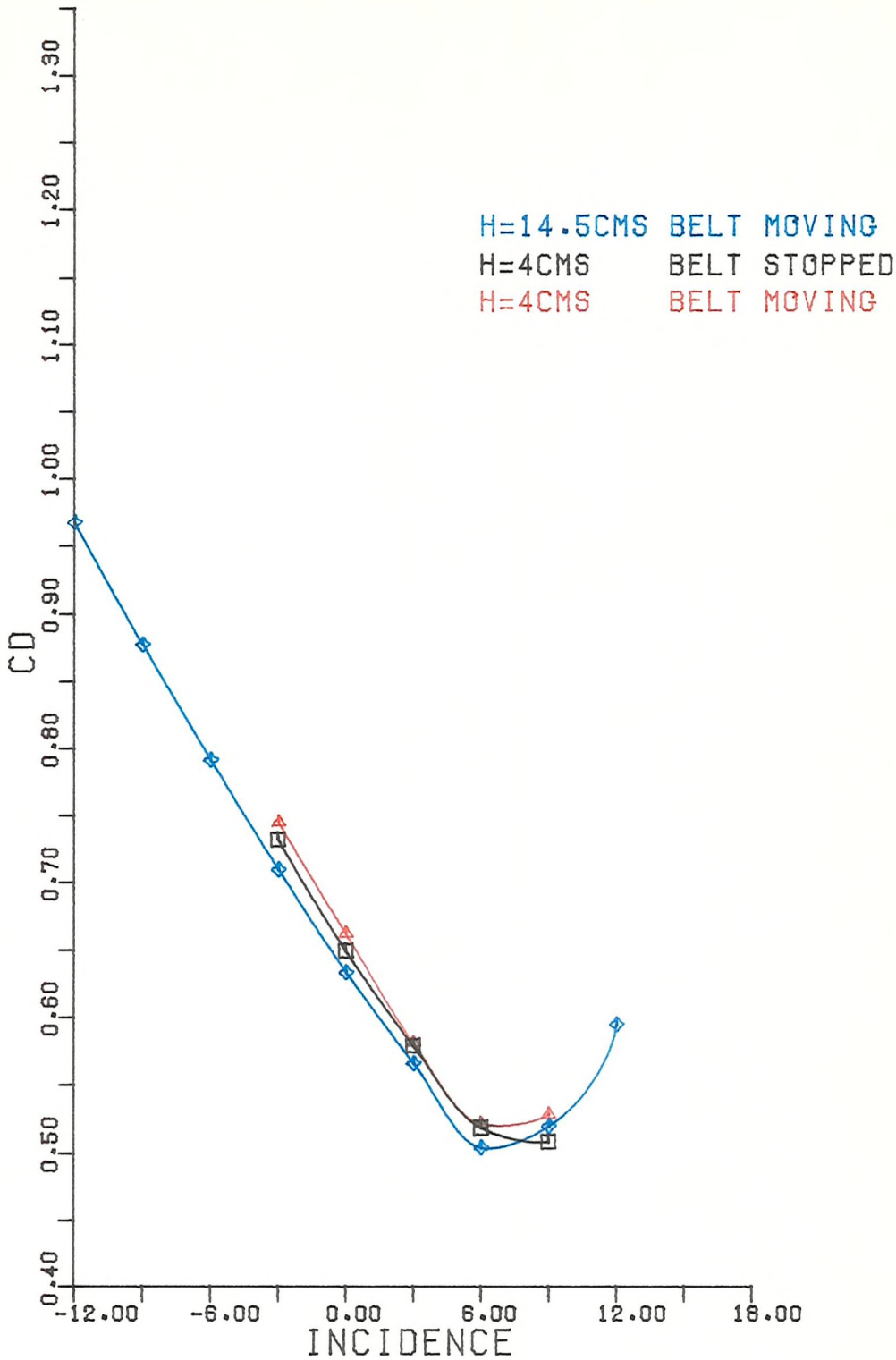

DRAG

10 TOP 10 BOTTOM

FIGURE 26

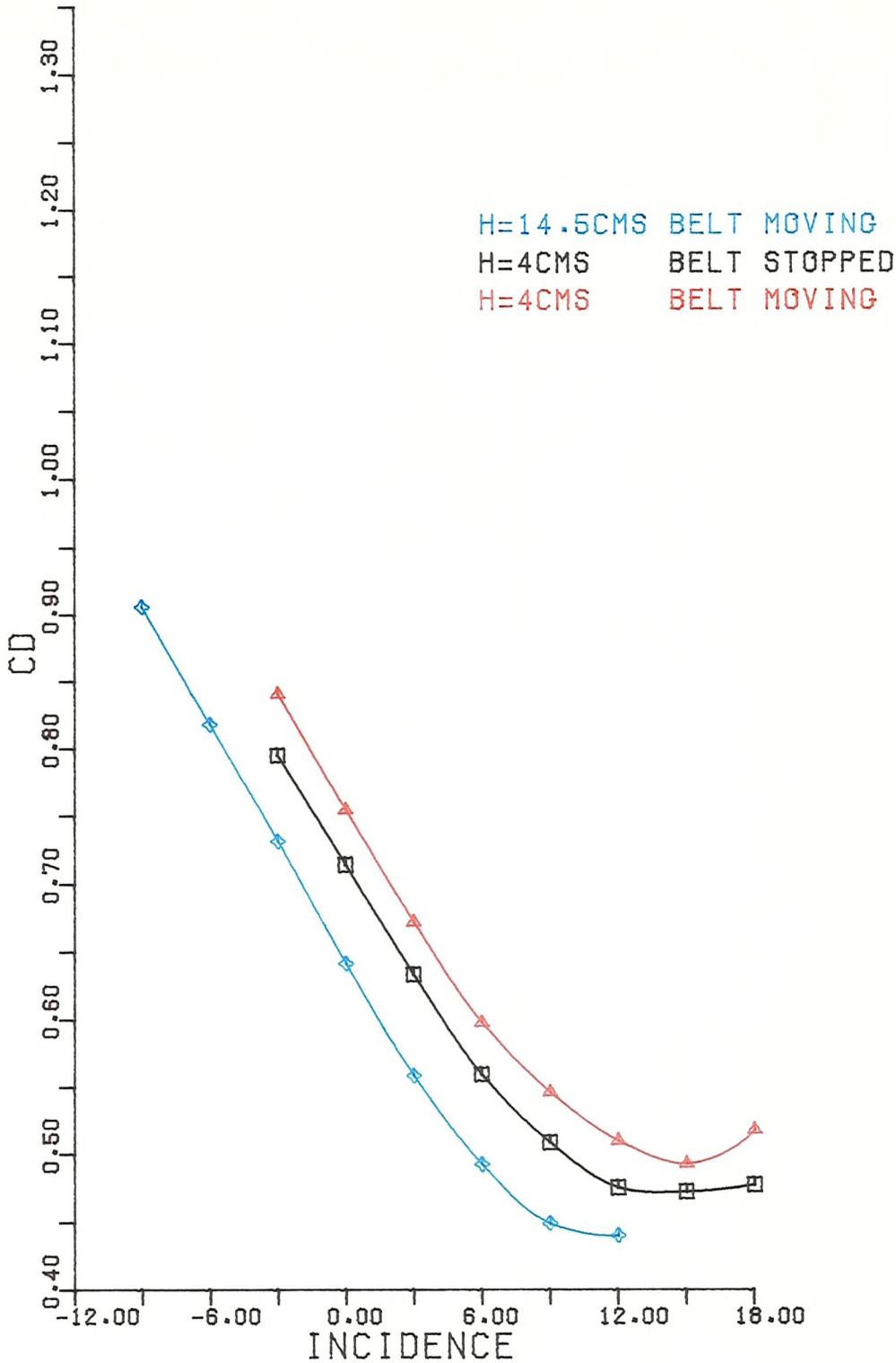

DRAG

10 TOP 20 BOTTOM

FIGURE 27

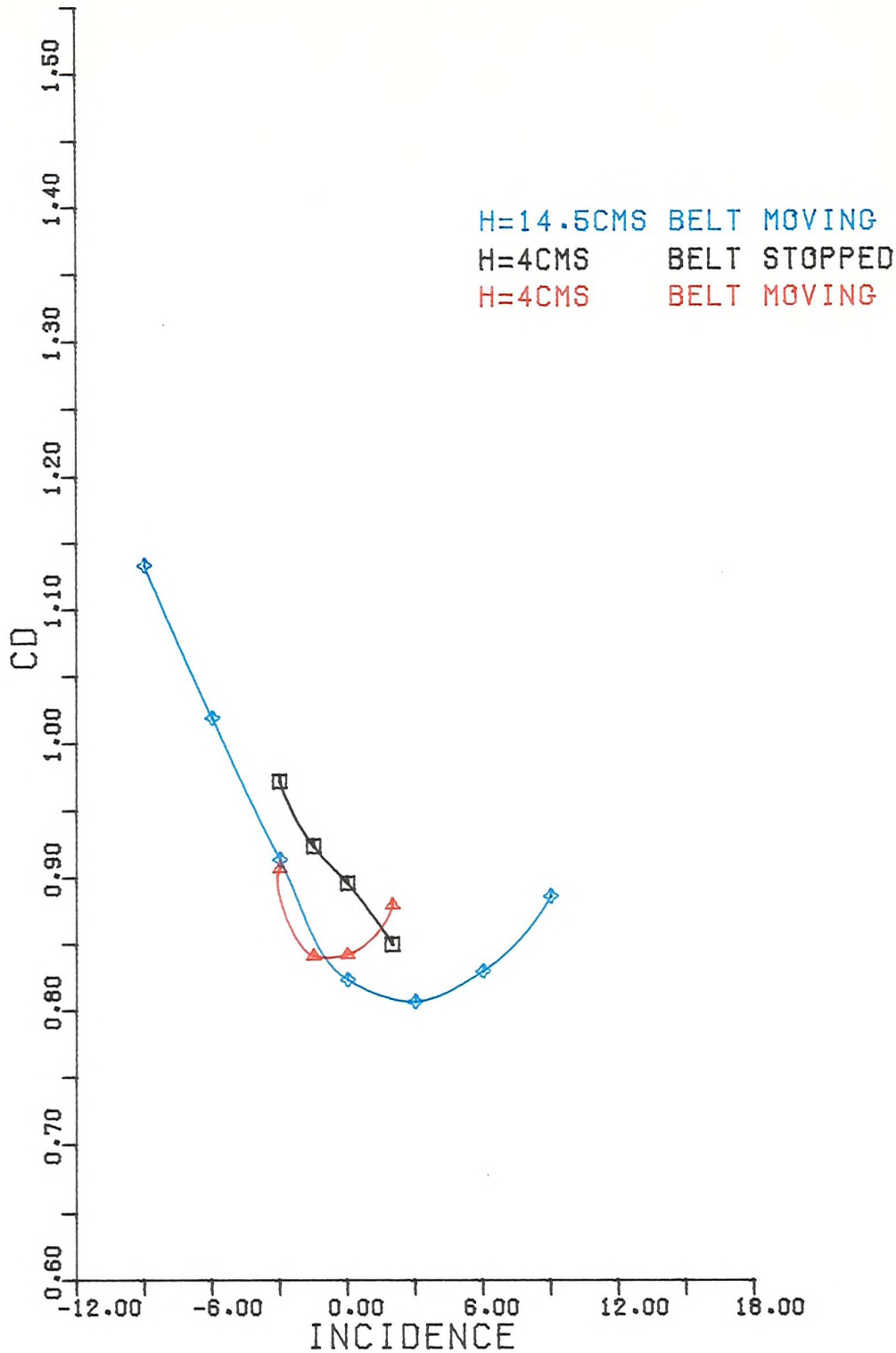

DRAG

20 TOP 0 BOTTOM

FIGURE 28

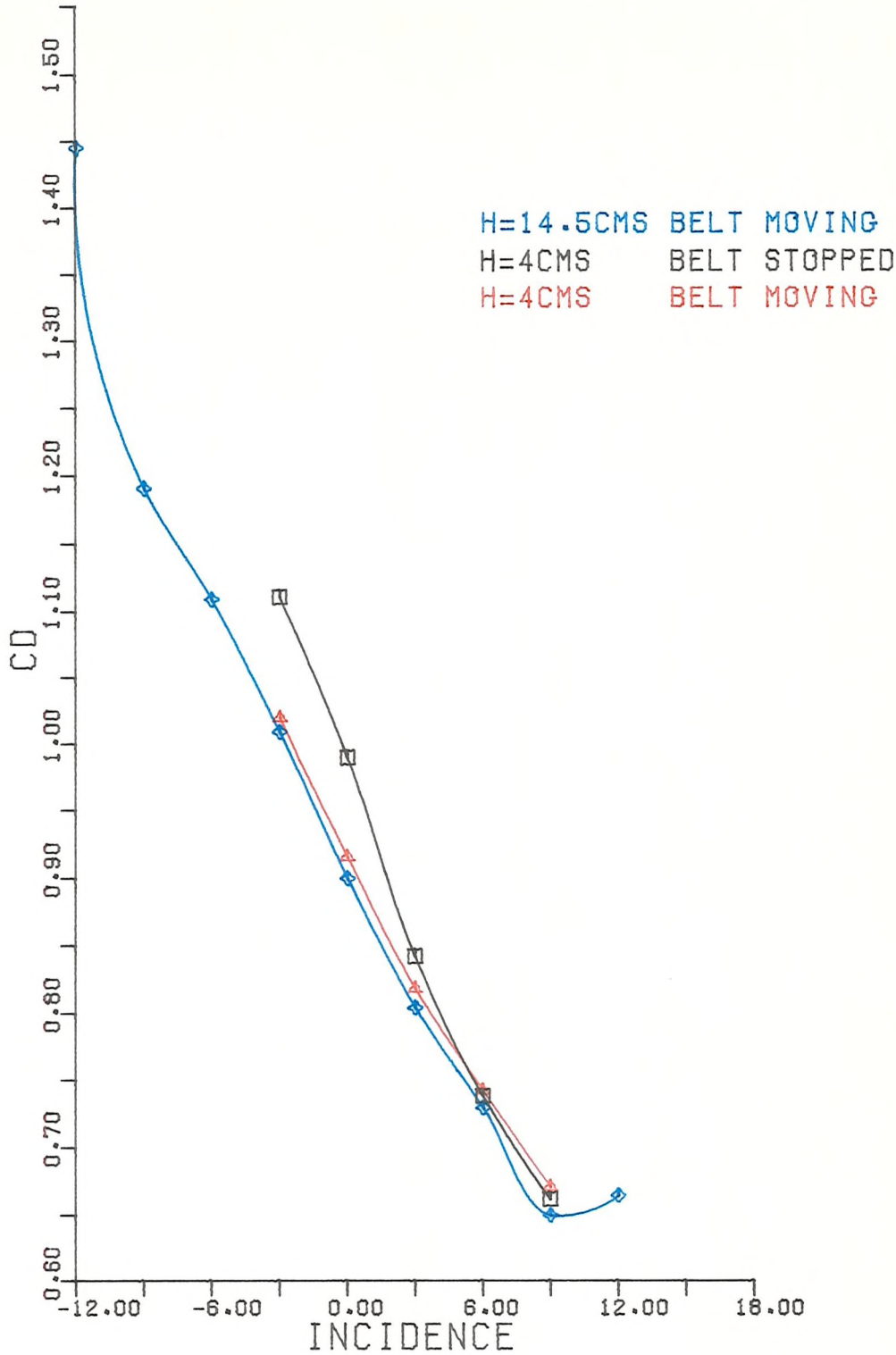

DRAG

20 TOP 10 BOTTOM

FIGURE 29

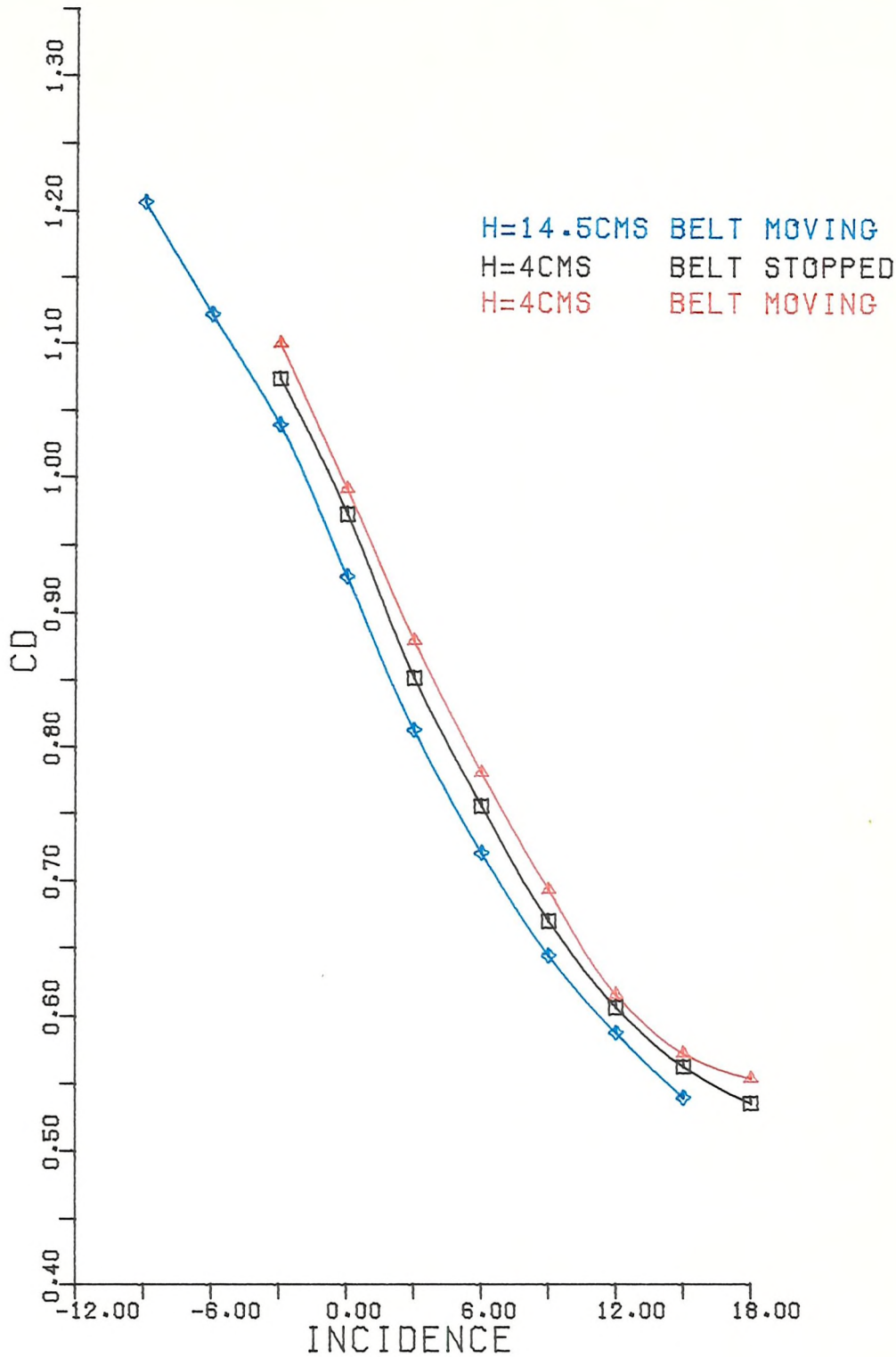

DRAG

20 TOP 20 BOTTOM

FIGURE 30

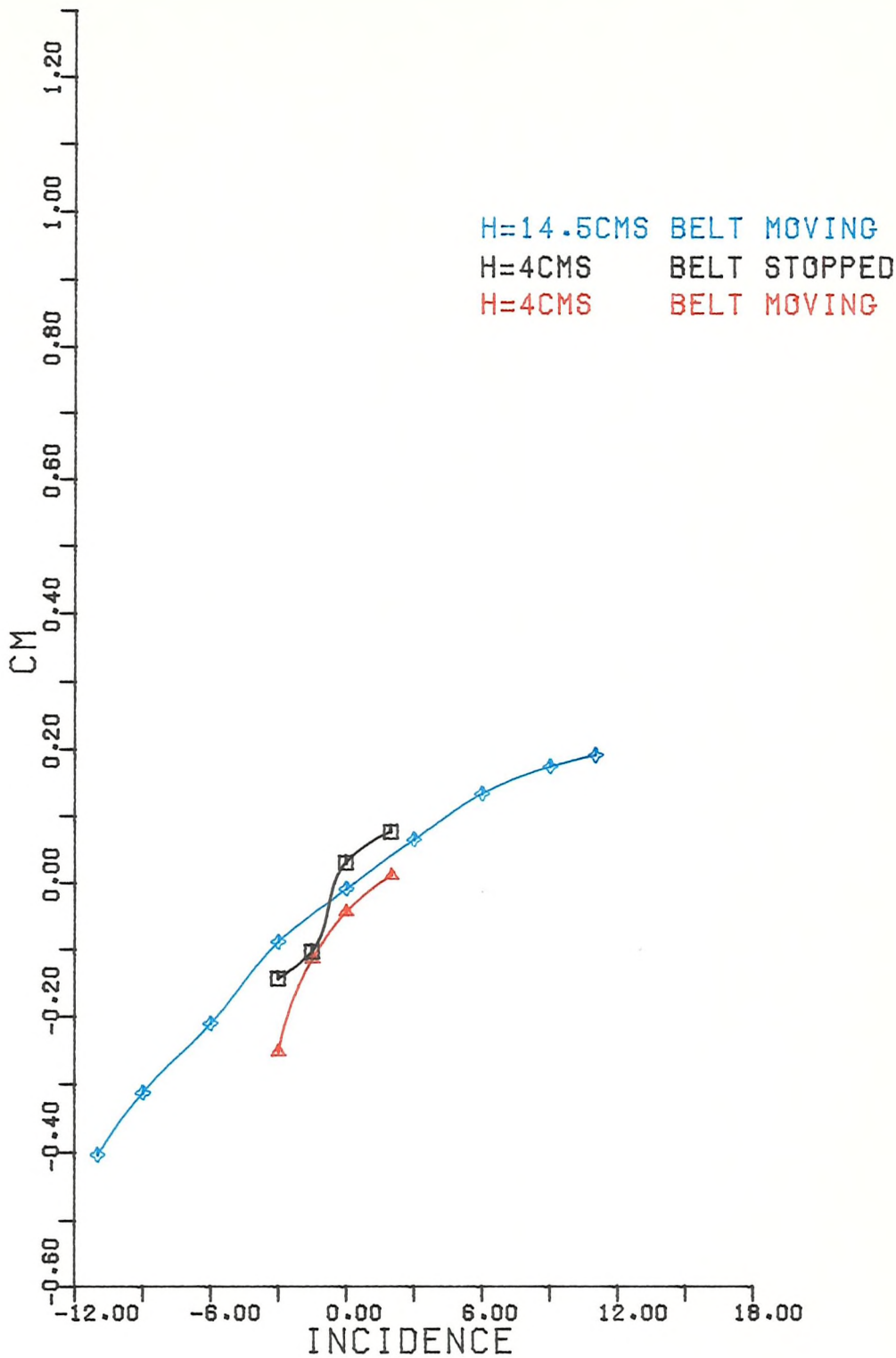

PITCHING MOMENT

O TOP O BOTTOM

FIGURE 31

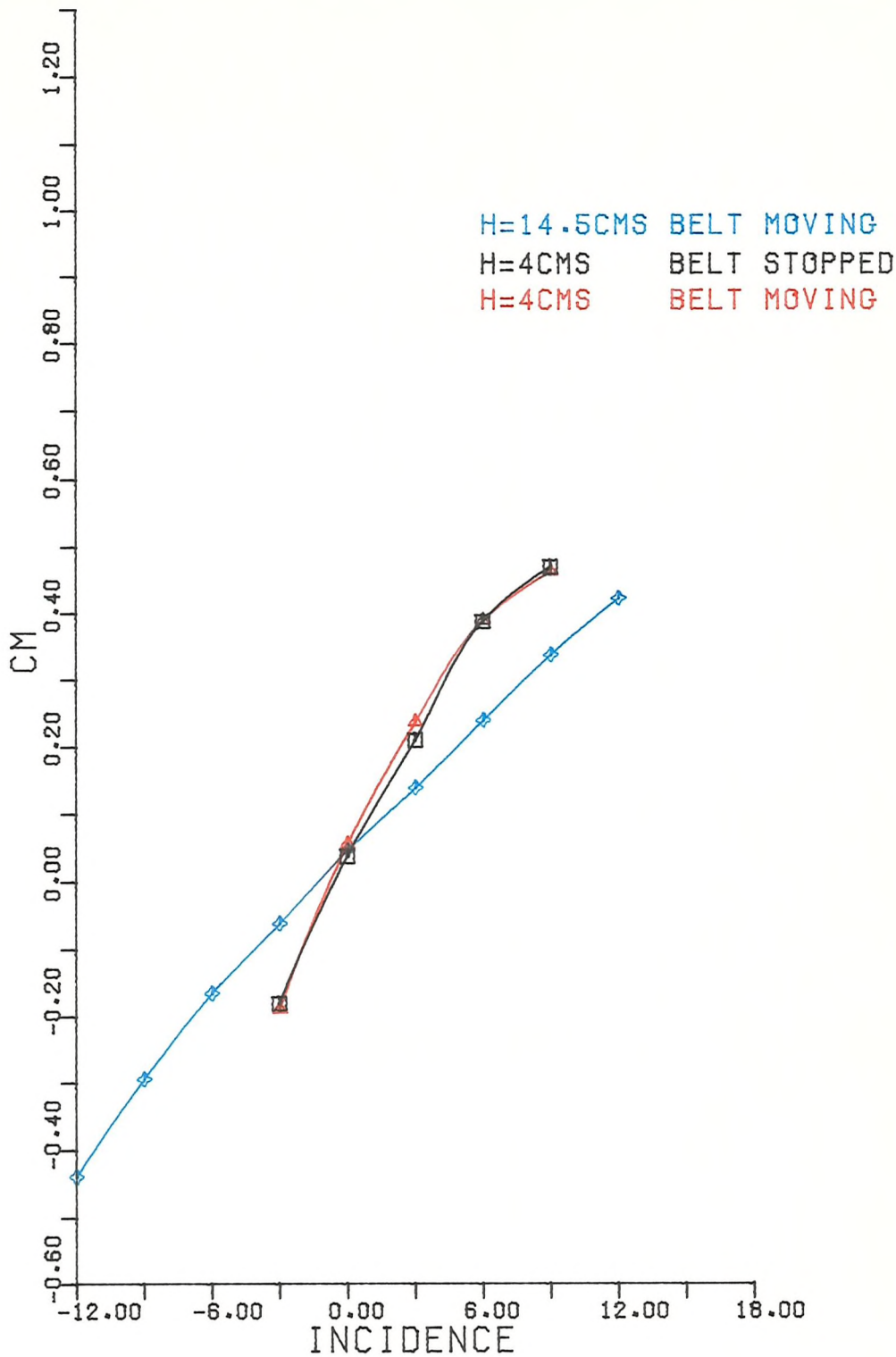

PITCHING MOMENT

0 TOP 10 BOTTOM

FIGURE 32

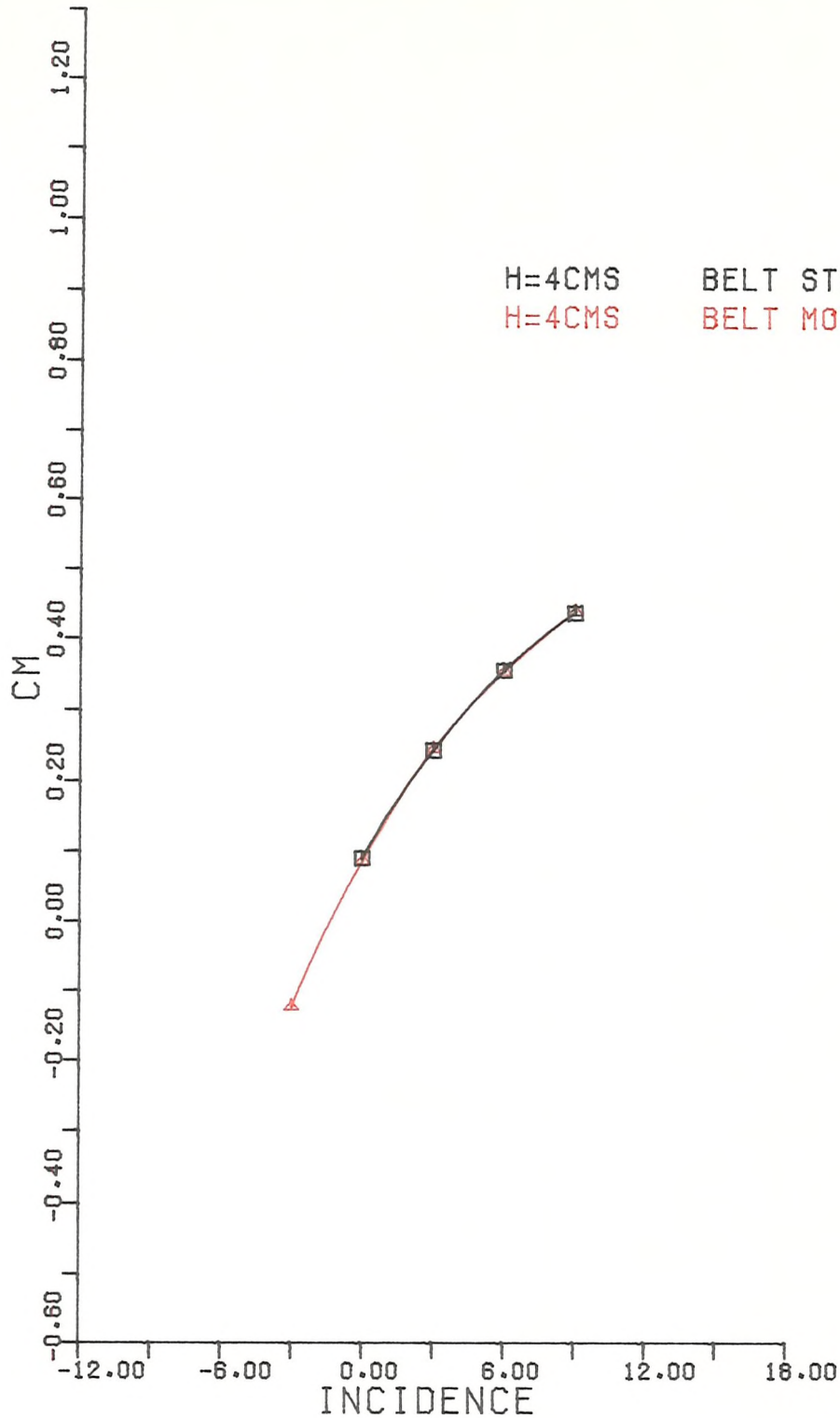

PITCHING MOMENT

0 TOP 10 BOTTOM

WITH DISTRIBUTED ROUGHNESS

FIGURE 33

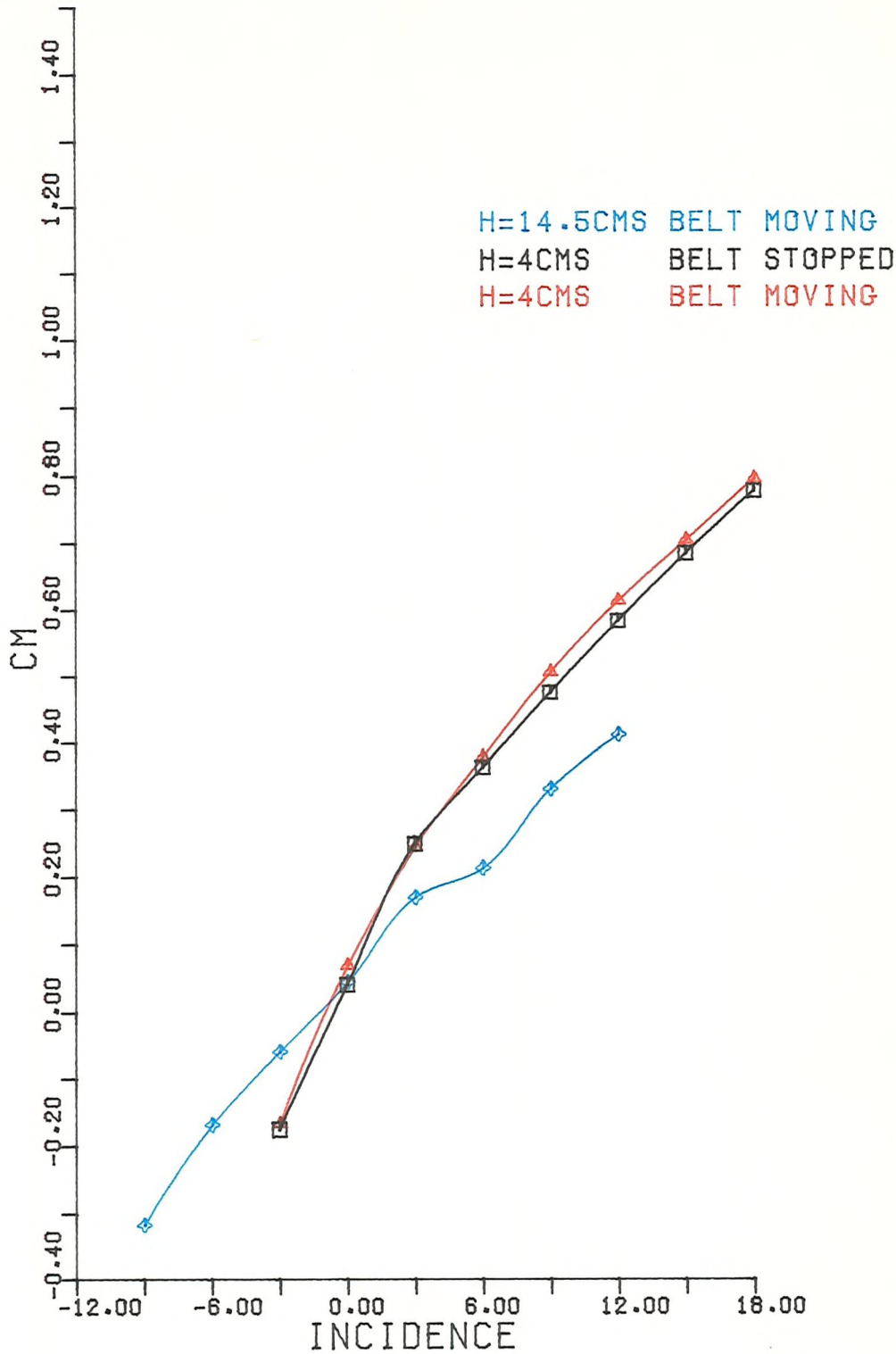

PITCHING MOMENT

0 TOP 20 BOTTOM

FIGURE 34

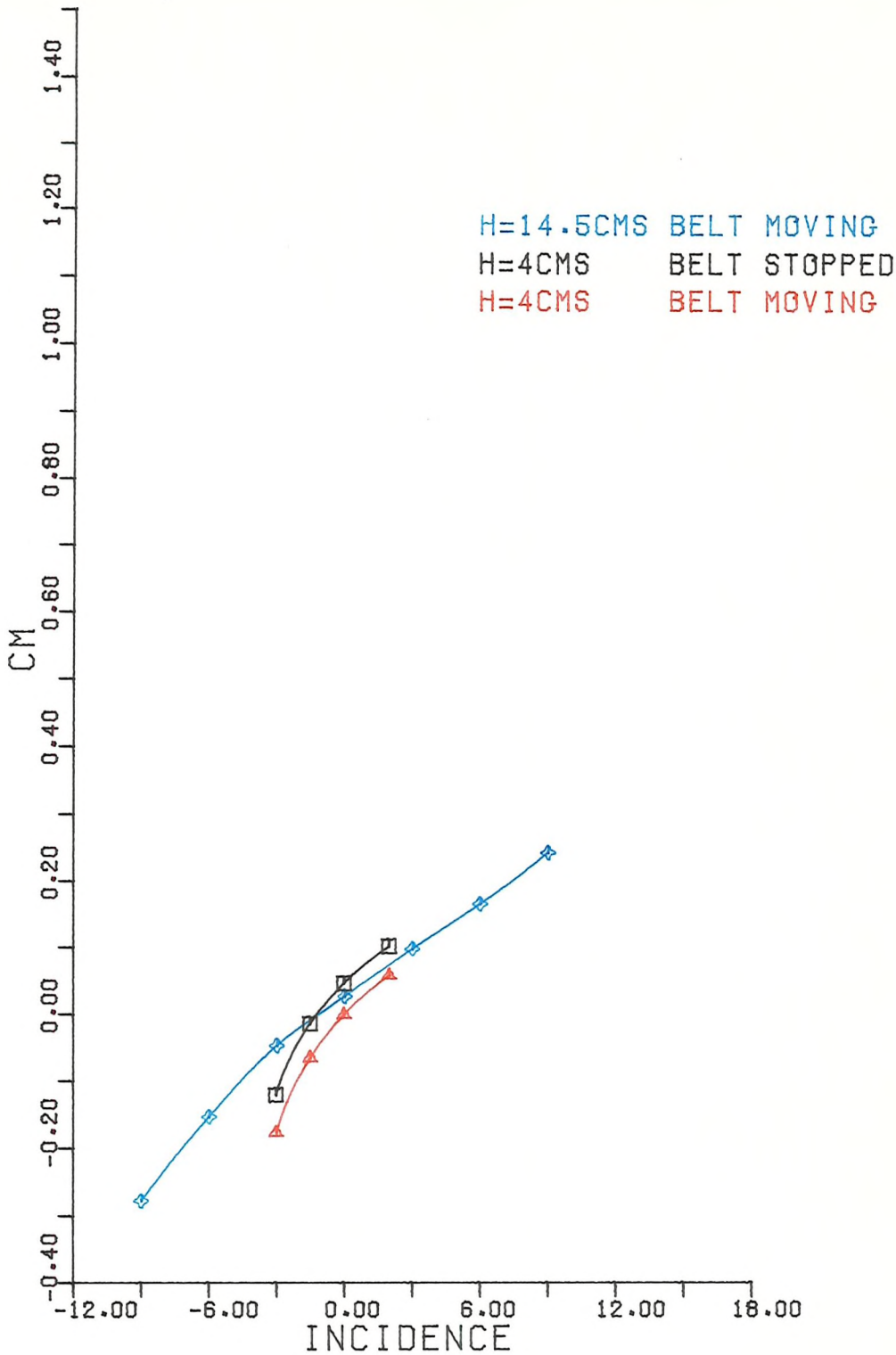

PITCHING MOMENT

10 TOP 0 BOTTOM

FIGURE 35

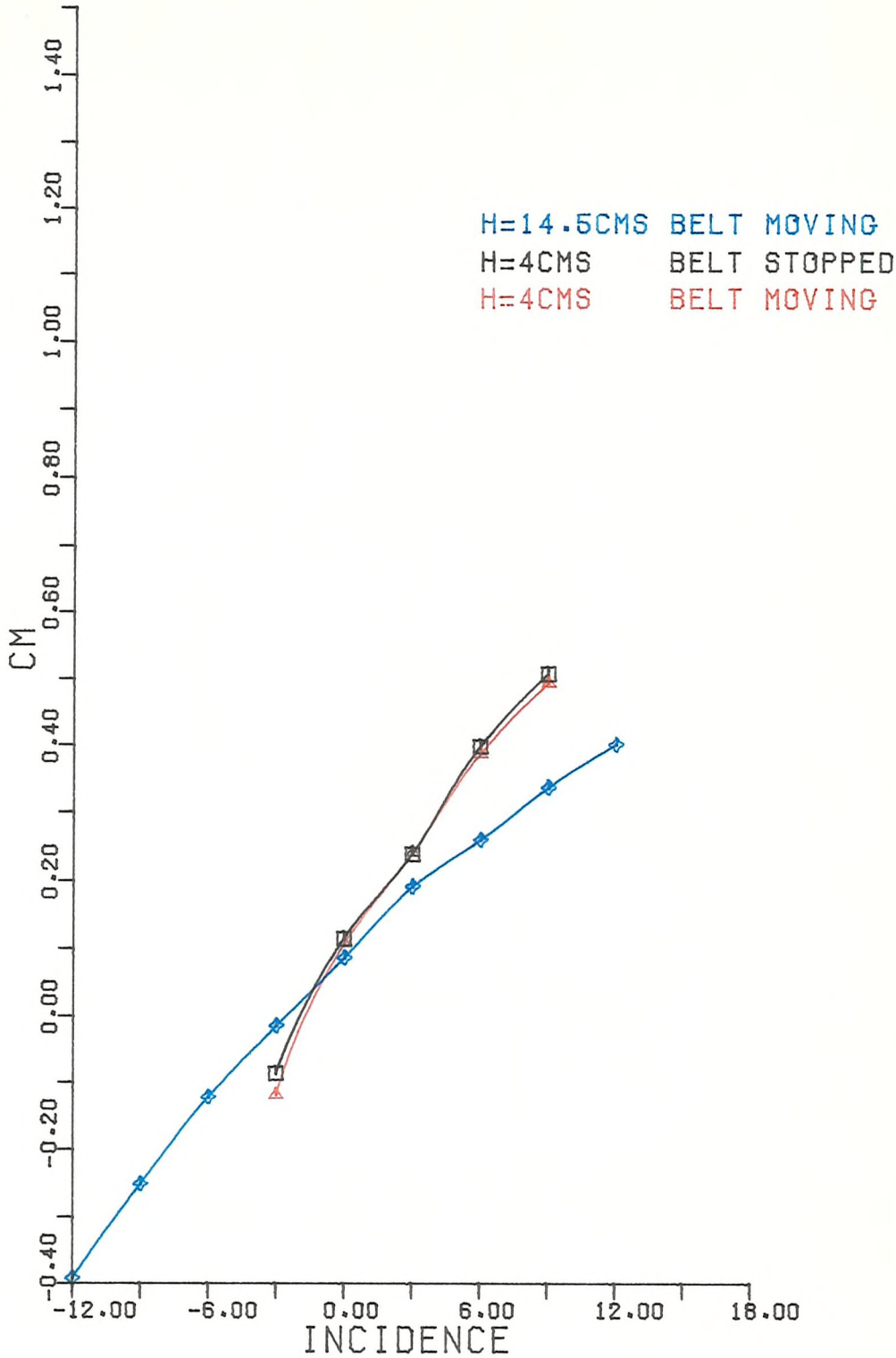

PITCHING MOMENT
10 TOP 10 BOTTOM

FIGURE 36

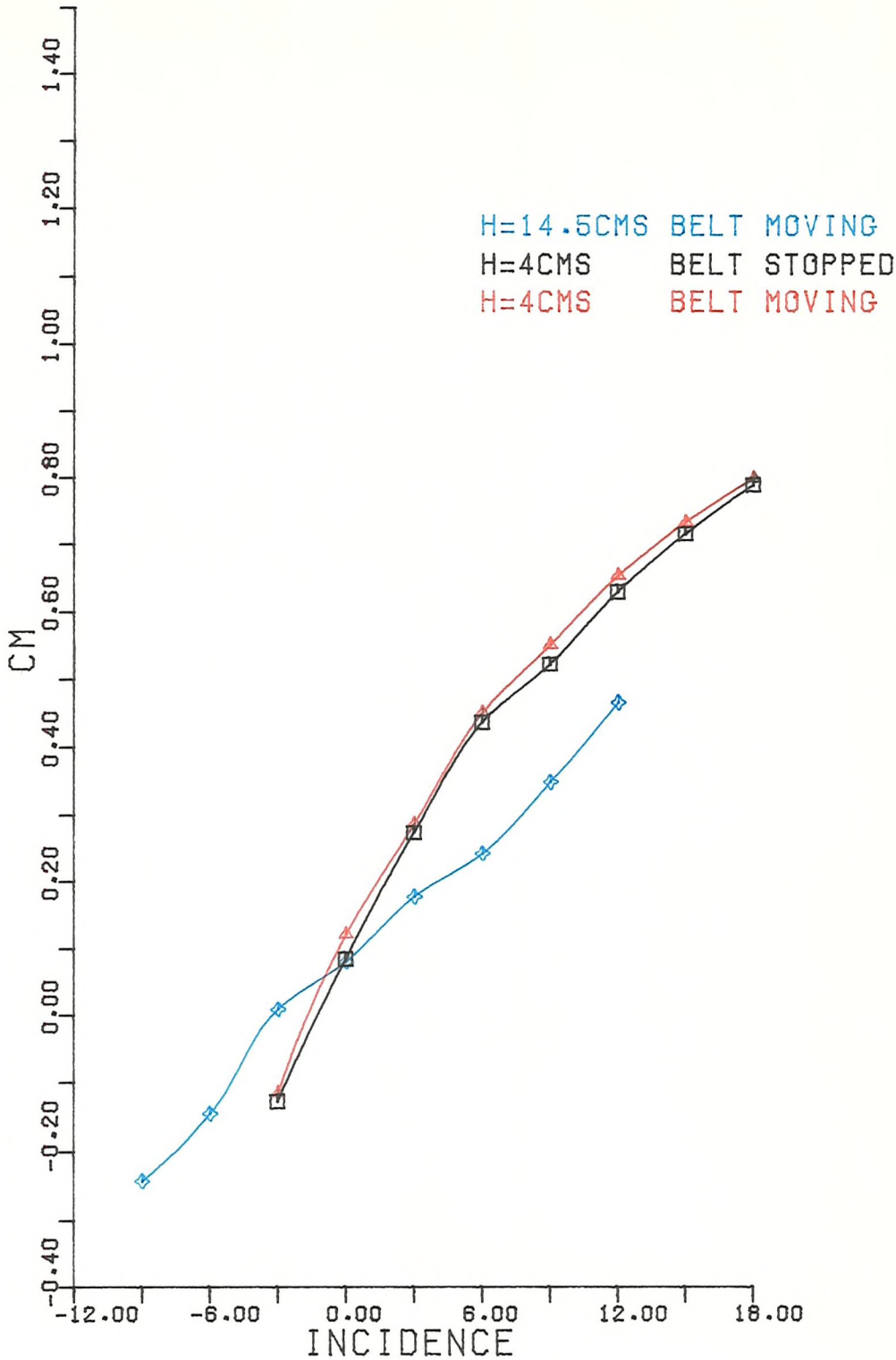

PITCHING MOMENT

10 TOP 20 BOTTOM

FIGURE 37

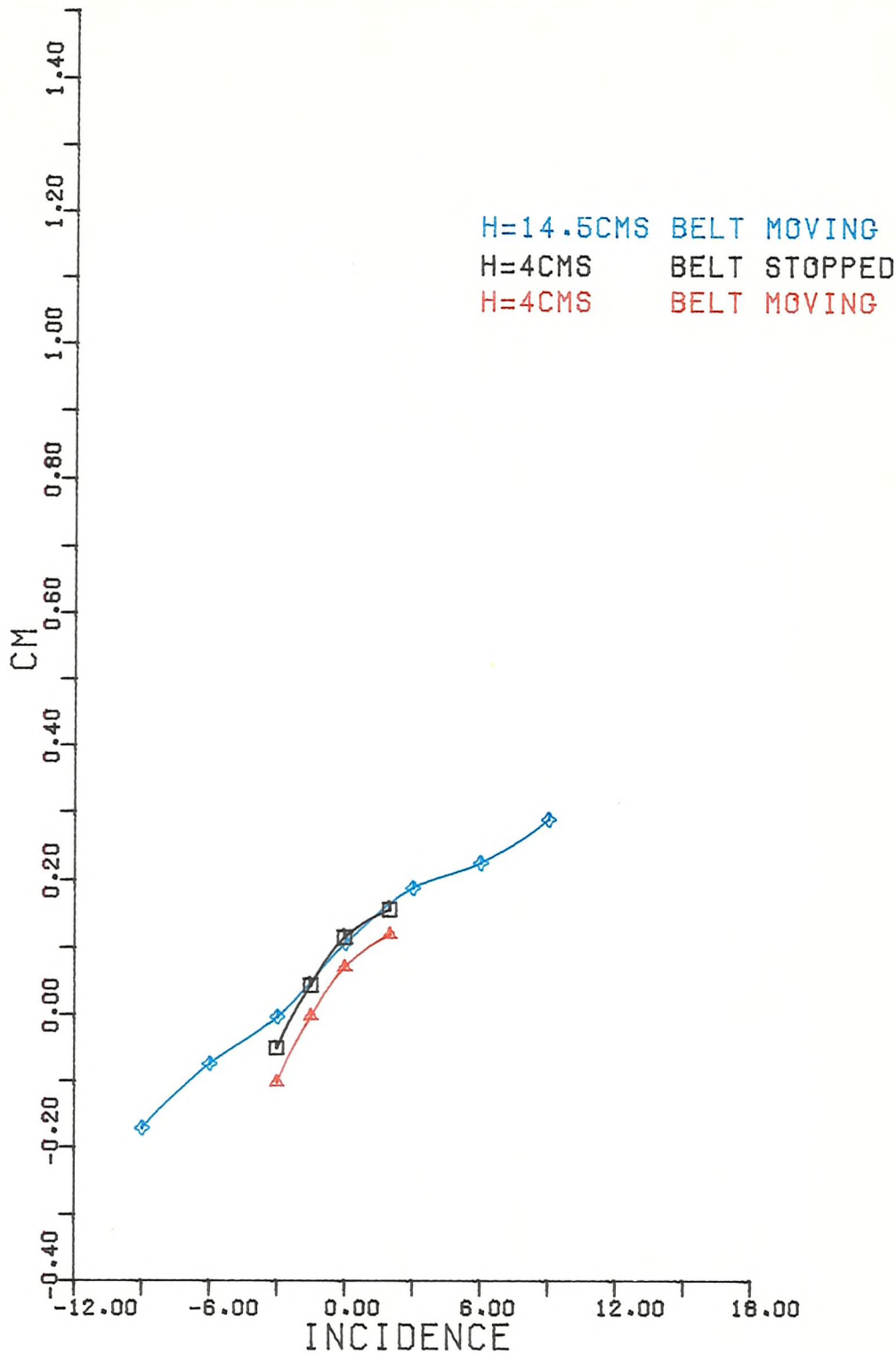

PITCHING MOMENT

20 TOP 0 BOTTOM

FIGURE 38

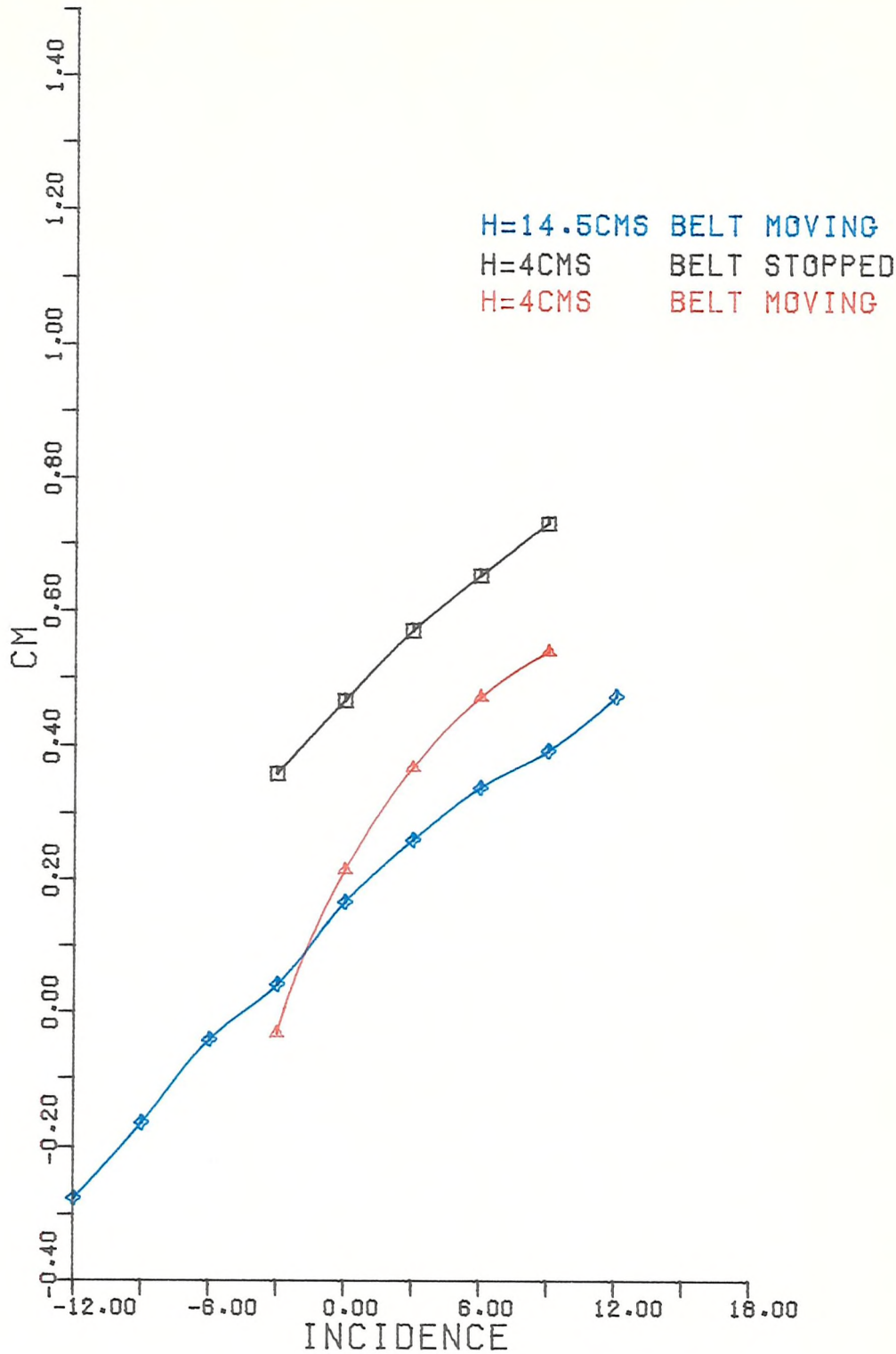

PITCHING MOMENT

20 TOP 10 BOTTOM

FIGURE 39

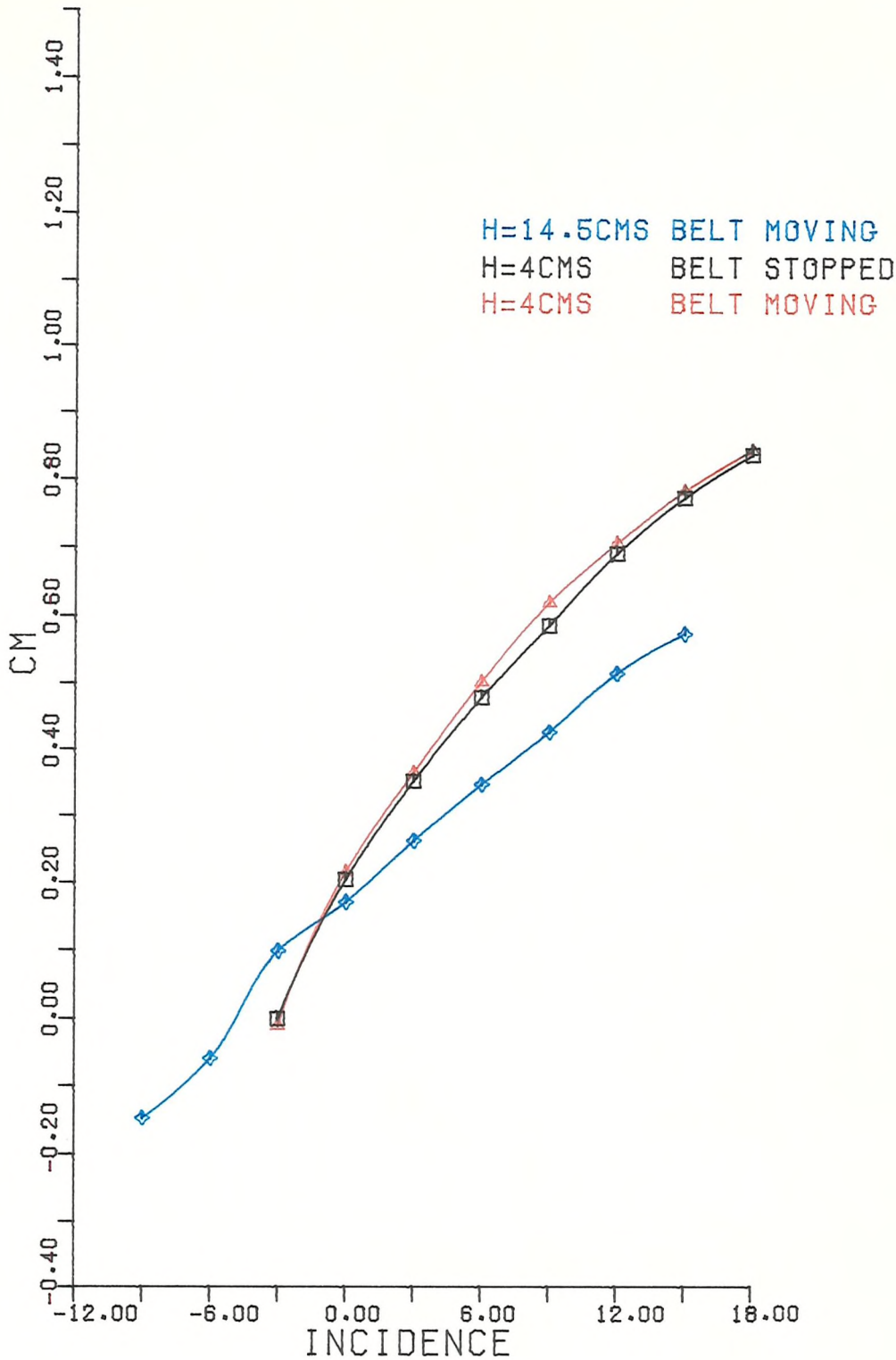

PITCHING MOMENT
20 TOP 20 BOTTOM

FIGURE 40

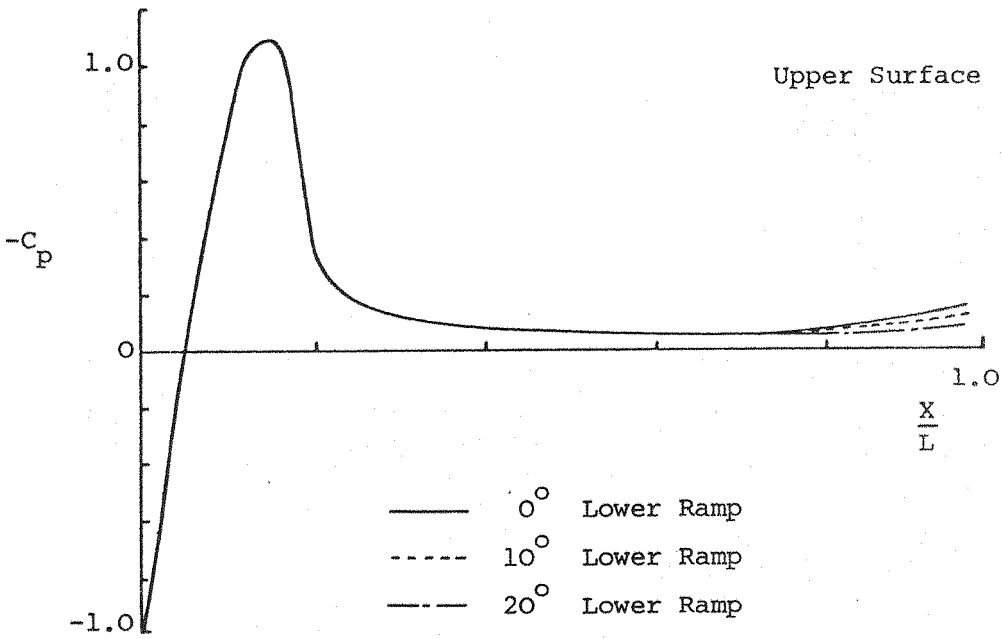

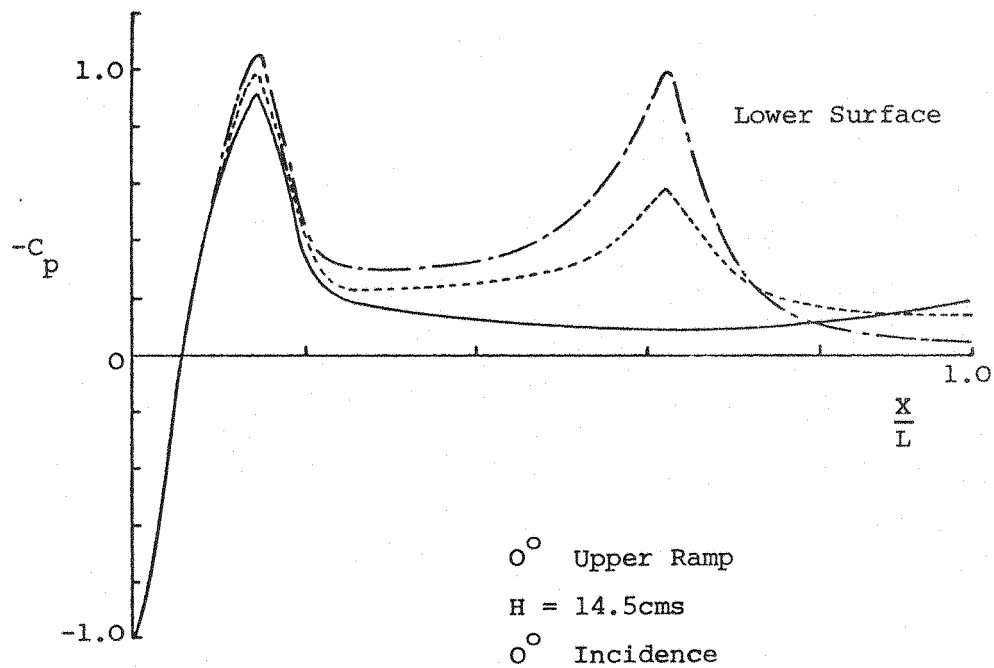

FIGURE 41 BLUFF BODY CENTRE LINE SURFACE PRESSURE DISTRIBUTIONS

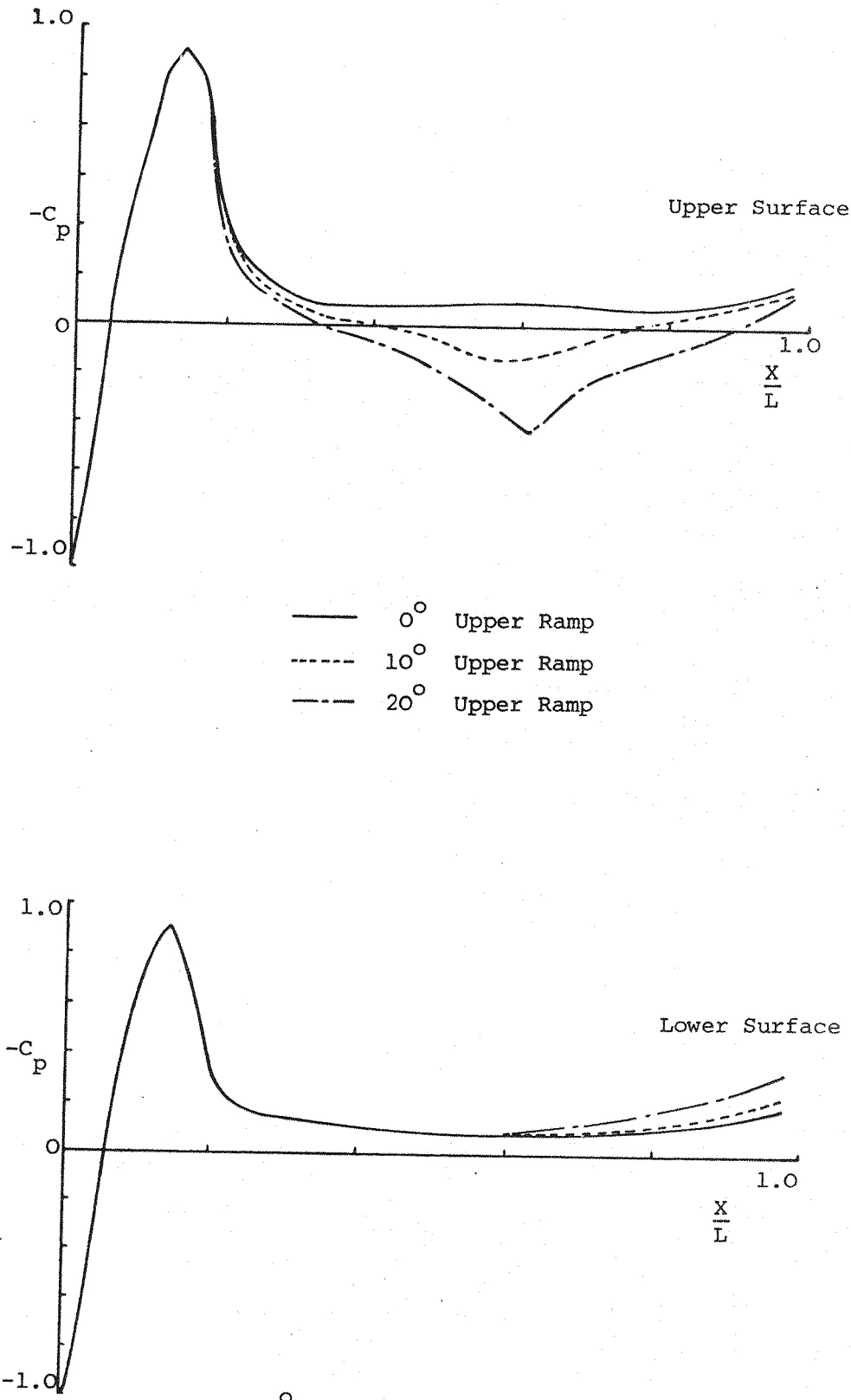

FIGURE 42 BLUFF BODY CENTRE LINE SURFACE PRESSURE DISTRIBUTIONS

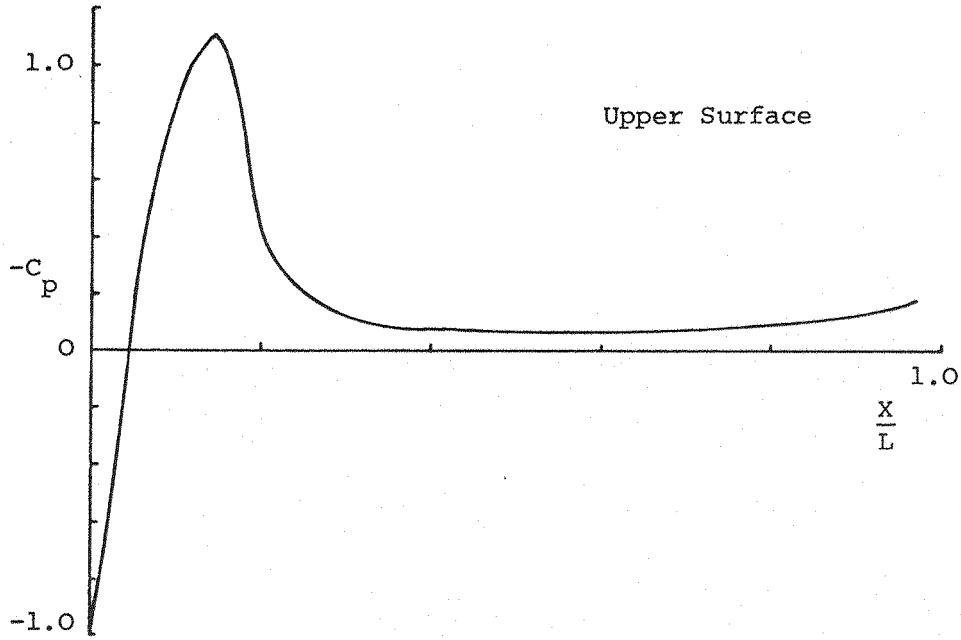

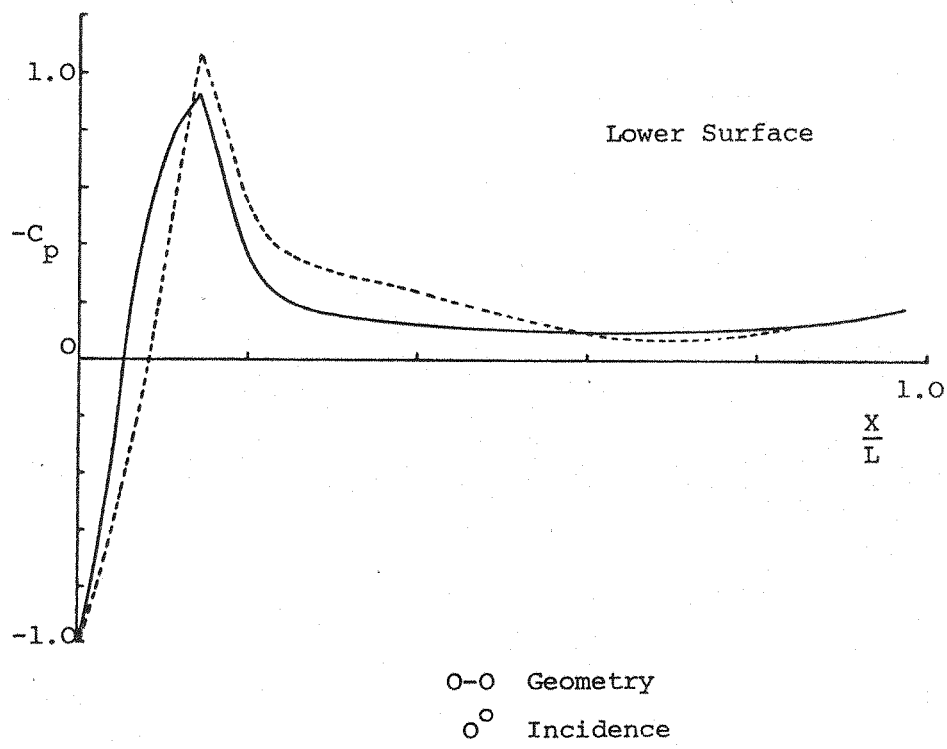

FIGURE 43 BLUFF BODY CENTRE LINE SURFACE PRESSURE DISTRIBUTIONS

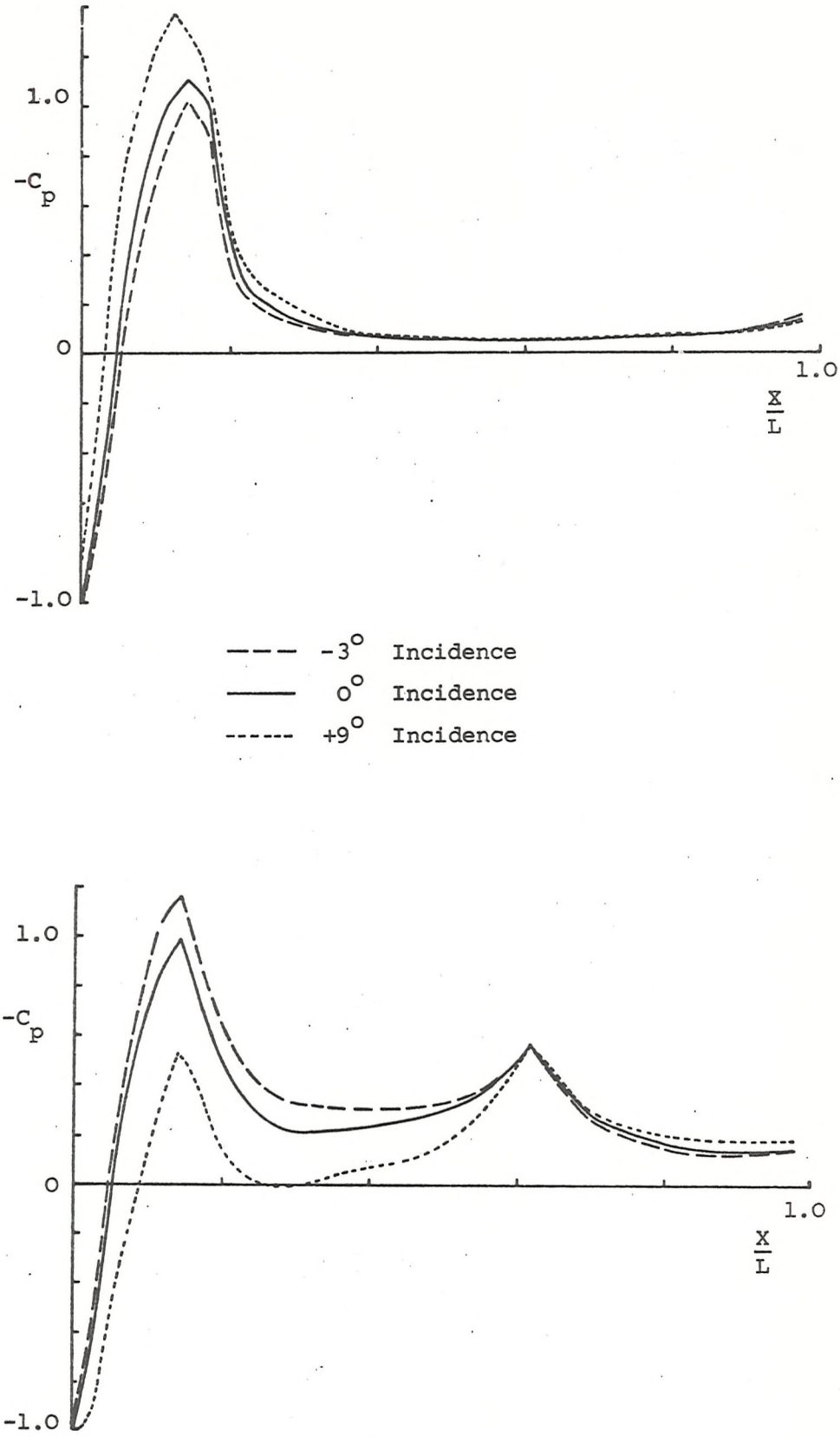

FIGURE 44 BLUFF BODY CENTRE LINE SURFACE PRESSURE DISTRIBUTIONS

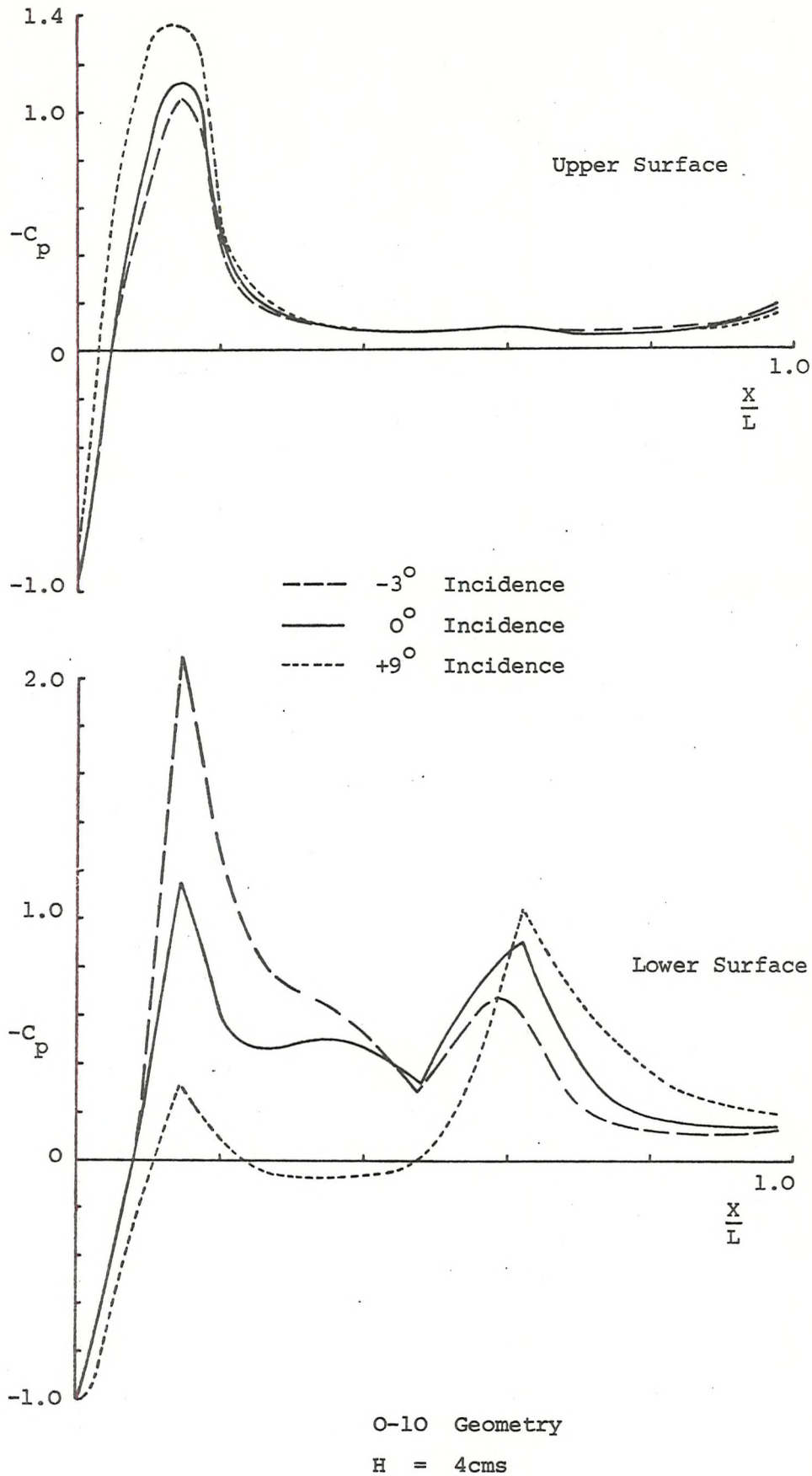

FIGURE 45 BLUFF BODY CENTRE LINE SURFACE PRESSURE DISTRIBUTIONS

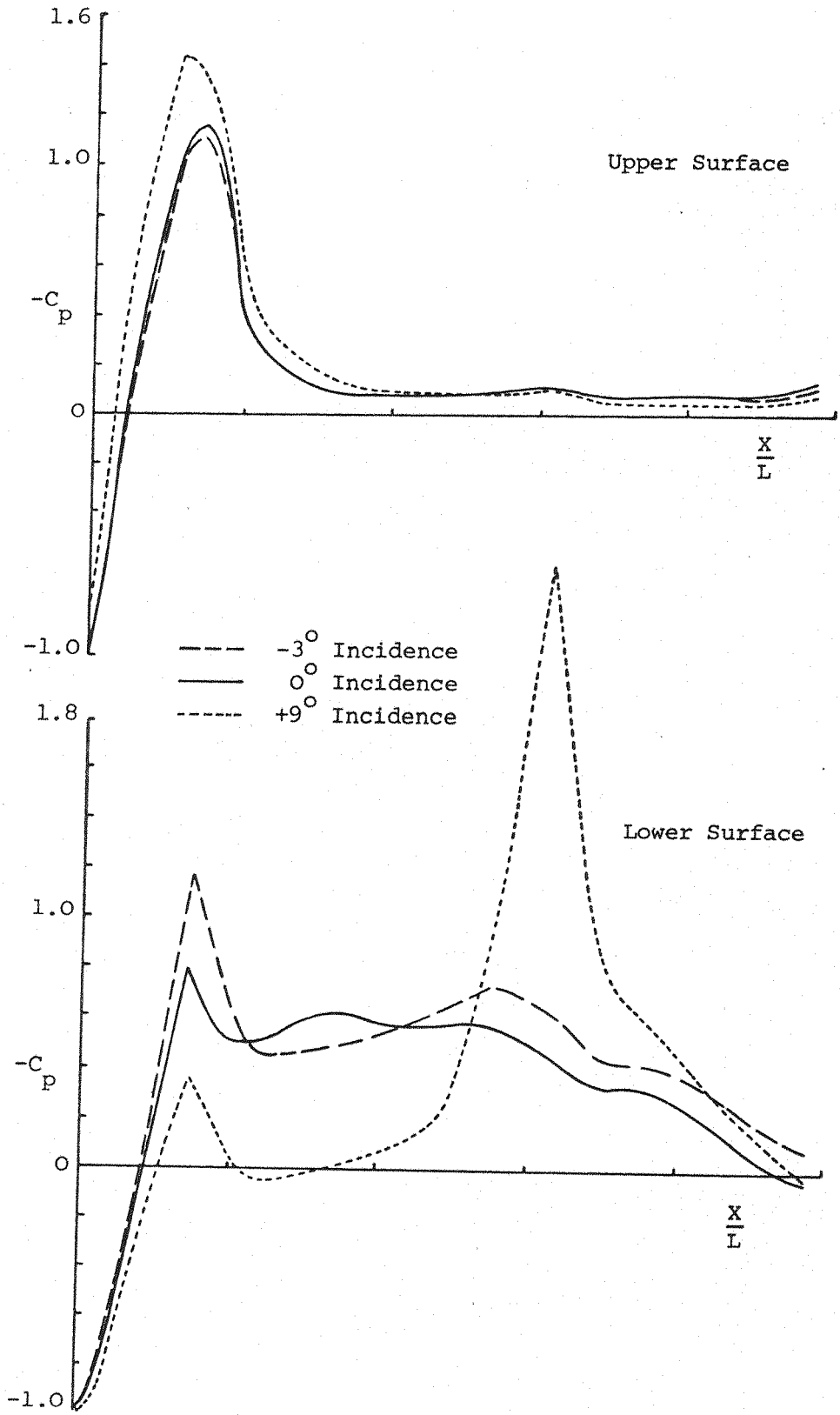

O-2O Geometry

H = 4cms

FIGURE 46 BLUFF BODY CENTRE LINE SURFACE PRESSURE DISTRIBUTIONS

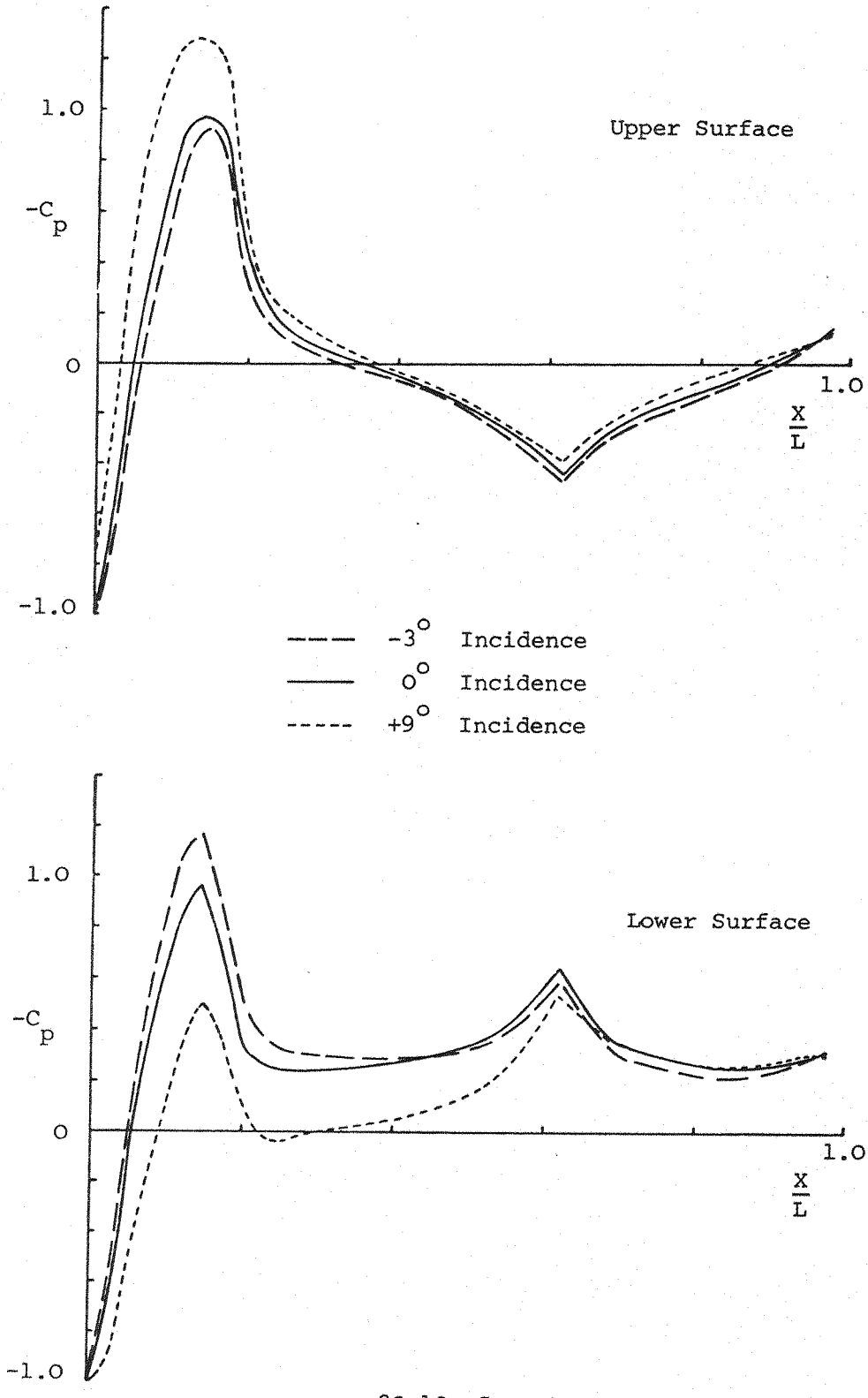

FIGURE 47 BLUFF BODY CENTRE LINE SURFACE PRESSURE DISTRIBUTIONS

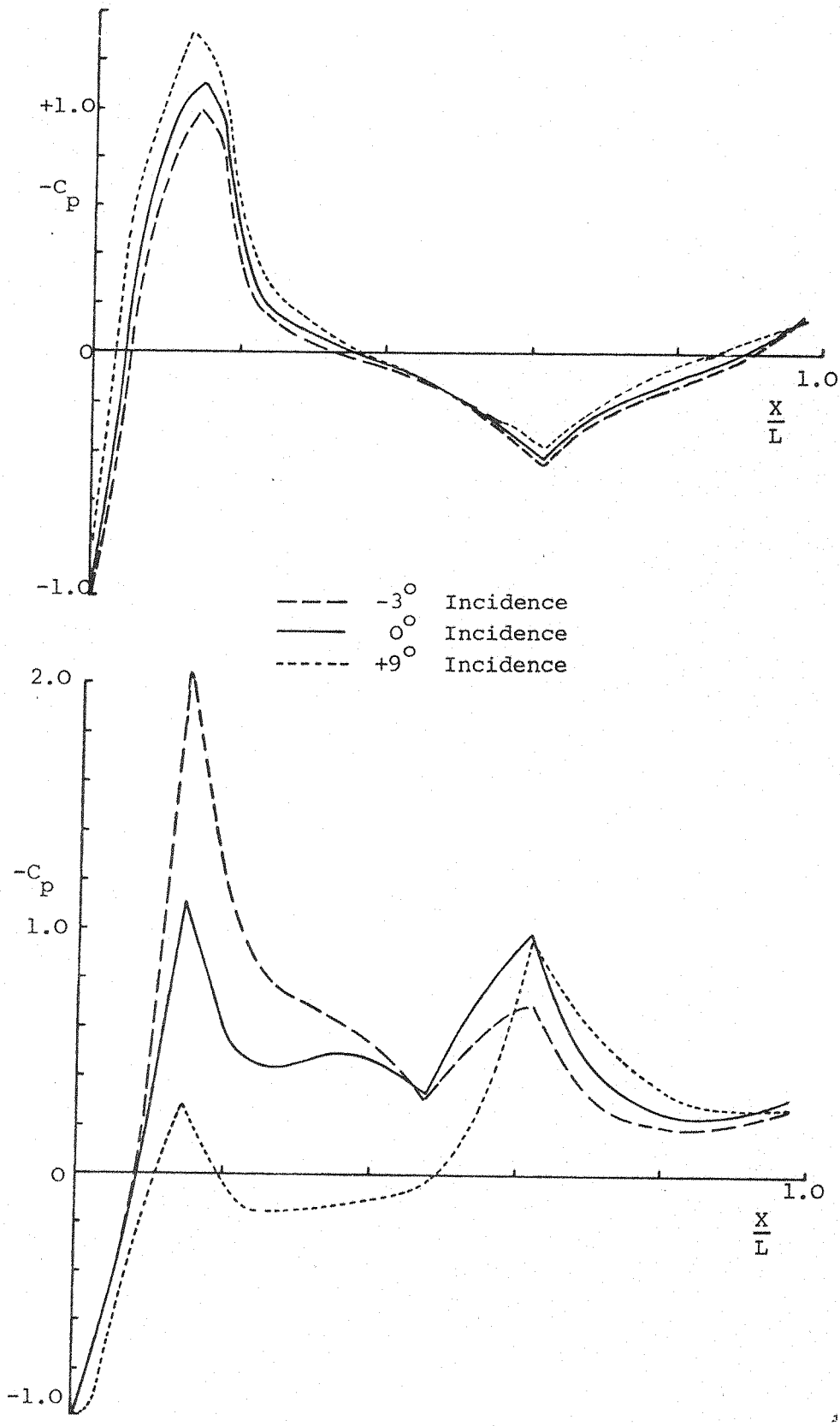

20-10 Geometry

H = 4cms

FIGURE 48 BLUFF BODY CENTRE LINE SURFACE PRESSURE DISTRIBUTIONS

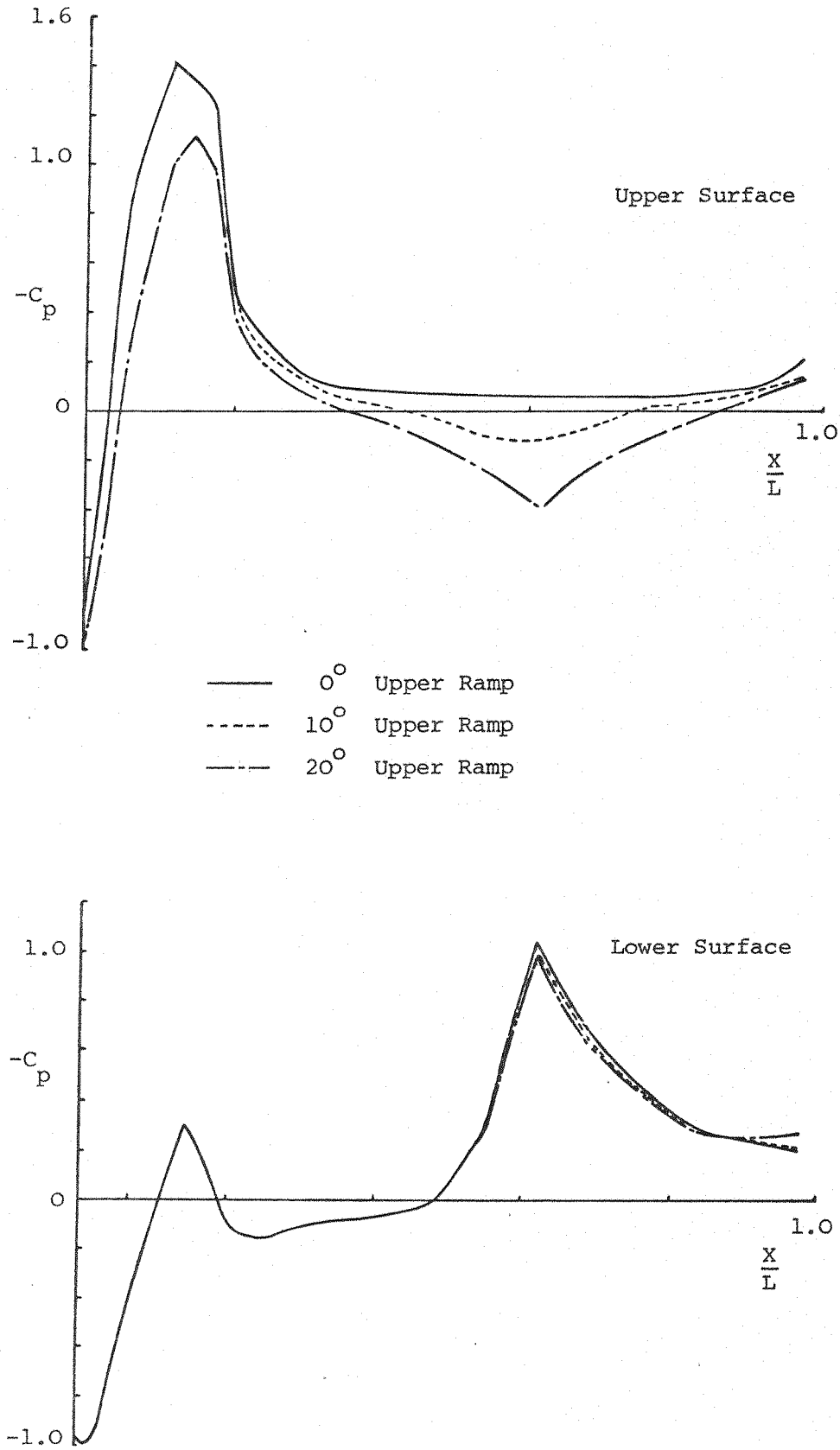

FIGURE 49 BLUFF BODY CENTRE LINE SURFACE PRESSURE DISTRIBUTIONS

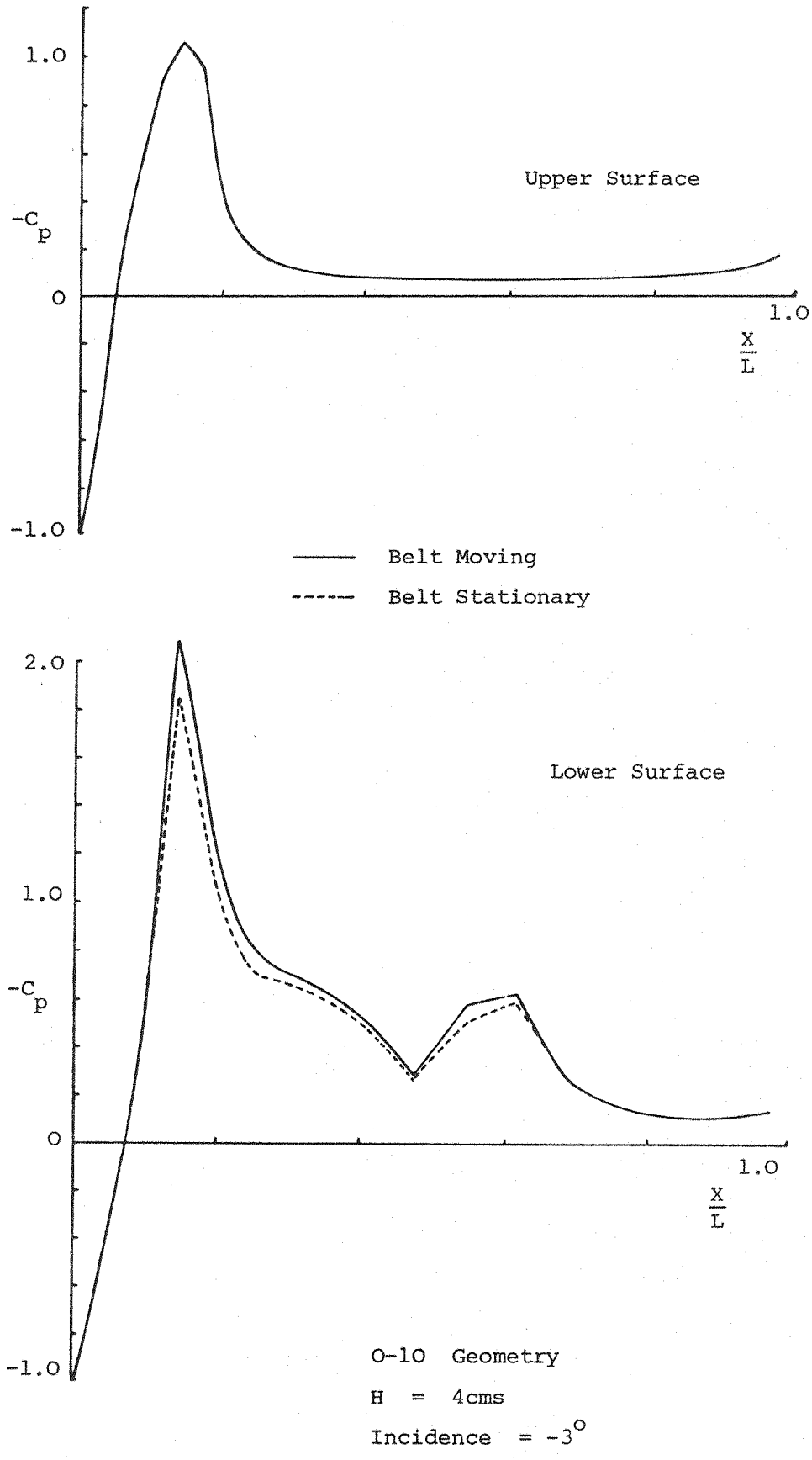

FIGURE 50 BLUFF BODY CENTRE LINE SURFACE PRESSURE DISTRIBUTIONS

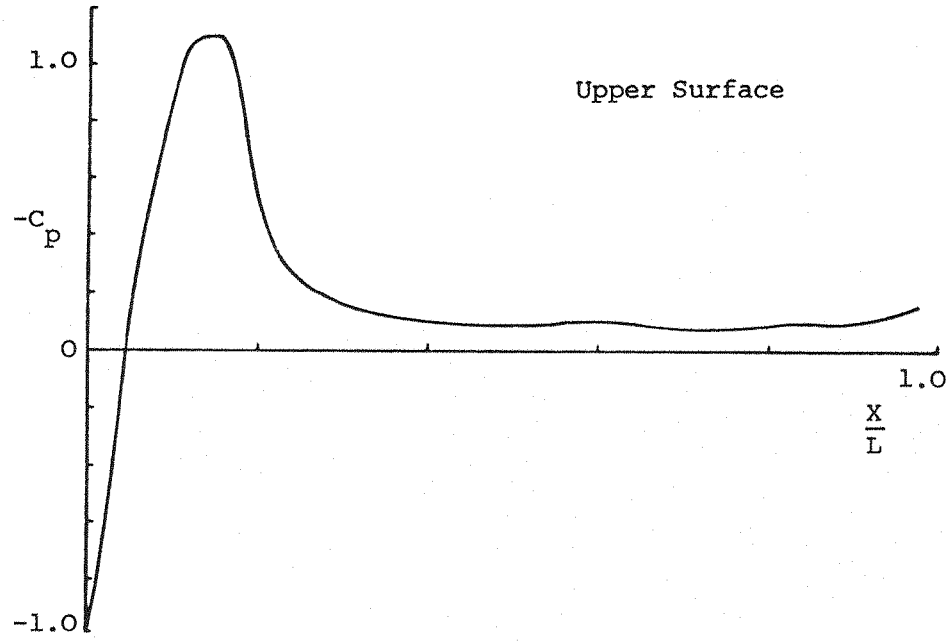

——— Belt Moving

------ Belt Stationary

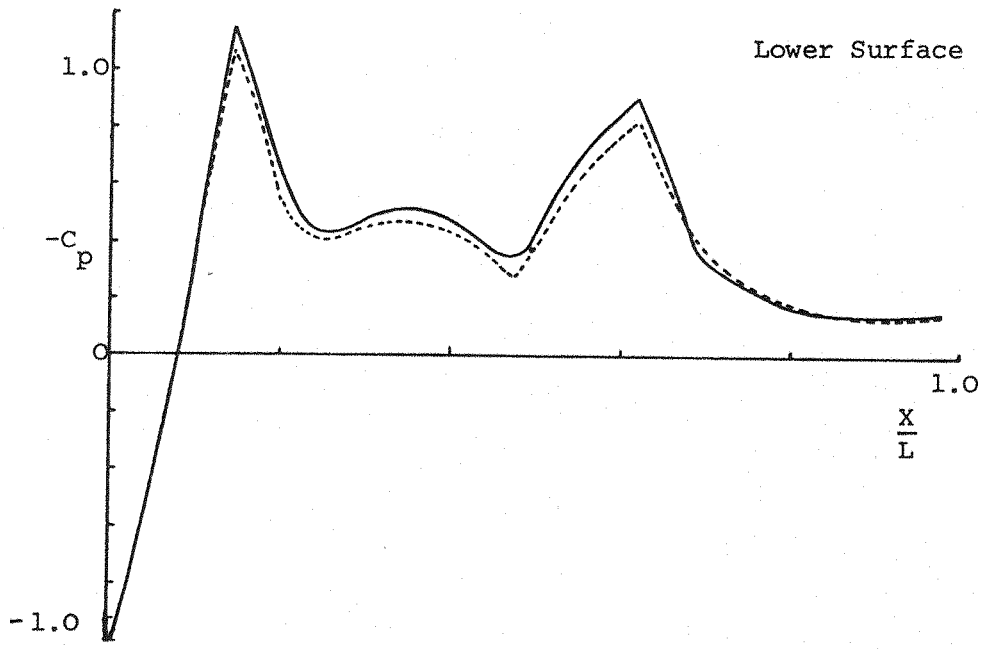

0-10 Geometry

H = 4cms

Incidence = 0^{o}

FIGURE 51 BLUFF BODY CENTRE LINE SURFACE PRESSURE DISTRIBUTIONS

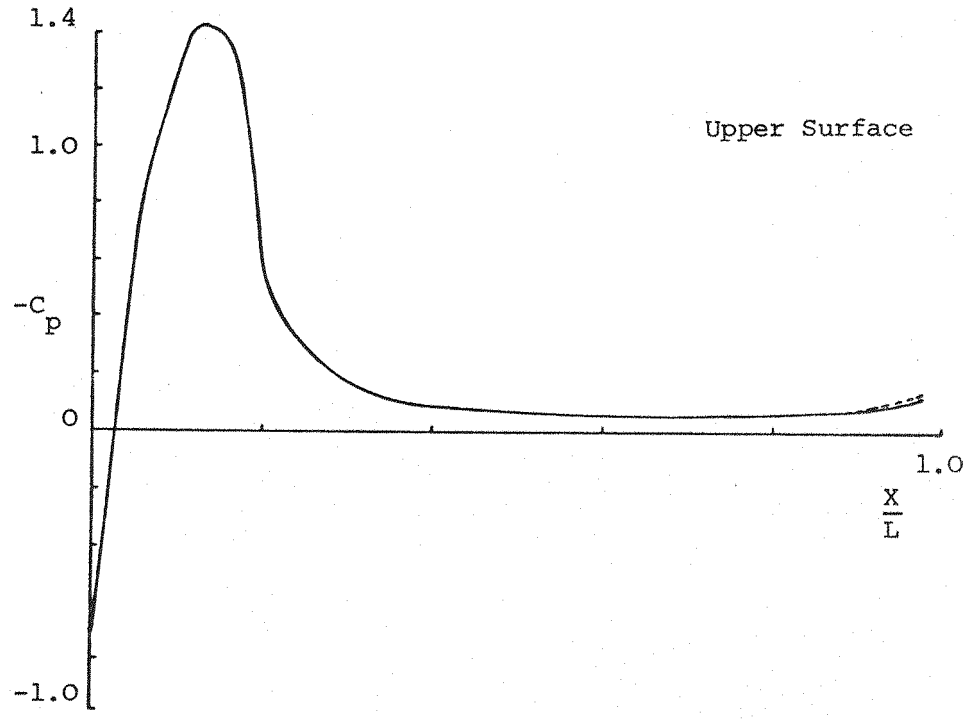

——— Belt Moving

------ Belt Stationary

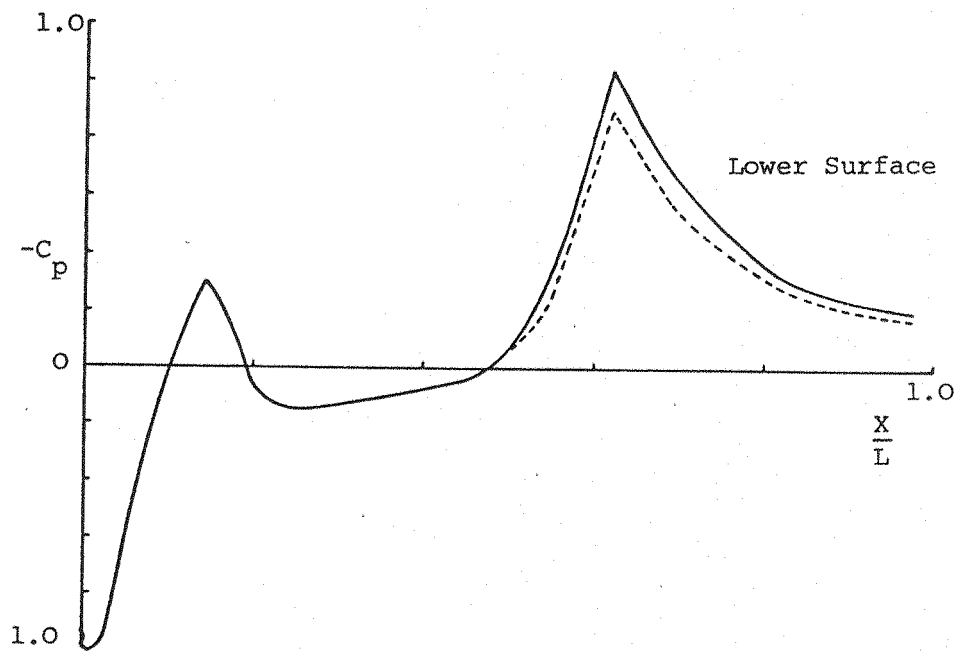

O-10 Geometry

H = 4cms

Incidence = +9°

FIGURE 52 BLUFF BODY CENTRE LINE SURFACE PRESSURE DISTRIBUTIONS

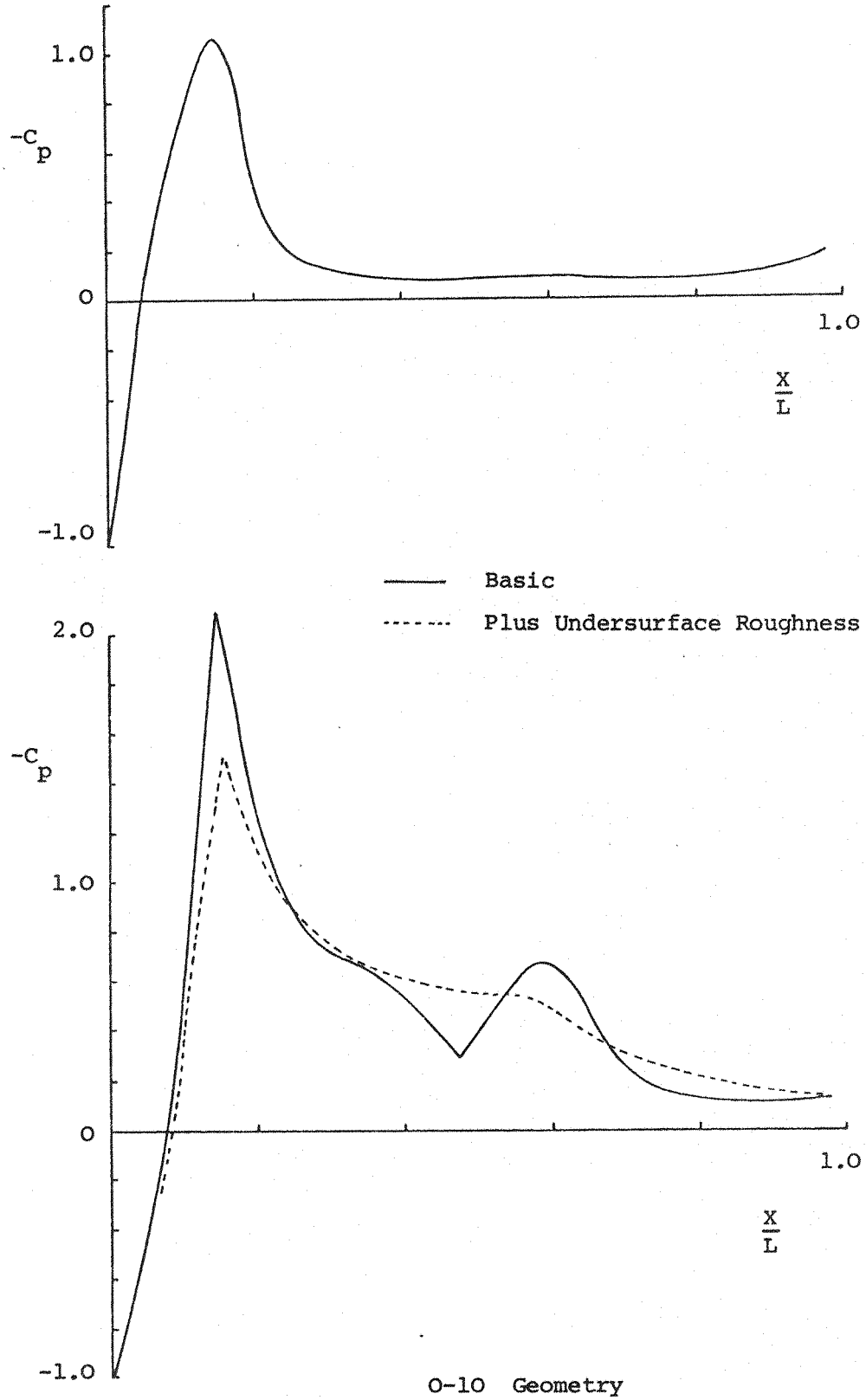

FIGURE 53 BLUFF BODY CENTRE LINE SURFACE PRESSURE DISTRIBUTIONS

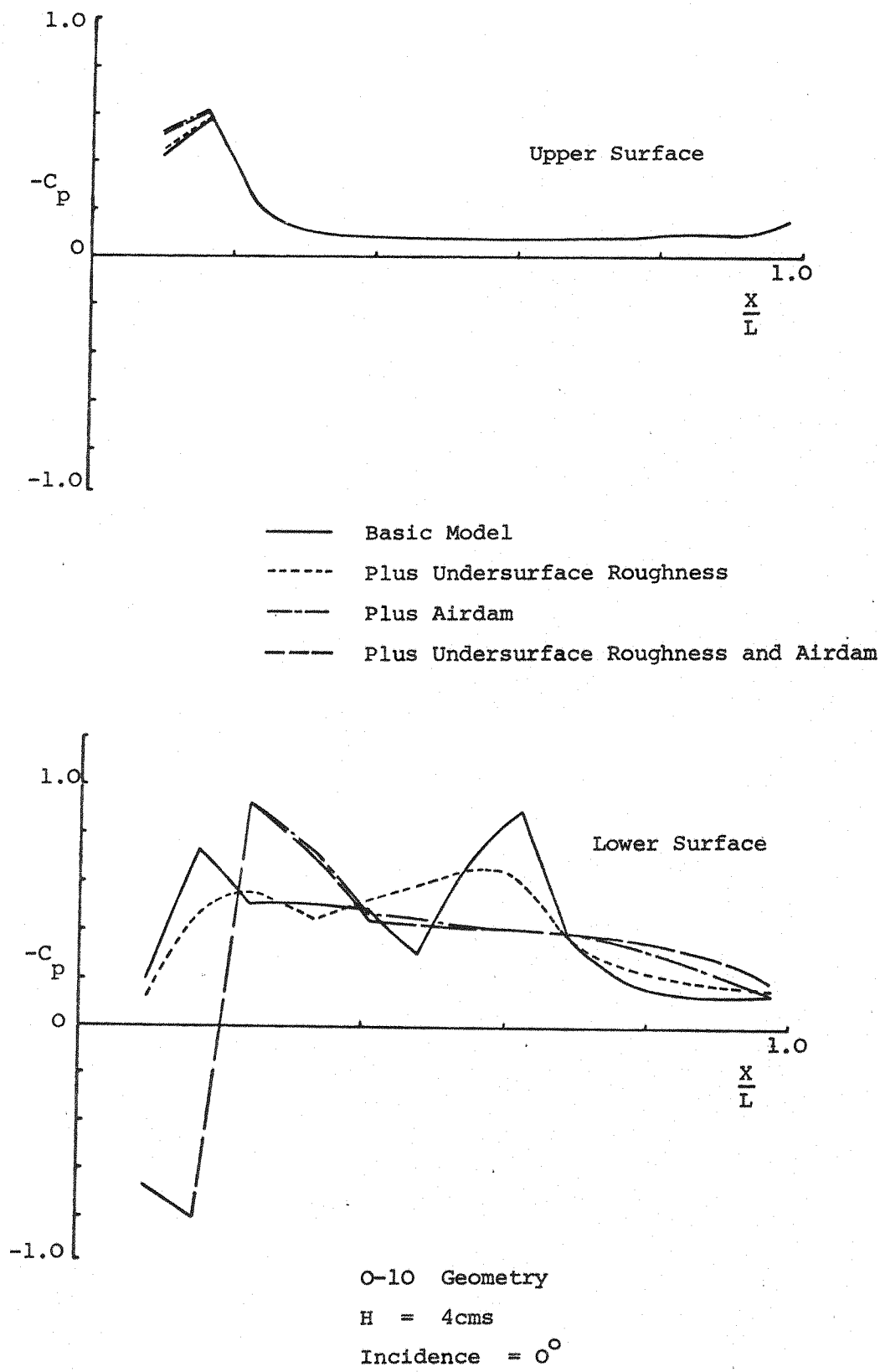

FIGURE 54 BLUFF BODY CENTRE LINE SURFACE PRESSURE DISTRIBUTIONS

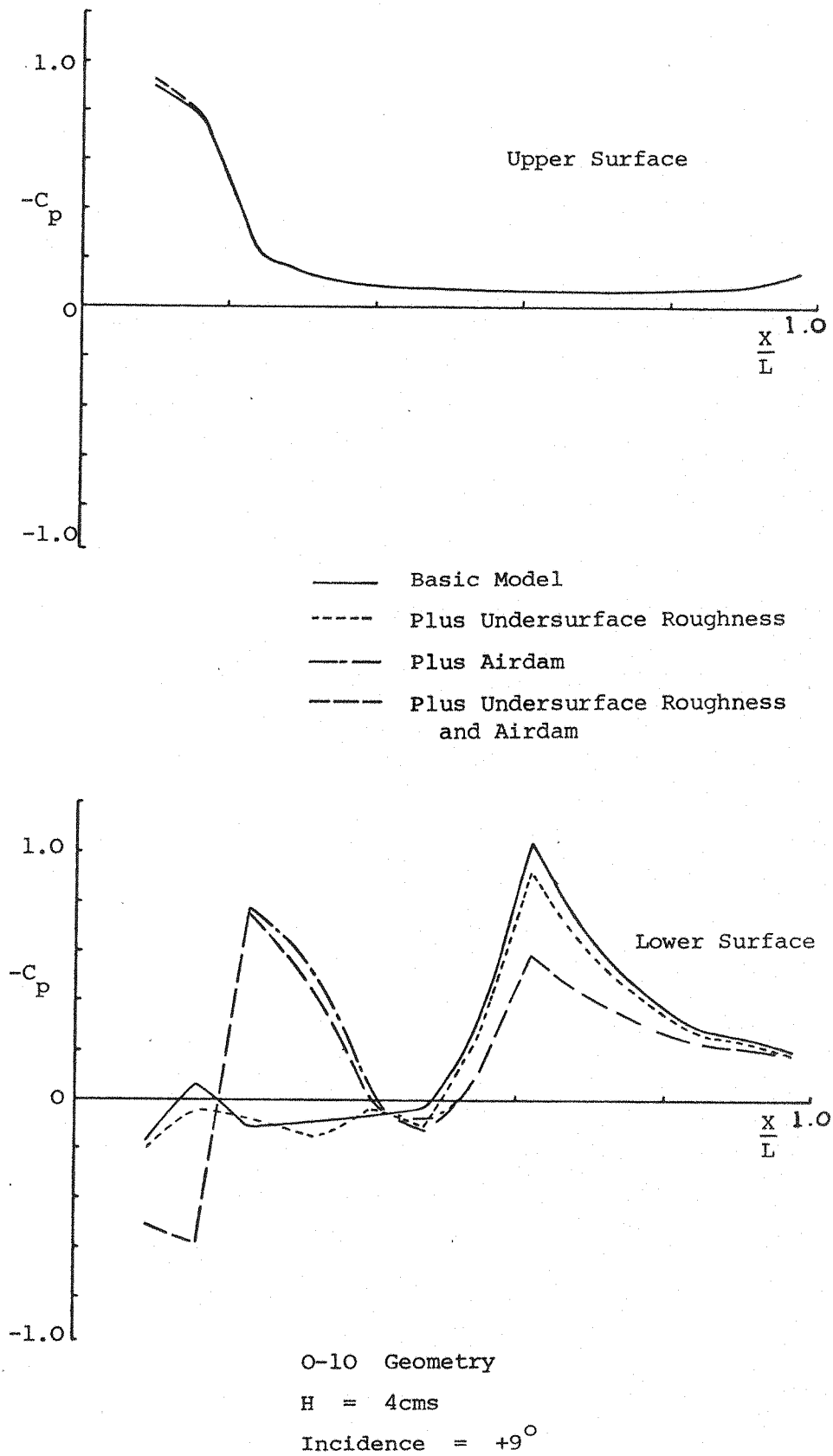

FIGURE 55 BLUFF BODY CENTRE LINE SURFACE PRESSURE DISTRIBUTIONS

FIGURE 56 EXPLANATION OF DIAGRAM USED FOR DISPLAY OF FOREBODY SURFACE PRESSURE ISOBARS

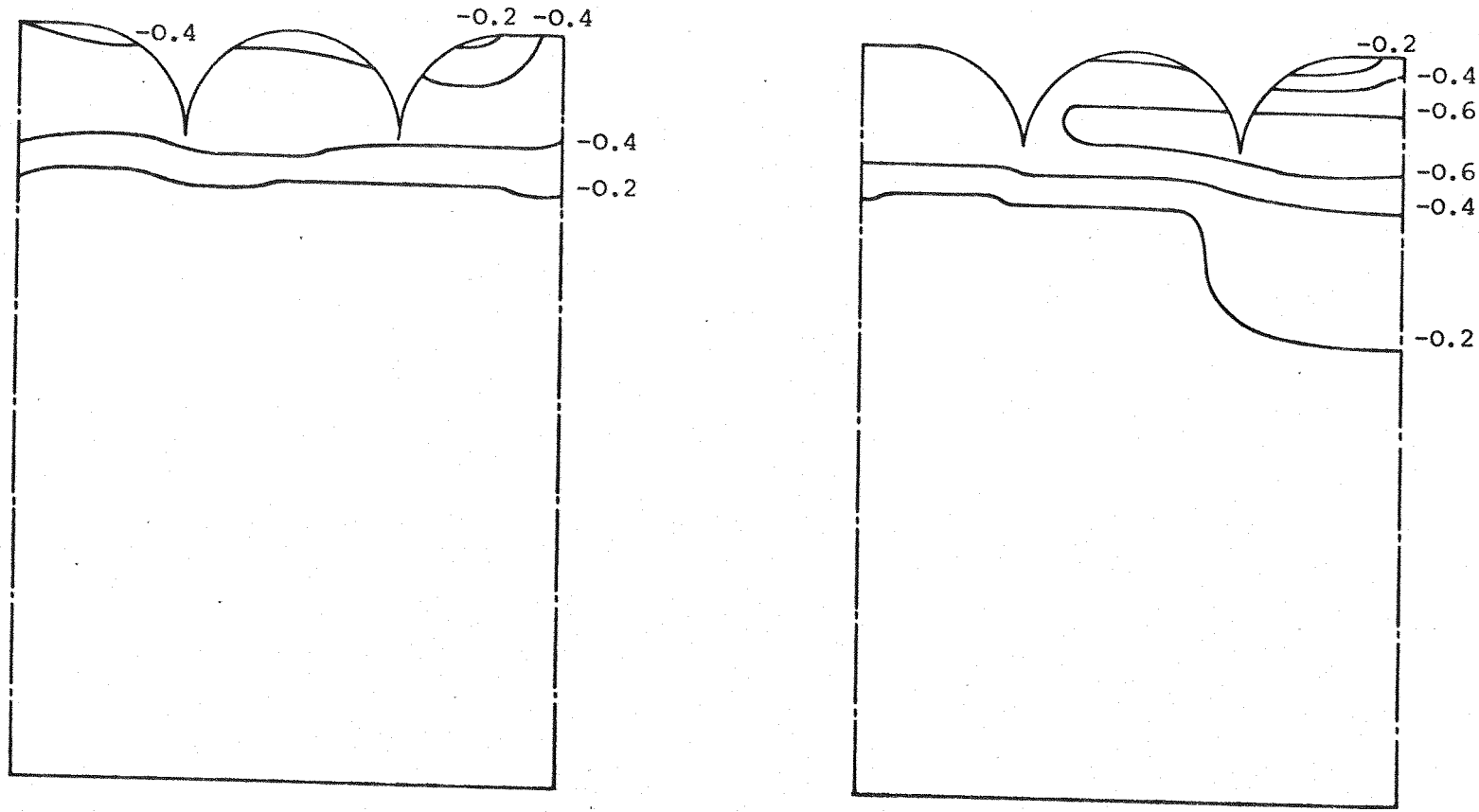

(a) H = 14.5cms

O-O Geometry

Incidence = 0^{o}

(b) H = 4cms

FIGURE 57 BLUFF BODY FOREBODY SURFACE PRESSURE ISOBARS

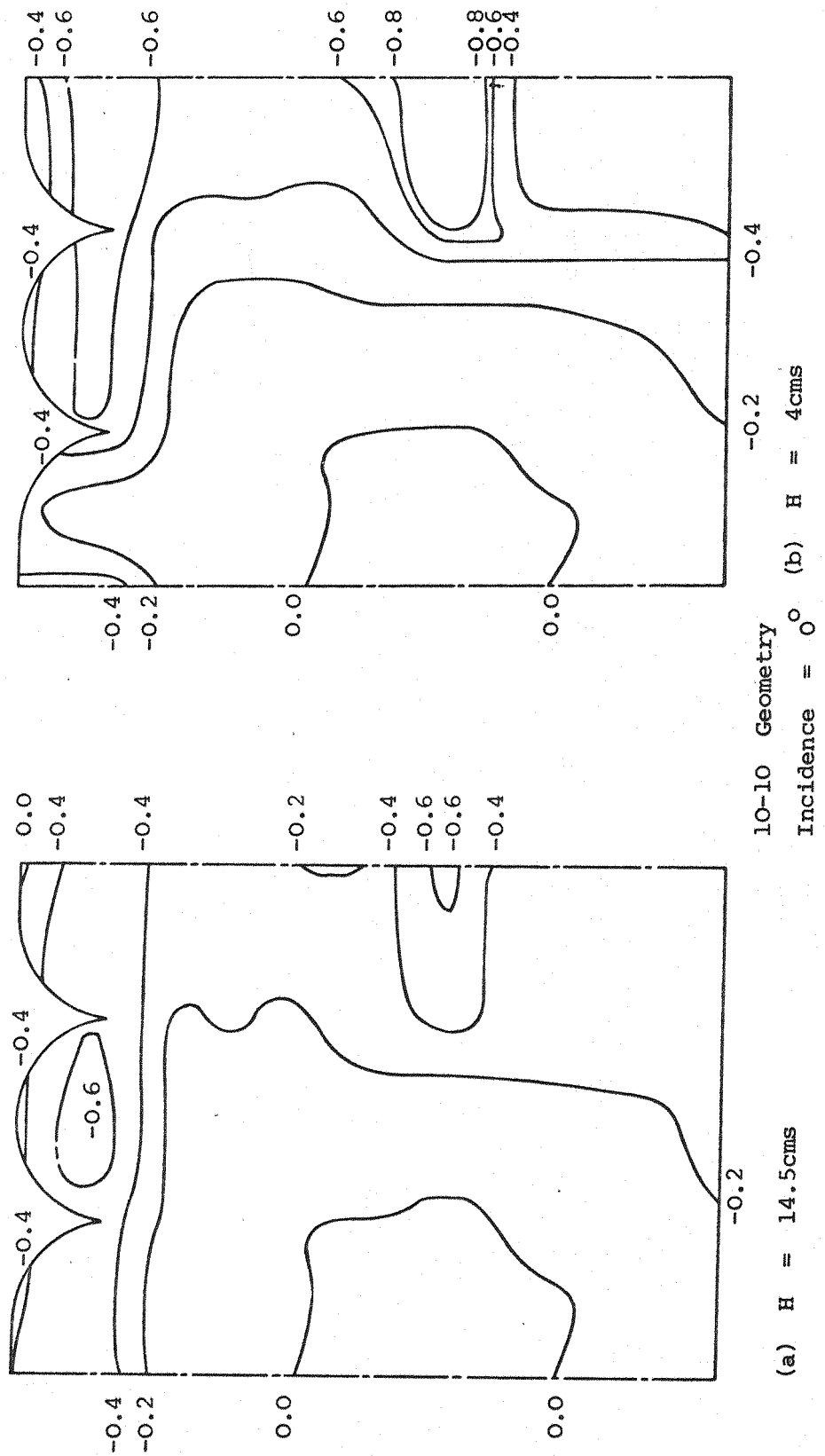

FIGURE 58 BLUFF BODY FOREBODY SURFACE PRESSURE ISOBARS

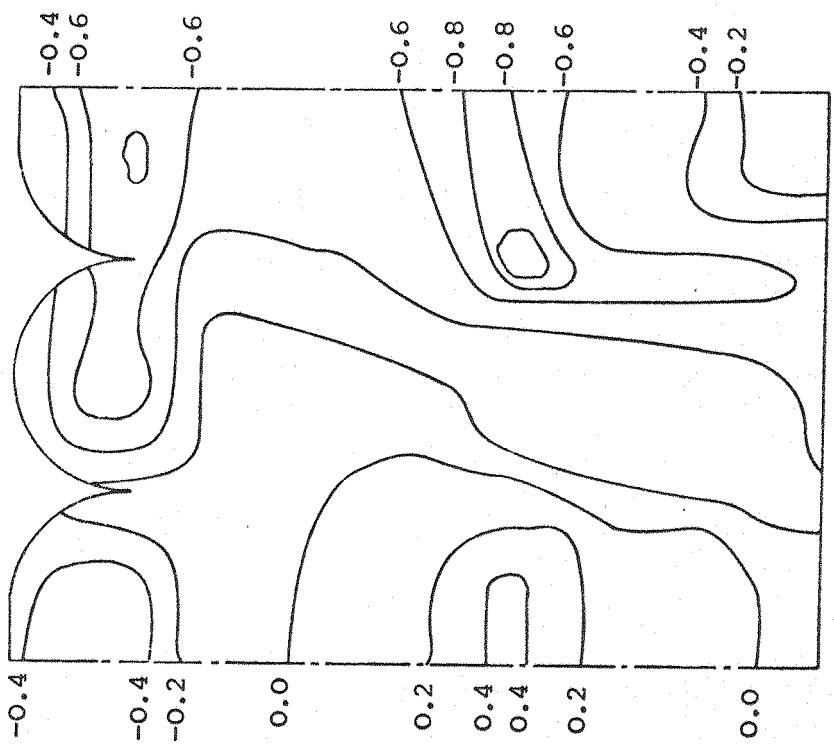

FIGURE 59 BLUFF BODY FOREBODY SURFACE PRESSURE ISOBARS

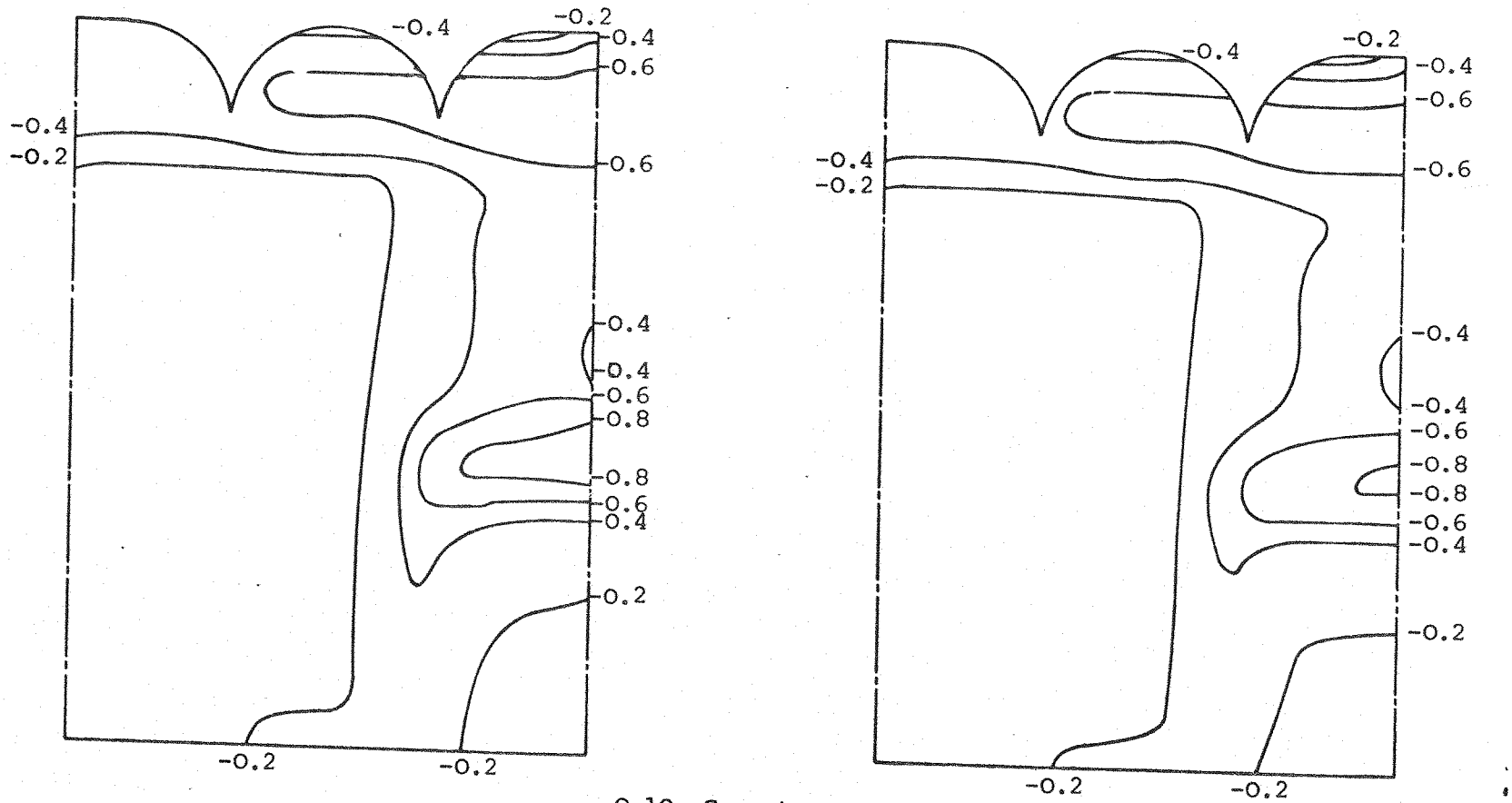

FIGURE 60 BLUFF BODY FOREBODY SURFACE PRESSURE ISOBARS

FIGURE 61 BLUFF BODY FOREBODY PRESSURE ISOBARS

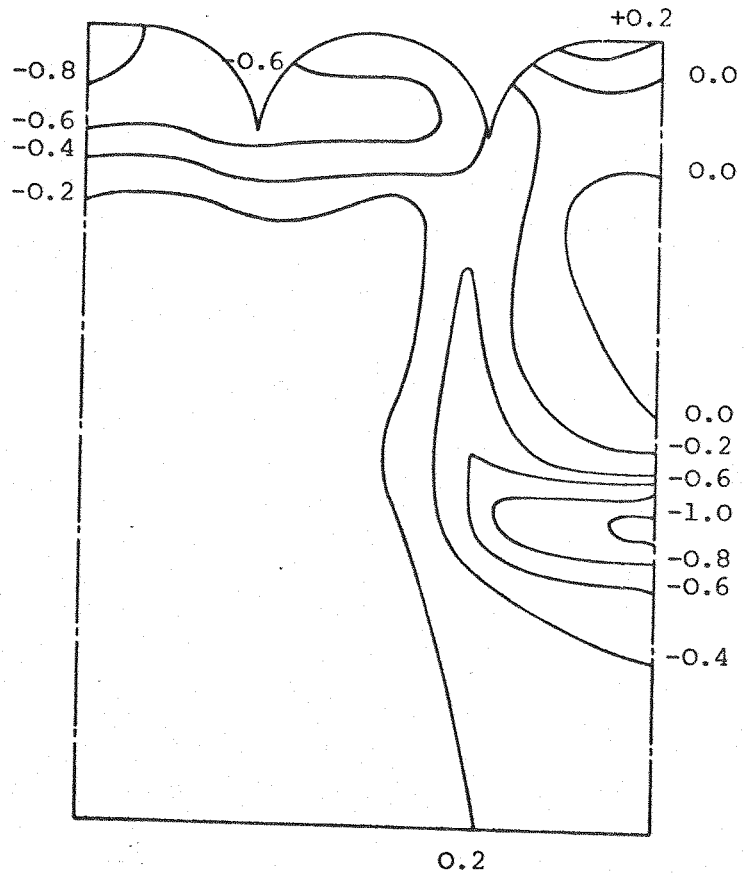

(a) Belt Moving

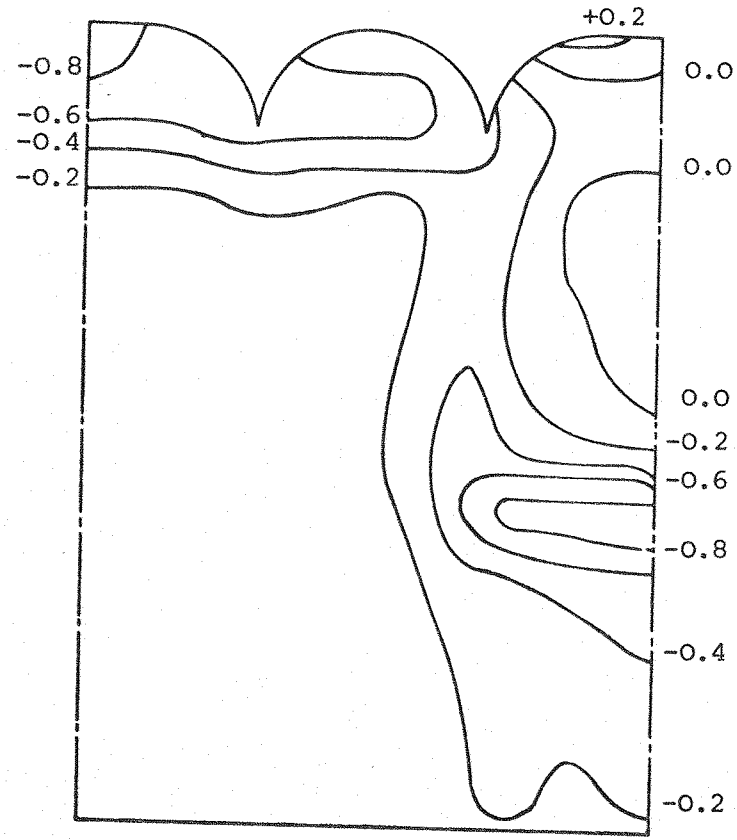

(b) Belt Stationary

O-10 Geometry

Incidence = $+9^{\circ}$

H = 4cms

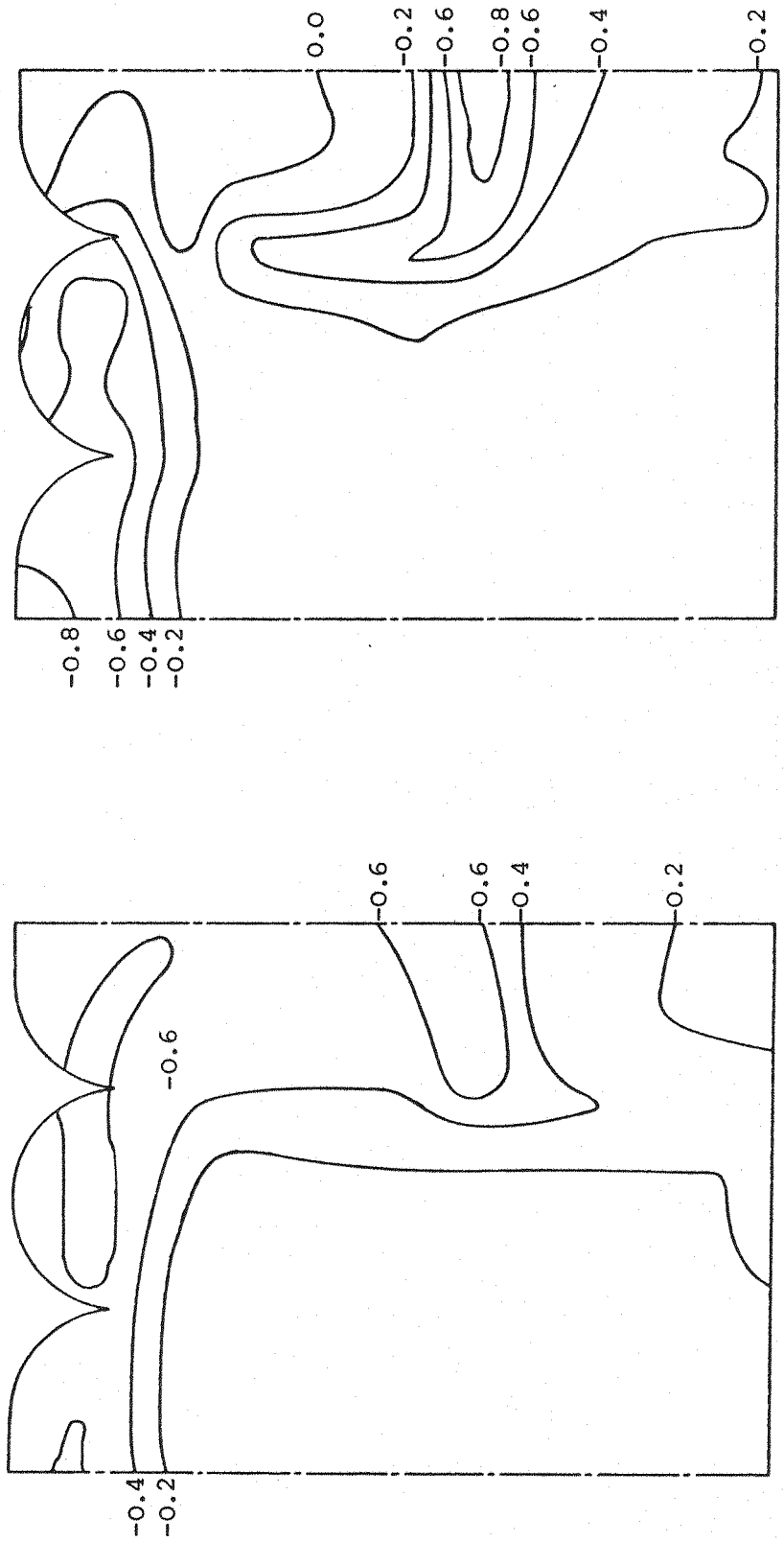

FIGURE 62 BLUFF BODY FOREBODY SURFACE PRESSURE ISOBARS

FIGURE 63 BLUFF BODY FOREBODY SURFACE PRESSURE ISOBARS

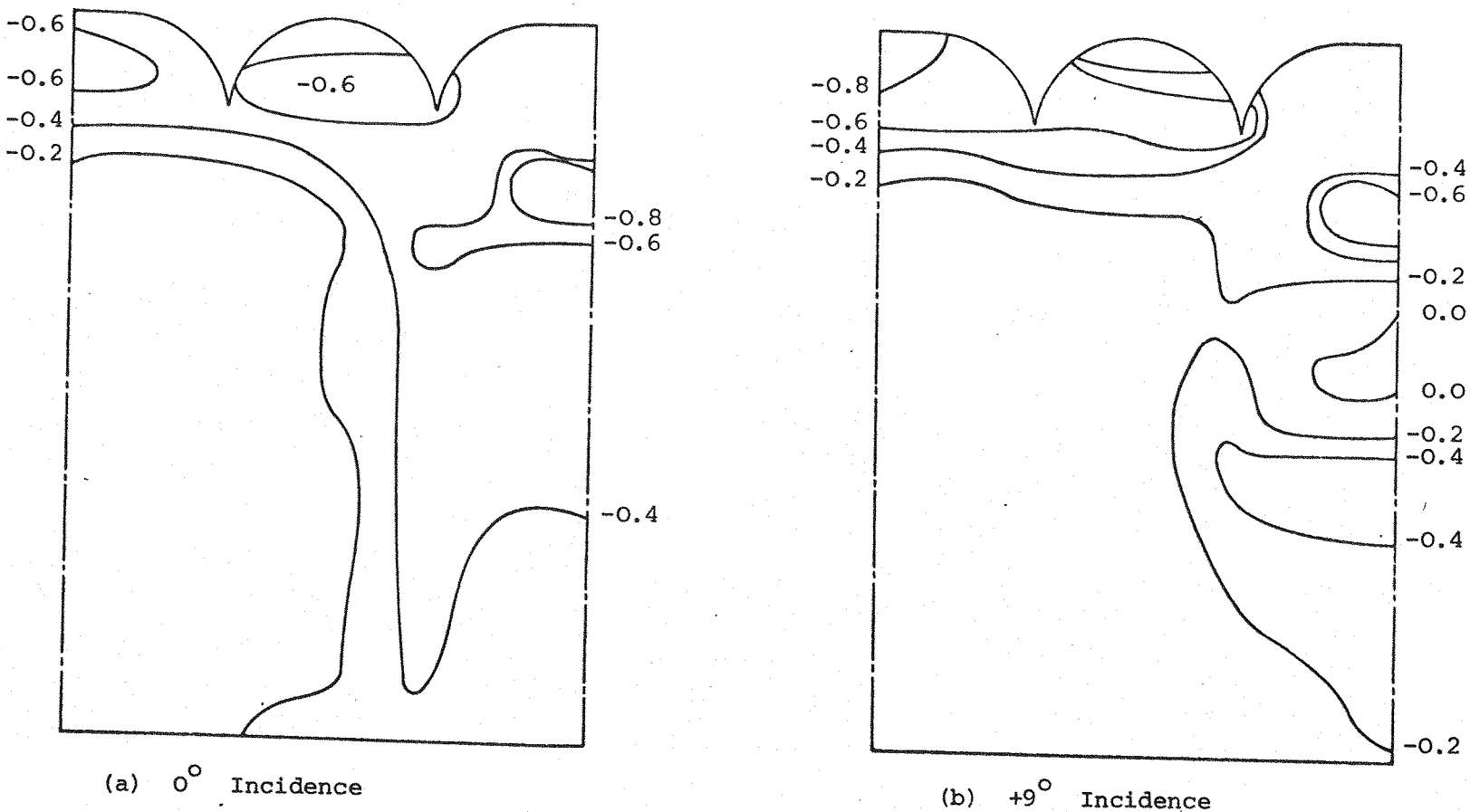

(a) 0° Incidence

(b) $+9^{\circ}$ Incidence

0-10 Geometry

Plus Distributed Roughness
and Airdam

H = 4cms

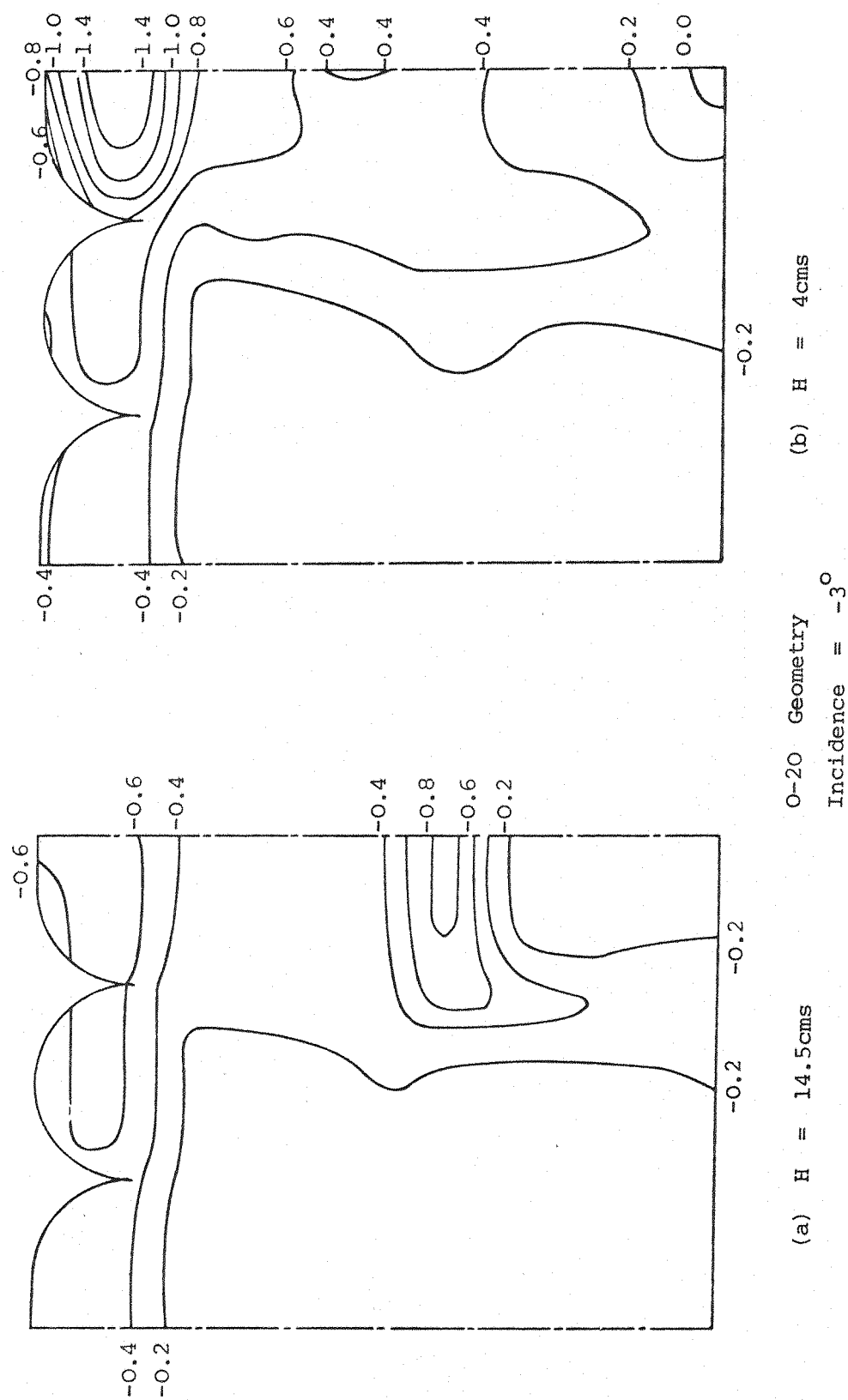

FIGURE 64 BLUFF BODY FOREBODY SURFACE PRESSURE ISOBARS

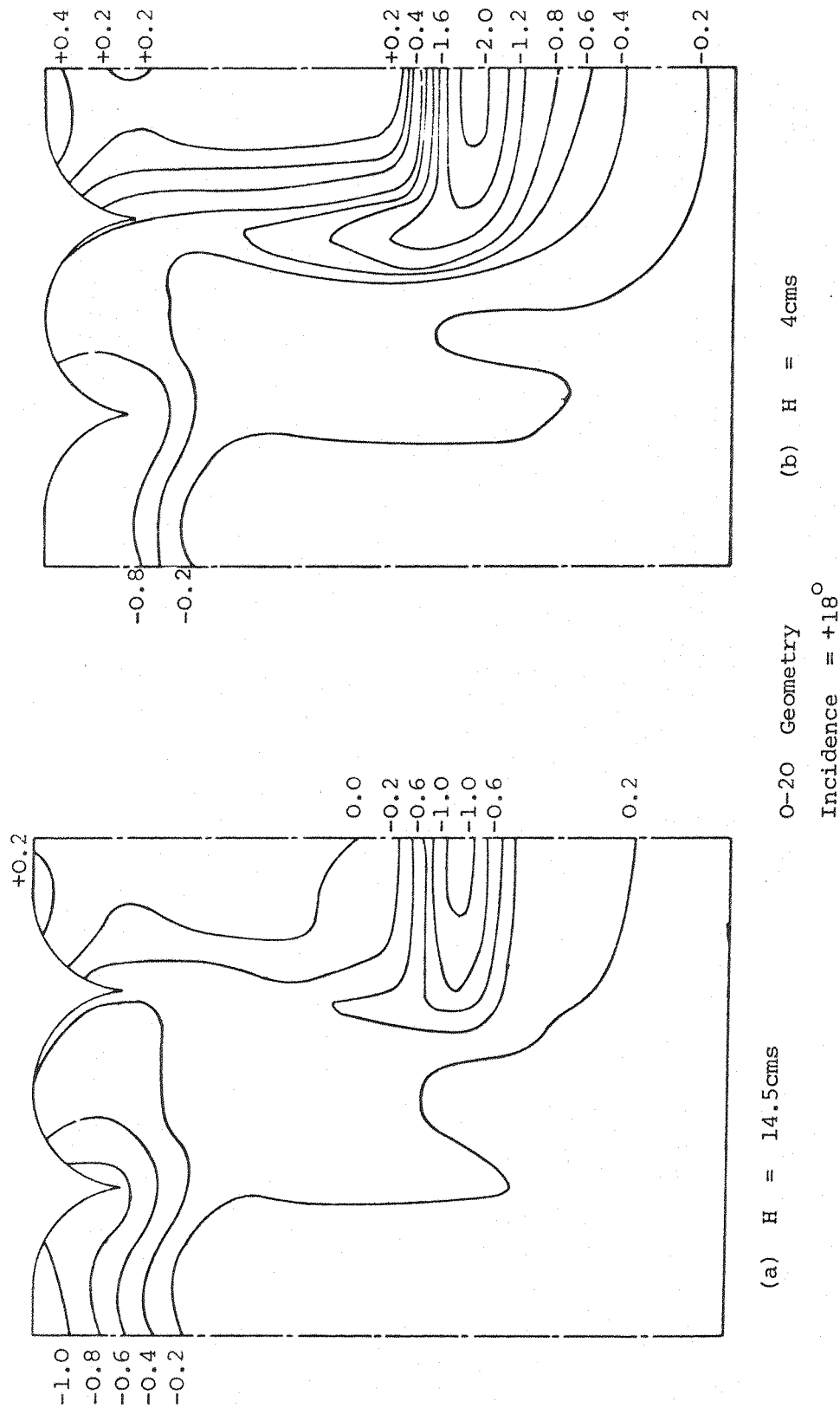

FIGURE 65 BLUFF BODY FOREBODY SURFACE PRESSURE ISOBARS

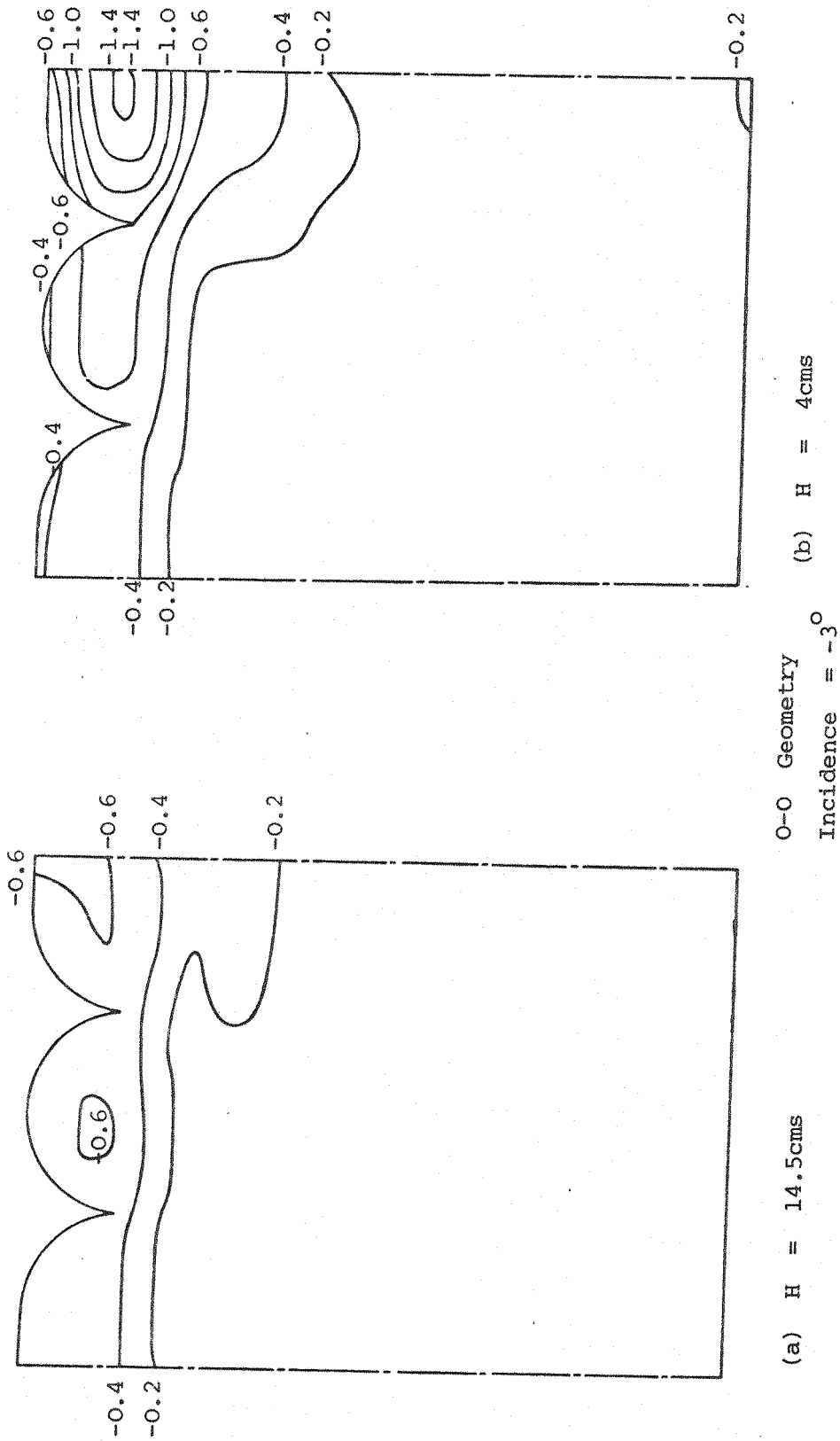

FIGURE 66 BLUFF BODY FOREBODY SURFACE PRESSURE ISOBARS

FIGURE 67 BLUFF BODY FOREBODY SURFACE PRESSURE ISOBARS

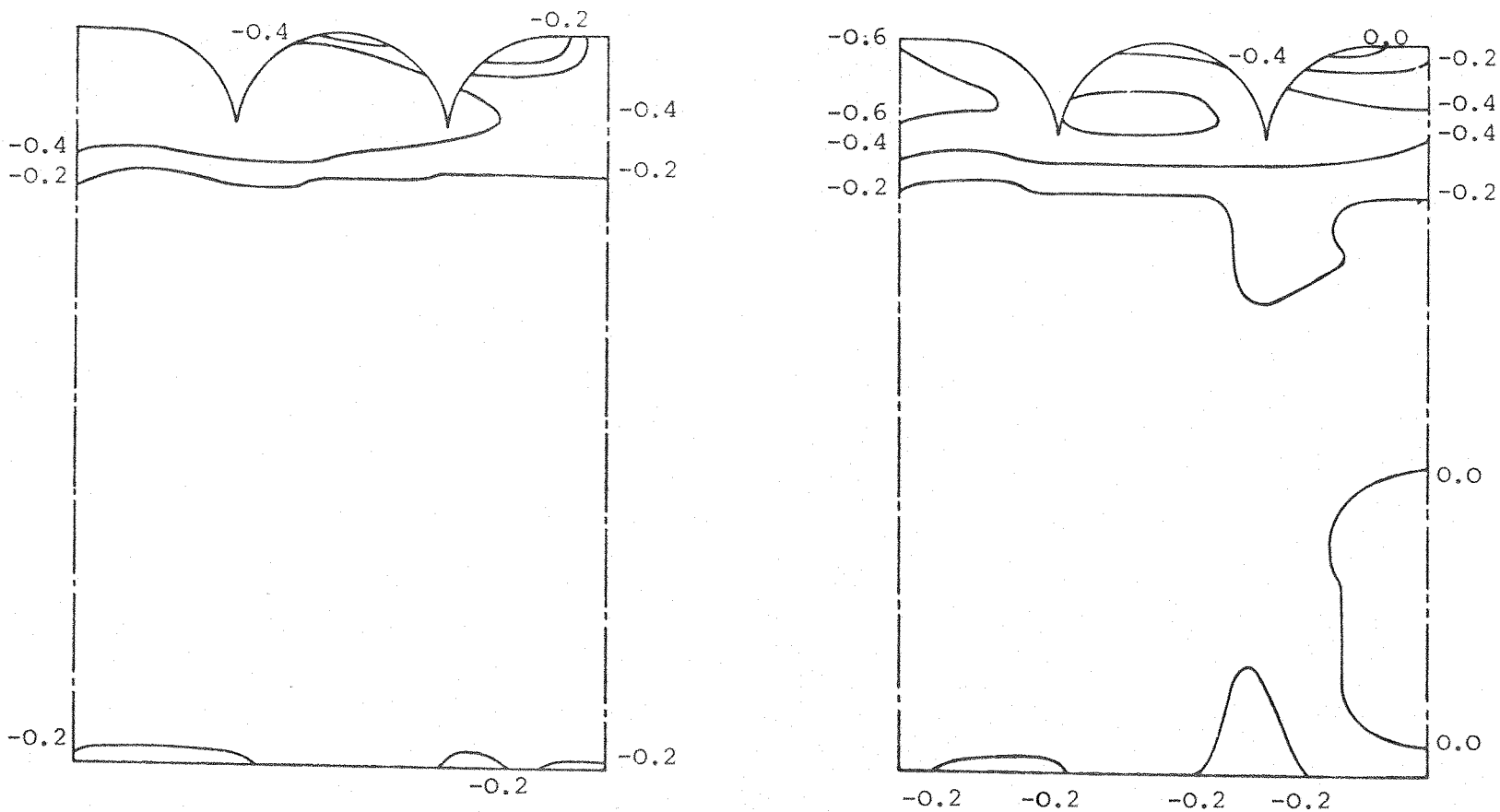

(a) H = 14.5cms

O-O Geometry

Incidence = $+2^{o}$

(b) H = 4cms

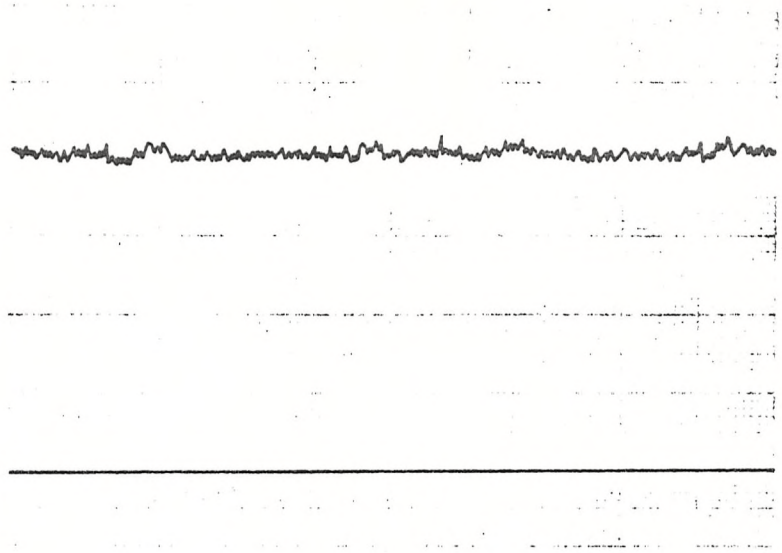

(a) Knee Position
O-20 Geometry
20^{o} Incidence

(b) Base Position
20-20 Geometry
o^{o} Incidence

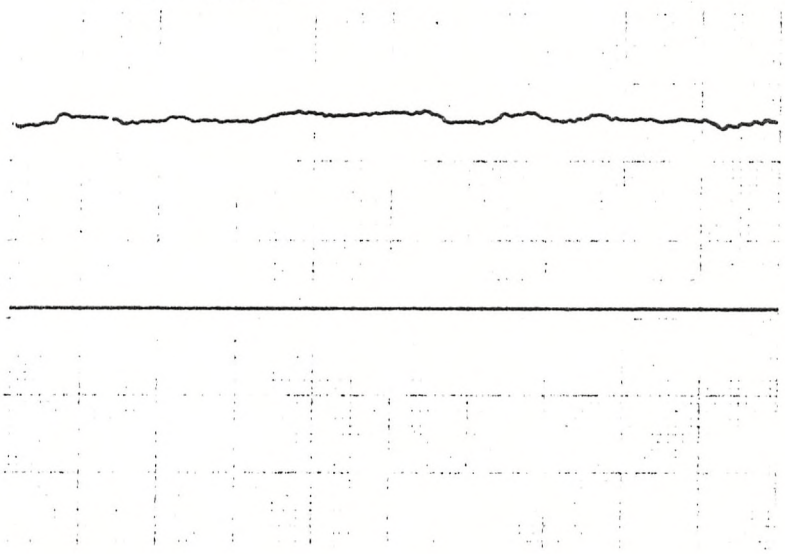

Horiz. Scale = 20cm/sec.
Vert. Scale = 0.05 V/cm

FIGURE 68 TIME DEPENDANT PRESSURE TRACES

FIGURE 69 BASE SURFACE PRESSURE ISOBARS

FIGURE 69 BASE SURFACE PRESSURE ISOBARS

FIGURE 70 BASE SURFACE PRESSURE ISOBARS

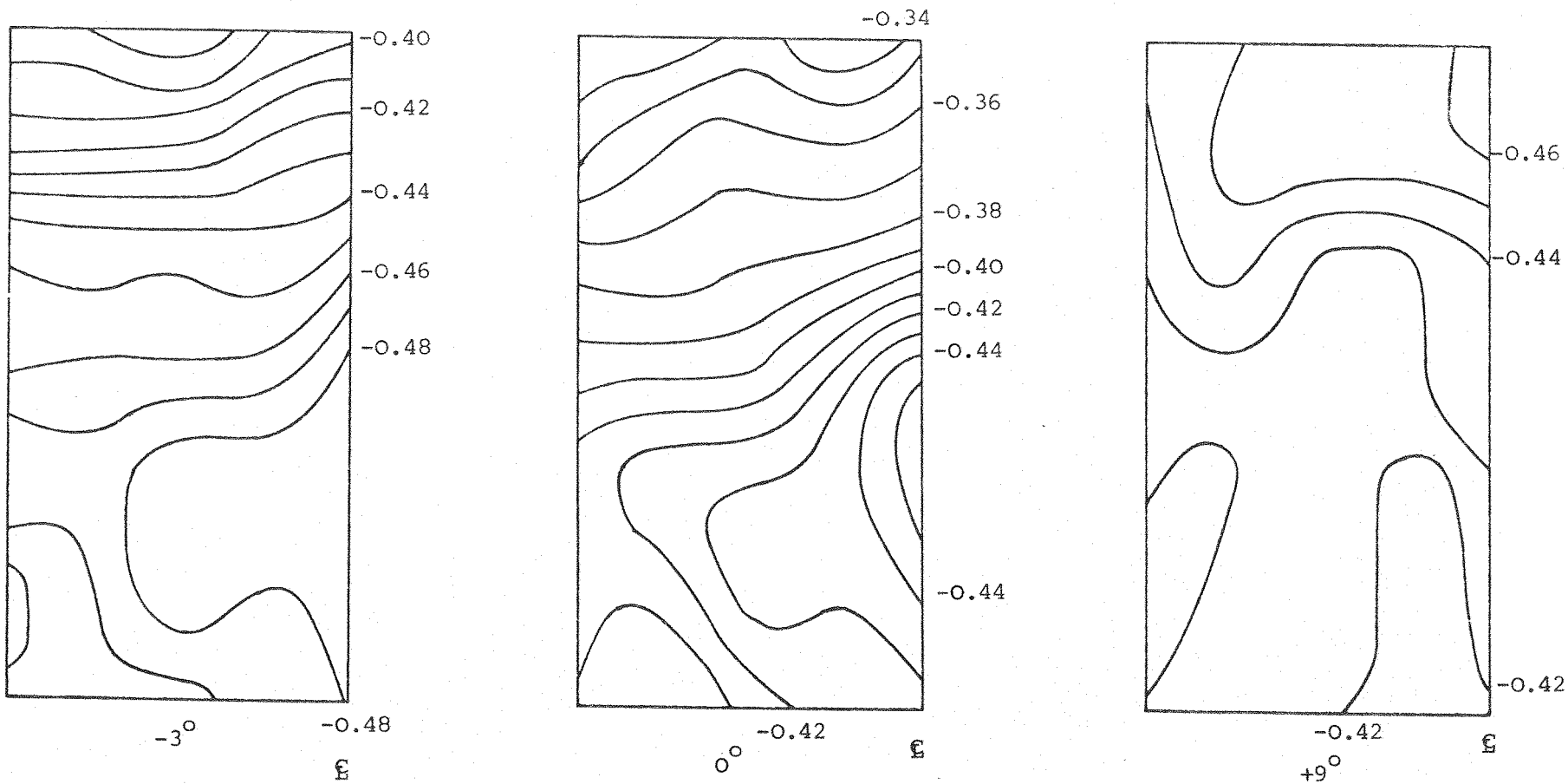

20-0 GEOMETRY

H = 14.5cm

(a) (b) (c)

FIGURE 71 BASE SURFACE PRESSURE ISOBARS

FIGURE 72 BASE SURFACE PRESSURE ISOBARS

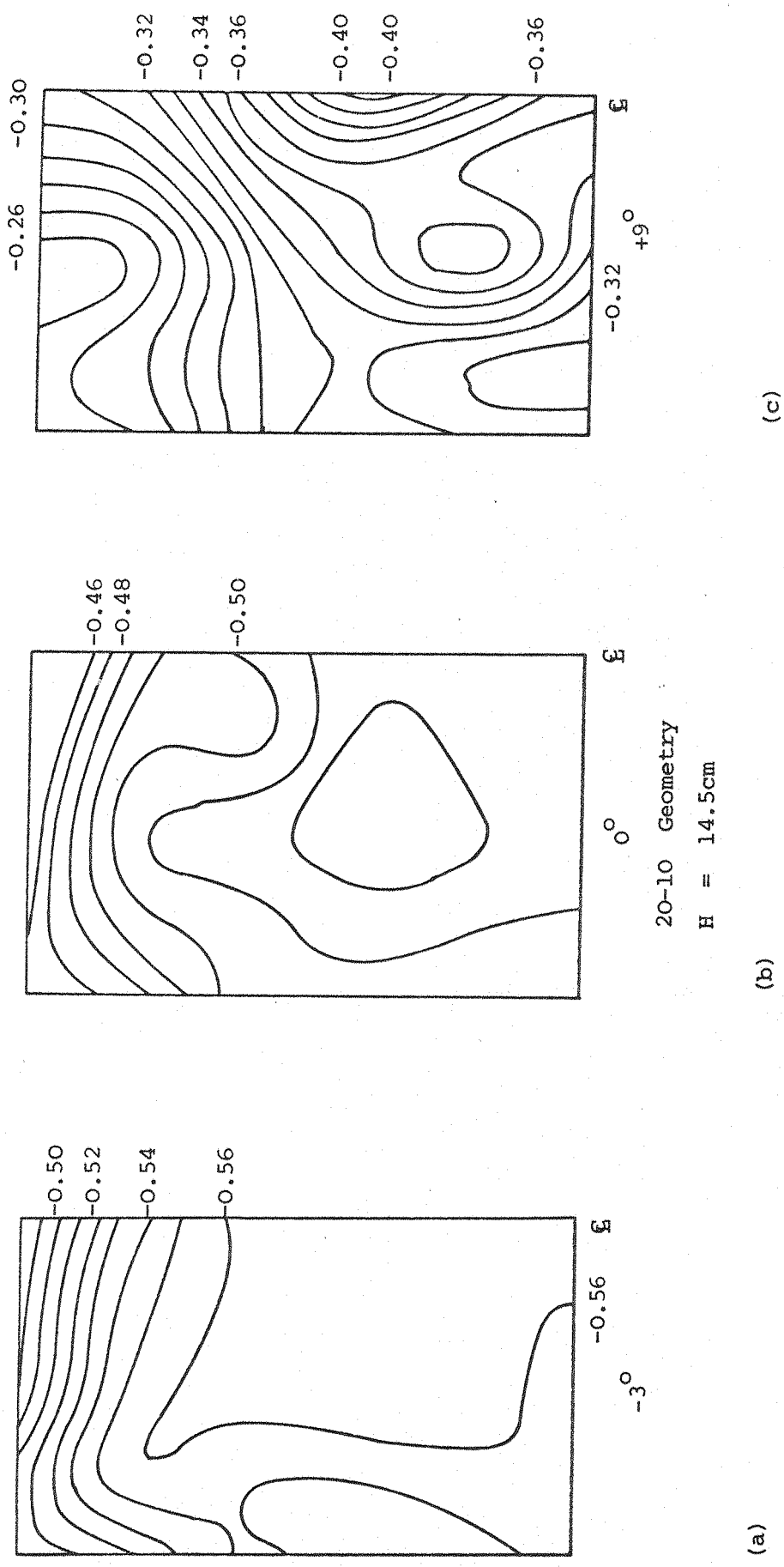

FIGURE 73 BASE SURFACE PRESSURE ISOBARS

FIGURE 74 BASE SURFACE PRESSURE ISOBARS

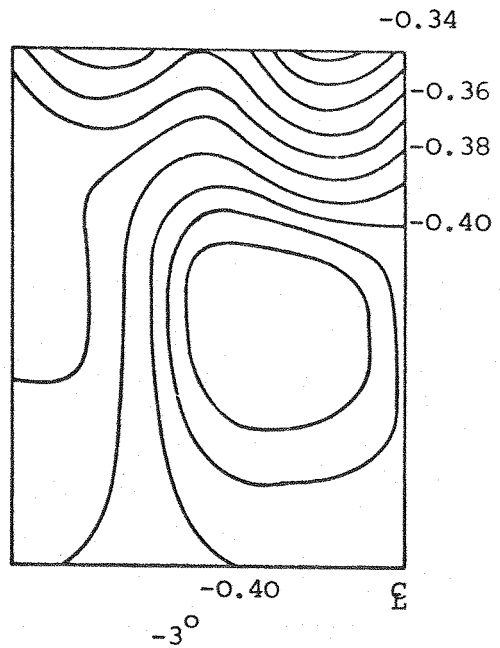

(a)

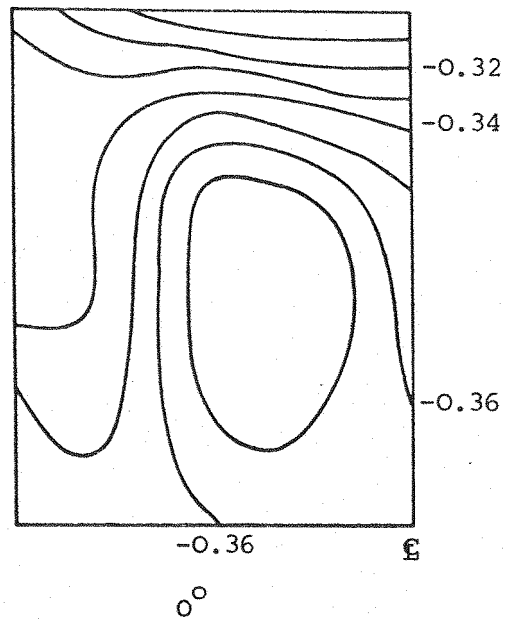

10-10 Geometry

H = 14.5cm

(b)

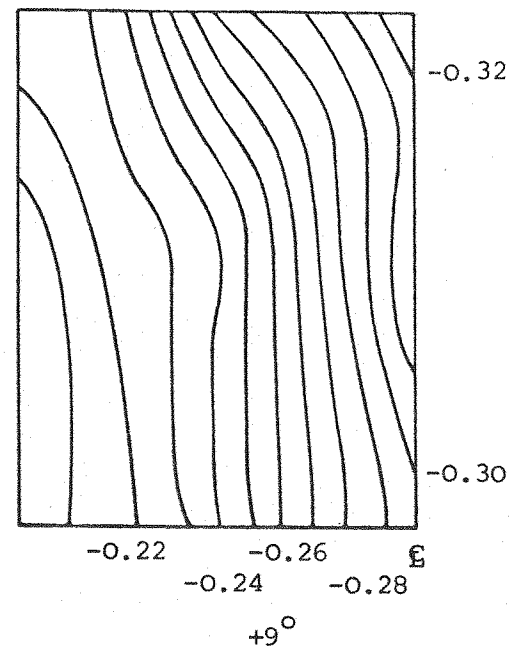

(c)

FIGURE 75 BASE SURFACE PRESSURE ISOBARS

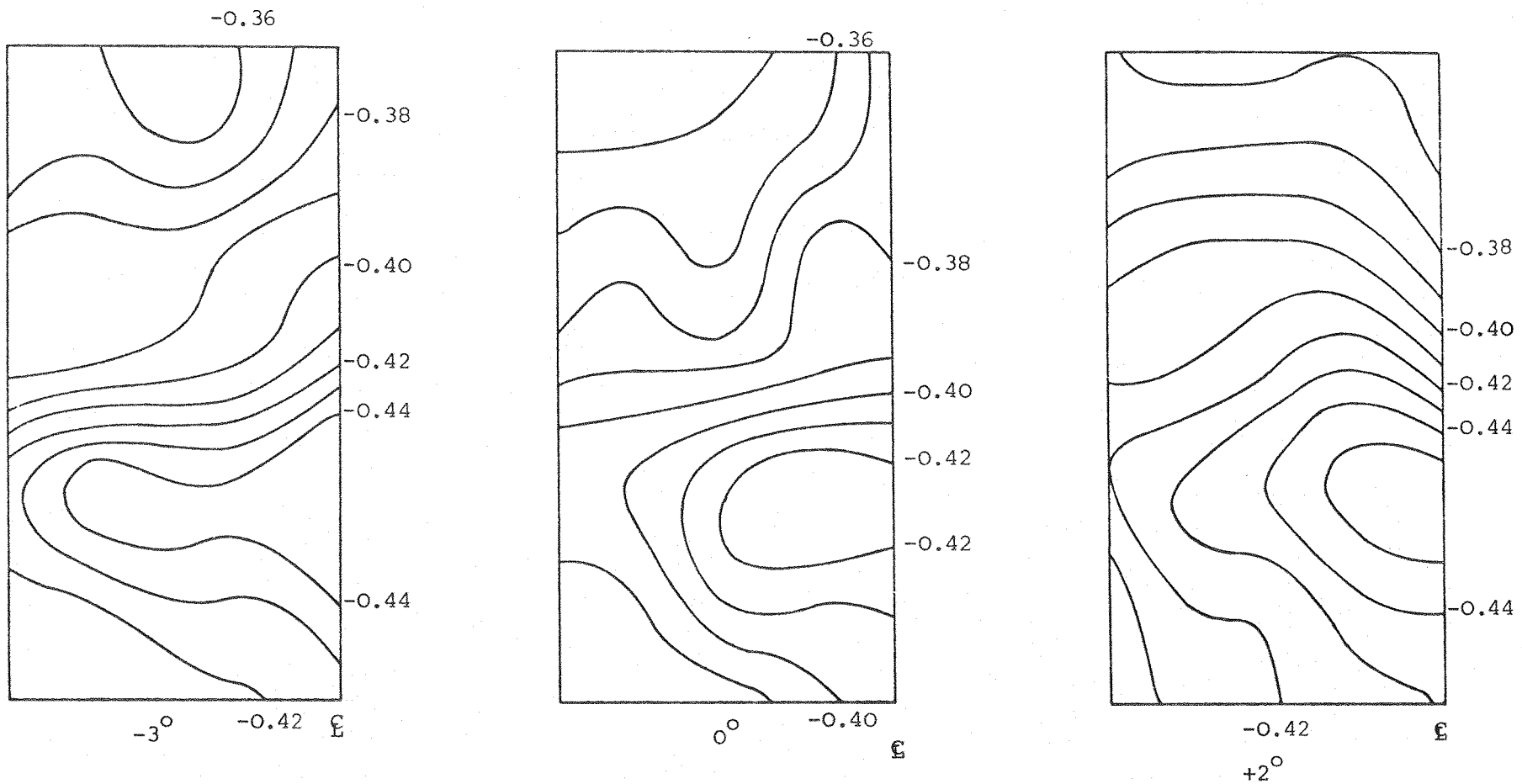

FIGURE 76 BASE SURFACE PRESSURE ISOBARS

FIGURE 77 BASE SURFACE PRESSURE ISOBARS

FIGURE 78 BASE SURFACE PRESSURE ISOBARS

FIGURE 79 BASE SURFACE PRESSURE ISOBARS

FIGURE 80 BASE SURFACE PRESSURE ISOBARS

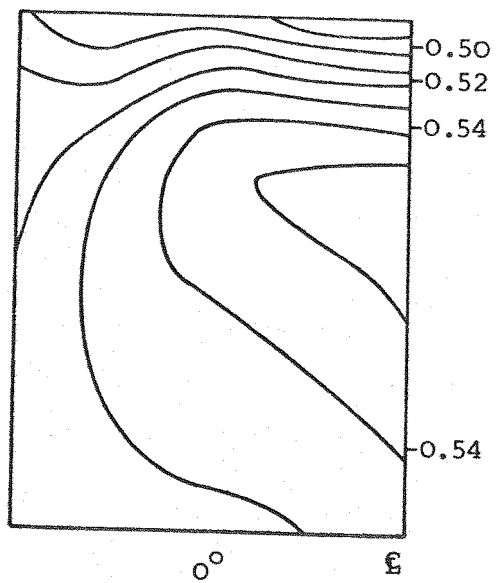

(a)

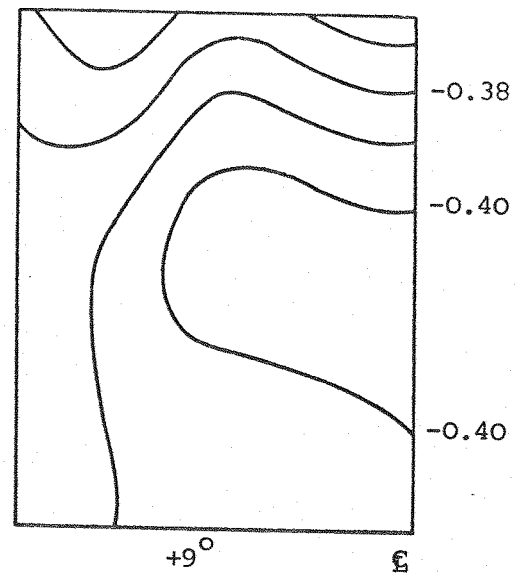

20-20 Geometry

H = 4cm

(b)

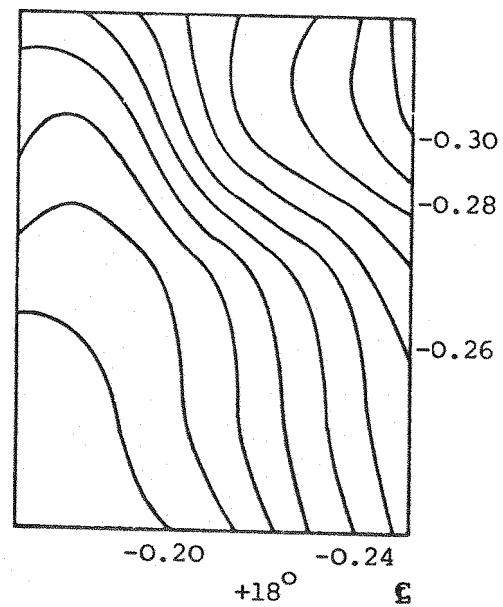

(c)

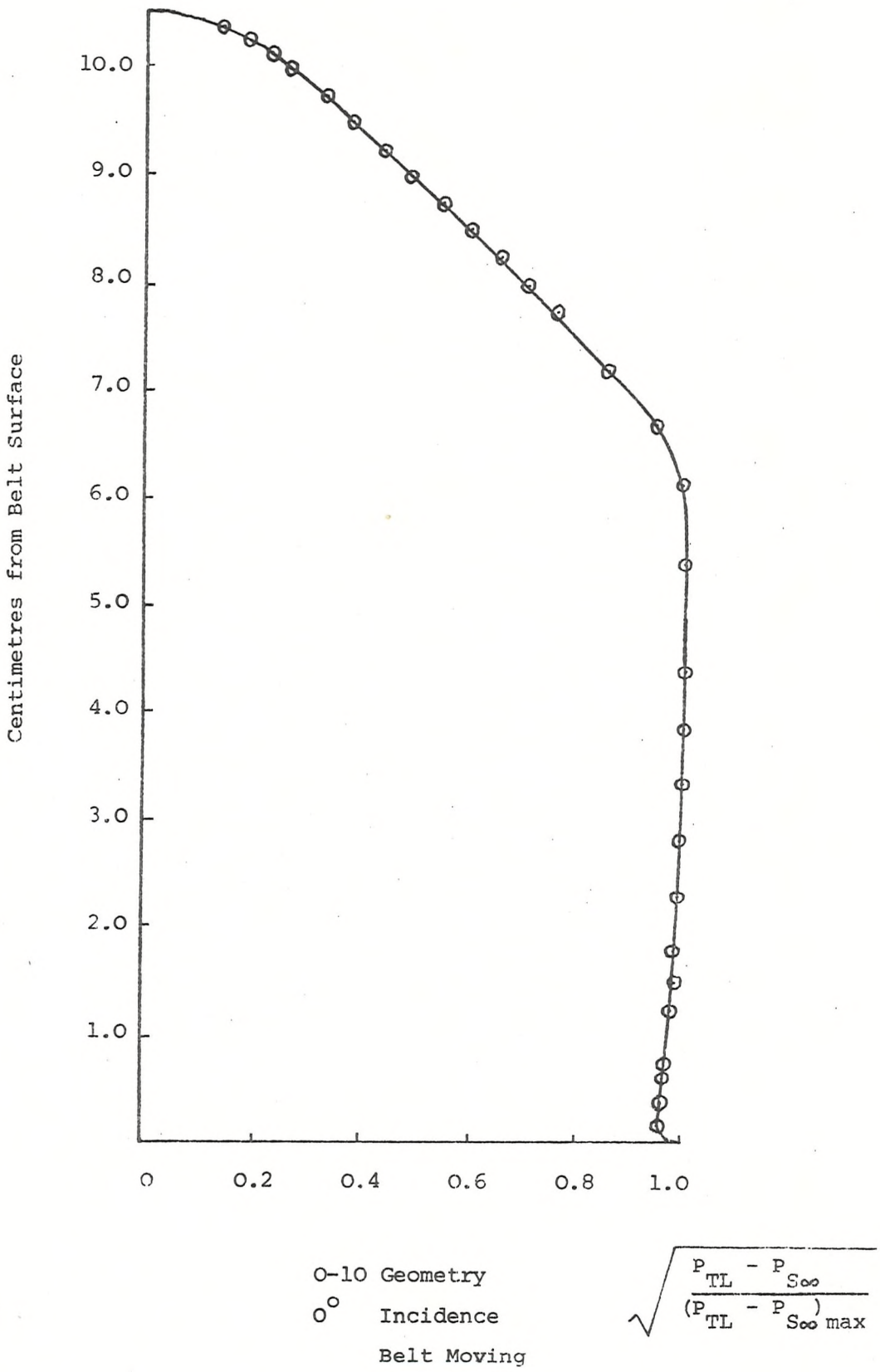

FIGURE 81 VERTICAL TOTAL PRESSURE TRAVERSE UNDER BODY

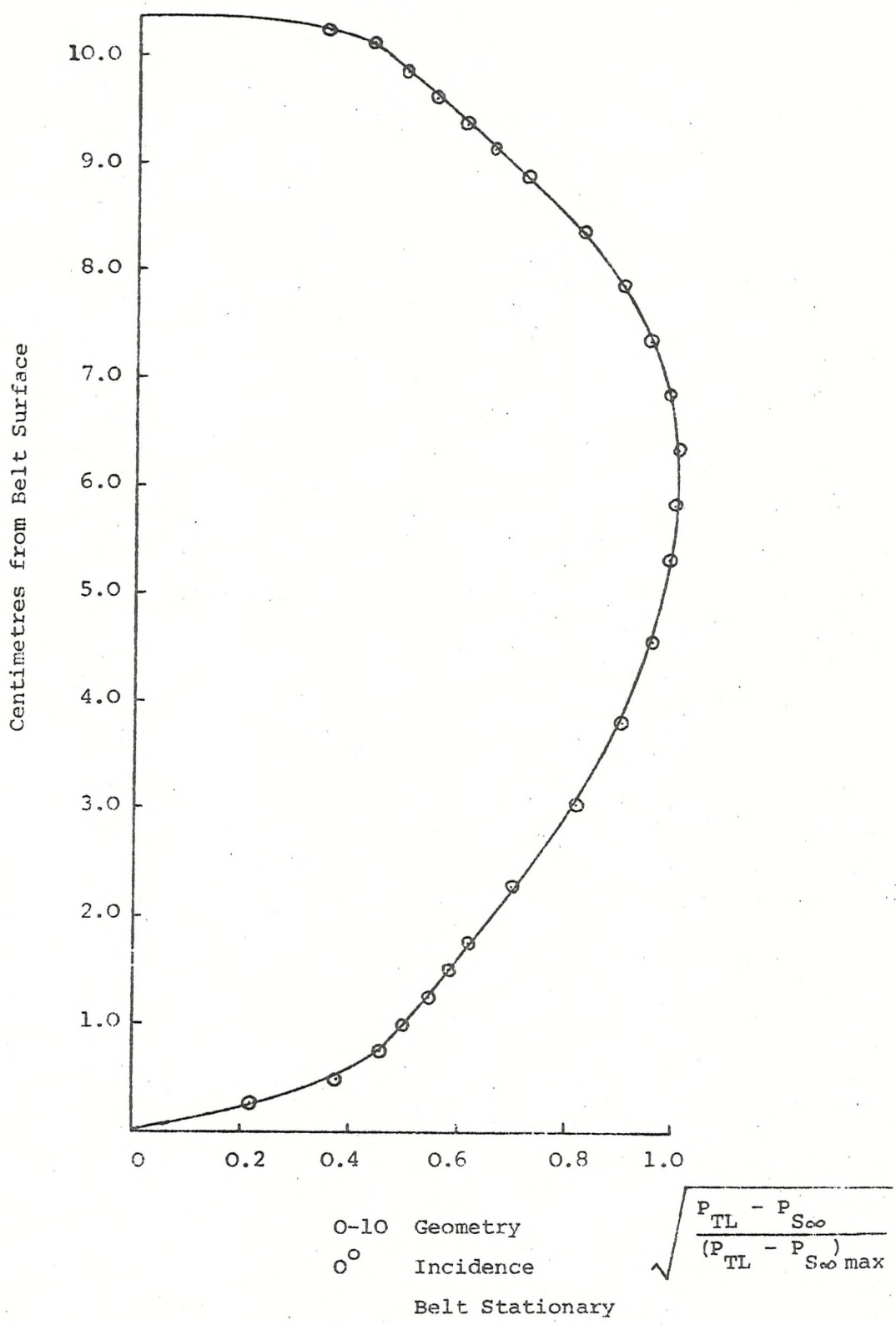

FIGURE 82 VETICAL TOTAL PRESSURE TRAVERSE UNDER BODY

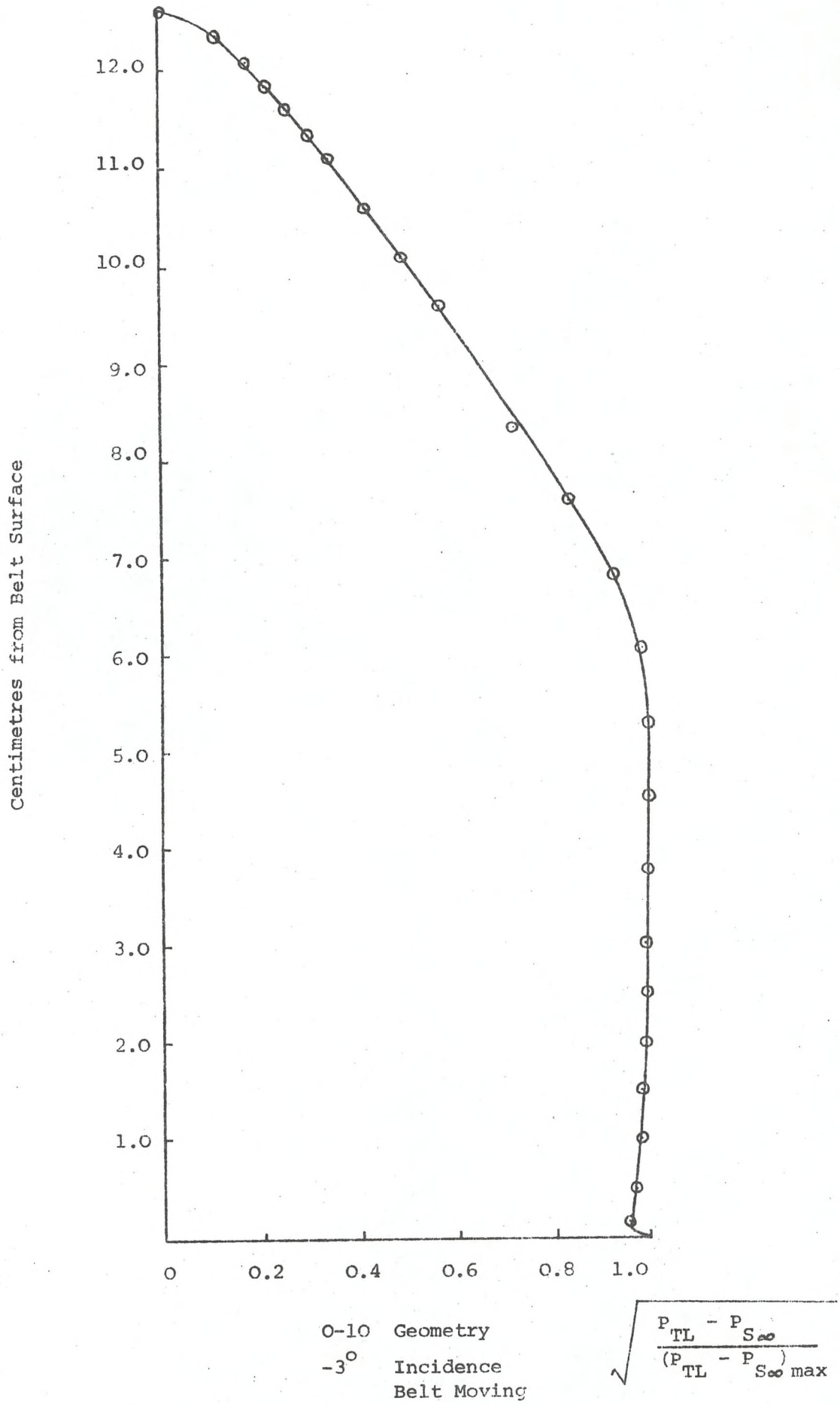

FIGURE 83 VERTICAL TOTAL PRESSURE TRAVERSE UNDER BODY

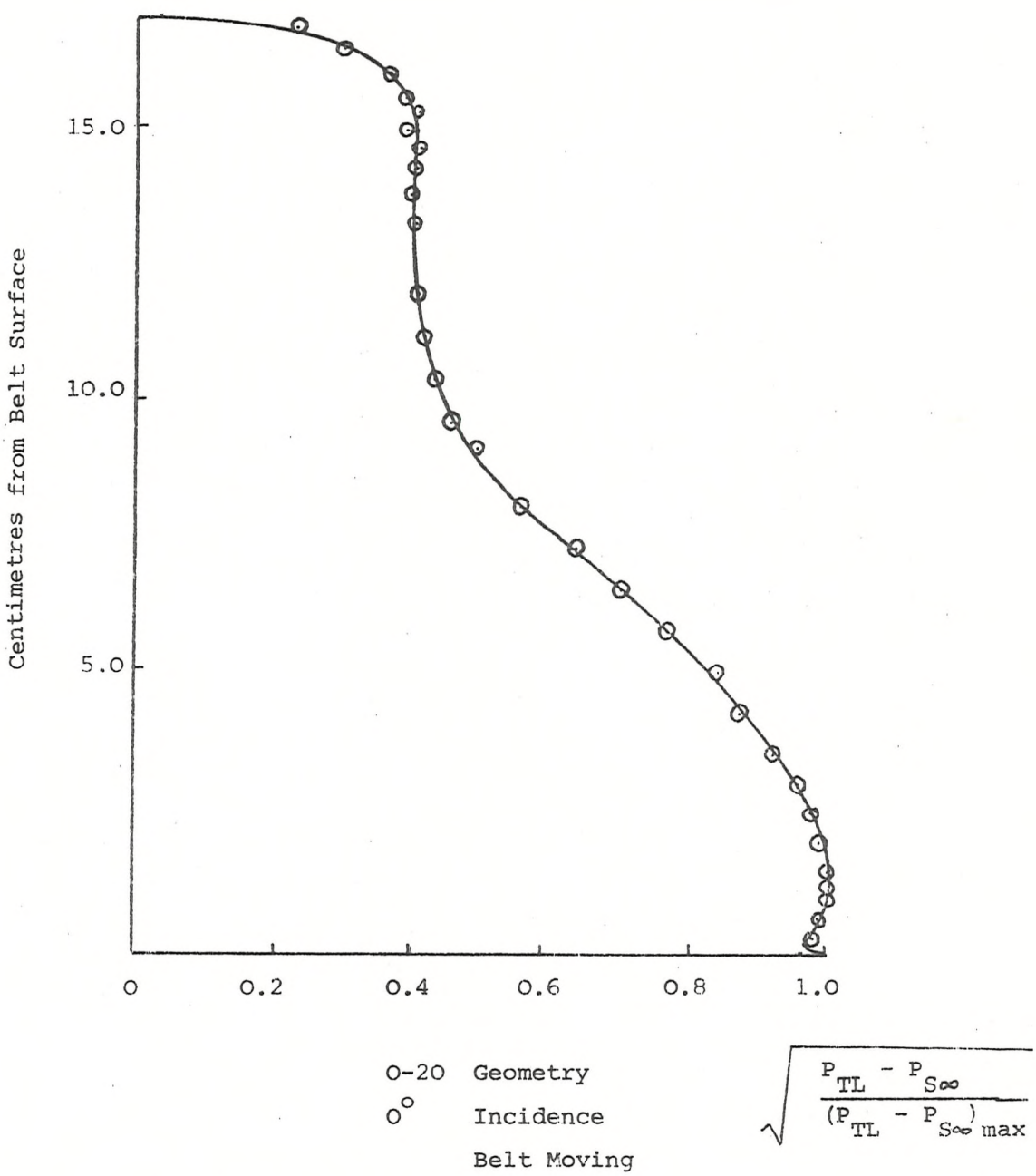

FIGURE 84 VERTICAL TOTAL PRESSURE TRAVERSE UNDER BODY

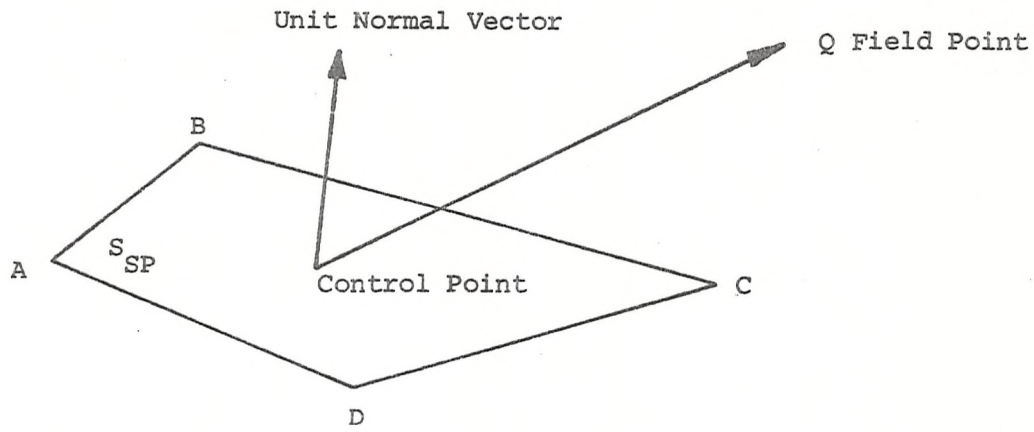

Source Panel

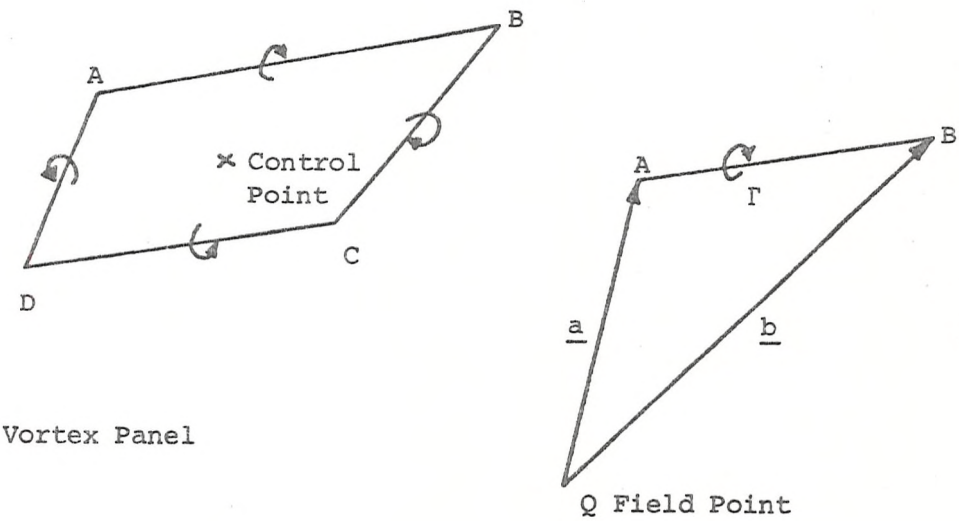

Vortex Panel

FIGURE 85 SOURCE AND VORTEX PANEL NOTATION

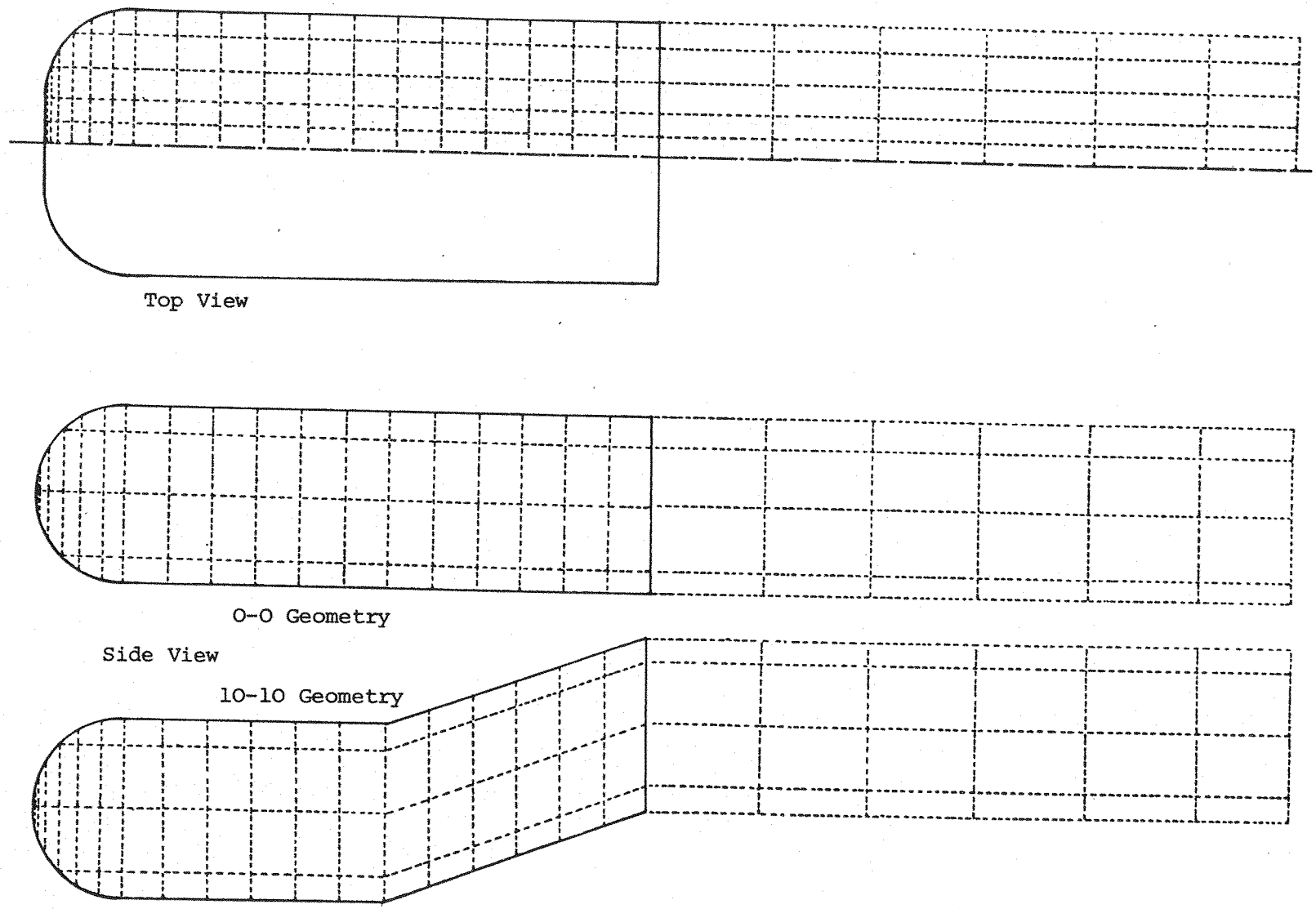

FIGURE 86 DISTRIBUTION OF SURFACE PANELS

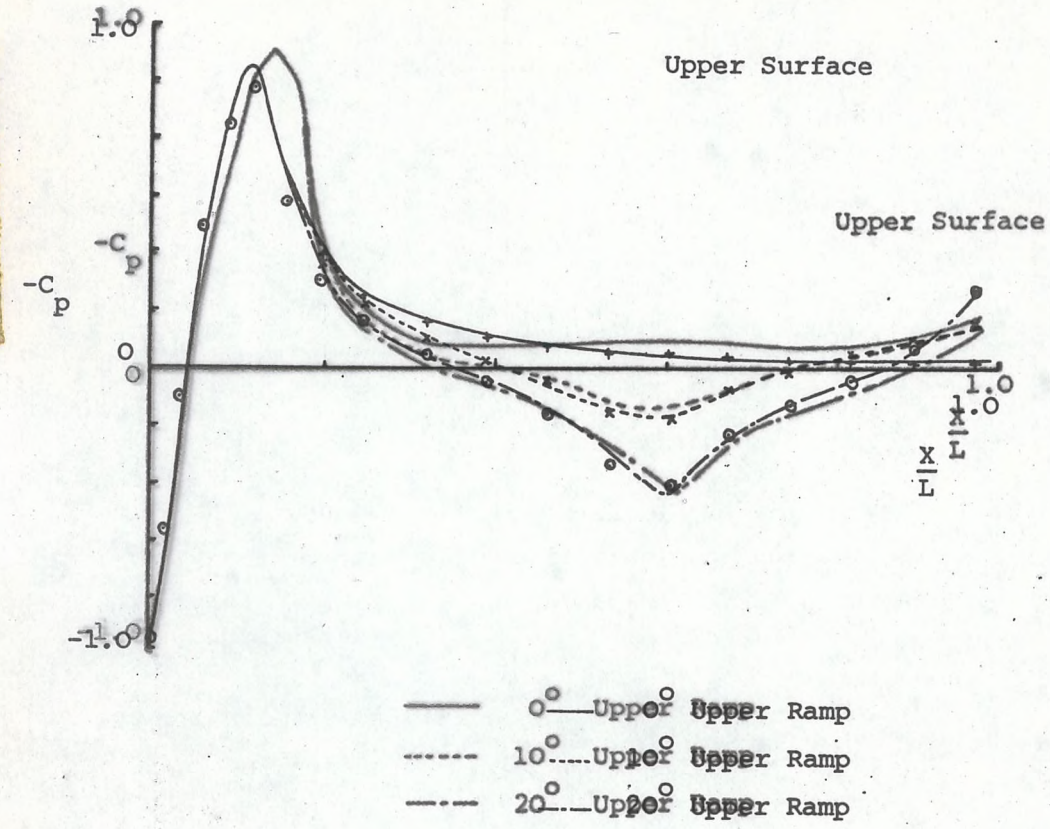

EXPERIMENTAL RESULTS

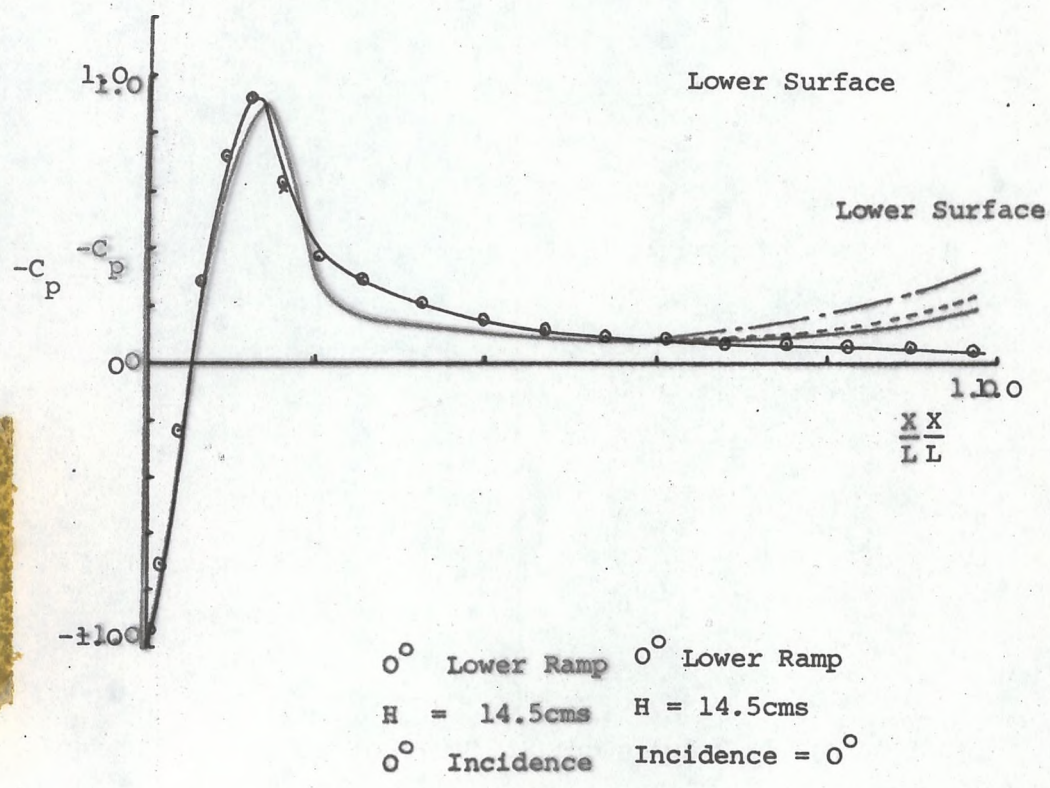

FIGURE 87a BLUFF BODY THEORETICAL CENTRE LINE SURFACE PRESSURE DISTRIBUTIONS

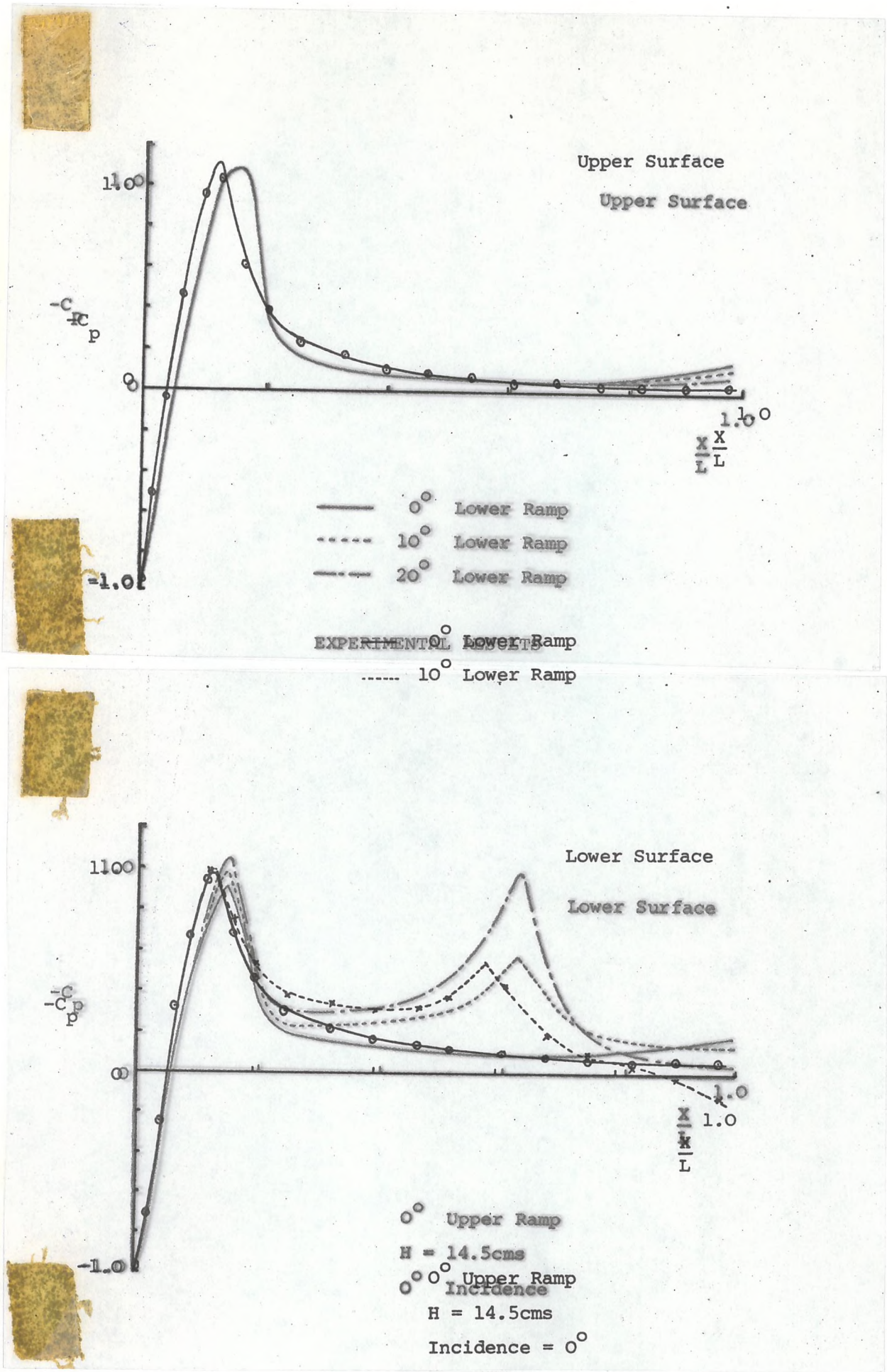

FIGURE 87b BLUFF BODY THEORETICAL CENTRE LINE SURFACE PRESSURE DISTRIBUTIONS

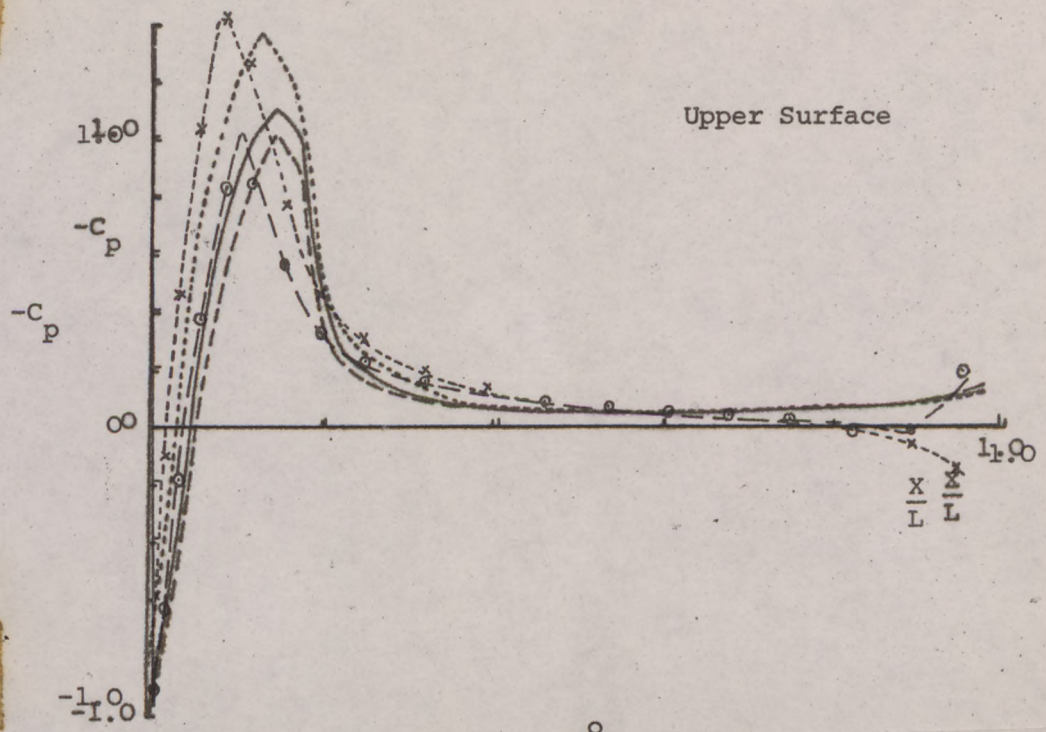

—— —— -3° Incidence
— — — -3° Incidence
—·—·— +9° Incidence
——— 0° Incidence
------ +9° Incidence

EXPERIMENTAL RESULTS

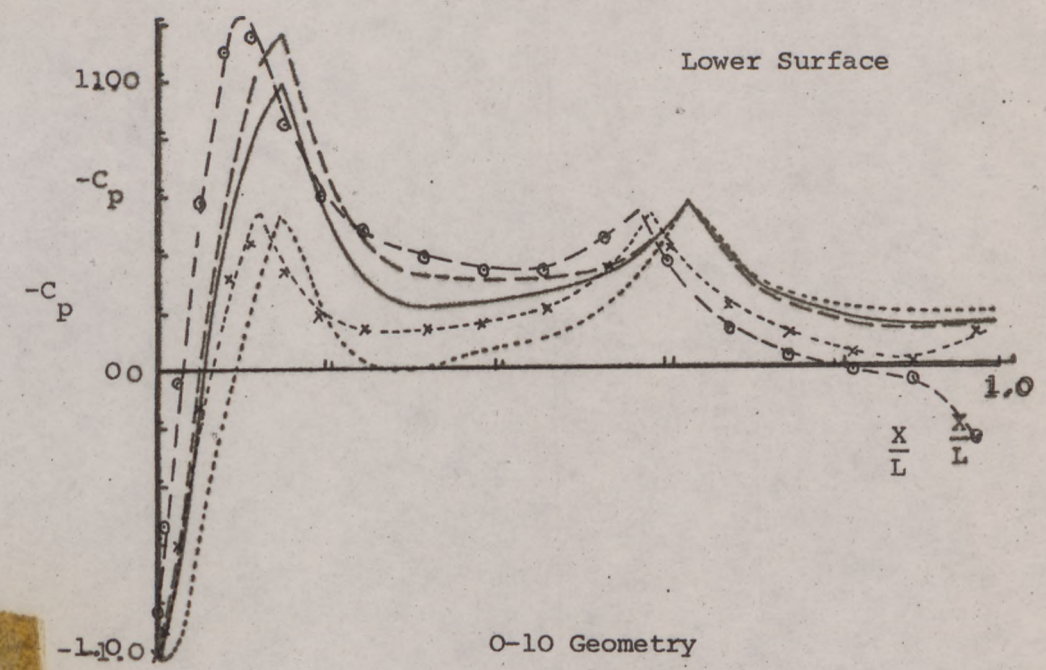

0-10 Geometry

H = 14.5cms

FIGURE 87c BLUFF BODY THEORETICAL CENTRE LINE SURFACE PRESSURE DISTRIBUTIONS

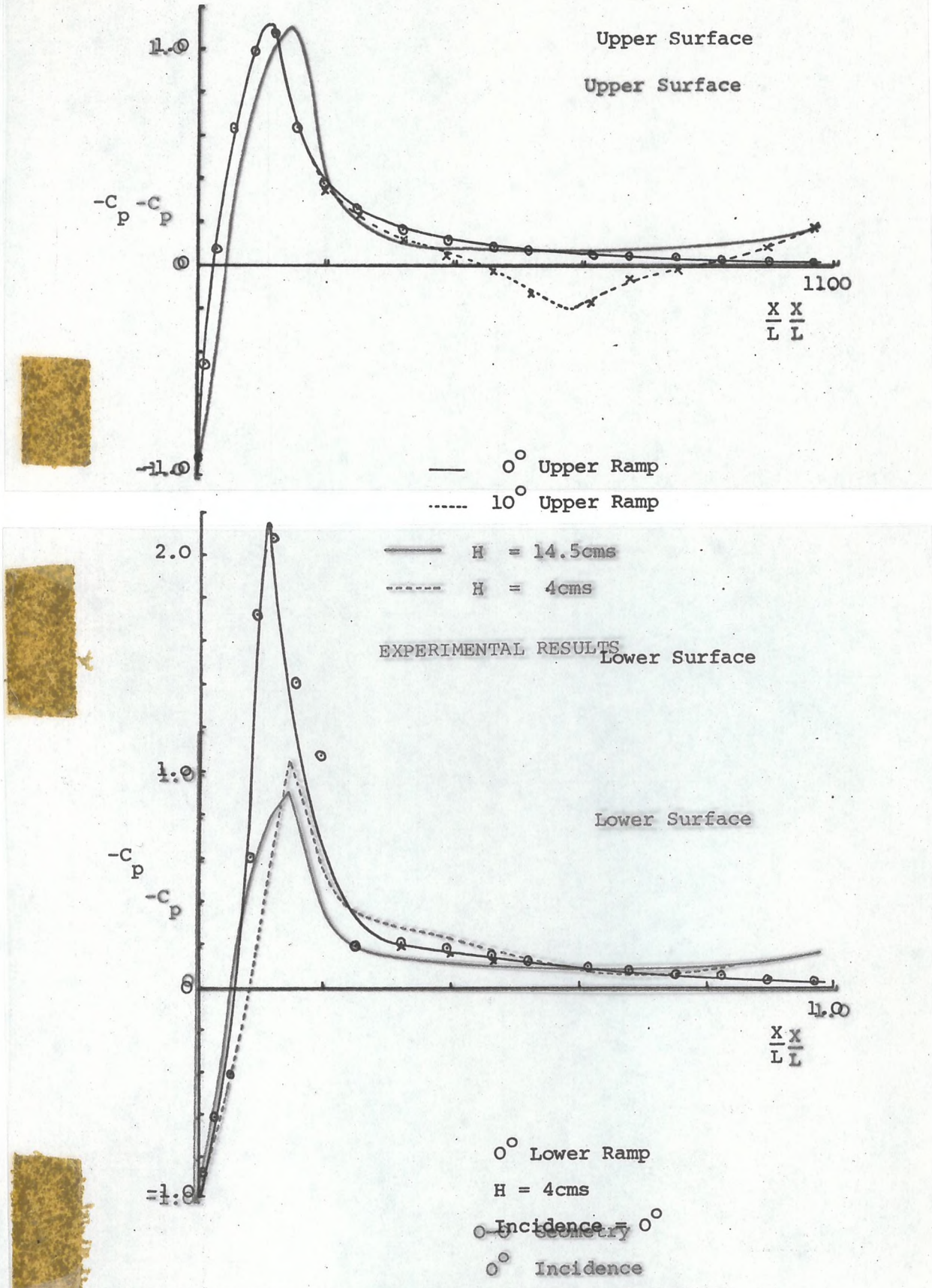

FIGURE 87d BLUFF BODY THEORETICAL CENTRE LINE SURFACE PRESSURE DISTRIBUTIONS

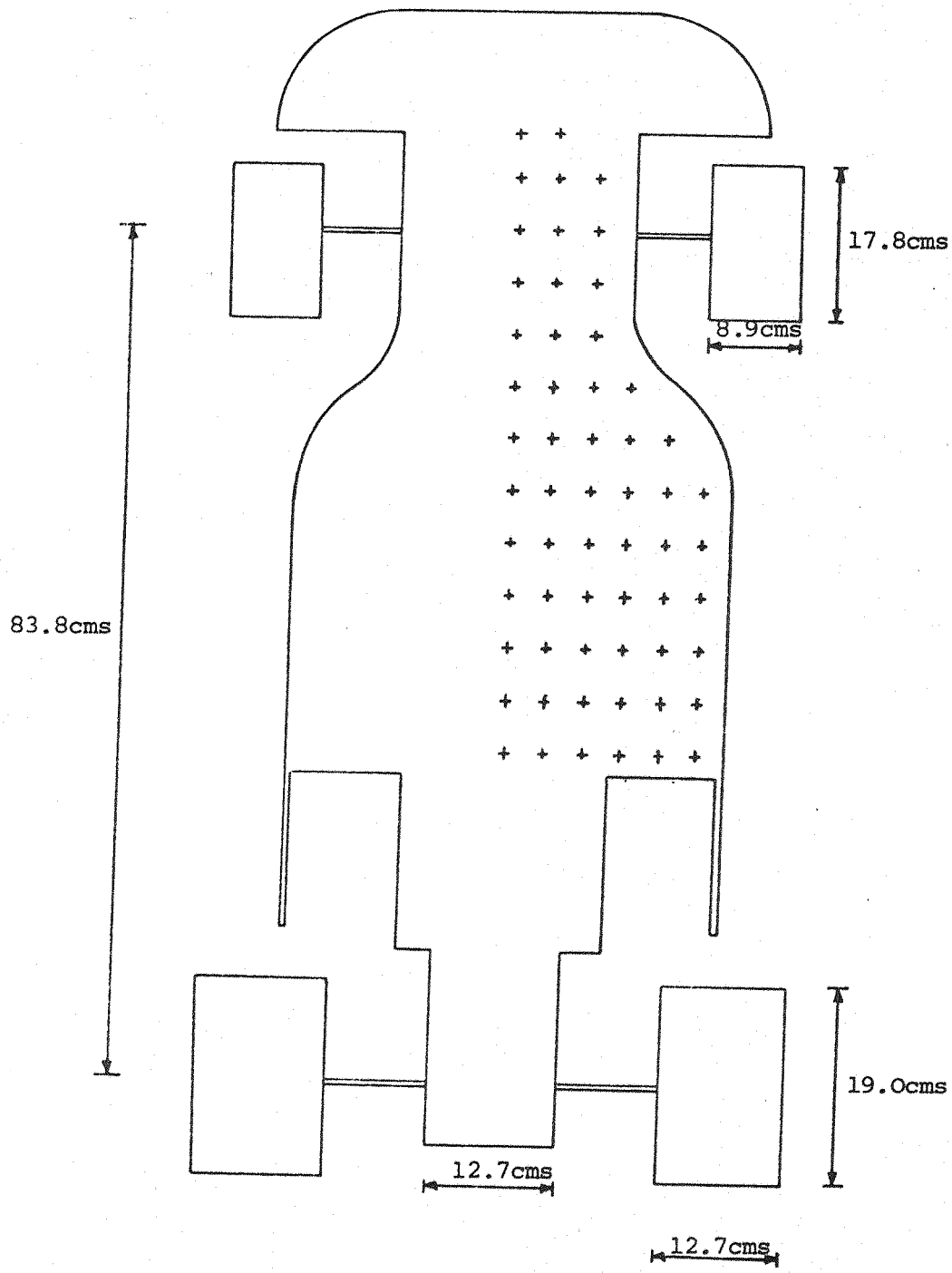

FIGURE 88 GEOMETRY OF MARCH 761 RACING CAR MODEL

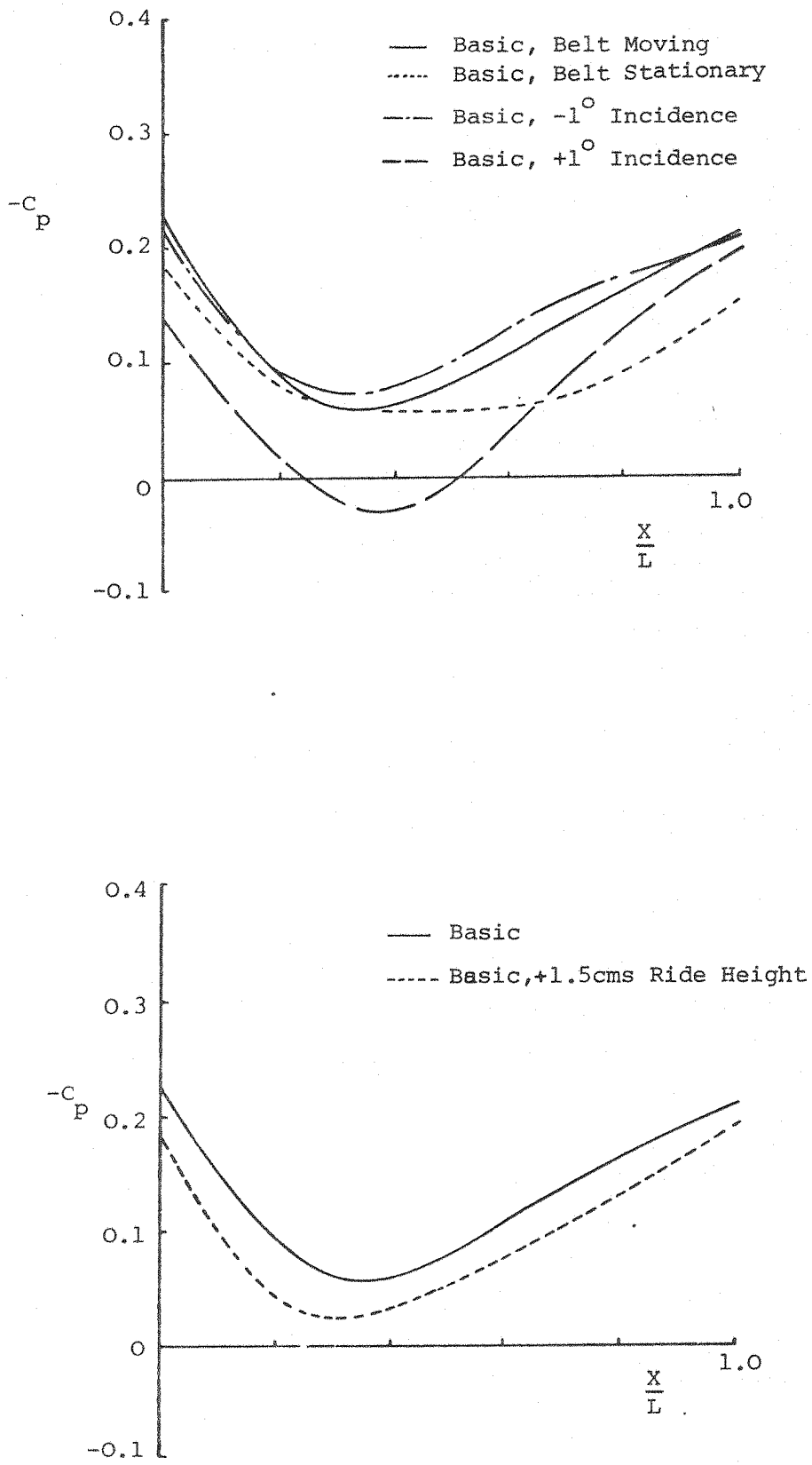

FIGURE 89 MARCH 761 MONOCOQUE UNDERSURFACE PRESSURE DISTRIBUTIONS

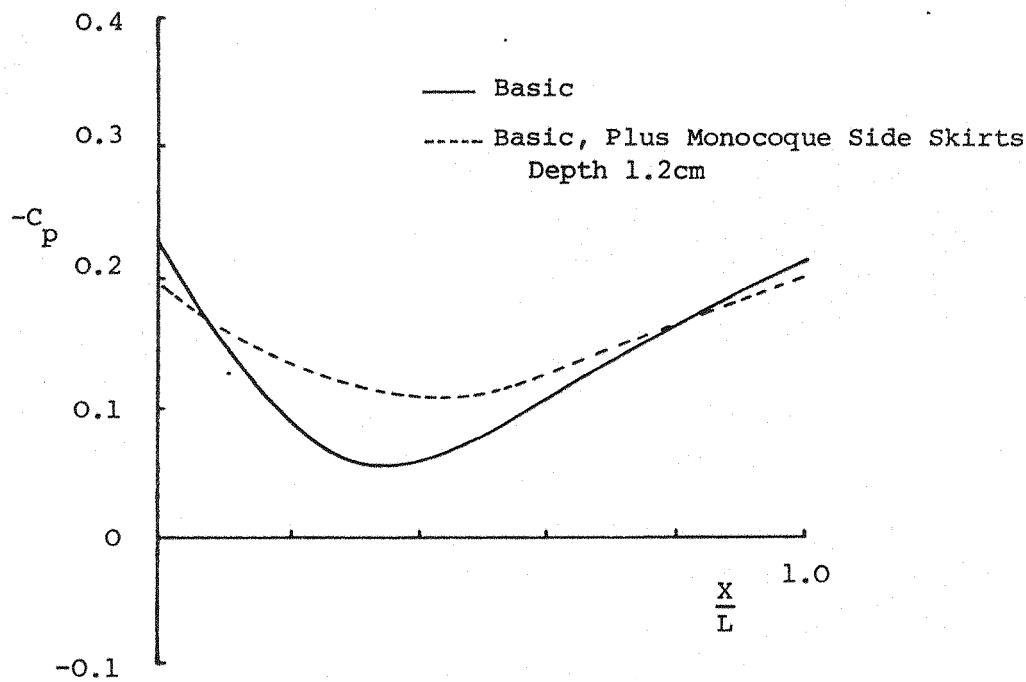

FIGURE 90 MARCH 761 MONOCOQUE UNDERSURFACE PRESSURE DISTRIBUTIONS

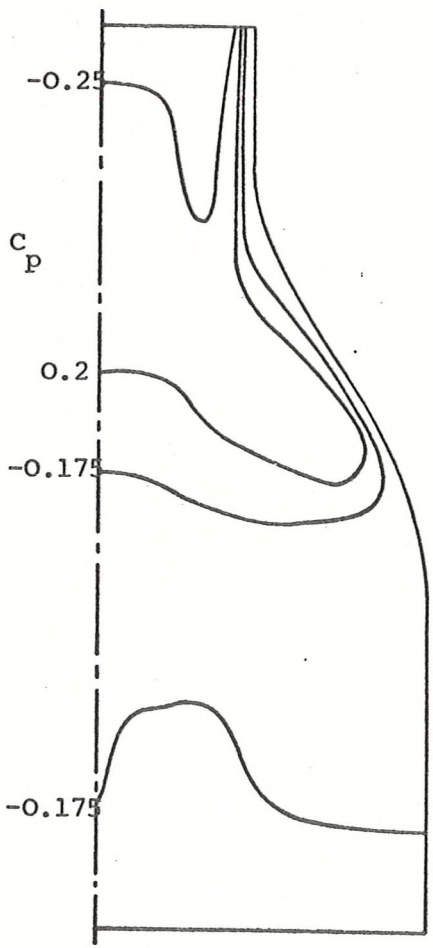

BASIC

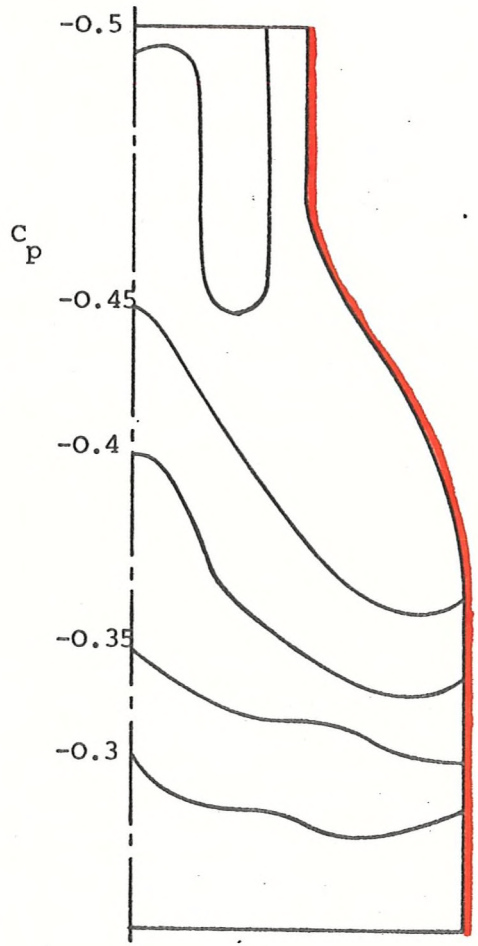

FULL DEPTH MONOCOQUE SIDE SKIRTS

FIGURE 91 MARCH 761 MONOCOQUE UNDERSURFACE PRESSURE ISOBARS

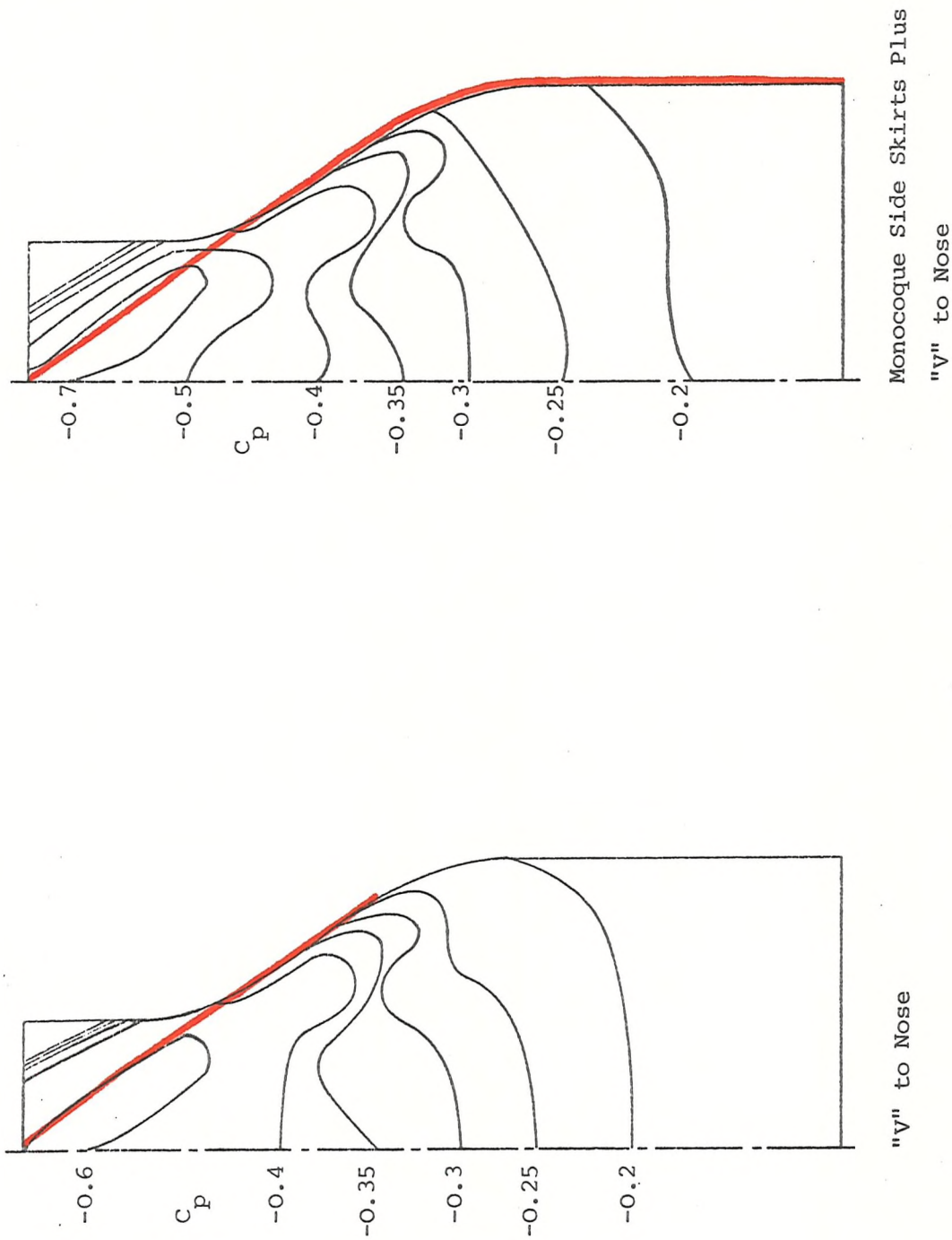

FIGURE 92 MARCH 761 MONOCOQUE UNDERSURFACE PRESSURE ISOBARS

FIGURE 93 MARCH 761 MONOCOQUE UNDERSURFACE PRESSURE ISOBARS

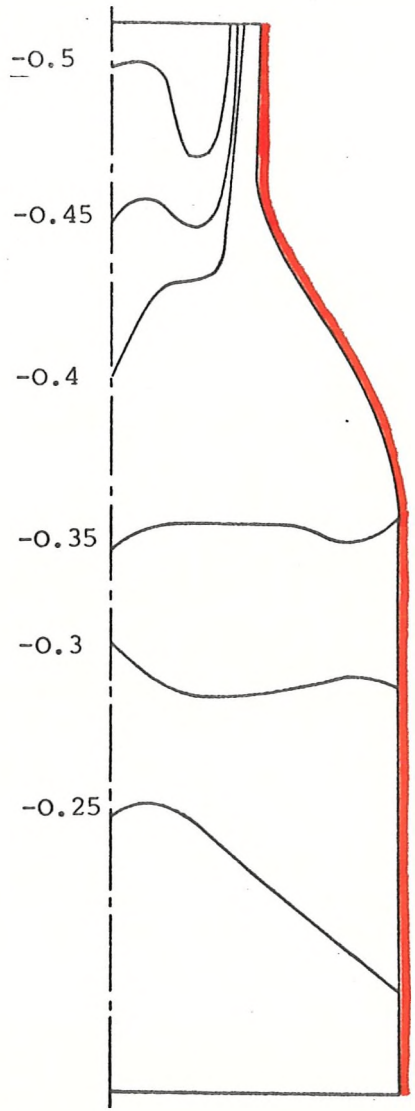

Extension Plate at 0^{o} Incidence
Side Skirts to Rear of Plate

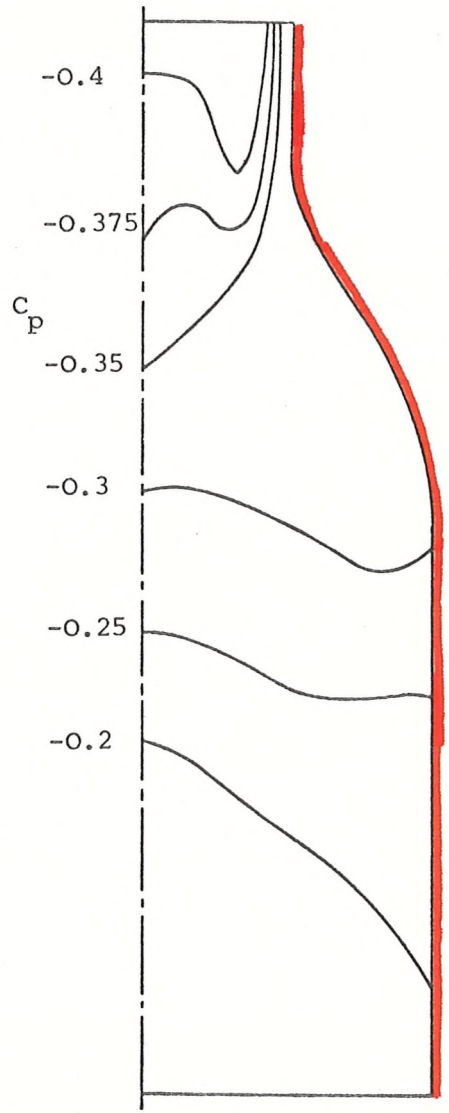

Extension Plate at 7^{o} Incidence
Side Skirts to Rear of Extension Plate

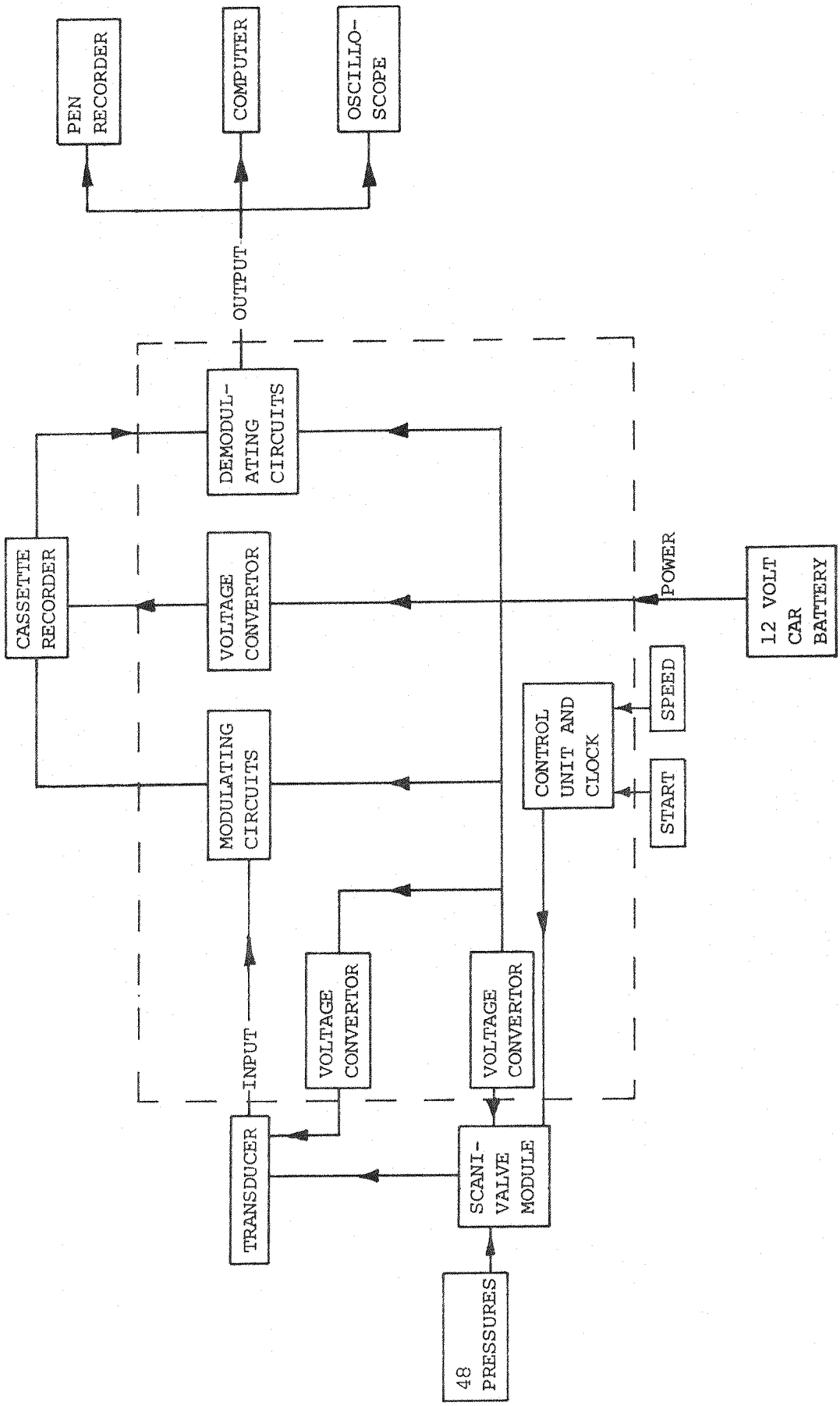

FIGURE 94 BLOCK DIAGRAM OF PORTABLE SCANIVALVE PRESSURE RECORDING SYSTEM

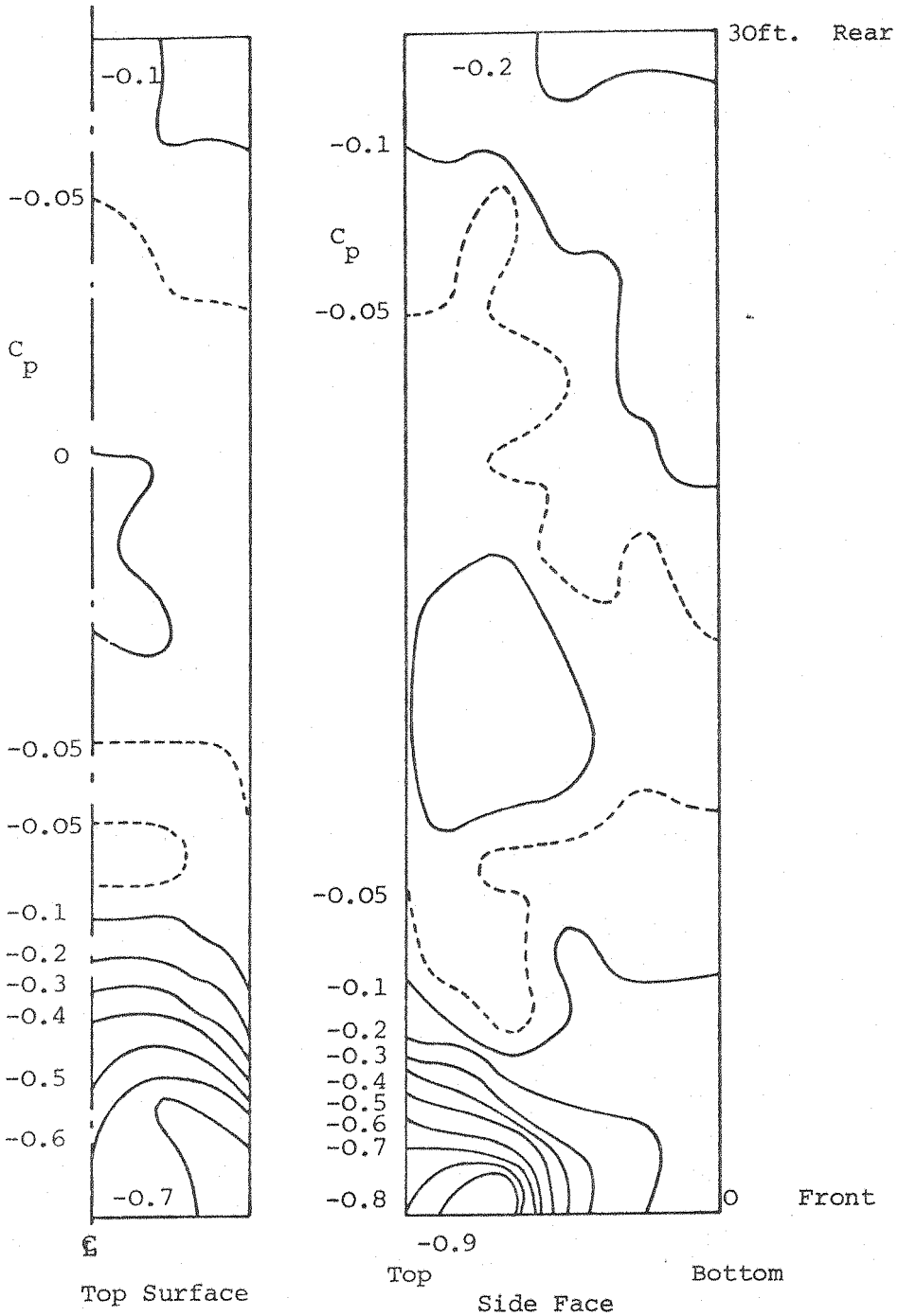

FIGURE 95a MODEL SCALE CONTAINER SURFACE PRESSURE DISTRIBUTION

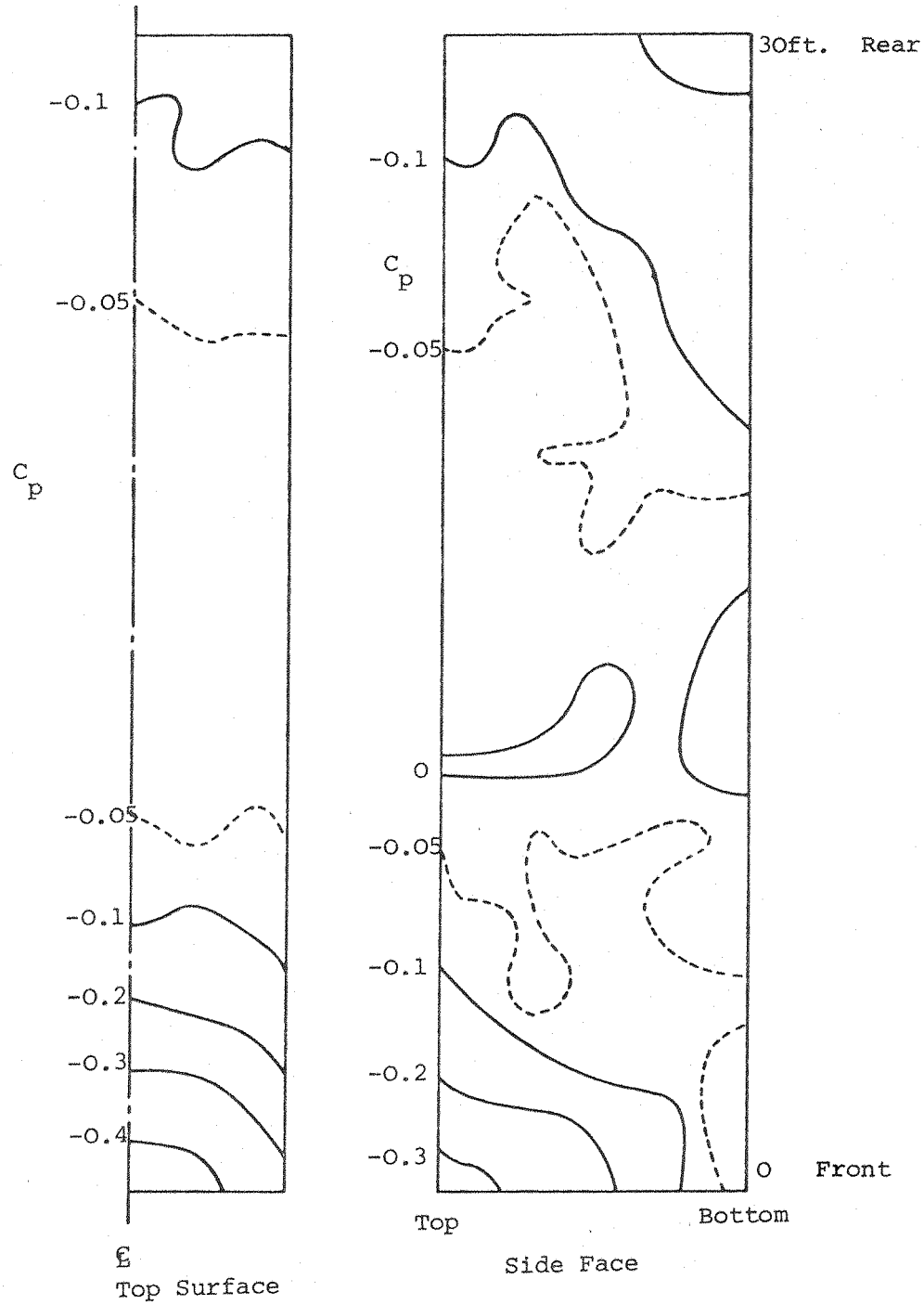

With Cab Mounted Plate

FIGURE 95b MODEL SCALE CONTAINER SURFACE PRESSURE DISTRIBUTION

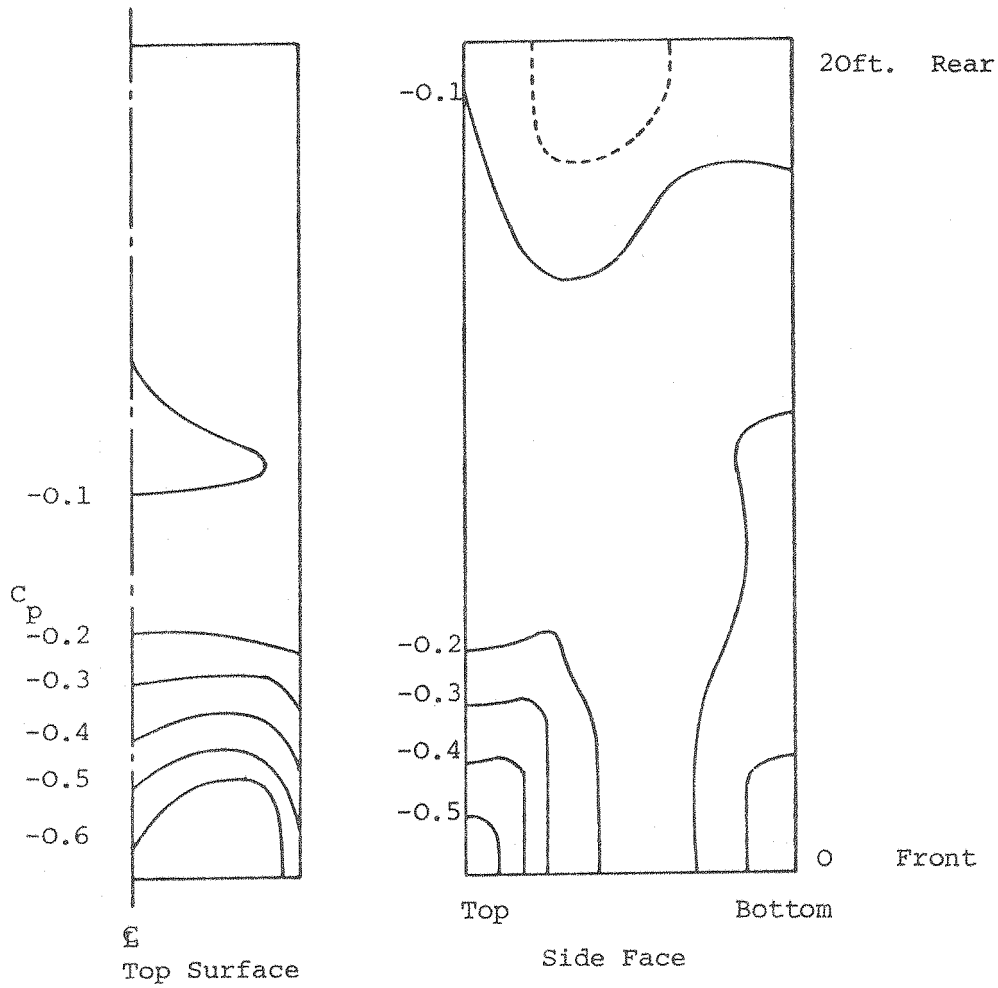

Without Cab Mounted Plate

FIGURE 96a FULL SCALE CONTAINER SURFACE PRESSURE DISTRIBUTION

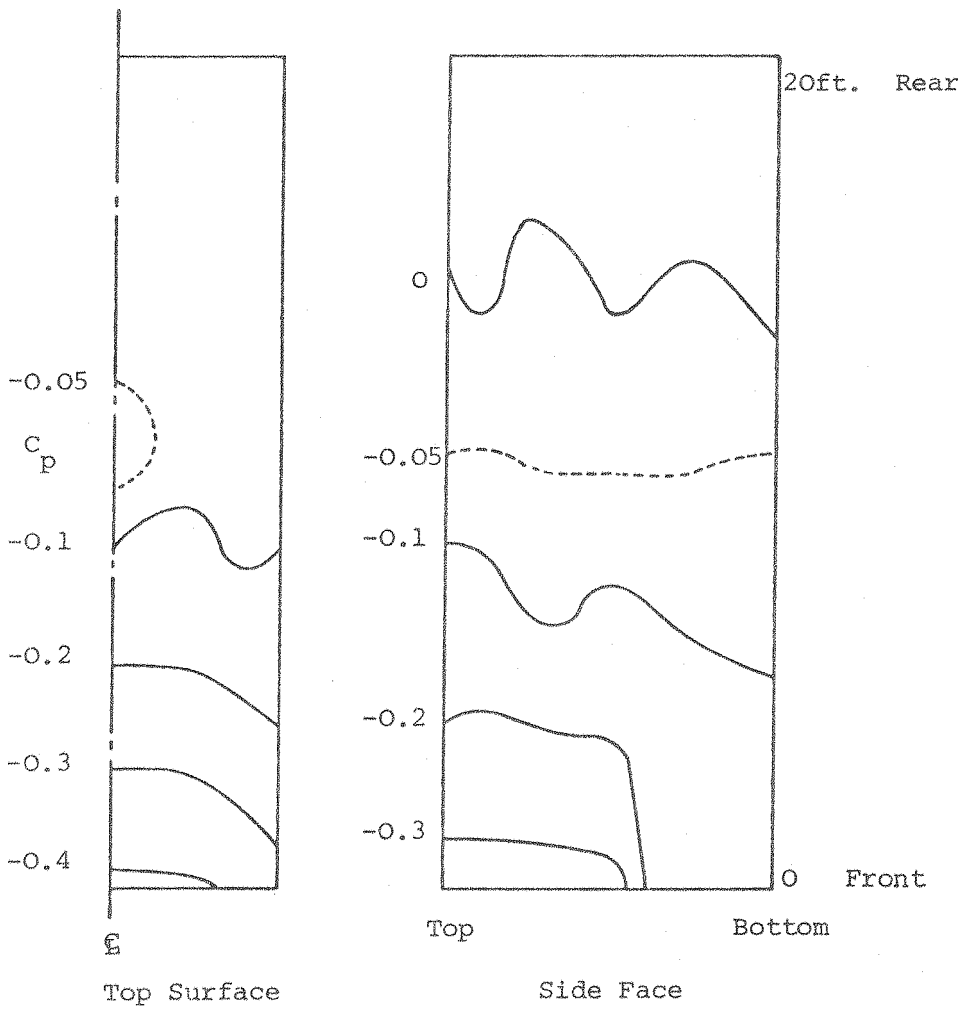

With Cab Mounted Plate

FIGURE 96b FULL SCALE CONTAINER SURFACE PRESSURE DISTRIBUTION

TABLE 1a

BLUFF BODY TEST CONFIGURATIONS

ANGLE	0-0	10-0	20-0
+18°			
+15°			
+12°			
+11°	†		
+ 9°	† *	†	† *
+ 6°	†	†	†
+ 3°	†	†	†
+ 2°	+ * ×	+ * ×	+ ×
0°	† + * ×	† + * ×	† + * ×
-1.5°	+	+	+
-3.0°	† + * ×	† + * ×	† + * ×
- 6°	†	†	†
- 7°	† *	†	†
-11°	†		
-12°			

† H = 14.5cms Force

\+ H = 4cms Force Moving + Stopped

* H = 14.5cms Pressure

× H = 4cms Pressure

TABLE 1b

BLUFF BODY TEST CONFIGURATIONS

ANGLE	0-10	10-10	20-10
+18°			
+15°			
+12°	†	†	†
+11°			
+ 9°	† + * ×	† + * ×	† + * ×
+ 6°	† +	† +	† +
+ 3°	† +	† +	† +
+ 2°			
0°	† + * ×	† + * ×	† + * ×
-1.5°			
-3.0°	† + * ×	† + * ×	† + * ×
- 6°	†	†	†
- 7°	†	†	†
-11°			
-12°	†	†	†

† H = 14.5cms Force

\+ H = 4cms Force Moving + Stopped

* H = 14.5cms Pressure

× H = 4cms Pressure

TABLE 1c

BLUFF BODY TEST CONFIGURATIONS

ANGLE	0-20	10-20	20-20
+18°	+ * ×	+ * ×	+ * ×
+15°	+	+	† +
+12°	† + *	† +	† +
+11°			
+ 9°	† + * ×	† + * ×	† + * ×
+ 6°	† +	† +	† +
+ 3°	† +	† +	† +
+ 2°			
0°	† + * ×	† + * ×	† + * ×
-1.5°			
-3.0°	† + * ×	† + * ×	† + * ×
- 6°	†	†	†
- 7°	†	†	†
-11°			
-12°			

† H = 14.5cms Force

\+ H = 4cms Force Moving + Stopped

* H = 14.5cms Pressure

× H = 4cms Pressure

TABLE 2

POSITIONS OF TAPPINGS ON BLUFF BODY NOSE

% Dist. From Leading Edge Based on Length of Nose	Dist. from Leading Edge Along Surface (cms)	Dist. Along Horiz. Plane (cms)
0	0.0	0.0
1.0	3.05	0.30
2.5	4.84	0.76
5.0	6.87	1.52
10.0	9.81	3.05
15.0	12.12	4.57
20.0	14.13	6.10
30.0	17.67	9.14
40.0	20.87	12.19
50.0	23.94	15.24
60.0	26.99	18.29
70.0	30.04	21.34
80.0	33.08	24.38
90.0	36.13	27.43
100.0	39.18	30.48

TABLE 3

CHINA CLAY MIXTURE

100 cc	Butyl Alcohol
100 cc	Butyl Acetate
50 cc	Xylene
100 gms	China Clay
100 cc	Frigilene

TABLE 4

O.O GEOMETRY, OVERALL FORCE COEFFICIENTS

Ground Clearance 14.5 cm Ground Moving

Incidence	C_L	C_D	C_M	L/D
-11°	0.874	0.665	-0.406	1.314
-9°	0.710	0.607	-0.315	1.169
-6°	0.483	0.534	-0.213	0.904
-3°	0.231	0.487	-0.091	0.474
0°	-0.003	0.501	-0.011	-0.007
3°	-0.216	0.586	0.064	-0.369
6°	-0.433	0.683	0.132	-0.635
9°	-0.654	0.807	0.173	-0.811
11°	-0.818	0.897	0.190	-0.912

Ground Clearance 4cm - Ground Moving

Incidence	C_L	C_D	C_M	L/D
-3°	0.457	0.529	-0.254	0.864
-1.5°	0.211	0.513	-0.115	0.412
0°	-0.002	0.529	-0.044	-0.003
2°	-0.295	0.557	0.010	-0.530

Ground Clearance 4cm - Ground Stopped

Incidence	C_L	C_D	C_M	L/D
-3°	0.738	0.574	-0.144	1.287
-1.5°	0.583	0.513	-0.103	1.136
0°	0.244	0.475	0.031	0.514
2°	-0.175	0.504	0.077	-0.348

TABLE 5

0.10 GEOMETRY OVERALL FORCE COEFFICIENTS

Ground Clearance 14.5 cm Ground Moving

Incidence	C_L	C_D	C_M	L/D
-12°	1.197	0.713	-0.442	1.678
-9°	0.957	0.623	-0.297	1.535
-6°	0.756	0.548	-0.168	1.379
-3°	0.566	0.489	-0.065	1.158
0°	0.379	0.441	0.043	0.859
3°	0.195	0.423	0.136	0.460
6°	0.007	0.437	0.236	0.016
9°	-0.170	0.492	0.335	-0.346
12°	-0.356	0.563	0.420	-0.631

Ground Clearance 4cm - Ground Moving

Incidence	C_L	C_D	C_M	L/D
-3°	1.040	0.549	-0.191	1.893
0°	0.716	0.499	0.053	1.434
3°	0.473	0.480	0.236	0.986
6°	0.208	0.466	0.387	0.447
9°	-0.069	0.501	0.461	-0.137

Ground Clearance 4cm - Ground Stopped

Incidence	C_L	C_D	C_M	L/D
-3°	0.930	0.534	-0.180	1.742
0°	0.630	0.472	0.038	1.333
3°	0.396	0.440	0.209	0.900
6°	0.153	0.447	0.387	0.343
9°	-0.110	0.468	0.470	-0.235

TABLE 6

0.10 GEOMETRY WITH UNDERSURFACE ROUGHNESS OVERALL FORCE COEFFICIENTS

Ground Clearance 4cm - Ground Moving

Incidence	C_L	C_D	C_M	L/D
-3°	1.037	0.590	-0.123	1.756
0°	0.719	0.530	0.086	1.355
3°	0.461	0.493	0.245	0.935
6°	0.189	0.479	0.354	0.395
9°	-0.110	0.509	0.439	-0.216

Ground Clearance 4cm - Ground Stopped

Incidence	C_L	C_D	C_M	L/D
-3°		0.572	-0.102	
0°	0.650	0.506	0.090	1.286
3°	0.403	0.461	0.245	0.873
6°	0.160	0.464	0.356	0.345
9°	-0.126	0.472	0.438	-0.266

TABLE 7

0.20 GEOMETRY OVERALL FORCE COEFFICIENTS

Ground Clearance 14.5cm Ground Moving

Incidence	C_L	C_D	C_M	L/D
-9^o	1.156	0.678	-0.319	1.707
-6^o	0.965	0.594	-0.171	1.624
-3^o	0.782	0.518	-0.061	1.512
0^o	0.615	0.454	0.043	1.355
3^o	0.457	0.409	0.168	1.118
6^o	0.300	0.387	0.211	0.775
9^o	0.140	0.385	0.329	0.363
12^o	-0.029	0.400	0.409	-0.073

Ground Clearance 4cm - Ground Moving

Incidence	C_L	C_D	C_M	L/D
-3^o	1.277	0.609	-0.169	2.096
0^o	0.991	0.548	0.068	1.809
3^o	0.814	0.503	0.243	1.617
6^o	0.683	0.470	0.377	1.454
9^o	0.561	0.449	0.505	1.251
12^o	0.405	0.441	0.614	0.918
15^o	0.203	0.451	0.705	0.450
18^o	-0.050	0.490	0.794	-0.102

Ground Clearance 4cm - Ground Stopped

Incidence	C_L	C_D	C_M	L/D
-3^o	1.130	0.574	-0.176	1.967
0^o	0.882	0.513	0.041	1.719
3^o	0.711	0.467	0.249	1.524
6^o	0.563	0.440	0.362	1.279
9^o	0.412	0.421	0.476	0.977
12^o	0.265	0.420	0.583	0.632
15^o	0.096	0.442	0.685	0.218
18^o	-0.131	0.486	0.778	-0.269

TABLE 8

10.0 GEOMETRY OVERALL FORCE COEFFICIENTS

Ground Clearance 14.5 cm Ground Moving

Incidence	C_L	C_D	C_M	L/D
-9°	0.943	0.857	-0.280	1.100
-6°	0.728	0.753	-0.155	0.967
-3°	0.502	0.672	-0.049	0.746
0°	0.232	0.600	0.025	0.386
3°	-0.005	0.646	0.096	-0.008
6°	-0.226	0.727	0.163	-0.311
9°	-0.447	0.846	0.241	-0.528

Ground Clearance 4cm - Ground Moving

Incidence	C_L	C_D	C_M	L/D
-3°	0.689	0.653	-0.179	1.055
-1.5°	0.427	0.607	-0.066	0.703
0°	0.221	0.613	-0.002	0.361
2°	-0.063	0.659	0.057	-0.096

Ground Clearance 4cm - Ground Stopped

Incidence	C_L	C_D	C_M	L/D
-3°	0.700	0.704	-0.120	0.994
-1.5°	0.481	0.666	-0.014	0.723
0°	0.276	0.641	0.046	0.430
2°	-0.007	0.650	0.102	-0.011

TABLE 9

10.10 GEOMETRY OVERALL FORCE COEFFICIENTS

Ground Clearance 14.5cm Ground Moving

Incidence	C_L	C_D	C_M	L/D
-12°	1.441	0.966	-0.394	1.491
-9°	1.211	0.876	-0.252	1.381
-6°	1.023	0.791	-0.124	1.294
-3°	0.847	0.709	-0.017	1.196
0°	0.665	0.633	0.085	1.051
3°	0.474	0.565	0.190	0.839
6°	0.237	0.503	0.258	0.472
9°	0.015	0.518	0.335	0.030
12°	-0.190	0.594	0.399	-0.321

Ground Clearance 4cm - Ground Moving

Incidence	C_L	C_D	C_M	L/D
-3°	1.298	0.744	-0.119	1.745
0°	0.985	0.662	0.107	1.490
3°	0.707	0.581	0.239	1.217
6°	0.418	0.521	0.387	0.802
9°	0.103	0.528	0.491	0.195

Ground Clearance 4cm - Ground Stopped

Incidence	C_L	C_D	C_M	L/D
-3°	1.198	0.732	-0.087	1.635
0°	0.910	0.650	0.115	1.401
3°	0.668	0.580	0.239	1.152
6°	0.406	0.519	0.398	0.781
9°	0.113	0.509	0.507	0.223

TABLE 10

10.20 GEOMETRY OVERALL FORCE COEFFICIENTS

Ground Clearance 14.5cm Ground Moving

Incidence	C_L	C_D	C_M	L/D
- 9°	1.406	0.905	-0.243	1.554
- 6°	1.219	0.817	-0.146	1.492
- 3°	1.054	0.731	0.009	1.443
0°	0.892	0.641	0.080	1.390
3°	0.732	0.558	0.177	1.311
6°	0.563	0.492	0.241	1.143
9°	0.382	0.449	0.348	0.851
12°	0.196	0.440	0.465	0.446

Ground Clearance 4cm - Ground Moving

Incidence	C_L	C_D	C_M	L/D
- 3°	1.579	0.840	-0.115	1.878
0°	1.303	0.754	0.121	1.728
3°	1.119	0.672	0.287	1.666
6°	0.973	0.598	0.451	1.627
9°	0.823	0.546	0.551	1.509
12°	0.641	0.510	0.653	1.258
15°	0.396	0.493	0.733	0.803
18°	0.107	0.518	0.799	0.206

Ground Clearance 4cm - Ground Stopped

Incidence	C_L	C_D	C_M	L/D
- 3°	1.442	0.795	-0.127	1.813
0°	1.198	0.714	0.085	1.679
3°	1.027	0.634	0.274	1.619
6°	0.871	0.560	0.437	1.555
9°	0.709	0.509	0.523	1.392
12°	0.527	0.476	0.630	1.107
15°	0.315	0.473	0.716	0.665
18°	0.038	0.478	0.790	0.079

TABLE 11

20.0 GEOMETRY OVERALL FORCE COEFFICIENTS

Ground Clearance 14.5 cm Ground Moving

Incidence	C_L	C_D	C_M	L/D
-9°	1.154	1.132	-0.174	1.019
-6°	0.952	1.017	-0.077	0.936
-3°	0.739	0.912	-0.005	0.810
0°	0.507	0.822	0.103	0.617
3°	0.264	0.806	0.186	0.301
6°	0.007	0.829	0.223	0.008
9°	-0.239	0.885	0.287	-0.270

Ground Clearance 4cm - Ground Moving

Incidence	C_L	C_D	C_M	L/D
-3°	0.934	0.906	-0.104	1.030
-1.5°	0.681	0.841	-0.004	0.810
0°	0.459	0.841	0.069	0.546
2°	0.170	0.879	0.119	0.194

Ground Clearance 4cm - Ground Stopped

Incidence	C_L	C_D	C_M	L/D
-3°	0.948	0.971	-0.050	0.975
-1.5°	0.731	0.923	0.044	0.791
0°	0.523	0.896	0.115	0.584
2°	0.229	0.850	0.157	0.269

TABLE 12

20.10 GEOMETRY OVERALL FORCE COEFFICIENTS

Ground Clearance 14.5cm Ground Moving

Incidence	C_L	C_D	C_M	L/D
-12°	1.596	1.445	-0.277	1.105
-9°	1.417	1.190	-0.167	1.191
-6°	1.248	1.107	-0.044	1.127
-3°	1.091	1.008	0.039	1.083
0°	0.927	0.899	0.164	1.031
3°	0.750	0.804	0.258	0.933
6°	0.546	0.728	0.336	0.750
9°	0.288	0.649	0.391	0.444
12°	0.041	0.664	0.472	0.062

Ground Clearance 4cm - Ground Moving

Incidence	C_L	C_D	C_M	L/D
-3°	1.579	1.019	-0.033	1.550
0°	1.261	0.915	0.213	1.378
3°	0.985	0.818	0.367	1.205
6°	0.689	0.742	0.471	0.930
9°	0.341	0.671	0.537	0.508

Ground Clearance 4cm - Ground Stopped

Incidence	C_L	C_D	C_M	L/D
-3°	1.567	1.111	0.358	1.411
0°	1.449	0.990	0.467	1.464
3°	1.167	0.842	0.570	1.386
6°	0.926	0.738	0.652	1.254
9°	0.526	0.662	0.731	0.794

TABLE 13

20.20 GEOMETRY OVERALL FORCE COEFFICIENTS

Ground Clearance 14.5cm Ground Moving

Incidence	C_L	C_D	C_M	L/D
-9°	1.626	1.205	-0.149	0.520
-6°	1.461	1.121	-0.061	0.854
-3°	1.318	1.039	0.097	1.079
0°	1.172	0.926	0.169	1.204
3°	1.021	0.812	0.260	1.258
6°	0.868	0.720	0.345	1.265
9°	0.694	0.644	0.425	1.269
12°	0.501	0.587	0.513	1.303
15°	0.280	0.539	0.572	1.349

Ground Clearance 4cm - Ground Moving

Incidence	C_L	C_D	C_M	L/D
-3°	1.805	1.100	-0.012	1.641
0°	1.541	0.991	0.215	1.554
3°	1.390	0.880	0.364	1.579
6°	1.254	0.781	0.501	1.606
9°	1.096	0.693	0.618	1.582
12°	0.890	0.616	0.705	1.446
15°	0.644	0.572	0.781	1.126
18°	0.318	0.553	0.841	0.574

Ground Clearance 4cm - Ground Stopped

Incidence	C_L	C_D	C_M	L/D
-3°	1.678	1.074	-0.000	1.562
0°	1.455	0.973	0.204	1.495
3°	1.293	0.852	0.352	1.518
6°	1.158	0.756	0.478	1.531
9°	1.001	0.670	0.586	1.494
12°	0.813	0.607	0.691	1.341
15°	0.591	0.562	0.773	1.050
18°	0.287	0.535	0.837	0.536

TABLE 14

BLUFF BODY LIFT CURVE SLOPES

Configuration	Ground Clearance 14.5cm	Ground Clearance 4cm Moving	Ground Clearance 4cm Stopped
0.0	-0.077	-0.150	-0.140
10.0	-0.077	-0.150	-0.141
20.0	-0.082	-0.153	-0.144
0.10	-0.062	-0.092	-0.087
10.10	-0.068	-0.0996	-0.090
20.10	-0.067	-0.103	
0.20	-0.056		
10.20	-0.057		
20.20	-0.056		
0.10 + Undersurface Roughness		-0.092	-0.088

TABLE 15

MAXIMUM NOSE AND KNEE SUCTIONS

(i) Lower Ramp Changes

0° Top 20° Bottom

Lower Knee Suctions

H = 14.5cm			H = 4cm		
	18°	-1.0725		18°	-2.063
	9°	-1.1626		9°	-2.424
	0°	-1.0053		0°	-0.730
	-3°	-0.838		-3°	-0.50

Nose Suctions

H = 14.5cm	Upper	Lower	H = 4cm	Upper	Lower
18°	-1.617	-0.180	18°	-1.629	+0.025
9°	-1.374	-0.600	9°	-1.443	-0.368
0°	-1.110	-1.040	0°	-1.171	-1.164
-3°	-1.020	-1.221	-3°	-1.117	-2.170

Lower Knee Suctions

0° Top 10° Bottom

H = 14.5cm			H = 4cm		
	$+9^{\circ}$	-0.567		$+9^{\circ}$	-1.0453
	0°	-0.578		0°	-0.906
	-3°	-0.550		-3°	-0.618

Nose Suctions

H = 14.5cm	Upper	Lower	H = 4cm	Upper	Lower
$+9^{\circ}$	-1.388	-0.528	$+9^{\circ}$	-1.413	-0.310
0°	-1.107	-0.992	0°	-1.147	-1.156
-3°	-1.018	-1.166	-3°	-1.066	-2.090

TABLE 16

MAXIMUM NOSE AND KNEE SUCTIONS

(ii) Upper Ramp Changes

20° Top 10° Bottom

Upper Knee Suctions

H = 14.5cm		H = 4cm	
$+ 9^{\circ}$	0.384	$+ 9^{\circ}$	0.389
0°	0.439	0°	0.426
$- 3^{\circ}$	0.464	$- 3^{\circ}$	0.451

Nose Suctions

H = 14.5cm	Upper	Lower	H = 4cm	Upper	Lower
$+ 9^{\circ}$	-1.302	-0.511	$+ 9^{\circ}$	-1.362	-0.287
0°	-1.013	-0.970	0°	-1.090	-1.113
$- 3^{\circ}$	-0.942	-1.169	$- 3^{\circ}$	-0.990	-2.042

Upper Knee Suctions

H = 14.5cm		H = 4cm	
$+ 9^{\circ}$	0.133	$+ 9^{\circ}$	0.120
0°	0.149	0°	0.139
$- 3^{\circ}$	0.165	$- 3^{\circ}$	0.153

Nose Suctions

H = 14.5cm	Upper	Lower	H = 4cm	Upper	Lower
$+ 9^{\circ}$	-1.352	-0.543	$+ 9^{\circ}$	-1.394	-0.297
0°	-1.075	-0.993	0°	-1.109	-1.110
$- 3^{\circ}$	-1.001	-1.184	$- 3^{\circ}$	-1.046	-2.097

TABLE 17

LOCAL MEAN DOWNFORCE COEFFICIENTS - LOWER AND UPPER SURFACES

UPPER SURFACE

H = 4cms

	L.U.C.			L.U.R.		
Incidence	0-10	10-10	20-10	0-10	10-10	20-10
-3°	-0.059	0.010	0.082	-0.093	-0.056	0.019
0°	-0.070	-0.003	0.078	-0.107	-0.049	0.025
$+9^{\circ}$	-0.096	-0.016	0.059	-0.161	-0.047	0.044

LOWER SURFACE

H = 14.5cms

	L.L.C.			L.L.R.		
Incidence	0-0	0-10	0-20	0-0	0-10	0-20
$+3^{\circ}$	0.156	0.283	0.367	0.139	0.248	0.299
0°	0.126	0.252	0.353	0.126	0.241	0.314
$+9^{\circ}$	0.017	0.152	0.262	0.065	0.258	0.331

H = 4cms

	L.L.C.			L.L.R.		
Incidence	0-0	0-10	0-20	0-0	0-10	0-20
-3°	0.213	0.500	0.538	0.194	0.328	0.364
0°	0.155	0.473	0.521	0.126	0.354	0.417
$+9^{\circ}$	-	0.199	0.395	-	0.411	0.661

L.U.C. Mean Downforce Coefficient Upper Centre Section

L.U.R. Mean Downforce Coefficient Upper Ramp Section

L.L.C. Mean Downforce Coefficient Centre Section

L.L.R. Mean Downforce Coefficient Lower Ramp Section

TABLE 18

LOCAL MEAN DOWNFORCE COEFFICIENTS - LOWER SURFACE

0.10 GEOMETRY - BASIC - PLUS ROUGHNESS - AIRDAM - BELT STATIONARY

L.L.R. Incidence	Moving	Stopped	Moving + Roughness	Stopped + Roughness	Moving + Airdam + Roughness	Moving + Airdam
-3°	0.327	0.299	0.326	0.294	-	-
0°	0.354	0.330	0.338	0.296	0.361	0.354
$+9^{\circ}$	0.411	0.380	0.369	0.349	0.289	0.279

L.L.C. Incidence	Moving	Stopped	Moving + Roughness	Stopped + Roughness	Moving + Airdam + Roughness	Moving + Airdam
-3°	0.500	0.462	0.514	0.480	-	-
0°	0.473	0.436	0.485	0.432	0.494	0.515
$+9^{\circ}$	0.199	0.159	0.173	0.183	0.160	0.120

TOTAL Incidence	Moving	Stopped	Moving + Roughness	Stopped + Roughness	Moving + Airdam + Roughness	Moving + Airdam
-3°	0.827	0.761	0.84	0.774	-	-
0°	0.827	0.766	0.823	0.728	0.855	0.869
$+9^{\circ}$	0.610	0.539	0.542	0.532	0.449	0.399

L.L.R. - Mean Downforce Coefficient Lower Ramp Section

L.L.C. - Mean Downforce Coefficient Lower Centre Section

TABLE 19

LOCAL MEAN DOWNFORCE COEFFICIENTS - LOWER SURFACE

10.0 GEOMETRY - H = 4cms AND 14.5cms

Inc = $+2^{O}$, 0^{O} and -3^{O}

H = 14.5cm	Incidence	L.L.R.	L.L.C.
	$+2^{O}$	0.126	0.090
	0^{O}	0.133	0.104
	-3^{O}	0.177	0.141

H = 4cm	Incidence	L.L.R.	L.L.C.
	$+2^{O}$	0.051	0.112
	0^{O}	0.120	0.173
	-3^{O}	0.177	0.245

L.L.R. - Mean Downforce Coefficient Lower Ramp Section

L.L.C. - Mean Downforce Coefficient Lower Centre Section

TABLE 20

LOCAL MEAN DRAG COEFFICIENTS

(a) Configuration 20-0, H = 4cm

Incidence	D.U.R.	D.U.C.	D.L.R.	D.L.C.
$+2^{\circ}$	0.012	-0.002	-0.002	-0.003
0°	0.014	0.00	0.00	0.00
-3°	0.016	0.004	0.010	0.011

(b) Configuration 0-10, H = 14.5cm

Incidence	D.U.R.	D.U.C.	D.L.R.	D.L.C.
$+9^{\circ}$	0.017	0.014	0.004	-0.024
0°	0.00	0.00	0.042	0.00
-3°	-0.005	-0.004	0.057	0.015

(c) Configuration 0-10, H = 4cm

Incidence	D.U.R.	D.U.C.	D.L.R.	D.L.C.
$+9^{\circ}$	0.018	0.017	0.007	-0.031
0°	0.00	0.00	0.062	0.00
-3°	-0.006	-0.004	0.076	0.026

D.U.R. - Mean Drag Coefficient Upper Ramp Section

D.U.C. - Mean Drag Coefficient Upper Centre Section

D.L.R. - Mean Drag Coefficient Lower Ramp Section

D.L.C. - Mean Drag Coefficient Lower Centre Section

TABLE 21

INTEGRATED BASE PRESSURE COEFFICIENTS

GEOMETRY	INCIDENCE	INTEGRATED BASE PRESSURE COEFFICIENTS GROUND CLEARANCE = 4cm	GROUND CLEARANCE = 14.5cm
0-0	-3^{o}		-0.232
	0^{o}		-0.252
	$+2^{o}$		-0.292
10-0	-3^{o}	-0.349	-0.353
	0^{o}	-0.350	-0.290
	$+2^{o}$	-0.369	-0.312
20-0	-3^{o}	-0.402	-0.449
	0^{o}	-0.382	-0.395
	$+2^{o}$	-0.407	
0-10	-3^{o}	-0.267	-0.217
	0^{o}	-0.240	-0.186
	$+9^{o}$	-0.238	-0.217
10-10	-3^{o}	-0.385	-0.388
	0^{o}	-0.348	-0.346
	$+9^{o}$	-0.278	-0.265

Belt Stationary	-0.252
Ground Clearance = 4cm	-0.216
	-0.215

Contd. . . .

TABLE 21 Contd.

INTEGRATED BASE PRESSURE COEFFICIENTS

GEOMETRY	INCIDENCE	INTEGRATED BASE PRESSURE COEFFICIENTS GROUND CLEARANCE = 4cm	GROUND CLEARANCE = 14.5cm
20-10	-3°	-0.493	-0.547
	0°	-0.469	-0.498
	$+9^{\circ}$	-0.311	-0.321
10-20	-3°	-0.263	-0.241
	0°	-0.252	-0.193
	$+9^{\circ}$	-0.169	-0.103
	$+18^{\circ}$	-0.141	-0.160
10-20	-3°	-0.428	-0.397
	0°	-0.389	-0.347
	$+9^{\circ}$	-0.270	-0.203
	$+18^{\circ}$	-0.222	-0.198
20-20	0°	-0.522	
	$+9^{\circ}$	-0.413	
	$+18^{\circ}$	-0.342	

TABLE 22

VERTICAL TOTAL PRESSURE TRAVERSES
IN CHANNEL UNDER MODEL

Configuration	Traverse Position	(Local - Freestream) Total Pressure (% Tunnel Dynamic Head)
0.10 -3°	Front	1.9
	Rear	-1.3
0.10 0°	Front	0
	Rear	-1.9
0.10 $+9^{\circ}$	Front	3.1
	Rear	-2.5
0.10 0° Belt Stopped	Front	1.2
	Rear	0
0.20 0°	Front	5.7
	Rear	-8.2

TABLE 23a

MARCH 761 - OVERALL FORCE COEFFICIENTS

CONFIGURATION	C_L	C_D	CENTRE OF PRESSURE (% MONOCOQUE LENGTH)
Basic model, no skirts, correct ride height	0.71	0.87	82
Basic model, full depth monocoque side skirts, correct ride height	1.03	0.86	68
Basic model, no skirts, $+1.75^{o}$ incidence	0.50	0.88	91
Basic model, full depth monocoque side skirts $+1.75^{o}$ incidence	0.59	0.87	84

Coefficients based on an area of 1.11 sq. metres.

TABLE 23b

MARCH 761 - INTEGRATED MONOCOQUE UNDERSURFACE PRESSURE DISTRIBUTIONS

CONFIGURATION	C_L	CENTRE OF PRESSURE (% MONOCOQUE LENGTH)
Basic	0.197	70
Monocoque side skirts, 1.25cms deep	0.227	69
"V", 1.25cms deep	0.291	66
Monocoque side skirts, full depth	0.404	69
"V", full depth	0.355	70
Monocoque side skirts and "V" and full width base plate 21cms long skirts 1.25cms deep	0.268	72
Skirt around front of nose, 1.25cms deep	0.197	70

Coefficients based on undersurface area of monocoque

(a) 10-0 geometry

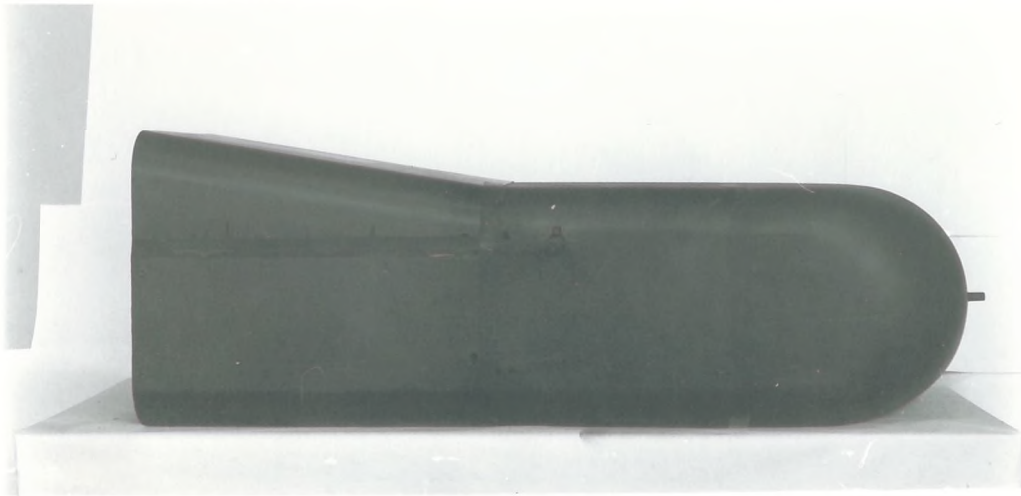

(b) 0-0 geometry

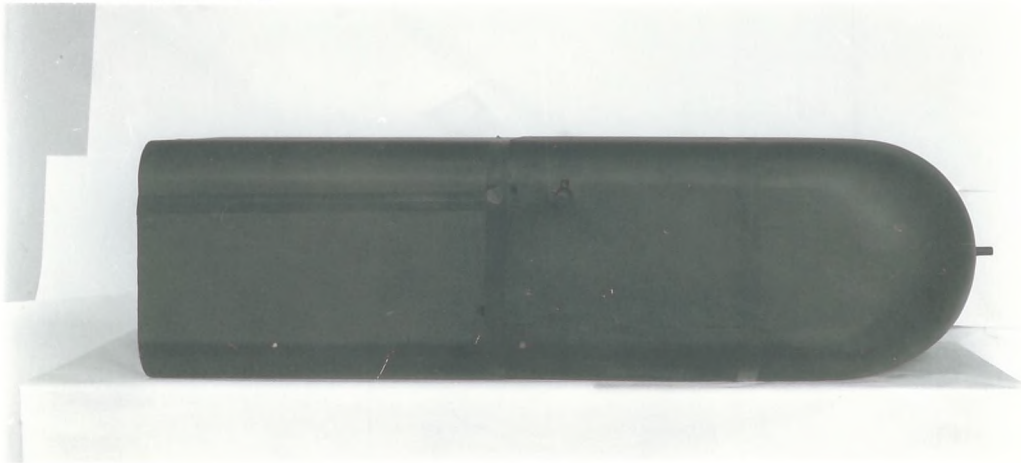

(c) 0-10 geometry

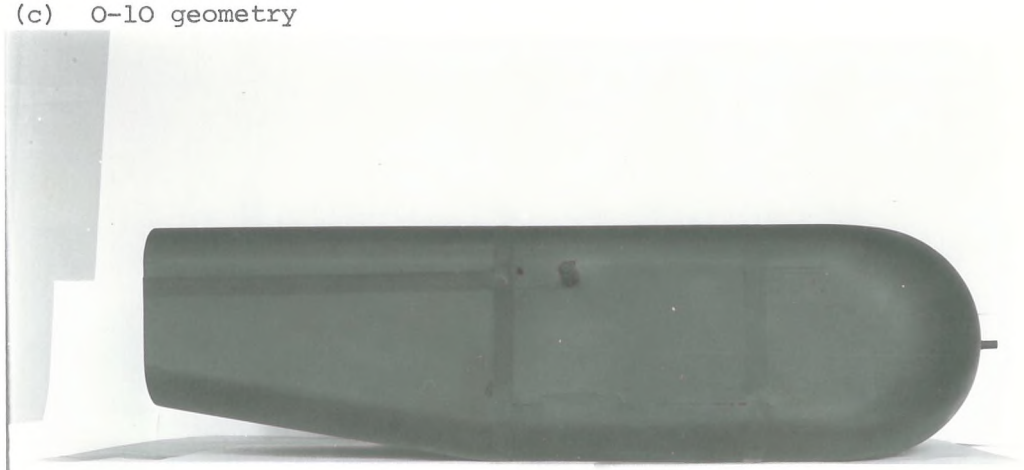

PLATE 1a SIDE VIEW OF BLUFF BODY MODEL

(a) 20-0 geometry

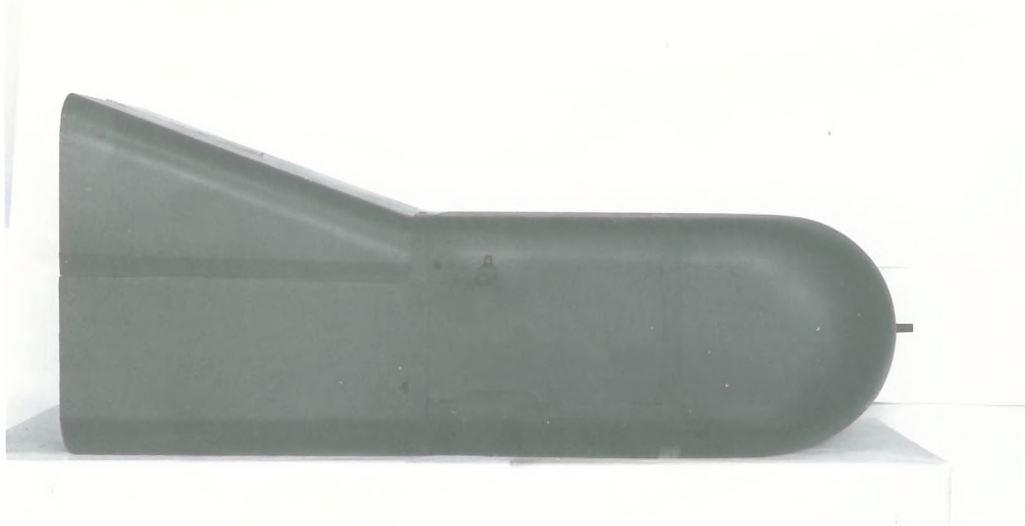

(b) 0-0 geometry

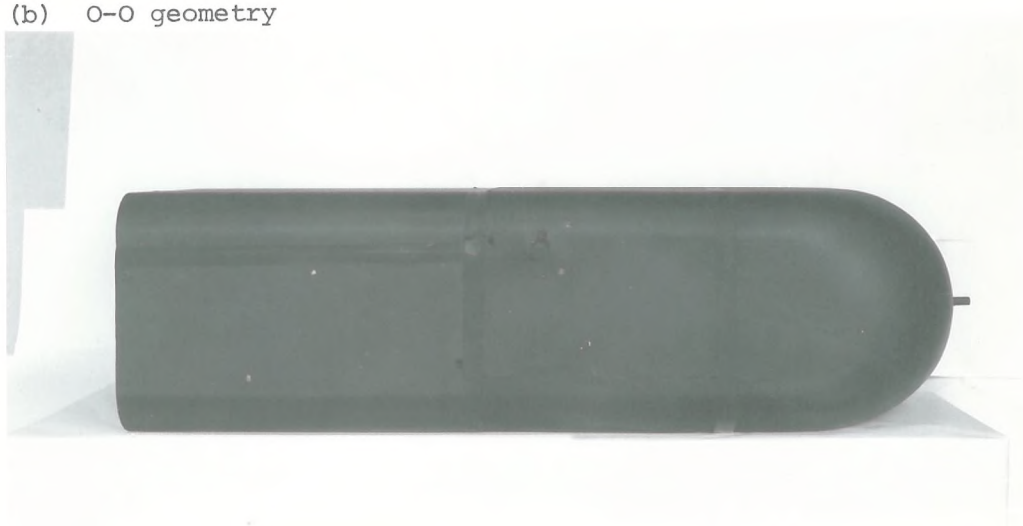

(c) 0-20 geometry

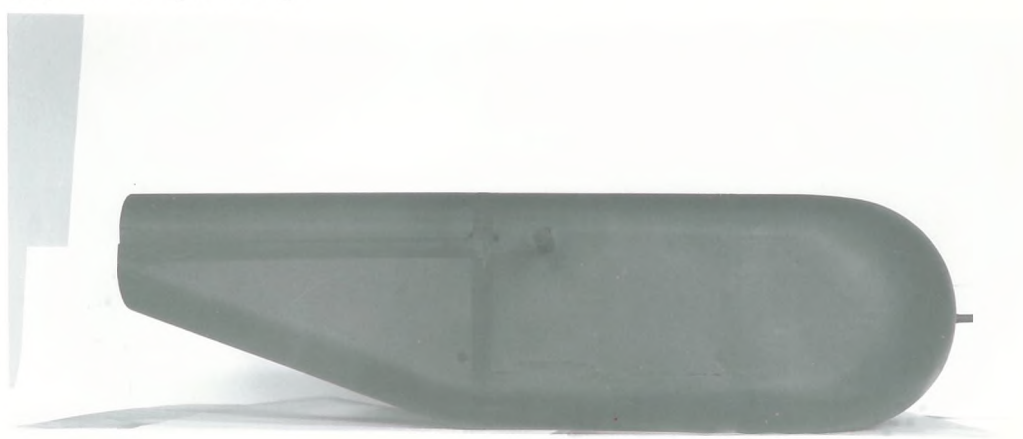

PLATE 1b SIDE VIEW OF BLUFF BODY MODEL

(a) Top view of bluff body model

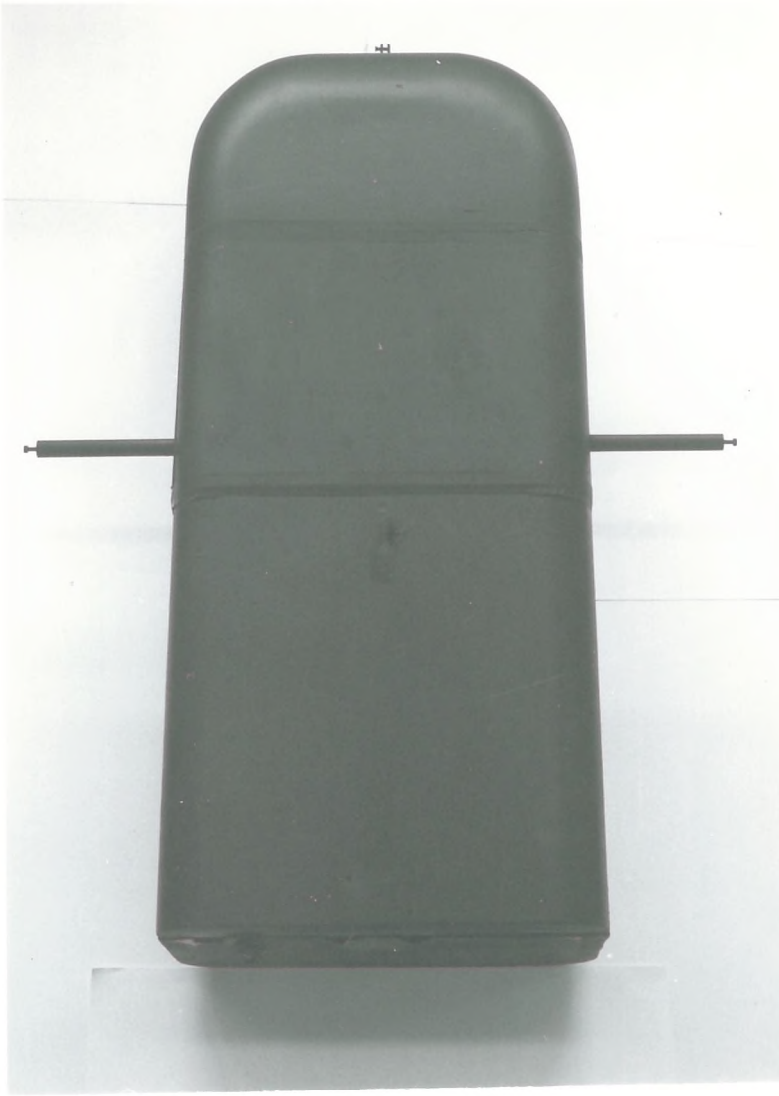

(b) Front view of bluff body model

PLATE 2

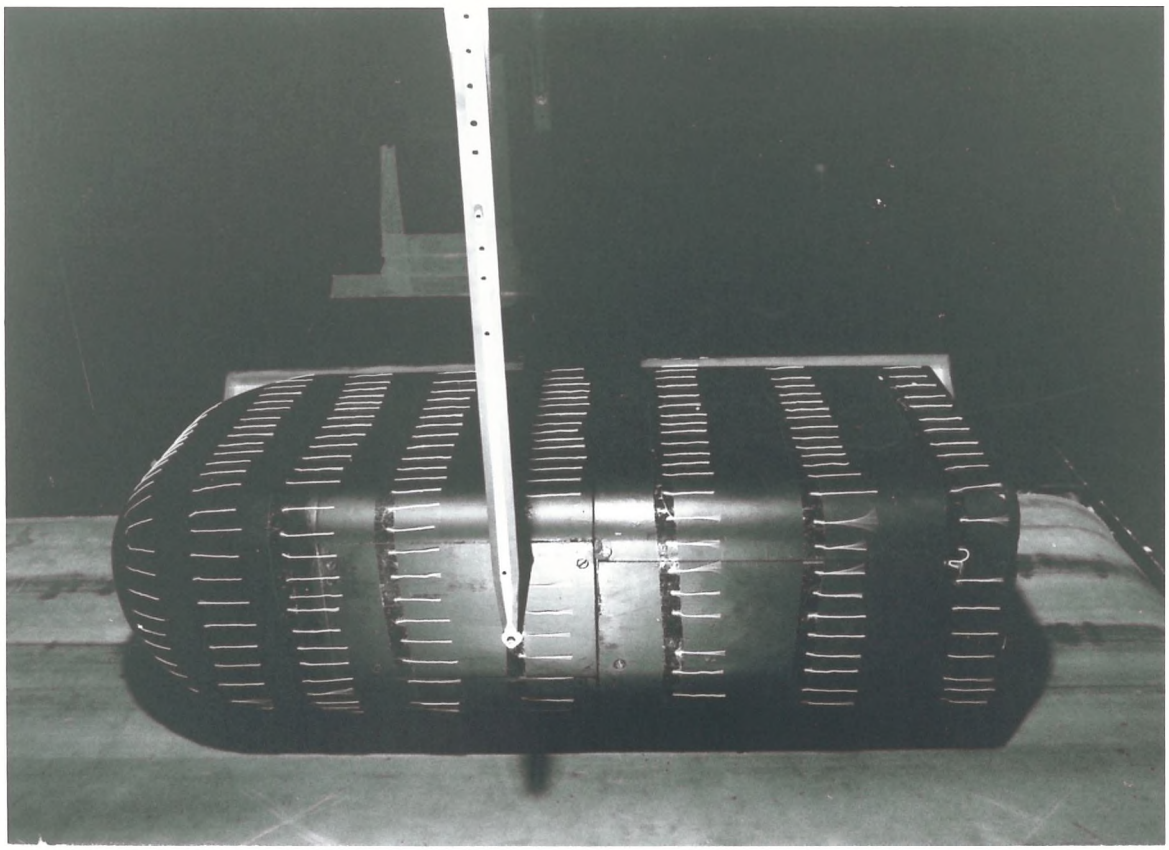

PLATE 3 O-O geometry, H = 14.5cms, 0^{o} incidence

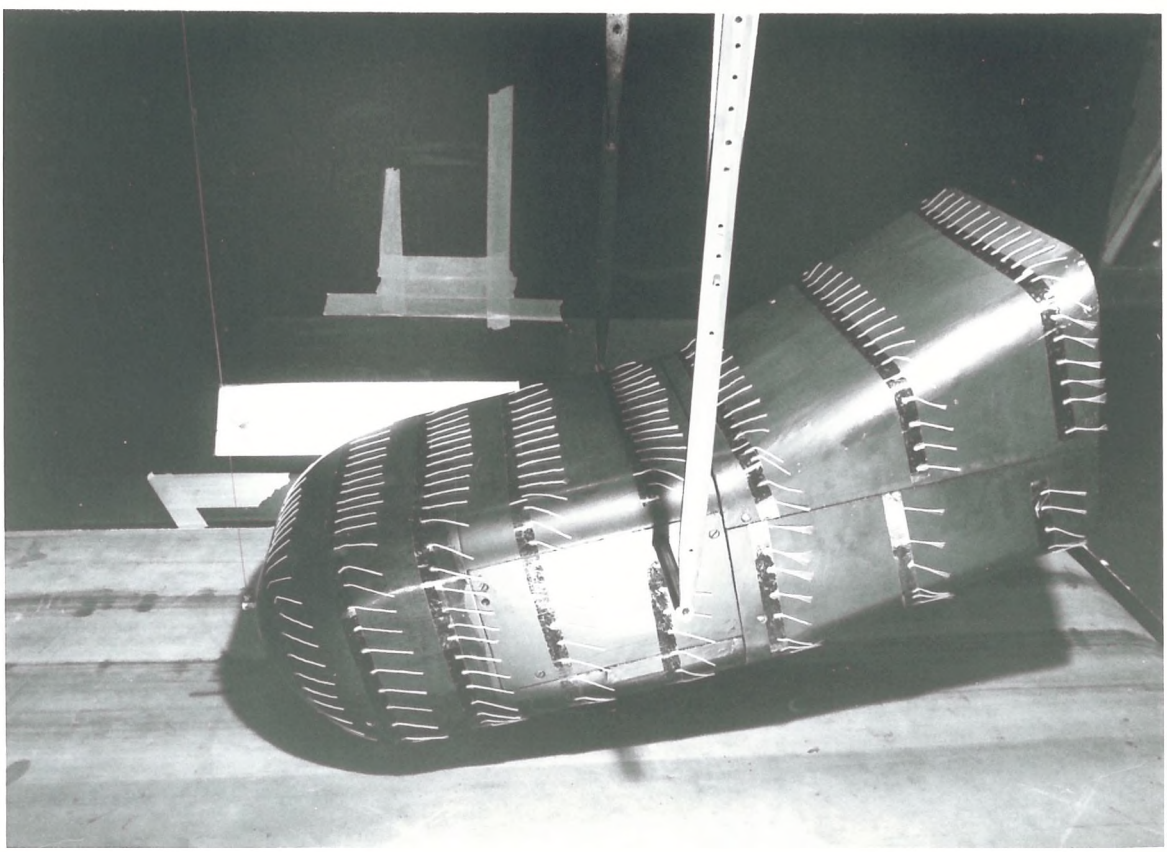

PLATE 4 20-10 geometry, H = 14.5cms, -14^{o} incidence

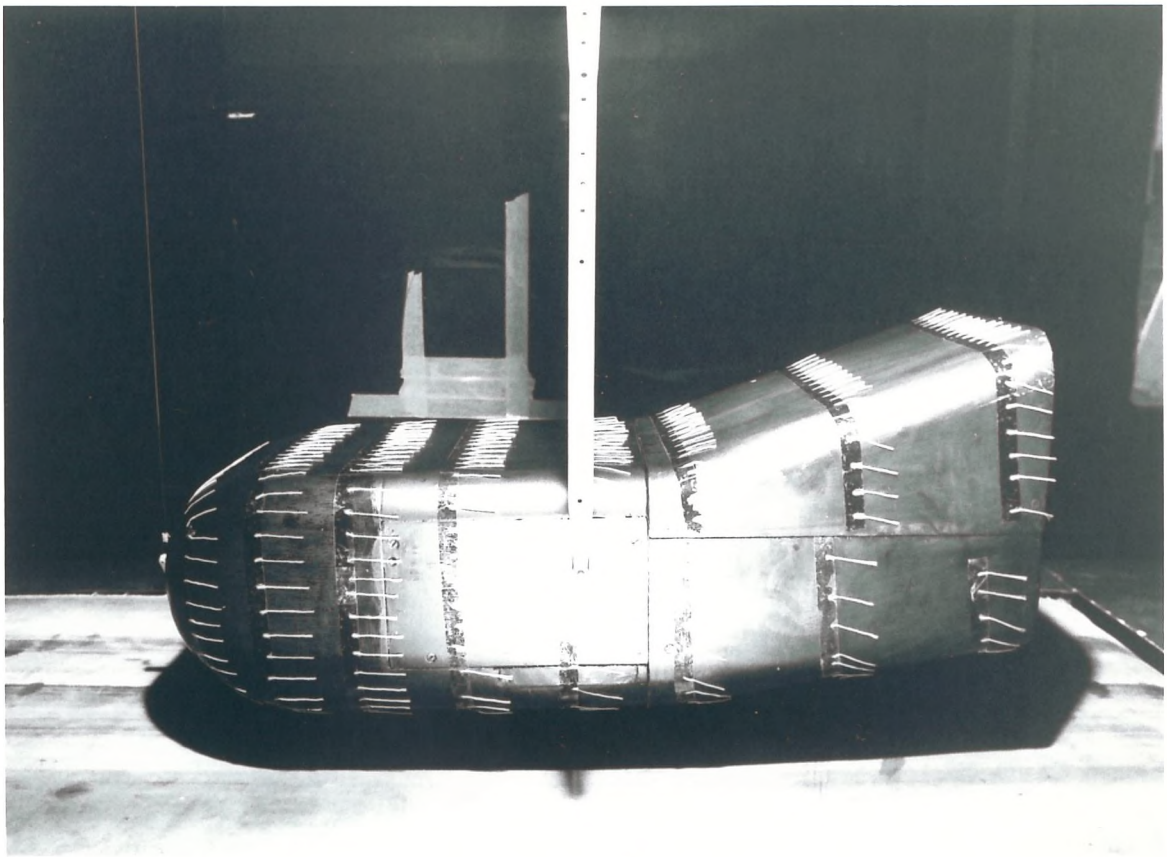

PLATE 5 20-10 geometry, H = 14.5cms, 0° incidence

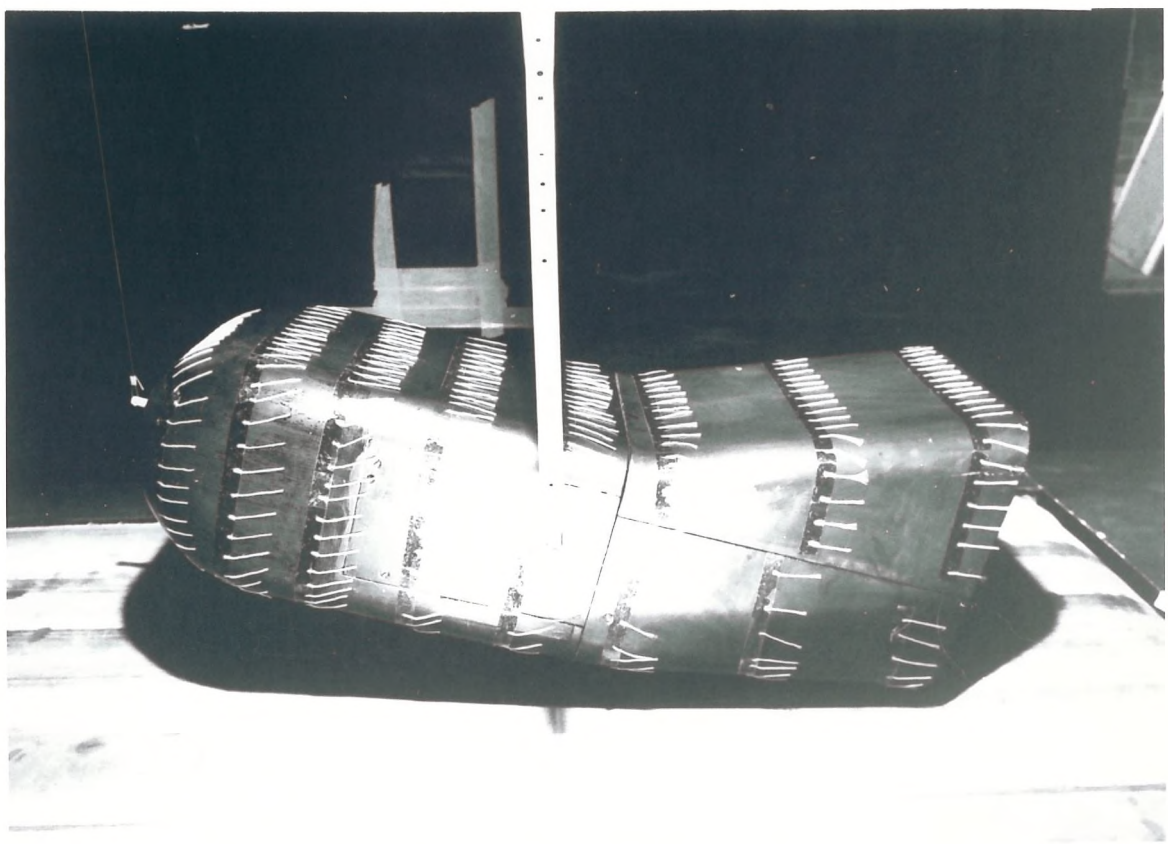

PLATE 6 20-10 geometry, H = 14.5cms, 12° incidence

(a) without sideplates

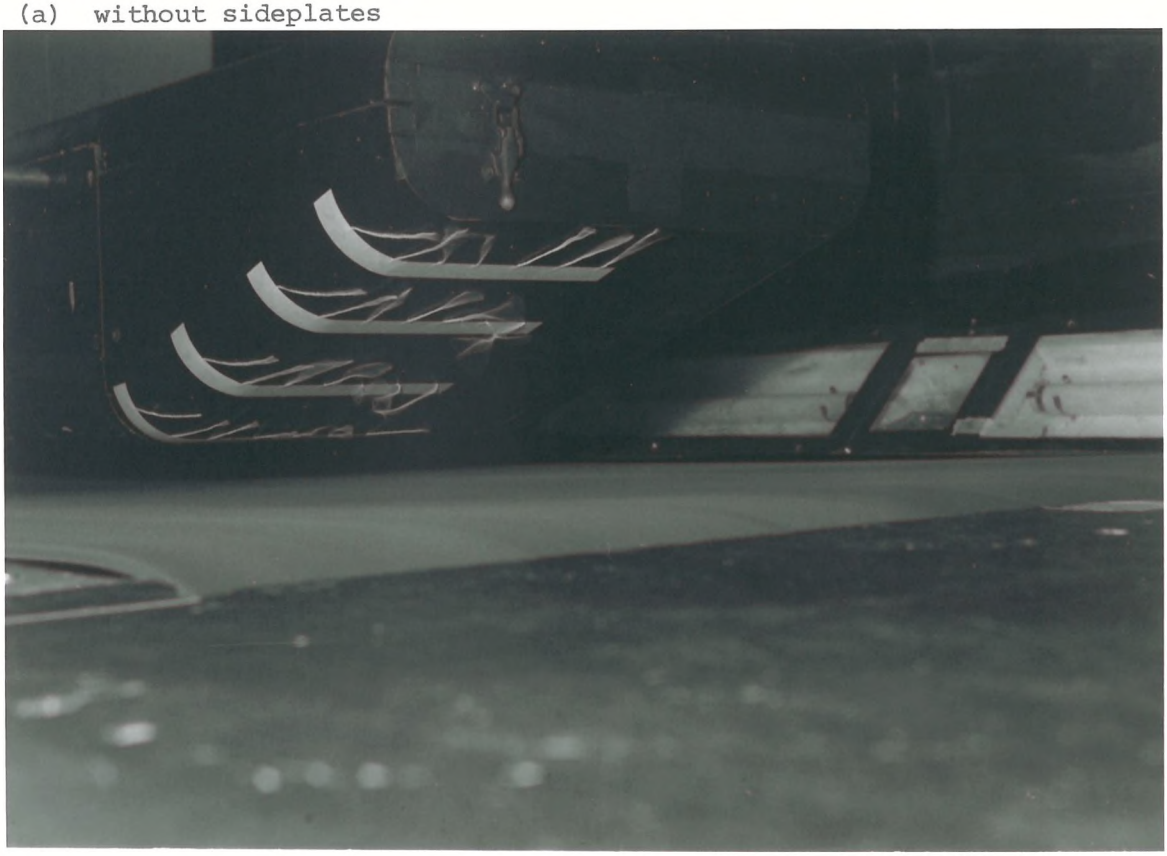

(b) with sideplates

PLATE 7 O-20 geometry, underbody flow, H = 4cms, 0° incidence

(a) without sideplates

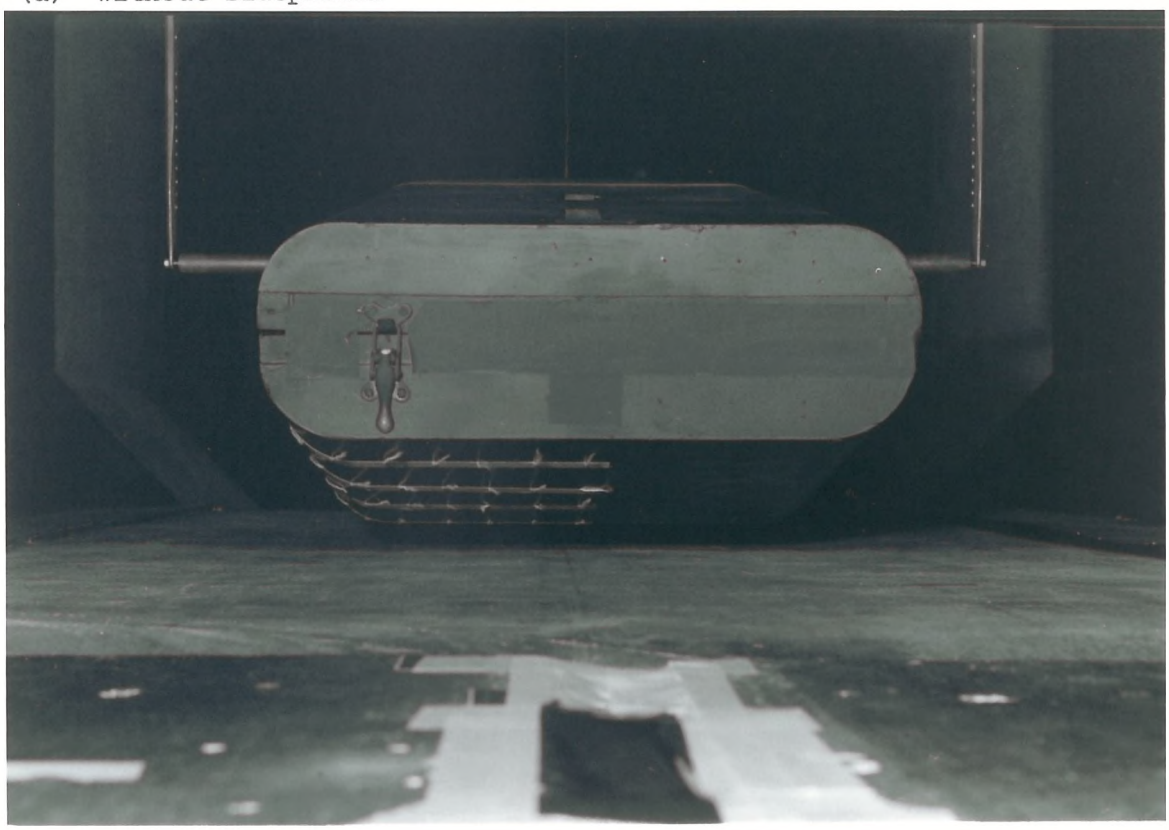

(b) with sideplates

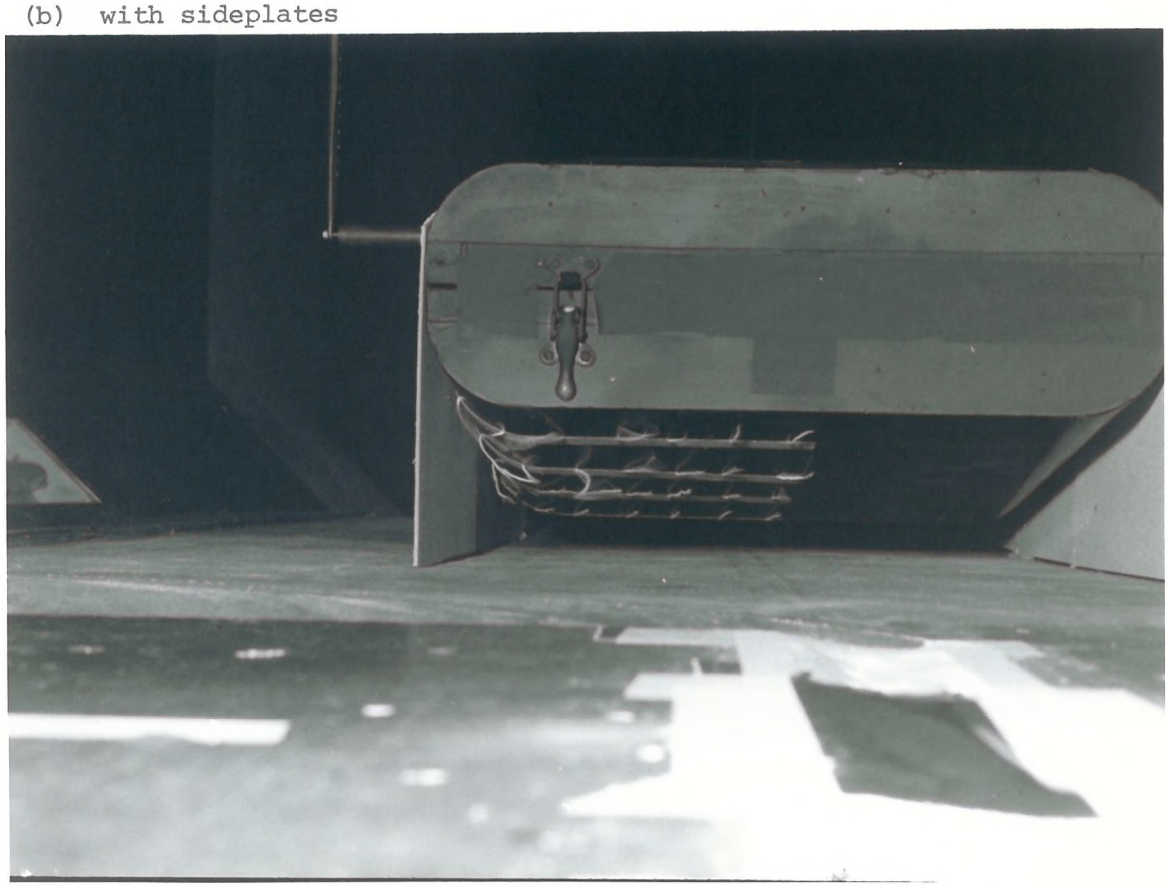

PLATE 8 O-20 geometry, underbody flow, H = 4cms, 10° incidence

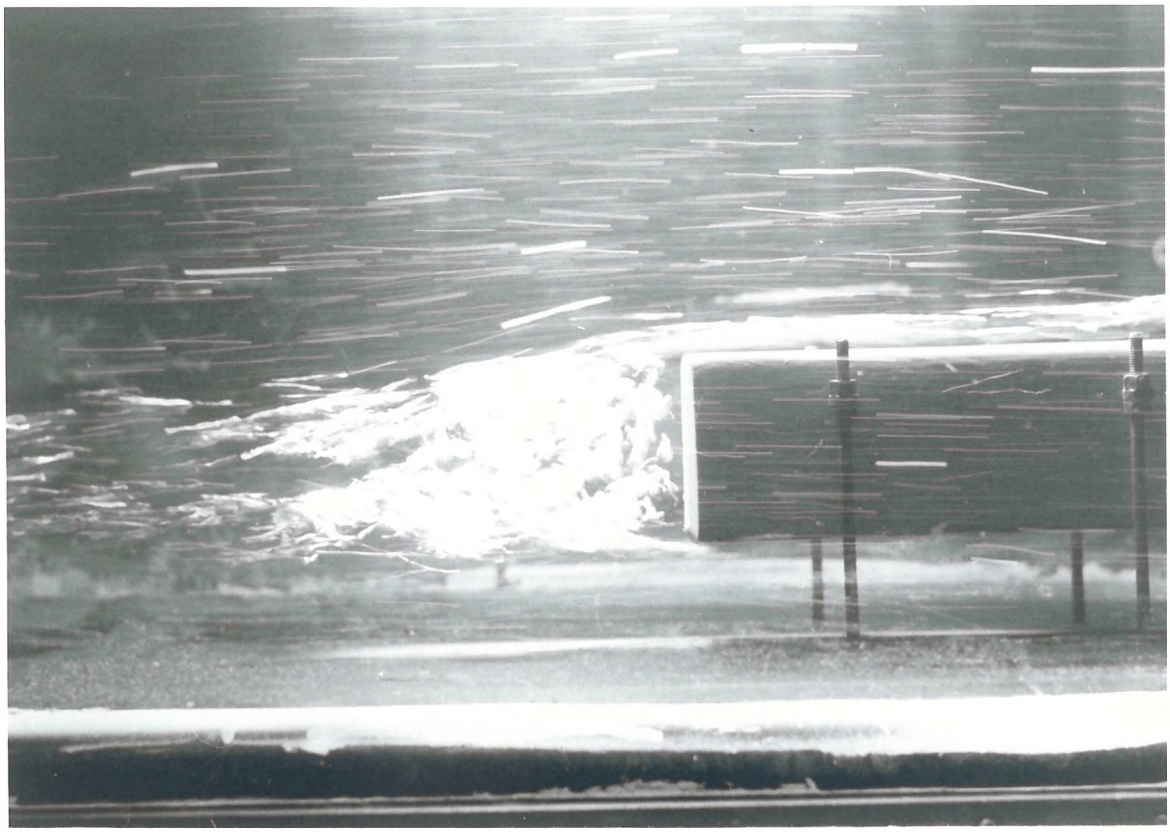

PLATE 9 O-O geometry, upper and lower surface tracers

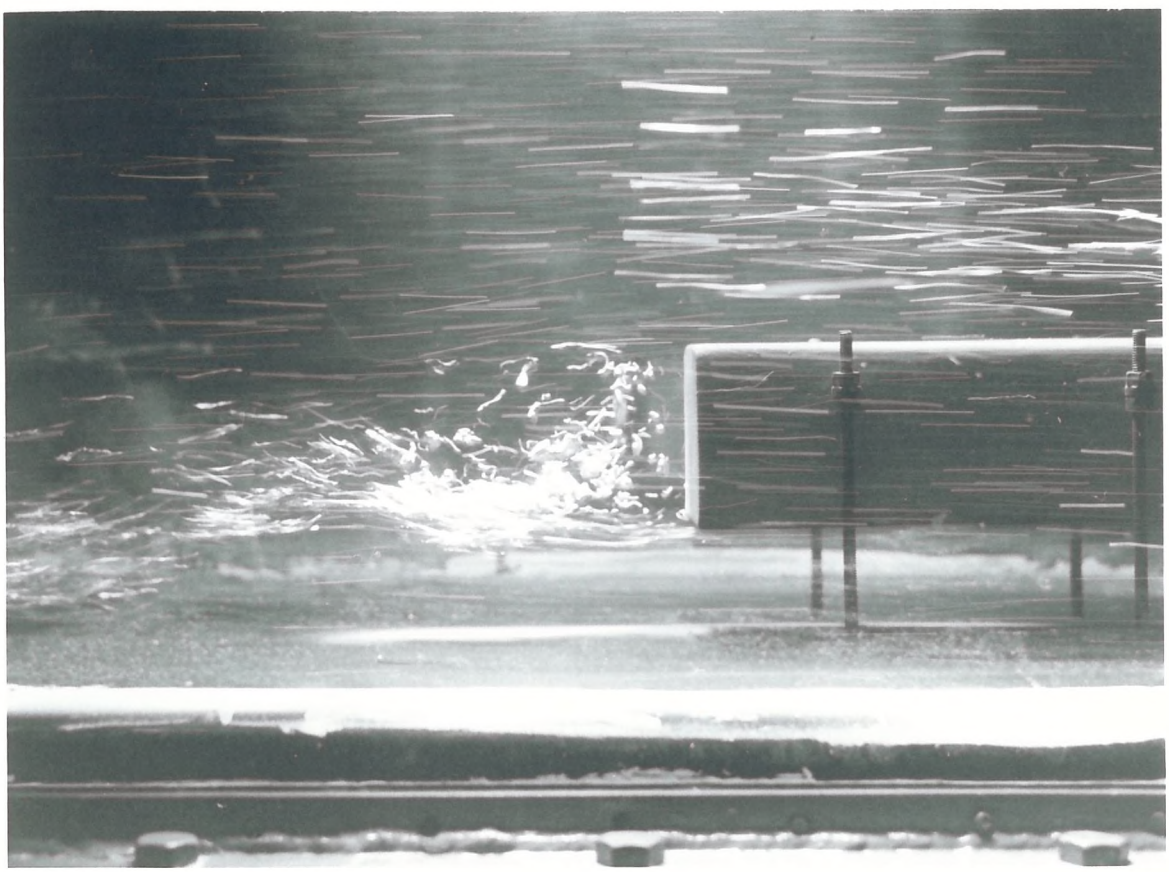

PLATE 10 O-O geometry, lower surface tracers

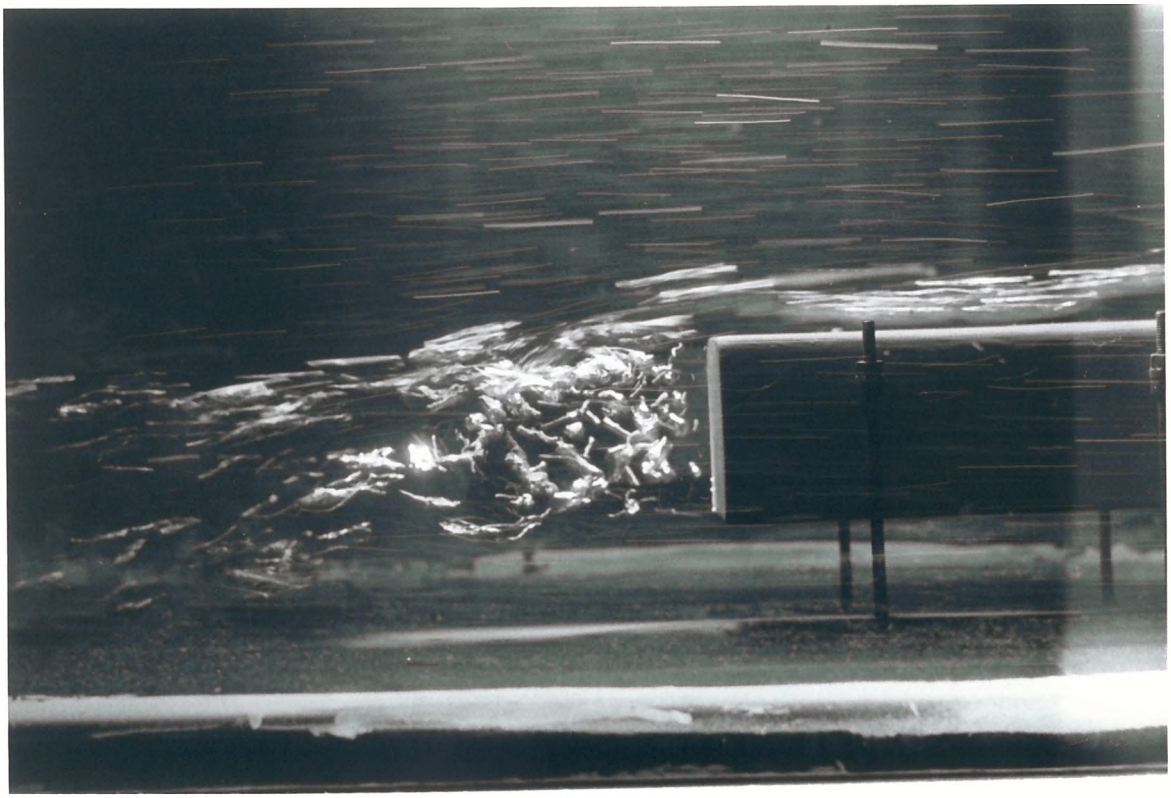

PLATE 11 O-O geometry, upper surface tracers

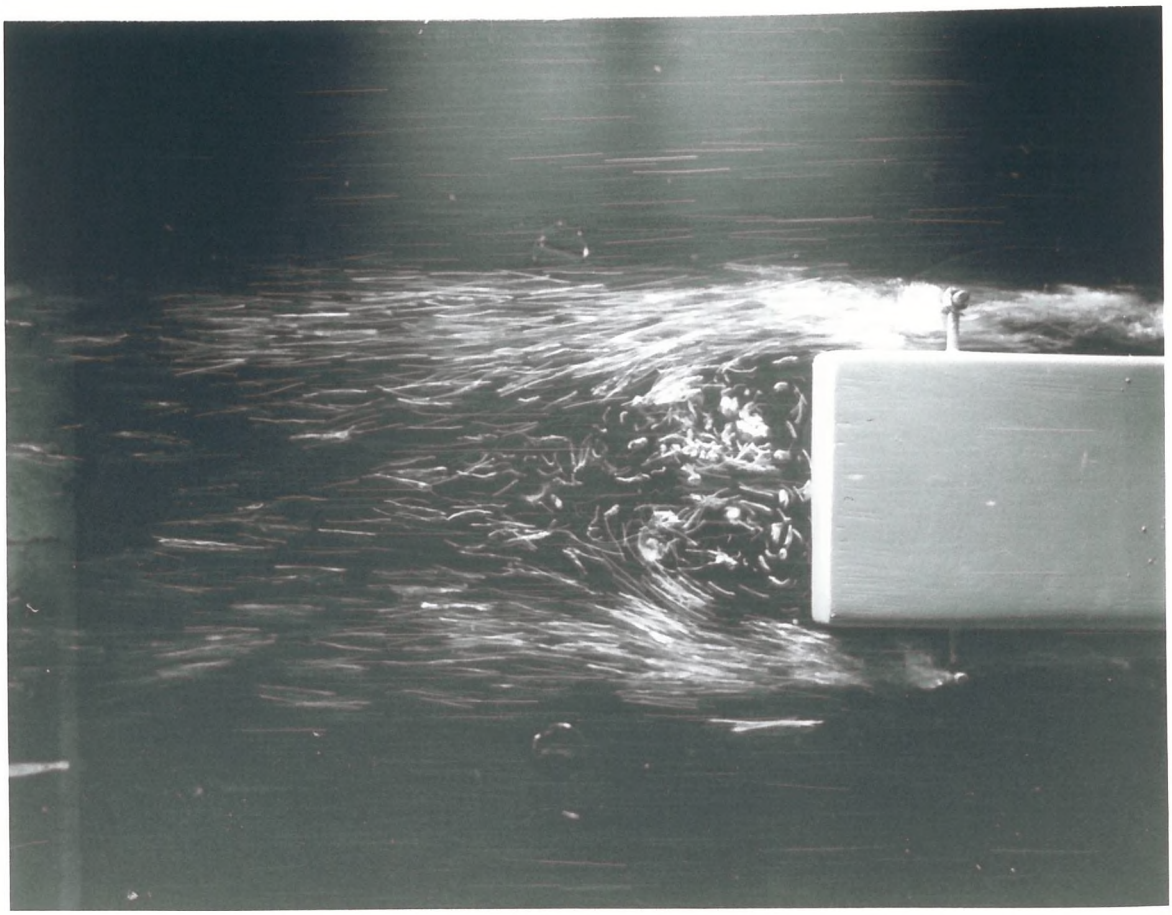

PLATE 12 O-O geometry, side surface tracers

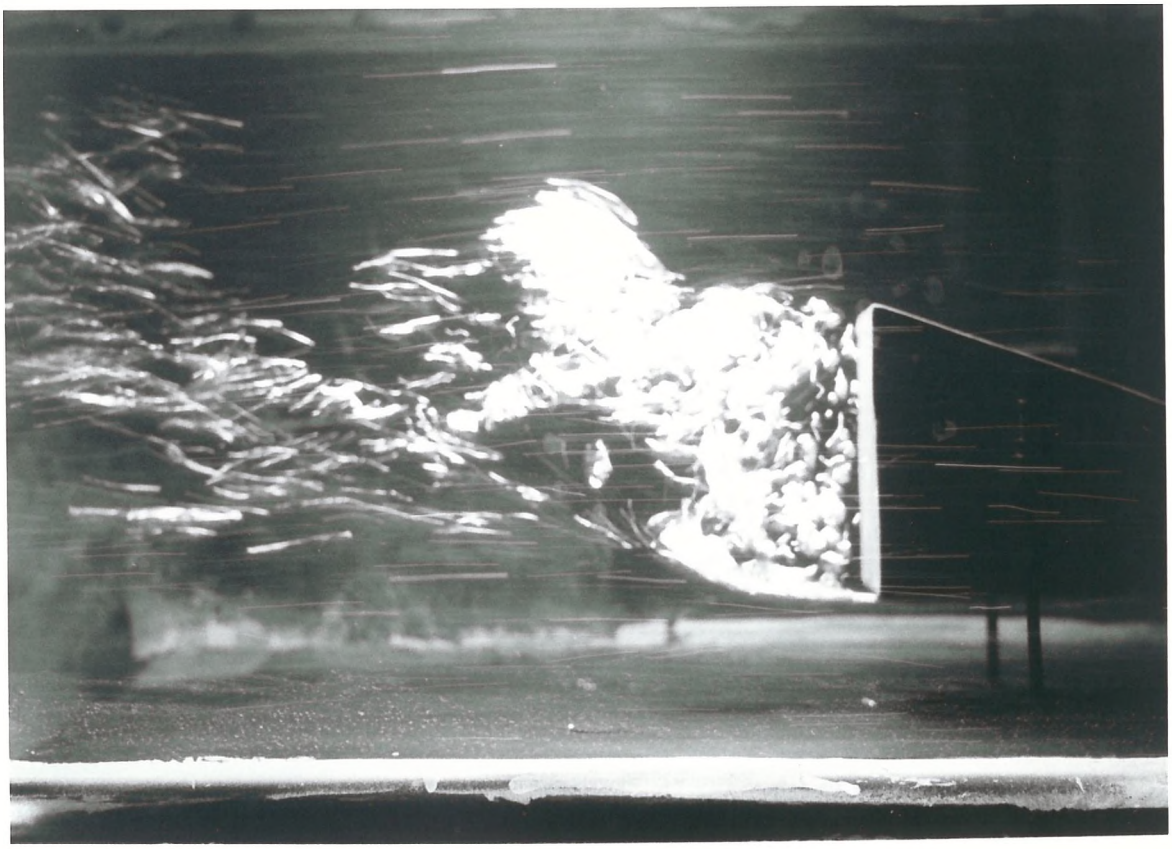

PLATE 13 20-0 geometry, lower surface tracers

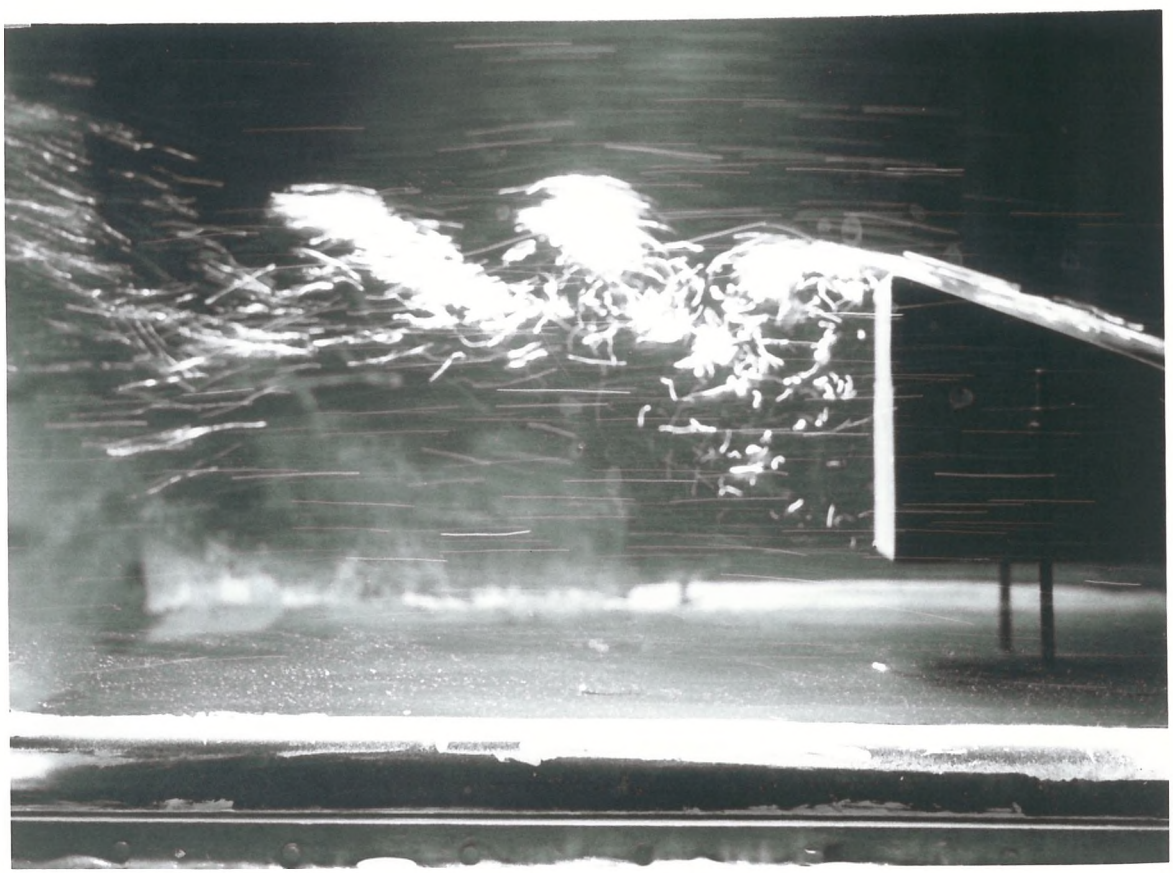

PLATE 14 20-0 geometry, upper surface tracers

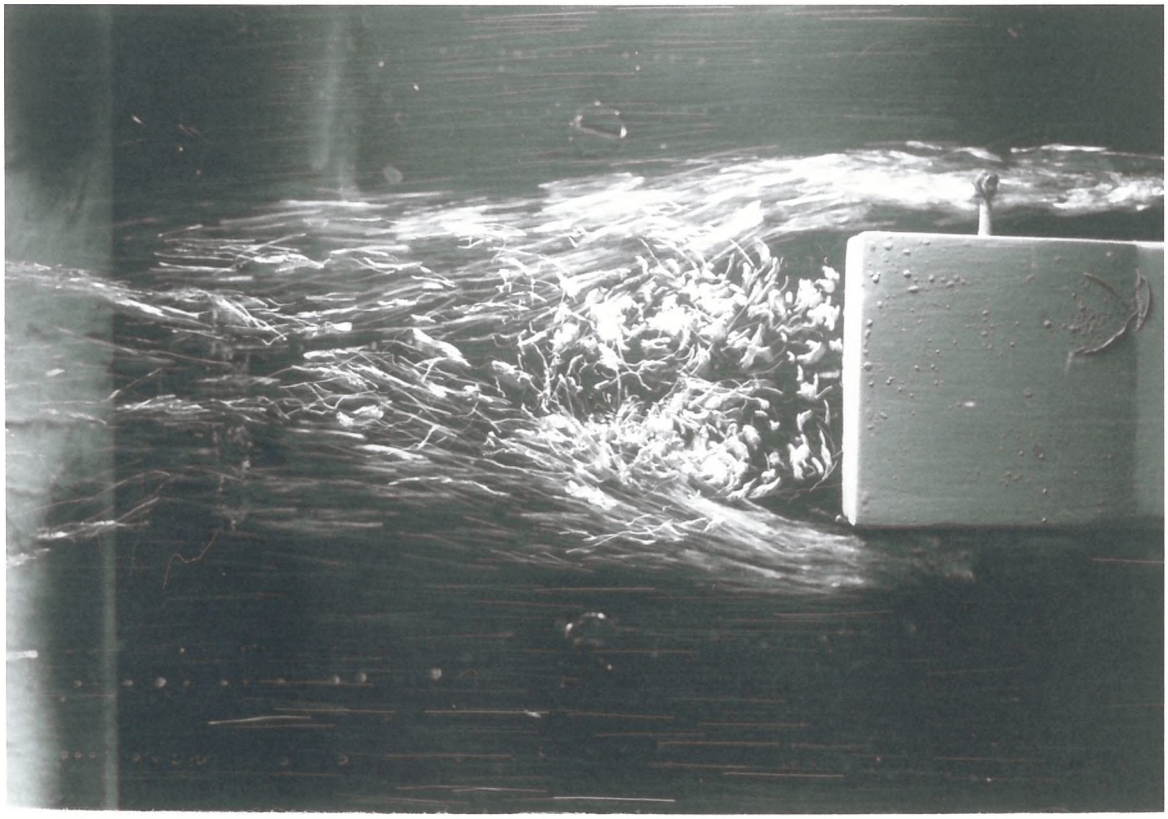

PLATE 15 20-0 geometry, side surface tracers

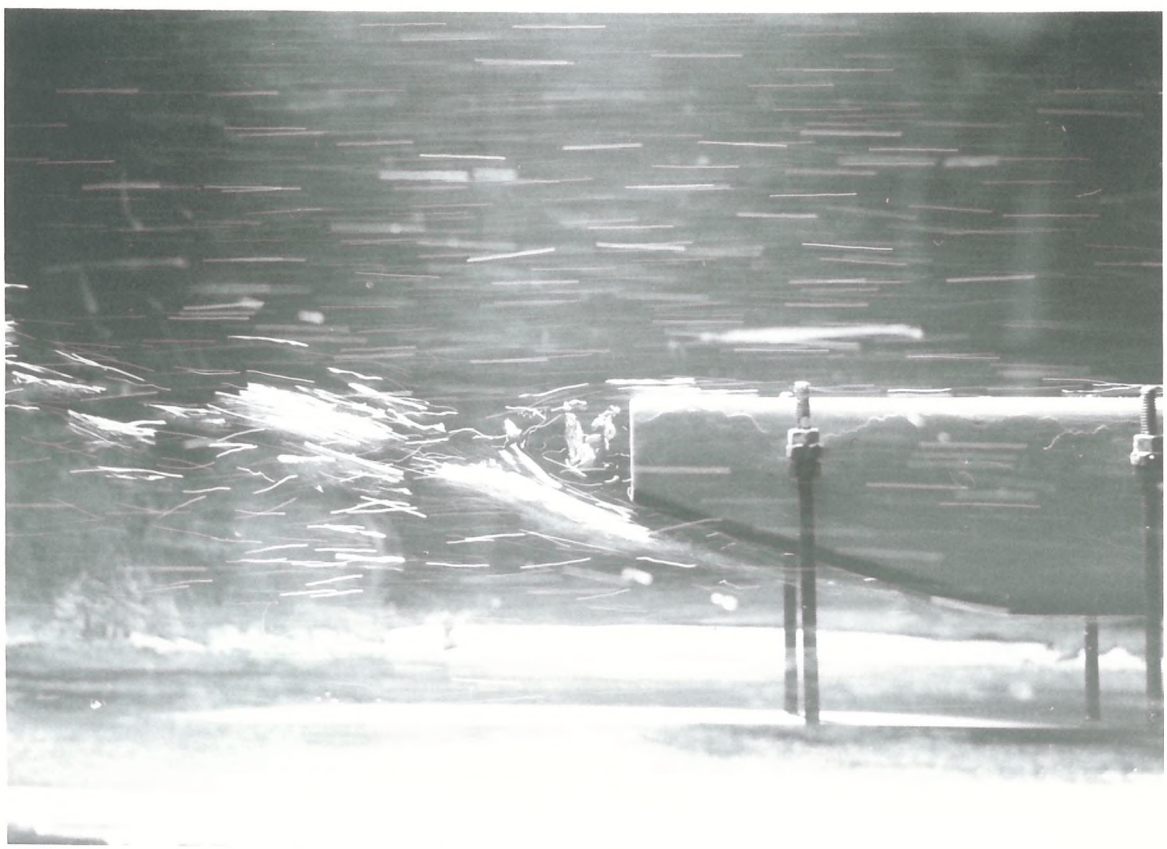

PLATE 16 0-20 geometry, lower surface tracers

PLATE 17 O-20 geometry, upper surface tracers

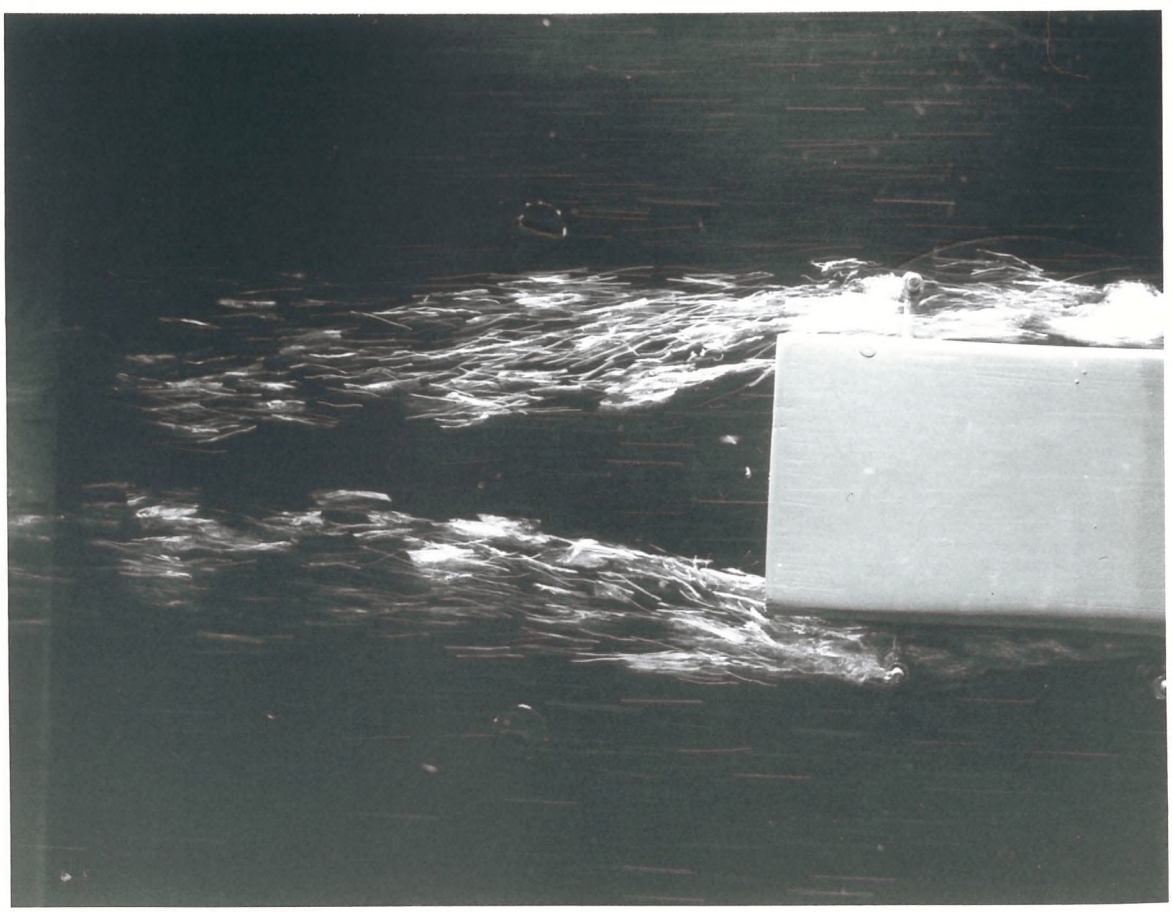

PLATE 18 O-20 geometry, side surface tracers

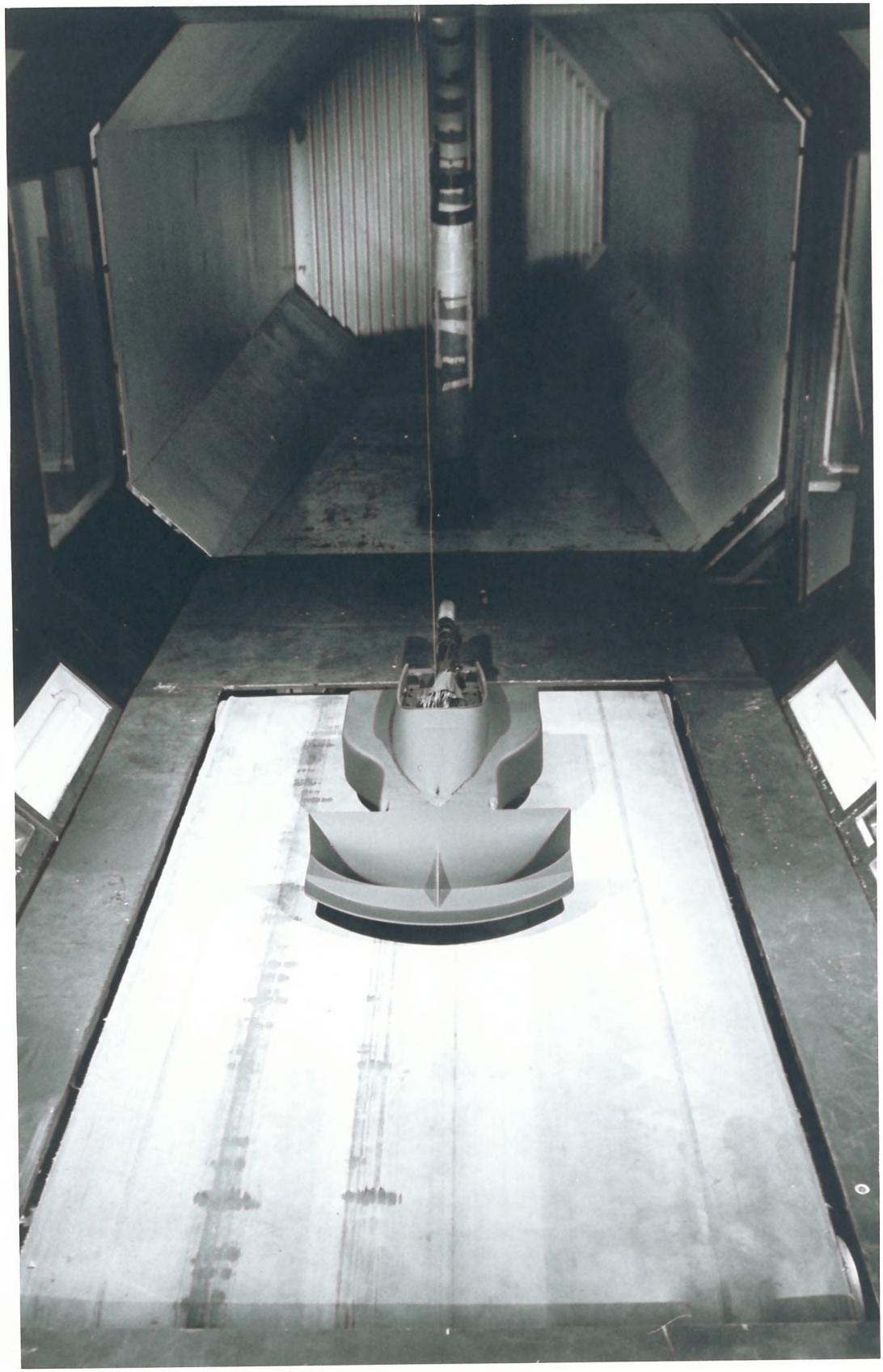

PLATE 19 RACING CAR MODEL MOUNTED OVER MOVING GROUND BELT FACILITY